Stony Brook University

Quantum Critical Behaviors in Magnetic Systems: Yb_3Pt_4, YFe_2Al_{10} and Yb_2Pt_2Pb

A Dissertation Presented

by

Liusuo Wu

to

The Graduate School

in Partial Fulfillment of the Requirements

for the Degree of

Doctor of Philosophy

in

Physics

Stony Brook University

August 2013

Stony Brook University

The Graduate School

Liusuo Wu

We, the dissertation committee for the above candidate for the Doctor of Philosophy degree, hereby recommend acceptance of this dissertation.

Meigan Aronson - Dissertation Advisor

Professor, Department of Physics and Astronomy, Stony Brook University

Barbara V. Jacak - Chairperson of Defense

Distinguished Professor, Department of Physics and Astronomy, Stony Brook University

Philip B. Allen

Professor, Department of Physics and Astronomy, Stony Brook University

Igor A. Zaliznyak

Department of Physics, Brookhaven National Laboratory

Seung-Hun Lee

Professor, Department of Physics, University of Virginia

The dissertation is accepted by the Graduate School.

Charles Taber

Interim Dean of the Graduate School

Abstract of the Dissertation

Quantum Critical Behaviors in Magnetic Systems: Yb_3Pt_4, YFe_2Al_{10} and Yb_2Pt_2Pb

by

Liusuo Wu

Doctor of Philosophy

in

Physics

Stony Brook University

2013

Quantum phase transitions have attracted a great deal of interest in the study of condensed matter physics. Normally, this refers to continuous transitions that occur at zero temperature ($T = 0$), where the correlation length and time scales diverge, and universal scaling is observed close to the Quantum Critical Point (QCP). Quantum critical scaling differs from its classical counterpart in that the spatial dimension d is replaced by an effective dimension $d + z$, where z is the dynamical critical exponent. In this thesis, we will discuss the search for quantum criticality in magnetic compounds: Yb_3Pt_4, YFe_2Al_{10} and Yb_2Pt_2Pb.

Yb_3Pt_4 is a local moment antiferromagnet (AF) that orders at 2.4 K in zero field. The AF order can be suppressed to zero temperature by a magnetic field of about 1.9 T. A field-temperature phase diagram was established, and it indicates that Yb_3Pt_4 can be tuned to a critical end point (CEP) at $T = 0$. The magnetic properties could be explained well by the mean field theory, and

it suggests that Yb_3Pt_4 was tuned to an AF-QCP with effective dimension $d + z > 4$.

A remarkable behavior of the quantum critical systems is the critical scaling near the QCP, where Fermi liquid (FL) physics usually break down. In the transition metal YFe_2Al_{10}, strong divergencies in magnetic susceptibility ($\chi \sim T^{-1.4}$) and magnetic specific heat ($C_M/T \sim -log\ T$) were observed. Universal scaling was found in the magnetic susceptibility ($d\chi/dT = B^{-1.4}\phi(T/B^{0.6})$) and specific heat ($\Delta C_M/T = \varphi(T/B^{0.6})$). This indicates that YFe_2Al_{10} may be located close to a QCP without tuning. Further scaling analysis indicates that the spatial dimension d is equal to the dynamical exponent z at this QCP.

Yb_2Pt_2Pb is a frustrated magnet that crystallizes in a 2D Shastry-Sutherland lattice (SSL). Elastic and inelastic neutron scattering experiments on aligned single crystals will be discussed. Spinon like excitations with broad continuum were observed in zero fields, indicating that the one-dimensional Luttinger liquid may be the dominant physics in this material. non-Fermi liquid behaviors were also observed near the field induced AF-QCP, indicating heavy fermion physics may also be relevant.

To my grandparents.

Contents

List of Figures

List of Tables

Acknowledgements

Many people have helped me during my graduate study, and it is really my pleasure to acknowledge them here. First of all, I would like to thank my advisor Prof. Meigan Aronson, for her support and guidance. I joined the group at the beginning of my third year of graduate school, which was a little bit late for a graduate student. I was wandering around without knowing what to do, and I really appreciate Prof. Meigan Aronson for introducing me to condensed matter physics at that time, and instructing me to start my Ph.D research. I have benefited a lot during these several years studying in the group. Meigan has provided me a lot of opportunities to access different facilities to perform the experiments we needed, and most important, to talk to and learn from many people around. This thesis work would not be possible without her constant help.

It is my pleasure to thank Dr. Igor A. Zaliznyak in Brookhaven National Laboratory. He is an expert on neutron scattering and low dimensional quantum magnetism. He has spent much of his time explaining the physics to me, and instructing me on neutron scattering analysis. I am really grateful for his advising. He first pointed out that Yb_2Pt_2Pb is actually a one-dimensional system. Although a lot of work is still needed, the overall picture of this material has become much clearer under his guidance.

I owe a lot to Moosung Kim, who has helped me with various things in the lab. Moosung always performed the most clean and careful experiments. The understanding of the neutron data of Yb_2Pt_2Pb presented in this thesis was based on many of his thermal property measurements. He is always helpful when I have problems, and he has served as one of my co-advisors and friends in the lab. He taught me many experimental techniques very patiently. During his 'smoking' time every afternoon, I have learned a lot from him, and it is really a pleasure to have worked with him. I would also like to thank Yuri Janssen, who instructed me in my first year study of the project Yb_3Pt_4 in the group. Yuri showed me lots of things in the lab, and we have worked together at many neutron beam times. Yuri is an expert on various things, including growing high quality single crystals and making high quality beers.

Although I am not good at drinking, I still want to thank him for bringing us many happy times with his wonderful beers. Additionally, I benefited a lot from Keeseong Park, who initiated the research on the system YFe_2Al_{10}, which has been continued in this thesis. Keeseong was always very nice to me and taught me a lot about electrical measurements, especially the low temperature resistivity measurements in the dilution refrigerator. I would also like to thank Monika Gamza, and she has put great effort into working on the doping experiments of the YFe_2Al_{10} system, and helped me with the neutron and X-ray experiments. Wojciech Miiller has put a lot of effort into the Yb_2Pt_2Pb project, and I would also like to thank him for the help with the neutron and X-ray experiments, and for teaching me how to use Fulprof and various other things. I have received lots of help from Jack Simonson in the lab. I really would like to thank him for staying with me during the neutron beam time. I would also like to thank Daniel McNally for the help during neutron beam times. I want to thank Mikhail Feygenson also, who had helped me a lot during the neutron experiments, and it is always nice to see him at Oak Ridge. Also, I would like to thank Carlos Marques. Without his continuous effort for refining the crystal growth, most of the neutron scattering experiments in this thesis would not have happened. I would also like to thank Marcus C. Bennett for his help of the project of Yb_3Pt_4. I would like to thank Jennifer Misuraca for the EDX experiments and Hua He for many useful discussions. I would also like to thank Greg Smith, Tom Orvis, Akshat Puri, Thomas Ciavatti, Jed Kistner-Morris, and Shelby Zellman for the sample growth and other helps in the lab.

I am grateful to all the instrument scientists who helped us during the neutron scattering experiments, especially Songxue Chi, Jeffrey W. Lynn, Yiming Qiu and John R. D. Copley at NCNR-NIST, and Georg Ehlers, Andrey Podlesnyak at SNS, Oak Ridge National Lab. I would like to thank Christie Nelson for the support during the X-ray experiments at NSLS, Brookhaven National Lab. I am very sorry that many times I have had to ask for their help in the midnights or in the weekends. Also many thanks go to the sample environment group for their help with many of our low temperature measurements.

I want to thank Prof. Alexei Tsvelik for the discussions of the materials YFe_2Al_{10} and Yb_2Pt_2Pb, and our collaborator Manuel Brando from Max-Planck Institute in Germany for the thermal expansion measurements. I would like to thank Prof. Jacobus Verbaarschot for his help during my second year study in Stony Brook University. I also want to thank Prof. Barbara V. Jacak, Prof. Philip B. Allen from Stony Brook University and Prof. Seung-Hun Lee from University of Virginia for being my defense committee members and

spending time on reading my thesis. Pat Peiliker, Pernille Jensen, and Sara Lutterbie in Stony Brook University and Lauri Peragine from Brookhaven National Lab have also helped me with many of the paperwork during my graduate study, and I want to thank all of them here.

I want to thank all my friends in Stony Brook, and they have made my life living in Long Island much more enjoyable. My family and my wife have been always supportive, and I can never thank them enough. I would also like to express my special thanks to two of my teachers, Mr. Weidong Sun, and Ms. Sufen Sun, for their constant encouragement over all these years.

Chapter 1

Introduction

It is the quantum criticality of $T = 0$ phase transitions and related behaviors that interest us in this thesis. In this chapter, we briefly introduce the role of critical behavior in classical phase transitions, and also their extension to quantum phase transitions. Heavy fermions, metal-insulator transitions and low dimensional frustrated quantum magnets, which have received extensive study as test systems for quantum phase transitions, are also discussed.

1.1 Classical Phase Transition

A phase transition is the change of a system between different states of matter, and it is something that we encounter everyday in our life, such as changes of liquid water to solid ice. Phase transitions and related phenomena are very important in condensed matter physics, and great success has been achieved in the last century in their description and classification [1, 2]. There is still considerable interest in this field today.

1.1.1 First Order and Second Order Phase Transitions

Based on the behaviors of the thermodynamic free energy, Ehrenfest has classified phase transitions into different classes through the derivatives of the free energy with respect to different variables [1, 2]. First order phase transitions are defined as having a discontinuity in the first derivative of the free energy, and it is the second derivatives that exhibit discontinuous changes in second order phase transitions. However, Ehrenfest did not account for the situation where the second derivative of the free energy diverges to infinity. A modern classification divides the phase transitions into discontinuous transitions and continuous transitions. The discontinuous phase

transitions are those that exhibit discontinuities in entropy S (fig. 1.1a), and thus involve a finite latent heat during the transition. This is similar to the Ehrenfest classification of first order phase transitions. In discontinuous phase transitions, the second derivative of the free energy is not well defined at the transition point T_c, and the experimentally measured specific heat, as the temperature derivative of the entropy, shows a 'infinite' sharp peak at T_c, as shown in fig. 1.1c. The second order or higher order phase transitions with continuous entropy are now defined as continuous transitions (fig. 1.1b), where no latent heat accompanies the phase transition. As shown in fig. 1.1c, the second derivative of the free energy could have a discontinuous jump or a power law like divergence to infinity at T_c, depending on the nature of critical fluctuations.

So far, we have considered transitions that happen at finite temperatures. The main differences between discontinuous transitions and continuous transitions is whether there is a latent heat or if there is an entropy change involved during the transition. Based on the system free energy F [1, 2]

$$F = U - TS, \tag{1.1}$$

these phase transitions are driven by the competition between the system internal energy U and entropy S, and are tuned by the change of temperature. A naive question could be asked: what will happen when the temperature T goes to zero? Now everything is constrained by the third thermodynamic law where the entropy change between different states is zero ($\Delta S = 0$). From this point of view, the classification we just mentioned above for first order discontinuous and second order continuous phase transitions will fail. Since the entropy change will always be zero at zero temperature, in principle one cannot distinguish these two kinds of phase transitions when $T = 0$. Experimentally, the transition at exact zero can never be reached, and one can only approach this point from finite temperatures. It turns out that the way a phase line is suppressed to zero temperature is very different for first order discontinuous transitions and for the second order continuous phase transitions. Based on the Clausius-Clapeyron relation [1, 2]

$$\frac{dT}{dP} = \frac{\Delta V}{\Delta S} \qquad \text{or} \qquad \frac{dT}{dB} = -\frac{\Delta M}{\Delta S}, \tag{1.2}$$

the volume change ΔV or magnetization change ΔM is always finite while ΔS is restricted to zero as $T = 0$. Thus the slope of the phase boundary dT/dP or dT/dB goes to infinity as a first order phase transition at $T_c = 0$ is approached, and this appears as a vertical phase line [6], as shown in fig. 1.2a. This has

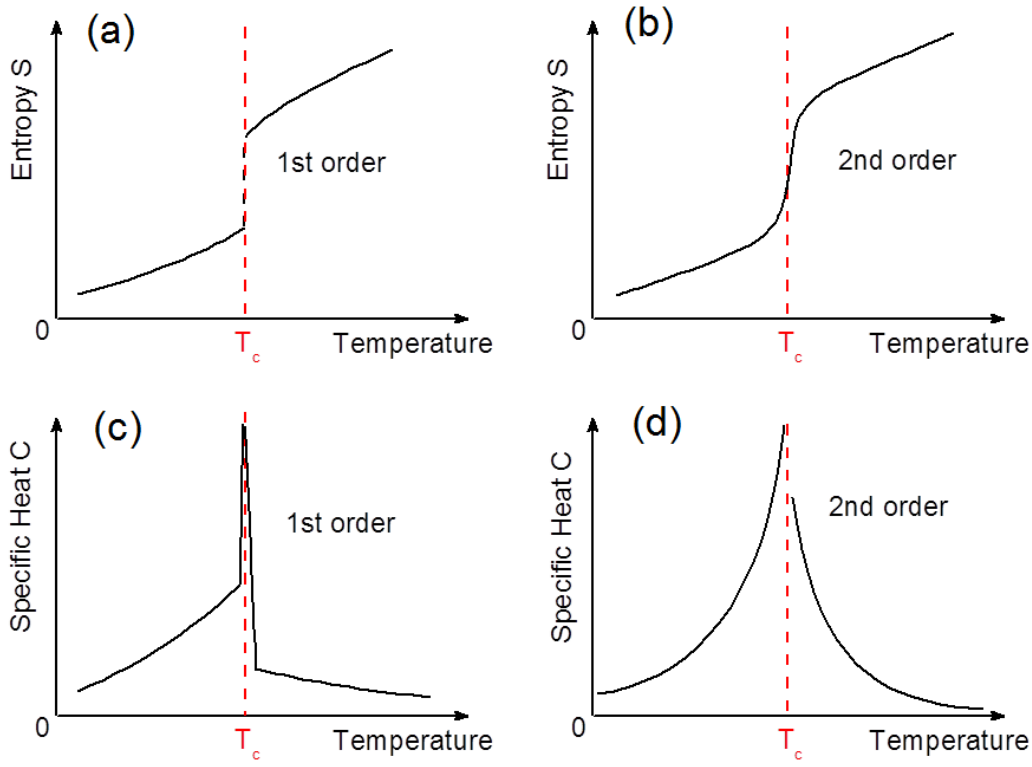

Figure 1.1: Schematic behaviors of the entropy respect to temperature for first order discontinuous transitions (a) and second order continuous transitions (b). (c)The measured specific heat shows an infinite sharp peat at the first order phase transition temperature T_c. (d) The specific heat could be discontinuous or power law like divergent at a second order continuous phase transition at T_c. [1, 2]

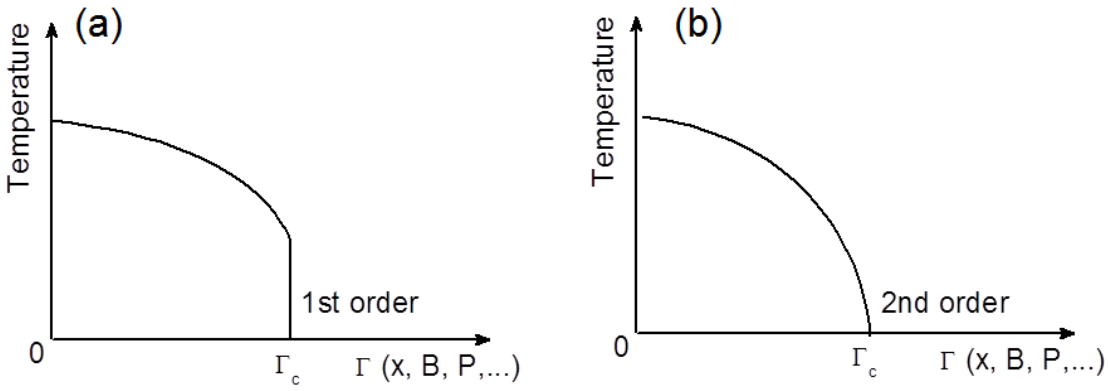

Figure 1.2: Schematic phase diagram as a system was tuned to a first order (a) or a second order (b) critical point at zero temperature based on the Clausius - Clapeyron relation. The tuning parameter Γ could be chemical doping x, pressure P or magnetic field B. [6]

been confirmed in real systems as in itinerant ferromagnetic critical points in $ZrZn_2$, and UGe_2 [7, 8, 9], where a first order ferromagnetic critical point was realized by tuning pressure. However, for a second order phase transition at zero temperature this is not necessarily the case, and hence the phase line can be suppressed to zero temperature in a power law (fig. 1.2b), as seen in the field driven second order antiferromagnetic critical point in $YbRh_2Si_2$ [10]. More interesting behaviors will be discussed later for phase transitions occurring at zero temperature, the so-called quantum phase transitions.

1.1.2 Critical Scaling

The critical phenomena associated with continuous phase transitions turns out to be very interesting. Peculiar properties are exhibited near the critical point, and universal values of the power law exponents are found for different systems [1, 2, 3, 4]. All of these are due to the scale invariant divergence of the spatial correlation length near the critical point. We start from a non-analytic thermodynamic free energy density f at the phase transition T_c, assuming it has a homogeneous form such as

$$f(t,h) = b^{-d} f_F(tb^z, hb^{y_h}) \tag{1.3}$$

near the critical point, where d is the system dimension, z and y_h are the scaling exponents associated with the two tuning parameters t and h [1, 2, 3, 4, 5]. Usually t is the reduced temperature $t = (1 - T_c/T)$, and thus z is referred

to as the dynamical exponent. Here b is an arbitrary length resealing factor, which could be renormalized as $b = t^{-1/z}$ or $b = h^{-1/y_h}$. Thus, we could rewrite the scaling function of the free energy density as

$$f(t,h) = t^{d/z} f_F(h/t^{y_h/z}) = h^{d/y_h} \tilde{f}_F(t/h^{z/y_h}), \tag{1.4}$$

We are going to show that all the other thermodynamic quantities can then be expressed in a similar way based on this same free energy.

Specific Heat

The specific heat typically diverges at the critical point as

$$C \sim t^{-\alpha}, \tag{1.5}$$

where α is the corresponding critical exponent. Based on the definition, we derive this directly from the free energy density f,

$$C \sim \frac{\partial^2 f(t,h)}{\partial t^2} = t^{d/z-2} f_c(h/t^{y_h/z}), \tag{1.6}$$

where f_c is the new scaling function for the specific heat. From this, we see that

$$\alpha = 2 - d/z. \tag{1.7}$$

This clearly shows that the critical exponent α is only dependent on the spatial and dynamic dimensionalities of the system.

Magnetization

Assuming this is a magnetic critical point with tuning parameter h, a similar scaling form for the magnetization can be derived using the expression

$$m(t,h) \sim \frac{\partial f_F(t,h)}{\partial h} \sim t^{(d-y_h)/z} f_m(h/t^{y_h/z}). \tag{1.8}$$

Here, we define another critical exponent β, where

$$m \sim t^{\beta} = t^{(d-y_h)/z}, \tag{1.9}$$

with

$$\beta = (d - y_h)/z, \tag{1.10}$$

in the $h \to 0$ limit. We rewrite equation 1.8 as

$$m(t,h) \sim h^{(d-y_h)/y_h} \tilde{f}_m(t/h^{z/y_h}). \tag{1.11}$$

Then in the $t \to 0$ limit, we have the field dependent magnetization as

$$m \sim h^{1/\delta} = h^{(d-y_h)/y_h}, \tag{1.12}$$

with the critical exponent

$$\delta = y_h/(d-y_h). \tag{1.13}$$

Magnetic Susceptibility

Knowing the magnetization, we now calculate the ac magnetic susceptibility as

$$\chi(t,h) \sim \frac{\partial m}{\partial h} \sim t^{(d-2y_h)/z} f_\chi(h/t^{y_h/z}), \tag{1.14}$$

and the critical exponent γ is defined here as

$$\gamma = (2y_h - d)/z \tag{1.15}$$

where $\chi \sim t^{-\gamma}$ in the $h \to 0$ limit.

Since all these thermal properties can be related to the derivatives of the free energy, the critical exponents α, β, δ and γ obtained here can be related to the scaling exponents d, z, and y_h, which are a set of particular values for the critical points for systems of the same universality class. As a result of the above relations, we can find two general identities between these different critical exponents:

$$\alpha + 2\beta + \gamma = 2, \tag{1.16}$$

and

$$\delta - 1 = \gamma/\beta. \tag{1.17}$$

These two relations are refereed as Rushbrook's identity (1.16) and Widom's identity (1.17), and these relations themselves are not dependent on the system dimension d [1, 2, 3, 4].

Correlation Length

Since the partition function Z is an extensive property, it scales with the system volume $V = L^d$. As indicated in the schematic fig. 1.3 of a magnetic system with blocked correlated spins on the length scale ξ, the number of these blocks scales as $(L/\xi)^d$, and thus $lnZ \sim (L/\xi)^d$ [1, 2, 3, 4]. The singular part of

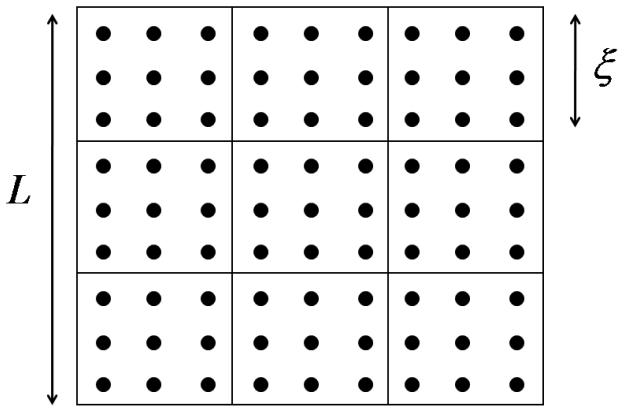

Figure 1.3: A schematic view of blocks of spins. The spins (•) are correlated with each other in the small box with length scale ξ in a system with volume $V = L^d$. [5]

the free energy density f depends on the length scale according to [1, 2, 3, 4, 5]

$$f = \frac{F}{Nk_BTV} = \frac{ln\ Z}{L^d} \sim \xi^{-d}. \tag{1.18}$$

A characteristic property of a second order critical point is the divergence of the correlation length ξ_t

$$\xi_t \sim t^{-\nu_t}, \tag{1.19}$$

at the critical point $t = 0$, where ν_t is another critical exponent. Any other microscopic length scale like lattice parameter a is now not important near the critical point, compared to the divergent correlation length ξ. Combining equation 1.18 and 1.19, we find that the singular free energy density diverges as

$$f \sim t^{\nu_t d}. \tag{1.20}$$

Comparing relation 1.20 with 1.4, we easily see that the new critical exponent ν_t is just the inverse of the dynamic scaling exponent z ($\nu_t = 1/z$). We can also rewrite the relation 1.7 as

$$2 - \alpha = d\nu_t. \tag{1.21}$$

This is Josephson's identity, which is also known as the hyperscaling relation, where the spatial dimension d is involved [1, 2, 3, 4]. The critical exponents for systems with different dimensions are listed below in table 1.1. Rushbrook's identity 1.16 and Widom's identity 1.17 are always valid with the exponents for different system dimensions. However, the hyperscaling relation 1.21 is only valid for $d \leq 4$, which is referred to as the upper critical dimension.

Table 1.1: Critical exponents for systems with different universality classes. [1, 2, 3, 4, 5]

		α	β	γ	δ	$\nu_t = 1/z$
$d = 2$	Ising	0	1/8	7/4	15	1
$d = 3$	Ising	0.12	0.31	1.25	5	0.64
$d = 3$	XY	0	0.33	1.33	5	0.66
$d = 3$	Heisenberg	-0.14	0.35	1.4	5	0.7
	Mean Field	0	1/2	1	3	1/2

1.2 Quantum Phase Transition

Quantum phase transitions usually refer to continuous transitions happening at $T = 0$ [11]. Different from the classical thermal phase transitions that occur at nonzero temperatures that are due to thermal fluctuations, quantum phase transitions are driven by quantum fluctuations with non-thermal external tuning parameters such as pressure P, doping x, or magnetic field B.

1.2.1 Quantum Critical Scaling

We have shown that the divergence of the correlation length is responsible for the singularity of the free energy density, and thus they lead to divergencies of all the other thermodynamic quantities near a temperature driven classical critical point [11]. Since quantum phase transitions occur at $T = 0$, quantum fluctuations are the dominating factor here. A fundamental difference between classical and quantum phase transitions is that not only the correlation length in the spatial dimension d is divergent, but the correlations also extend to infinity along the direction of the imaginary time $\tau = 1/kT$ as $T \to 0$ [11].

Since the imaginary time scales with the correlation length as

$$\tau \sim \frac{1}{T} \sim \xi^z, \tag{1.22}$$

it is thus natural that the extra dynamical dimension z adds to the system, and the singular part of the free energy for a quantum phase transition now turns out to be

$$F(T, B) = b^{-(d+z)} f(Tb^z, hb^{y_h}). \tag{1.23}$$

This function can be written in the scaling form as

$$F(T, B) = T^{\frac{d+z}{z}} f_F(\frac{h}{T^{y_h/z}}) = h^{\frac{d+z}{y_h}} \tilde{f}_F(\frac{T}{h^{z/y_h}}). \tag{1.24}$$

Following the same strategy that we followed for the classical phase transitions, we can derive all the divergent thermal properties from the free energy. Thus, the critical part of the specific heat scales as

$$\frac{C(T, h)}{T} = \frac{\partial^2 F(T, h)}{\partial T^2} = T^{\frac{d+z}{z}-2} f_c(\frac{h}{T^{y_h/z}}), \tag{1.25}$$

and we define the critical exponent α as

$$\alpha = 2 - (d + z)/z. \tag{1.26}$$

Similarly, the magnetization $M(T, h)$ scales as

$$M(T, h) = \frac{\partial F(T, h)}{\partial h} = T^{\frac{d+z}{z}-\frac{y_h}{z}} f_M(\frac{h}{T^{y_h/z}}) = h^{\frac{d+z}{y_h}-1} \tilde{f}_M(\frac{T}{h^{z/y_h}}), \tag{1.27}$$

and the critical exponent β and δ is defined as

$$\beta = (d + z - y_h)/z, \tag{1.28}$$

and

$$\delta = y_h/(d + z - y_h). \tag{1.29}$$

The ac magnetic susceptibility

$$\chi(T, h) = \frac{\partial M(T, h)}{\partial h} = T^{\frac{d+z}{z}-2\frac{y_h}{z}} f_M(\frac{h}{T^{y_h/z}}), \tag{1.30}$$

and thus

$$\gamma = 2y_h/z - (d + z)/z. \tag{1.31}$$

We can also see by inspection that the two identities

$$\alpha + 2\beta + \gamma = 2, \qquad \text{(Rushbrooke's Identity)} \tag{1.32}$$

and

$$\delta - 1 = \gamma/\beta \qquad \text{(Widom's Identity)} \tag{1.33}$$

are still valid for quantum phase transitions.

By comparing the scaling functions of the specific heat, magnetization, and magnetic susceptibility to those we obtained before for classical phase transitions, we found that all the scaling forms are very similar, just with the change of the spatial dimension d to the effective dimension $d+z$ for quantum phase transitions. Accordingly, the hyperscaling relation for quantum phase transitions is modified in the same way as

$$2 - \alpha = (d + z)\nu_t, \tag{1.34}$$

where ν_t is defined as $\xi_t \sim T^{-\nu_t} \sim T^{-1/z}$.

1.2.2 Phase Diagrams and the Quantum Critical Point (QCP)

From the discussion above, we can see that a quantum phase transition in d dimensions can be modeled as a $d+z$ classical phase transition. The dynamical exponent z here could be an integer, or a fractional number depending on the nature of the system [11, 13, 24].

One consequence is that the upper and lower critical dimensions of the system must be modified by z for quantum phase transitions [11, 13, 24]. For example, for a one dimensional (1D) ferromagnetically coupled Ising spin S_z chain, no magnetic order exists at any nonzero temperature. However, at $T = 0$, this 1D Ising system can now mapped to a 2D Ising model where $z = 1$, and it is magnetically ordered for $B \leq B_c$ [11]. In this case, long range magnetic order exists as a phase line at $T = 0$, as marked in fig. 1.4a that terminates at the QCP at B_c. On the other hand, the upper critical dimension is much easier to reach near the QCP than for a classical phase transition. For example, for a three dimensional (3D) Ising spin antiferromagnet, the universality class associated with the field induced QCP should map onto that of a four dimensional (4D) mean field model. This has indeed been observed in the three dimensional local moment antiferromagnet $MnCl_2{\cdot}4H_2O$ [14], where crossovers to four dimensional mean field behaviors were observed near the QCP around $B_c^{\perp} \simeq 2.33$ T, with the critical exponent β gradually increasing from the 3D Ising value 0.3 to the mean field value 0.5 below ~ 0.5 K. In this

case, the critical fluctuations were cut off as expected for systems over the upper critical dimension ($d + z \geq 4$).

For systems where the effective dimension is between the lower and upper dimensional limits ($1 < d + z < 4$), a thermal phase transition is expected at $T > 0, h = 0$ and a quantum phase transition at $T = 0, h = h_c$. These two transitions are then connected by a line of classical phase transitions with $T_c > 0$ as indicated in fig. 1.4b [11, 13]. Although the quantum phase transition is only present at $T = 0$, physical properties in a broad region of nonzero temperatures are affected through the competition of the two different kinds of critical fluctuations near the QCP. As $T \to 0$, the correlation length corresponding to the thermal fluctuations diverges as

$$\xi_T \sim T^{-\nu_t}, \tag{1.35}$$

while the correlation length related to quantum fluctuations diverges as

$$\xi_h \sim h^{-\nu_h}. \tag{1.36}$$

Here we introduced a critical exponent ν_h of the correlation length with respect to the non-thermal tuning parameter h, which differs from the thermal critical exponent ν_t as $\nu_h/\nu_t = z/y_h$. When $\xi_h > \xi_T$, quantum fluctuations are dominant, and the temperature ranges with $T > h^{z/y_h}$ are referred to as quantum critical regions. As marked by the red fan-shaped region in fig. 1.4, this quantum critical region extends from the QCP at $T = 0$ to much higher temperatures [11, 13, 24]. In the other limit, when $\xi_T > \xi_h$, the thermal fluctuations become more important in temperature regions $T < h^{z/y_h}$. Crossover behaviors were observed at $T \sim h^{z/y_h}$ that connect these two limits, where these two fluctuations have comparable strengths. The fan shaped critical region is determined by the critical exponents z/y_h, which could be linear when $z/y_h = 1$, or depends in particular ways on the nature of different QCPs [11, 13]. An alternative way to understand the microscopic picture of the quantum criticality is explained by Subir Sachdev in [11, 13]. In the quantum critical region, the thermal equilibration time $\tau \propto 1/T$ is very short, and it is actually the shortest time allowed by quantum mechanics for the system to relax back to local thermal equilibrium [11, 13]. It was suggested that from this point of view that the quantum critical region is an analogy to a nearly perfect fluid [15].

The additional divergencies of the correlation lengths with imaginary time in quantum phase transitions actually result from the vanishing of a characteristic energy scale, and experimentally this results in E/T scalings near the QCP, as observed in some quantum critical systems [16, 17]. Since

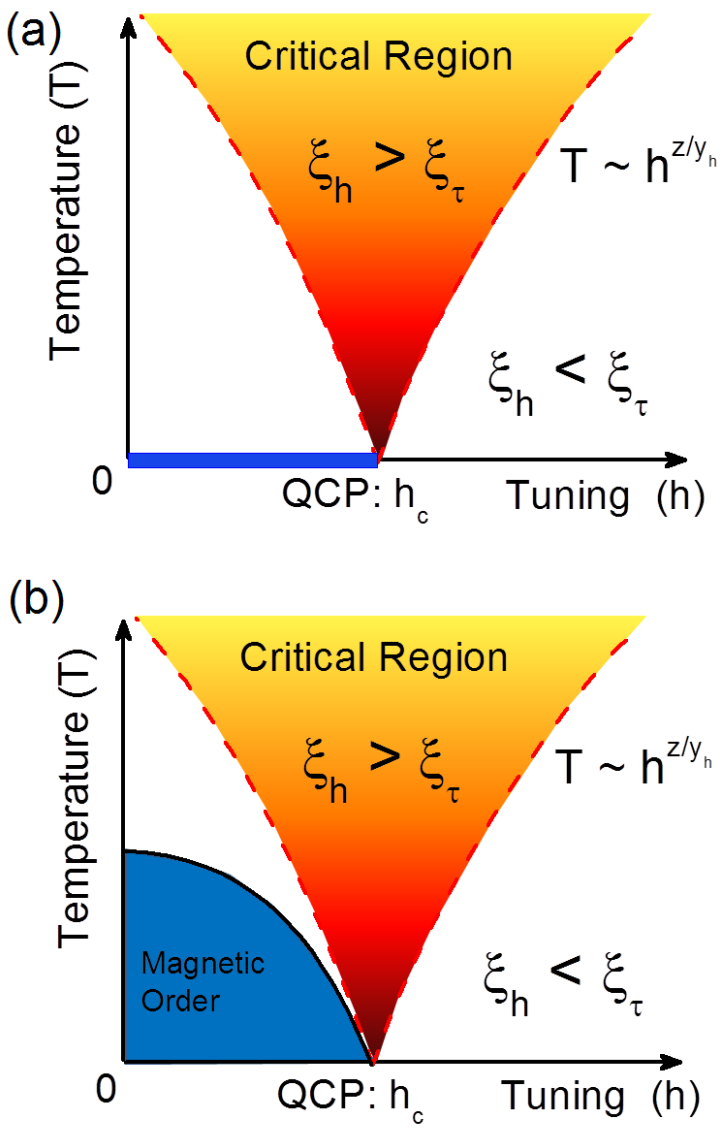

Figure 1.4: A schematic view of phase diagram with a quantum critical point for systems with different dimensions. (a) For the one dimensional ferromagnetic coupling Ising spin chain, no magnetic order exists at non-zero temperatures. However, the system is mapped to a 2D Ising model at $T = 0$, which orders up to the critical field h_c. (b) A higher dimensional system magnetically ordered and this order can be gradually suppressed to a QCP at h_c. The fan-shaped region in both (a) and (b) indicates the quantum critical region where quantum fluctuations are dominant. The red dashed line is the crossover from the quantum critical region to the normal heavy fermion region, where classical thermal fluctuations are dominating. [11, 13]

Table 1.2: Critical exponents of the temperature dependent specific heat, magnetic susceptibility and resistivity predicted by several different theories by Hertz-Millis [24, 25], Moriya et al. [26], and Lonzarich et al. [27] for the itinerant ferromagnetic and antiferromagnetic quantum phase transitions in different dimensions. [12]

Hertz/Millis [24, 25]	AFM	AFM	FM	FM
	$d = 3, z = 2$	$d = 2, z = 2$	$d = 3, z = 3$	$d = 2, z = 3$
C/T	$\gamma - a\sqrt{T}$	$-c\ log\ (T/T_0)$	$-c\ log\ (T/T_0)$	$T^{-1/3}$
$\Delta\chi$	$T^{3/2}$	$\chi_0 - dT$		
$\Delta\rho$	$T^{3/2}$	T	T	

Moriya *et al.* [26]	AFM	AFM	FM	FM
	$d = 3$	$d = 2$	$d = 3$	$d = 2$
C/T	$\gamma - a\sqrt{T}$	$-log\ T$	$-log\ T$	$T^{-1/3}$
χ_Q	$T^{-3/2}$	$-(log\ T)/T$	$T^{-4/3}$	$-T^{-1}/log\ T$
$\Delta\rho$	$T^{3/2}$	T	$T^{5/3}$	$T^{4/3}$

Lonzarich et al. [27]	AFM	FM	FM
	$d = 3, z = 2$	$d = 3, z = 3$	$d = 2, z = 3$
C/T	$\gamma + \sqrt{T}$	$-\ log\ T$	$T^{-1/3}$
$\Delta\chi$	$T^{-3/2}$	$T^{-4/3}$	T^{-1}
ρ	$T^{3/2}$	$T^{5/3}$	$T^{4/3}$

the energy scale E is proportional to the tuning parameter h, scaling behaviors of the thermal properties as functions of $h/T^{y_h/z}$ are also found[18, 19, 20]. In general, a 'naive' scaling analysis near a QCP that assumes the existence of hyperscaling is no longer appropriate, since the effective dimension at $T = 0$ is usually larger than 4 ($d_{\text{eff}} = d + z > 4$) [21, 22, 23]. Several different theories have been proposed to explain the critical phenomena near magnetic quantum critical points. One representive work is the Herz-Millis-Moriya theory [24, 25, 26]. Millis has extended Hertz's work on quantum phase transitions assuming that all the systems considered are above the upper critical dimension. He proposed that the dynamical exponent $z = 2$ for itinerant antiferromagnetic quantum phase transitions and $z = 3$ for itinerant ferromagnetic quantum phase transitions [25]. The exponents predicted by

this theory that govern the temperature dependencies of different measured quantities are listed in table 1.2. The critical exponents calculated with some other self-consistent renormalization models by Moriya et al. [26] and Lonzarich et al. [27] are also listed. We notice that the exponents for the temperature dependent specific heat are basically the same for the three models. However, the exponents for the temperature dependent resistivity and susceptibility are different. Since hyperscaling has broken down, these exponents no longer have the universal values predicted by the 'naive' scaling analysis, and instead reflect the importance of the dangerously irrelevant variables above the critical dimension. More details of the quantum critical scaling can be found in [22, 23].

1.3 Heavy Fermion

Heavy fermion compounds have attracted a lot of attention in the last two decades as prototypical systems for studying quantum criticality and unconventional superconductivity [28, 29]. The heavy fermions are usually rare earth based intermetallic metals, where f electrons are located near the border between the itinerant and localized states. Since the f electron level sits very close to the Fermi energy, they are strongly hybridized with the band of conduction electrons. A great advantage of heavy fermions is that the relevant energy scales can be very small, and different ground states are experimentally accessible through various tuning parameters [30, 32].

1.3.1 The Kondo Effect

Heavy fermion materials involve a lattice of rare-earth moments that are strongly hybridized with the conduction electrons. They are usually referred to as "Kondo Lattice" compounds. There are many wonderful reviews such as [30, 32], and references therein. Heavy fermion systems can be described by the Hamiltonian [30, 32]

$$H = \sum_{ij} t_{ij} c^{+}_{i\sigma} c_{j\sigma} + \sum_{ij} I_{ij} \mathbf{S}_i \cdot \mathbf{S}_j + (1/2) \sum_{i} J \mathbf{S}_i \cdot \mathbf{s}_i. \tag{1.37}$$

The first term describes the conduction electron band with the hopping matrix element t_{ij} and I_{ij} implies the near neighbor exchange interactions between local f moments. The last term determines the interaction between the spins of the conduction electrons

$$\mathbf{s}_i = c^{+}_i \sigma c_i$$

and the onsite localized moments $\mathbf{S}_i$ through the Kondo coupling J. The Kondo effect describes the screening of a localized magnetic ion by the spins of the conduction electrons. This screening process is characterized by the Kondo temperature [30, 32]

$$T_K \sim e^{-1/J\rho(E_F)}, \tag{1.38}$$

where $\rho(E_F)$ is the electron state density at the Fermi level E_F. At high temperatures $T \gg T_K$, the local moments are decoupled by the thermal fluctuations, and behave like free magnetic ions, where Curie-Weiss behaviors with $\chi \propto 1/(T-\theta)$ in magnetic susceptibility are observed [32]. With decreasing temperature, the screening of the local moments by the conduction electrons become significant. As the temperature $T \leq T_K$, the magnetic moments starts to be "quenched" in the conduction electron sea, and a logarithmic correction of the resistivity $\rho \sim ln(T/T_{\mathrm{K}})$ is observed [32]. It is worth noticing that the new characteristic energy scale T_K for heavy fermions is only about $10^1 \sim 10^2$ K, and this is much smaller than the Fermi energy in normal metals, which is usually around $T_F \simeq 10^3 \sim 10^4$ K [32].

1.3.2 The RKKY Interaction

For heavy fermion metals, the overlap of neighboring f electron wave functions is small, and the direct dipolar interactions are usually weak. The dominant interaction between the local moments is the indirect RKKY (Ruderman and Kittel [33], and Kasuya [34] and Yosida [35]) exchange interaction, mediated by the conduction electrons. The RKKY interaction was originally proposed to explain the hyperfine coupling between the nuclear spin and the conduction electrons in metals. In the RKKY model, the local moments are correlated with each other through the polarization of the conduction electrons. Considering a magnetic moment $\mathbf{S}_i$ that sits at position $r = r_i$, the spin $\mathbf{s}_i$ of the conduction electron at r sees the local moment $\mathbf{S}_i$ through the generated effective field $H_{\mathrm{eff}} \sim J\mathbf{S}_i \cdot \delta(r)$. Thus the modulated conduction spin density then acts on another local moment $\mathbf{S}_j$ at position $r = r_j$ through spin $\mathbf{s}_i$. As a result, the two spatially distinct local moments are correlated to each other through the exchange interaction mediated by the conduction electron spin. The total RKKY exchange interaction is given by

$$E = \frac{18\pi n^2}{E_F} J^2 \mathbf{S}_i \cdot \mathbf{S}_j f(2k_F \mid r_j - r_i \mid), \tag{1.39}$$

where $n = N/V$ is the average conduction electron density, E_F is the Fermi energy, and k_F is the Fermi wave vector. Here

$$f(x) = \frac{sinx - xcosx}{x^4}$$

is a damped oscillating function whose sign alternates between positive (AF) and negative (FM) as the separation of the magnetic ions is varied. In contrast to the Kondo screening, the RKKY interaction tends to drive long range magnetic order of the system.

1.3.3 The Doniach Phase Diagram

The competition between the Kondo effect and the RKKY exchange interaction plays the central role in our understanding of the heavy fermion materials. Doniach [36] has proposed a simplified phase diagram for a Kondo lattice model in one dimension, as shown in fig. 1.5. Since the energy scale for the RKKY interaction increases as a function of the coupling J as [30, 32, 36]

$$T_{\mathrm{RKKY}} \propto J^2 \rho(E_F), \tag{1.40}$$

it grows much faster than the exponential expression for the Kondo temperature T_K (equation 1.38) when J is small. On this weak coupling range in the Doniach phase diagram, the RKKY exchange interaction is dominant, and the magnetic ordering temperature T_N increases in a similar way to T_{RKKY}. However, as the coupling J increases, the Kondo effect starts to be more significant, and the magnetic moment is reduced by the Kondo screening. It is thus expected that, after some point, the ordering temperature T_N will start to decrease and finally the magnetic order will be suppressed to $T_N = 0$ at the critical value $J = J_c$. In the strong coupling limit with large values of $J \gg J_c$, the Kondo effect dominates, and the ground state is a non ordered paramagnetic state with quenched magnetic moments. The process of Kondo screening can also be viewed as the melting of the local magnetic f electrons into the conduction electron sea [10, 30, 32]. On the paramagnetic delocalized side of the $J = J_c$ QCP, the quenched moments contribute to the Fermi surface, and the system evolves from a localized small Fermi surface in the magnetic ordered state and a large fermi surface in the paramagnetic state where the f electrons are delocalized. In this sense, the quantum phase transition in heavy fermions is a Mott-like transition that corresponds to the localization - delocalization of f electrons as proposed in [10, 30, 32, 43].

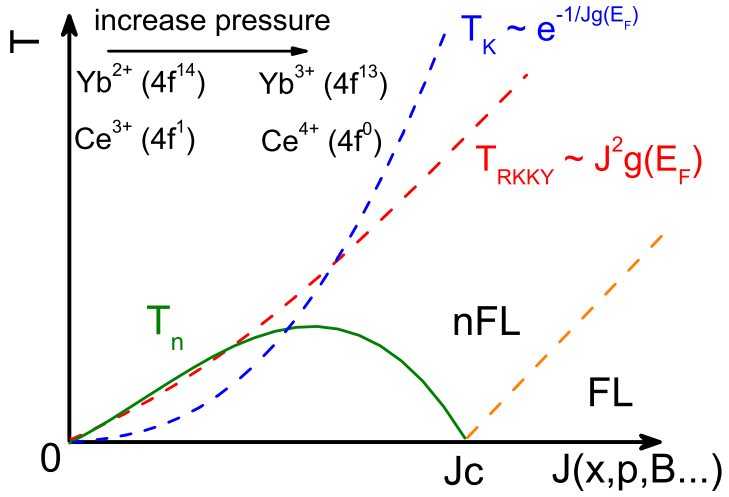

Figure 1.5: The Doniach phase diagram for heavy fermion compounds [10, 30, 36]. The blue line indicates the Kondo temperature T_{K}, and the red line indicates the RKKY temperature T_{RKKY}. The heavy Fermi liquid region was restored in the strong coupling limit as marked by the orange line. In the weak coupling range in the Doniach phase diagram, the RKKY exchange is the dominant interaction, and the magnetic ordering temperature T_N increases in the similar way as T_{RKKY}. However, with increased coupling J, the Kondo effect starts to be more significant, and the magnetic moment is increasingly screened by the Kondo effect. Thus a QCP is expected at some critical value $J = J_c$ where $T_N = 0$. non-Fermi liquid behaviors are usually observed in the critical region. With increasing pressure, the magnetic moments of Ce ions and Yb ions are driven in opposite directions due to their different $4f$ electron configurations.

The Heavy Fermi Liquid Regime

As shown in fig. 1.5, there are two regimes around the $T = 0$, $J = J_c$ QCP besides the magnetic order. The strong coupling state with large Fermi surface can still be described by the Fermi liquid theory, but with a 'heavily' dressed mass [32, 40]. It was proposed by Landau that the excitation spectrum in a strong interacting Fermi system develops continuously from single-particle excitations in a noninteracting system as the interaction increases in strength. Such excitations are called quasiparticles, and they are enhanced by their correlations with other particles. When measuring a single electron property in an interacting system, which is a collection of many electrons, the bare electron mass m is renormalized to an effective mass m^* [32, 40]. In the Landau Fermi liquid theory, the properties of such a Fermi liquid are related to the quasiparticle state density $g(E_F) = m^* k_F/\pi^2\hbar^2$ near the Fermi level E_F [32, 40]. It was shown that the linear Sommerfeld coefficient γ of the electronic specific heat behaves as

$$C/T \sim \gamma, \tag{1.41}$$

where

$$\gamma = \frac{\pi^2 k_B^2 g(E_F)}{3} = \frac{k_B^2 m^* k_F}{3\hbar^2} \propto m^*$$

is a direct measurement of the effective mass m^*. In normal metals such as copper or aluminum, the value of γ is of the order $\sim 1 - 10\text{mJ/mol} \cdot \text{K}^2$. For heavy fermion systems, the effective masses of the electrons are greatly renormalized due to strong correlations, and γ has been found to be as large as $1600\text{mJ/mol}\cdot\text{K}^2$ in the rare earth compound $CeAl_3$ [37]. This is about 1000 times more than conventional metals, and this is also where the name 'heavy fermion' comes from [32, 40].

The magnetic susceptibility for an interacting system is also enhanced in a similar way with [32, 40]

$$\chi = \mu_B^2 g(E_F) \frac{1}{1 + F_0^a} = \frac{\mu_B^2 k_F m^*}{\pi^2\hbar^2} \frac{1}{1 + F_0^a}, \tag{1.42}$$

where F_0^a is the s wave ($l = 0$) dimensionless Landau parameters. It was found by Wilson that the dimensionless ratio

$$R_W = \frac{\pi^2 \mu_B^2}{\mu_B^2} \frac{\chi}{\gamma} = 2, \tag{1.43}$$

is equal to the theoretical value expected from the impurity Kondo model [32,

38, 39].

In the Landau Fermi liquid, the electron-electron scattering near the Fermi energy gives a quadratic temperature dependence of the resistivity ρ

$$\rho = \rho_0 + AT^2, \tag{1.44}$$

where the coefficient A is related to the effective mass as $A \propto (m^*)^2$. It was observed by Kadowaki and Woods [41] that the ratio between the coefficient A and the square of the Sommerfeld ratio γ

$$\frac{A}{\gamma^2} = 10\mu\Omega - \text{cm} \cdot \text{mol}^2\text{K}^2/\text{J}^2 \tag{1.45}$$

does not depend on the quasiparticle mass, but it is a universal constant for many heavy fermions. The Wilson ratio R_W (equation 1.43) and Kadowaki-Woods ratio A/γ^2 (equation 1.45) are usually used to classify different heavy fermion materials [32].

non-Fermi Liquid Behavior

Although Fermi liquid theory is still adequate for the description of the physical properties as $T \to 0$ in the Kondo quenched moment state with strong interaction $J \gg J_c$, it fails in the region near the quantum phase transition. Instead, some spectacular phenomena called "non-Fermi liquid" (nFL) behavior develop in the vicinity of the QCP ($J = J_c$) [21, 32, 40]. Although the quantum phase transition is only defined at the temperature $T = 0$, this nFL behavior extends over a wide temperature region for $T > 0$, as indicated in fig. 1.5. Such behaviors have been explored in a number of bulk d and f electron systems with logarithmic or power-law like divergencies in their temperature dependent specific heat and magnetic susceptibility as

$$C/T \sim -log\ T, \quad \text{or} \quad T^{-\alpha} \tag{1.46}$$

$$\chi \sim T^{-\gamma} \tag{1.47}$$

in the nFL region. These behaviors are distinct from the Fermi liquid behavior we discussed above where C/T and χ approach constant values as temperature goes to zero. In addition, the resistivity is often found to have unconventional temperature dependencies such as

$$\rho \sim \rho_0 + AT^n, \quad n \simeq 1 - 1.5 \tag{1.48}$$

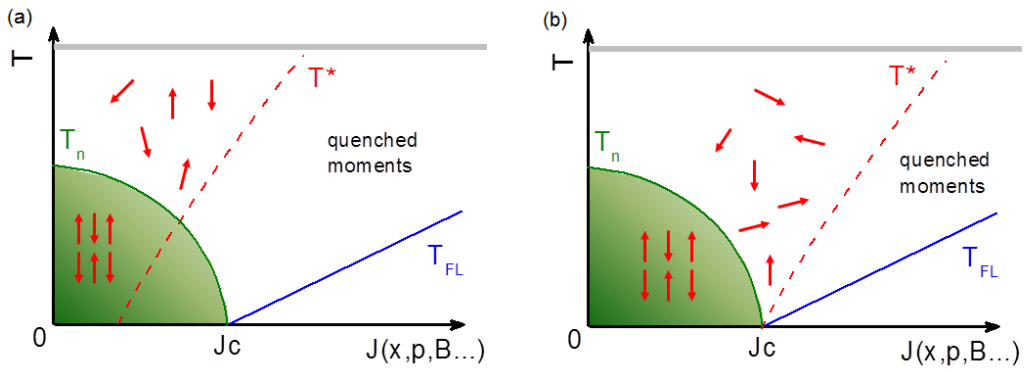

Figure 1.6: A schematic view of two types of phase diagrams for heavy fermions near the antiferromagnetic QCP at $J = J_c$. (a) is the spin-density-wave QCP where the magnetic moments are already quenched above the quantum phase transition. (b) is the Kondo-breakdown type of QCP, where the local moments still survives until $T \to 0$, and a new energy scale T^* that relates to the Kondo screening develops just at the QCP. The gray line indicates the temperature scale, above which the local moments are incoherent and behave as free Curie moments. The dashed line T^* represents the energy scale below which the local f moments are fully delocalized into a large Fermi surface, and the line T_{FL} indicates the crossover to the low temperature Fermi liquid region. [10, 30]

with powers n different from 2 in many heavy fermion systems at the boundary of the magnetic instability [32]. The breakdown of the Fermi liquid theory indicates that there are very strong electron-electron interactions near the QCP, and that quantum critical fluctuations are at the heart of this problem. Since in practice all physical properties can only be measured at $T > 0$, the identification of the nature of the quantum criticality at $T = 0$ relies on the scaling behaviors found at finite temperatures. Theoretical scaling analyses near the QCP have been developed for a long time, as discussed in the previous section. However, analyses that are consistent with basic thermodynamical principles like the Maxwell relations of the measured thermal properties such as specific heat and magnetic susceptibility have only been realized experimentally in a few systems [17, 18, 20].

1.3.4 Quantum Criticality in Heavy Fermions

A lot of experimental and theoretical studies of heavy fermions have taken place since their first discovery in 1970s [37, 42]. However, a universal

description of the unusual behaviors in different heavy fermion materials is still lacking. It is generally believed that the quantum critical fluctuations are responsible for the breakdown of the standard Landau Fermi liquid theory of normal metals. Two models of quantum criticality in heavy fermions have been proposed. One is the itinerant spin-density wave (SDW) QCP first studied by Hertz and Millis [24, 25], and the other is the so called Kondo-breakdown QCP introduced by Qimiao Si [43] et al., and P. Coleman et al. [44]. Shown in fig. 1.6 is the schematic view of the two quantum critical phase diagrams in heavy fermions near the antiferromagnetic QCP [10, 30]. The gray lines indicate the temperature scales, above which the local moments are incoherent and behave as free Curie moments. Fig. 1.6a represents the spin-density-wave QCP, and fig. 1.6b is the Kondo-breakdown type QCP. The dashed line T^* represents the energy scale below which the local f moments are fully delocalized into a large Fermi surface, and the line T_{FL} indicates the crossover to the low temperature Fermi liquid region. The main difference of these two scenarios is whether the local moments survive or not in the vicinity of the $T = 0$ QCP.

For the SDW type QCP, the energy scale T^* intercepts the magnetic order boundary at $T_N > 0$, and the f moments are fully quenched before the QCP is reached. The ordered state near the quantum phase transition is thus an itinerant SDW state. This kind of quantum criticality falls into the category of Hertz-Millis theory of the itinerant antiferromagnetic QCP with $z = 2$ [24, 25]. However, if the Kondo screening breaks down just at the boundary of the magnetic order, the quenched f electrons only exist in the paramagnetic state, and the strongly correlated local moments persist down to the lowest temperatures as $T \to 0$. In this case, the QCP separates an ordered state with local magnetic moments and a small Fermi surface from a quenched moment paramagnetic state with a large Fermi surface [10, 30, 32, 43]. At this 'local' QCP, the $4f$ electrons are involved in the $T = 0$ localization-delocalization transition, and additional critical fluctuations are expected besides the order parameter fluctuation of the magnetic phase transition itself. A new energy scale T^* was introduced for this Kondo-breakdown QCP, which indicates the crossover from the small Fermi surface to the large Fermi surface regime at finite temperatures [10, 30, 32, 43].

Studies of quantum criticality in heavy fermions are mainly performed in the $5f$ Uranium (U) and $4f$ Cerium (Ce) and Ytterbium (Yb)based systems [45]. It was noted that the trivalent configuration Yb^{3+} ($4f^{13}$) can be considered as a hole counter part of the Ce^{3+} ($4f^1$) configuration [6]. However, we have to mention that the magnetic trivalent stable Ce^{3+} is the stable configuration at low pressures (large volumes), while for Yb non-magnetic Yb^{2+} is the more stable configuration at low pressure. This difference makes

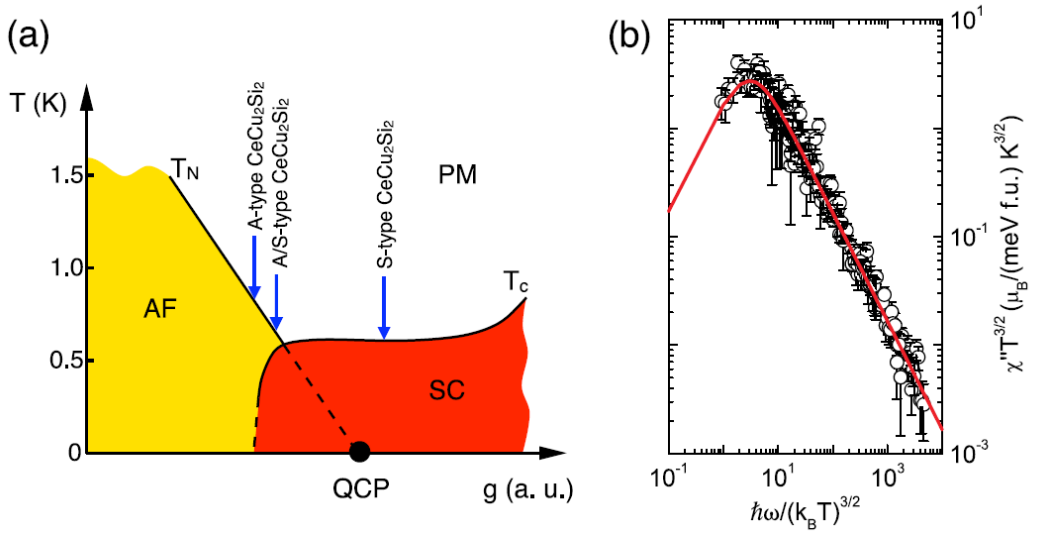

Figure 1.7: (a) Schematic phase diagram of $CeCu_2Si_2$ in a narrow homogeneity range with different compositions close to 1:2:2. Different states are observed from the antiferromagnetic order (A type) to the superconducting state (S type). (b) Scaling plot of the dynamical susceptibility as a function of energy and temperature on $CeCu_2Si_2$ S-type single crystals. [30]

opposite trends in Ce and Yb based systems when the tuning parameter is pressure, as indicated in fig. 1.5. Here we briefly introduce a few well studied Ce and Yb based compounds ($CeCu_2Si_2$ [42], $CeCu_{6-x}Au_x$ [17], $YbRh_2Si_2$ [10]) as examples of the different types of quantum criticality found in heavy fermions.

$CeCu_2Si_2$ is the first discovered heavy fermion compounds that shows bulk superconductivity near the AF-QCP [30, 42]. It crystallizes in the famous $ThCr_2Si_2$ structure [42]. The physical properties of $CeCu_2Si_2$ are very sensitive to the sample stoichiometry, and the crystals can vary from antiferromagnetic order (A type) to superconductivity (S type) in a very narrow composition range [30, 42]. The schematic phase diagram is shown in fig. 1.7a [30]. Inelastic neutron scattering experiments were performed on $CeCu_2Si_2$ S-type single crystals, and a scaling of the dynamical susceptibility $\chi''(Q,\omega)$ was observed following

$$\chi''(Q,\omega) = T^{-3/2} f[\hbar\omega/(k_B T)^{3/2}], \tag{1.49}$$

as seen in fig. 1.7b. This scaling, together with the temperature dependent line width $\Gamma(T) = \Gamma_0 + aT^{3/2}$, is argued to be evidence that $CeCu_2Si_2$ is close to an itinerant 3D SDW QCP [30].

$CeCu_6$ is another well established heavy fermion compound where the

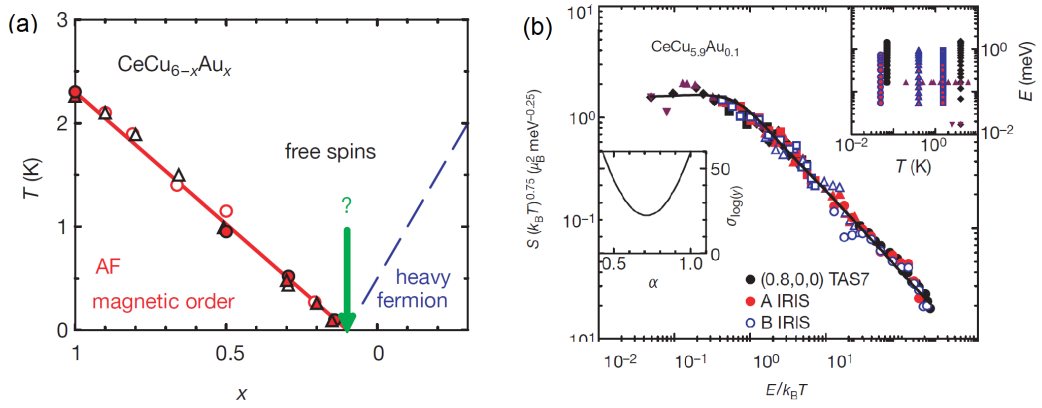

Figure 1.8: (a) Temperature (T) - doping (x) phase diagram of the system $CeCu_{6-x}Au_x$ with an AF-QCP at the critical composition $x = 0.1$. (b) Scaling of the dynamical magnetic susceptibility as a function of E/T at various q vectors. [17]

antiferromagnetic order can be suppressed by doping with gold (Au) [17]. Fig. 1.8a shows the temperature doping ($T - x$) phase diagram of the system $CeCu_{6-x}Au_x$ with an AF-QCP at the critical composition $x = 0.1$ [17]. Heavy fermion behaviors were observed above the critical concentration. One question asked here is whether there are any local moments surviving at the critical point. Single crystal neutron scattering experiments were performed on the critical compound $CeCu_{5.9}Au_{0.1}$, and scaling of the dynamic susceptibility was observed as a function of E/T as [17]

$$\chi''(Q, \omega) = T^{-3/4} f(E/T). \tag{1.50}$$

This universal scaling was not just found for $q = 0$, but at different q positions along a line in the Brillouin zone [17]. The E/T scaling was introduced with the assumption of Curie-Weiss like behaviors of free local spins near the critical point [17]. This argues that the Kondo breakdown local moment QCP is more appropriate for the case of $CeCu_{6-x}Au_x$ [17].

$YbRh_2Si_2$ is isostructural to $CeCu_2Si_2$, with the same tetragonal $ThCr_2Si_2$ crystalline structure [10]. Antiferromagnetic order has been found in this material at $T_N \sim 70$ mK in zero field. This magnetic order can be driven to an AF-QCP at $B_c \sim 0.66$ T with field along the crystal c axis [10]. Similar to other quantum critical heavy fermion systems, Fermi liquid behavior was found in high fields at low temperatures, with an enhanced value of γ. nFL behaviors, such as a linear temperature dependent resistivity ($\rho \sim T$) were

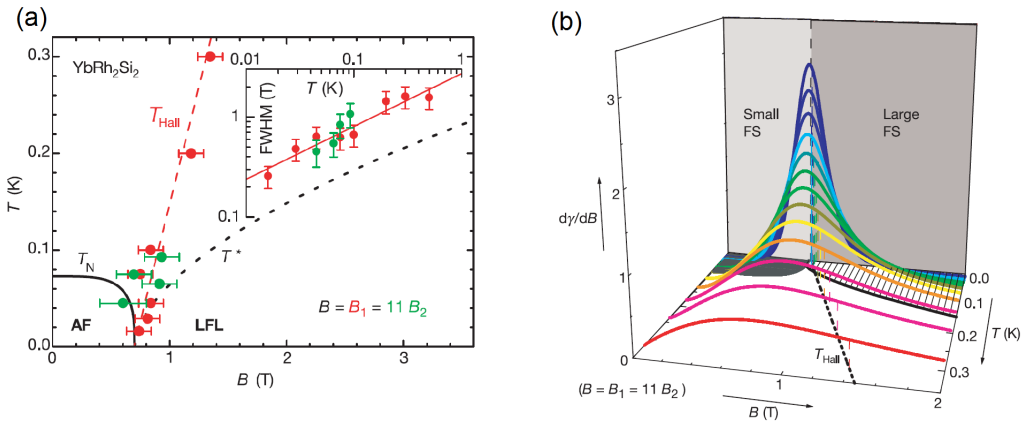

Figure 1.9: (a) Field temperature phase diagram of $YbRh_2Si_2$ with field along the c axis. The red points are the new energy scale determined from the Hall effect resistivity measurements, which signifies the crossover from the small Fermi surface to the large Fermi surface. (b) The field derivative of the crossover function $\gamma(b)$ becomes very large as $T \to 0$. [10, 31, 122, 152, 156]

observed near the critical point.

A crossover temperature scale is defined from the full width at half maximum (FWHM) of the magnetoresistivity which vanishes as $T \to 0$ at the field tuned AF-QCP, as shown in fig. 1.9. This crossover line was initially found in Hall effect measurements [31], and has also been found in measurements of magnetostriction, magnetization, and ac magnetic susceptibility[156]. It was proposed to account for the jump in the Fermi surface volume at finite temperatures [10, 31, 122, 152, 156], and it corresponds to the Kondo breakdown line in fig. 1.6b. It was shown in [10, 122, 152, 156] that all these energy scales merge to the same QCP at $T \to 0.$, The multiple vanishing energy scales indicate that the quantum criticality in $YbRh_2Si_2$ can be categorized as a Kondo breakdown QCP. Based on the Maxwell relation $dM/dT = dS/dH$, additional signatures of this T^* line are confirmed from inflection points observed in dM/dT. It has also been argued that the crossover temperature T^* may relate to Zeeman physics of Yb ions in $YbRh_2Si_2$ [160], and further study of the origin of this T^* is still needed.

1.4 Metal Insulator Transition (MIT)

The metal-insulator transition (MIT) is the transition from a metallic phase to an insulator phase, and it is one of the most fundamental subjects in condensed

matter physics [46, 47]. The MIT can be characterized into different classes based on the nature of the interactions [46]. Many MITs are due to the electron-ion interaction, which can be understood on the basis of the single electron theory. Examples are transitions in band insulators, Peierls insulators, and Anderson insulators [46]. Different from all these, Mott insulators are induced by the interactions among electrons, and they are understood as a collective electron phenomena [46]. We give a brief introduction of the Mott MIT below.

From the point of view of quantum criticality, the Mott MIT is an exact example of a quantum phase transition. In the Mott-Hubbard picture, the electronic system is described by the Hubbard Hamiltonian [46]

$$H_{HUB} = -\sum_{ij}(tc^{+}_{i\sigma}c_{j\sigma} + h.c.) + \sum_{j}\epsilon_j c^{+}_{j\sigma}c_{j\sigma} + U\sum_{j} c^{+}_{j\uparrow}c_{j\uparrow}c^{+}_{j\downarrow}c_{j\downarrow}. \qquad (1.51)$$

Here ϵ in the second term is the site energy, t is the hopping element that is proportional to the kinetic energy, and U represents the Coulomb repulsion between electrons. For the limit with $t \gg U$, the the kinetic energy is strong enough to overcome the Coulomb potential U, and the electrons can spread over the entire crystal, resulting an itinerant metallic ground state. However, on the other hand with $t \ll U$, the kinetic energy is too weak for the electrons to hop to different sites, and the electrons prefer to localize themselves in order to minimize the potential energy U [46]. A charge gap opens in this Mott insulating state, and the electrons at each site behave as localized magnetic moments. The Mott MIT is the consequence of the competition between the electron kinetic energy t and Coulomb repulsion U. In some sense, we can also understand the itinerant metallic state and the localized insulating state as two different ground states where the electrons are localized in momentum space and real space, respectively. The Mott MIT that separates them at $T = 0$ is a true quantum phase transition that can be tuned by external parameters such as chemical doping, or pressure that change the coupling strength. A schematic view of the MIT phase diagram is shown in fig. 1.10 [47]. The T^* line indicates the quantum critical crossover from metallic state to insulator, where the slope of the temperature dependent resistivity changes [47]. From the point of view of a localization-delocalization transition, the Mott MIT-QCP has a lot in common with the localized AF-QCP in the heavy fermions. The primary difference is that only f electrons are considered in the delocalization process induced by the hybridization interaction to the conduction electrons [10, 30, 32, 43], and the material is metallic on both sides of the heavy fermion localized AF-QCP, while in the case of the Mott MIT-QCP, the conduction electrons themselves are localized due to the Coulomb

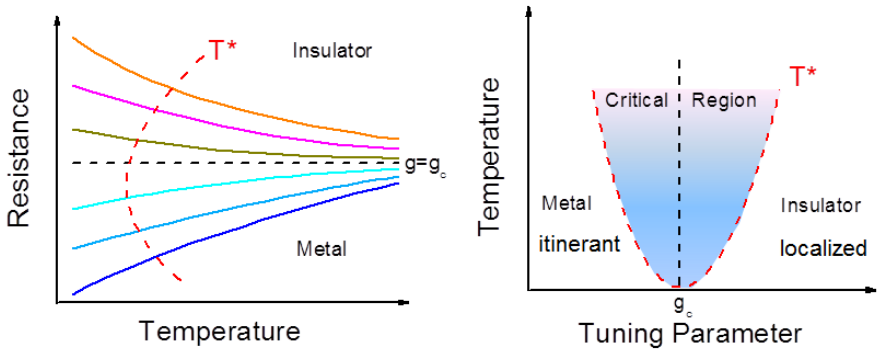

Figure 1.10: (a) Sketch of the temperature dependent resistivity close to a MIT QCP. The T^* line indicates the quantum critical region. As the system crosses over from metallic state to insulator, the slope of the temperature dependent resistivity changes. (b)Schematic view of a general Metal-Insulator transition phase diagram with tuning parameter g. [47]

interactions [46, 47].

It has to be emphasized here that, although localized magnetic moments develop at the MIT-QCP, it is not necessary for these pre-formed local moments to be magnetically ordered, and no breaking of the lattice symmetry or periodicity is required for the Mott insulating phase. However, in realistic situations, the exchange interaction between localized spins usually leads to long range magnetic order at low temperatures in the insulating state. The layered organic charge-transfer salts κ-(BEDT-TTF)$_2$X have been well studied as excellent examples of Mott MITs [48, 49, 50]. The temperature pressure $(T - P)$ phase diagram has been established by the studies of κ-(BEDT-TTF)$_2X$ series under pressure or with different kinds of monovalent anions X, as shown in fig. 1.11a [48, 49]. Bulk superconductivity was observed near the MIT QCP, and it was separated from the antiferromagnetic insulating state by a first order MIT phase line, which ends at the critical end point $T_c \simeq 39.7$ K, and $P_c \simeq 25.8$ MPa [48, 49]. As expected in other quantum critical systems, universal critical behaviors are observed near the MIT-QCPs. Regardless of the microscopic details, scaling analyses based on simple and fundamental physical concepts are always powerful techniques for understanding the nature of the criticality. Critical scaling of the conductivity and thermal expansion observed near the MIT critical end point has indicated that this system belongs to the two dimensional (2D) Ising universality class. The singular part of the

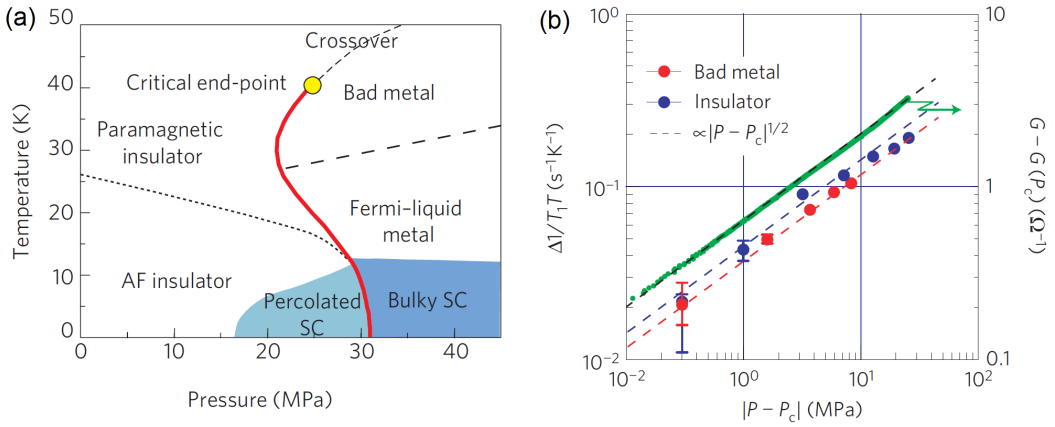

Figure 1.11: (a) Simplified temperature pressure $(T - P)$ phase diagram of the κ-(BEDT-TTF)$_2$X family. The thick solid line is the first order phase transition from the Mott insulator to the high pressure metallic or superconductor phases. The phase line terminates at the critical end point (●) at $T_c \simeq 39.7$ K, and $P_c \simeq 25.8$ Mpa. (b) Logarithmic plot of spin lattice relaxation rate divided by T $(1/T_1T)$ and conductance measured at the critical end point against $\mid P - P_c \mid$. The dashed black line indicates the pressure dependence of $\mid P - P_c \mid^{1/2}$ [49, 51].

free energy based on the measured thermal properties was proposed by [50]

$$f(t,h) = \frac{1}{8\pi} t^2 log t^2 + |h|^{d/y_h} \Phi(t/|h|^{z/y_h}). \tag{1.52}$$

Here $t = [T - T_c - \zeta(P - P_c)]/T_0$, and $h = [P - P_c - \lambda(T - T_c)]/P_0$ are normalized scaling variables with small linear mixing terms (details explained in [50]). It is interesting to notice that although the MIT itself is a quantum phase transition that separates the localized insulating state and the itinerant metallic state, the scaling analysis performed here for κ-(BEDT-TTF)$_2$Cu[N(CN)$_2$]Br is actually classical since the critical end point occurs at $T_c \neq 0$, just like the critical end point of the liquid gas transition of water.

Many of the studies of the MIT are based on measurements of the charge and lattice degrees of freedom [49], and very little is known about the dynamics of the spins near the MIT. Since the lattice of localized moments melts into a delocalized electron fluid near the Mott MIT, changes of the magnetic properties are also expected, even if no magnetic order is involved [51]. Formation of localized spins may cause divergencies of the magnetic susceptibilities near the critical point [51]. It is thus intriguing to see that the spin lattice relaxation rate divided by T $(1/T_1T)$ measured by NMR

follows the same power law as the conductivity near the critical end point against $\mid P - P_c \mid$ in κ-(BEDT-TTF)$_2$X (fig. 1.11b) [51]. This suggests that the spins also display strong critical fluctuations at the Mott MIT. However, since many of these systems are tuned by pressure, comprehensive studies of the evolution of the magnetization in these kinds of QCPs are still lacking due to technical issues.

1.5 Low Dimension and Frustration

Quantum fluctuations are often observed in systems on the verge of the magnetic ordering, and they are thought to be responsible for the non Fermi liquid critical behaviors. In low dimension and frustrated systems, quantum fluctuations are also enhanced and quantum critical behaviors are expected.

1.5.1 1D Quantum Magnet, Luttinger Liquids

Landau's Fermi liquid theory has proven to be very successful for describing high dimensional systems with interacting electrons. Quasiparticle excitations are still well defined as interactions are switched on, leading to renormalized quasiparticles similar to the free electrons in the noninteracting Fermi gas. However, this description fails in one dimensional systems. A straightforward way to understand this is from the interactions, as described in [52, 53]. In higher dimensions, electrons can move in all directions, and the quasiparticles can still be viewed as individual particles. But for one dimensional systems, there is only one direction for the electrons to go, and no individual electrons can move without interacting with other electrons [52, 53]. Thus only collective electronic excitations are possible [52, 53]. This makes the one dimensional systems dramatically different from interacting electron systems in high dimensions. The analogy to the Fermi liquid found in higher dimensional systems is the Lutinger liquid in one dimensional systems and a good review can be found in [52] and references therein.

One main property of the one dimensional Luttinger liquid is fractional excitations [52]. Since excitations can only be collective, different quantum numbers like charge or spin can exist as two separate excitations, and the electrons are broken into two elementary excitations that carry spin (Spinon) and charge (Holon), respectively [52, 53]. Spinon excitations have been observed in one dimensional antiferromagnetic spin ($S = 1/2$) chain systems [54, 55]. In this spin $S = 1/2$ chain, the single spin flip state correspond to an $S = 1$ excitation. This is similar to a one magnon excitation found in higher dimensional magnets. However, in one dimension, this $S = 1$

magnon is decomposed into two domain wall excitations that each carrying spin $S = 1/2$ [52, 53, 54, 55]. As indicated in the sketch in fig. 1.12a by the red dashed lines, these two domain walls can then separately propagate along the chain [52, 53]. These excitations, known as spinons, are the new basic excitations. This could also be viewed as a deconfinement of a $S = 1$ magnon to two $S = 1/2$ spinons using the language of Quantum-Chromodynamics (QCD). Since spinons are always created in pairs by flipping one spin, except at the end of the chain, the excitation spectrum is defined by a continuum that consists of two spinons as observed in [54, 55]

$$q = q_1 + q_2 \tag{1.53}$$

$$E = \frac{\pi J}{2}[sin(q_1) + sin(q_2)]. \tag{1.54}$$

Here J is the nearest neighbor interaction along the chain. Because each spinon propagates over two lattice spacings $2a$ at one time (fig. 1.12a (ii-iii-iv)), the momenta q_1 and q_2 vary only in the range of the half Brillouin zone $[0, \pi/a]$, and the total momentum q is the sum of the two 1.53 [52, 53]. The excitation spectrum for the spin half ($S = 1/2$) Heisenberg chain is shown in fig. 1.12b. The colored contour indicates different spectral weight, which alters depending on the types of interactions. For the change from isotropic Heisenberg model to the XY anisotropic planar model, the spectrum weight will shift from low to higher energies, and for the Ising limit, the point at $q = \pi$ will become gapped [56, 57].

Another crucial property of the Luttinger liquid is the power law dependence of the correlation function [52, 53]. This is familiar to us, as we have seen such behavior in high dimensional systems near the critical point. As was discussed in earlier sections, when the system is tuned close to a QCP, and the quantum fluctuations are strong enough to break up the quasiparticles, non-Fermi liquid behaviors were observed in the critical region that could be described by critical scaling with universal power exponents [10]. The power law behaviors in one dimensional Luttinger liquids can be understood in a similar way. Since no long range order is allowed in one dimensional systems for any finite temperature, it could be alternatively viewed that one dimensional systems are always located at the verge of static order [52, 53]. Thus, they always behave in a critical way, just like the systems that are tuned close to a QCP. The key point is that, in both cases, the quantum fluctuations are so strong as to preclude the quasiparticle scenario, and the Fermi liquid theory always breaks down. However, different from the universal exponents found near the QCP in higher dimensional systems, the power laws in a one dimensional Luttinger liquid are characterized by the two Luttinger

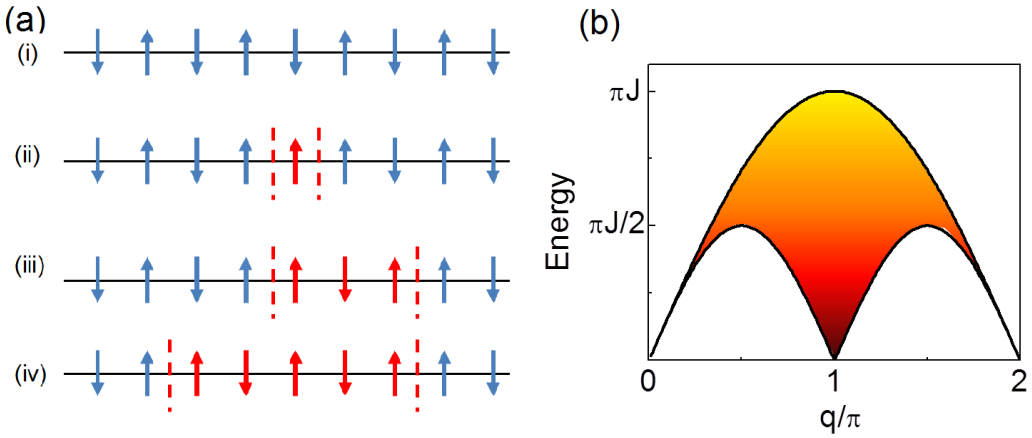

Figure 1.12: (a) Sketch of the spinon excitation in a one dimensional antiferromagnetically coupled spin chain system. (i) The spin $S = 1$ magnon with a single flipped spin is decomposed into two domain wall excitations (Spinon) with each carrying spin $S = 1/2$ (red dashed lines). The two spinon excitations can propagate along the chain separately with a shift by two lattice spacings at a given time (ii-iii-iv). (b) Energy spectrum of the two spinon excitation for the Heisenberg spin half chain. The color contour indicates the scattering spectrum weight which depends on different models. [52, 53, 54, 55]

liquid parameters: the velocity of density excitation μ and the dimensionless parameter K. A detailed description of these parameters can be found in the book of T. Giamarchi [52]. Experimentally, these power law like behaviors can be tested by the temperature and frequency dependent conductivity in real materials [52, 58]. A linear temperature dependence of the resistivity has been observed in the one dimensional organic conductors $(TMTSF)_2PF_6$, which was argued to be consistent with the Luttinger liquid behavior, where $\rho(T) \sim T^{4n^2K_\rho - 3}$ with $n = 2$, $K_\rho = 0.23 \sim 0.25$ [52, 58].

1.5.2 2D Shastry-Sutherland Lattice (SSL)

Exotic excitations are not only limited to one dimensional spin systems. Frustrated spin systems in higher dimensions have attracted a lot of interest over these years also, and fractionalized excitations have been recently observed in the two dimensional spin half $S = 1/2$ Kagome lattice antiferromagnet $ZnCu_3(OD)_6Cl_2$ (Herbertsmithite) through inelastic neutron scattering experiments [59]. Consider three Ising spins residing on the corners of a triangle, with antiferromagnetic interactions between nearest neighbors, as shown in fig. 1.13a(i), there is no way to make every pair of spins anti-parallel to each other, and the third spin is always frustrated since it cannot simultaneously satisfy the AF interaction with the other two spins. The ground state of this lattice thus consists of many energy degenerate states. The situation becomes slightly different for a square lattice, as shown in fig. 1.13a(ii). The ground state of a square lattice is a classical Neel ordered magnet. If we only consider the nearest neighbor antiferromagnetic interactions, all four spins can be satisfied without inducing any frustration. However, if the next near neighbor interaction is included and if it also happens to be antiferromagnetic, then the spins located along the diagonal direction become frustrated too, as indicated in fig. 1.13a(iii). Different from the geometrical frustration in the triangular lattices, the square lattice itself is not frustrated, and the frustration is induced by the competion of the nearest and next nearest neighbor interactions.

A well known two dimensional frustrated spin model based on the square lattice is the Shastry-Sutherland Lattice (SSL), proposed by Shastry and Sutherland in 1981 [60]. In the SSL, the spins on the square lattice interact through the antiferromagnetic nearest neighbor interaction J' and next near neighbor interaction J along the diagonal direction, as indicated by the dashed and the solid lines in fig. 1.13b. In the limit with $J/J' = 0$, the SSL is a traditional antiferromagnet with classical spin wave excitations. However, in the other limit with $J'/J = 0$, Shastry and Sutherland have shown that the quantum spin liquid with singlet dimers is an exact ground state [60]. A

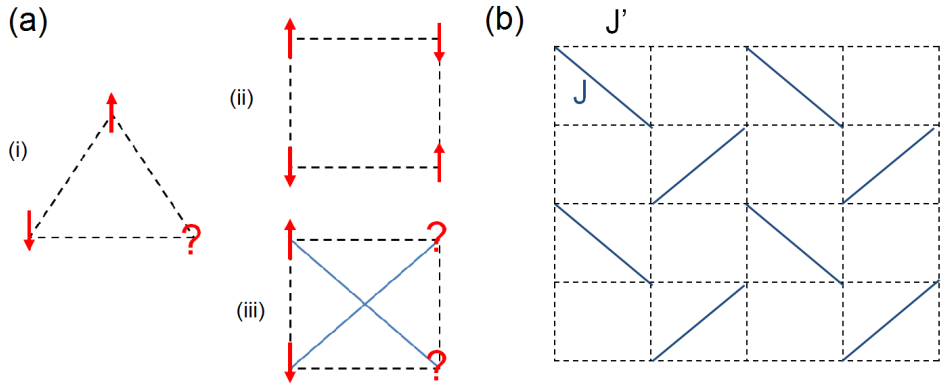

Figure 1.13: (a) The two dimensional triangular and square lattices with Ising spins (red arrows) on the corners. (i) The triangular lattice is geometrically frustrated with the nearest neighbor antiferromagnetic interactions. (ii) The square lattice is not frustrated, considering only the antiferromagnetic nearest neighbor interactions. However, when the antiferromagnetic next nearest neighbor interactions are included (iii), the square lattice becomes frustrated by the competition between these two interactions. (b) Sketch of the original Shastry-Sutherland model. J' and J represent the nearest and next nearest neighbor antiferromagnetic interactions [60].

QCP was expected near $J'/J = 0.68$ [62]. A plaquette-like singlet state is also proposed to exist near this QCP [61, 62]. Experimentally, it is very hard to make a real compound that represents the SSL model, however, recently it was found that there are a few systems where the magnetic ions form an orthogonal dimer lattice which is topologically equivalent to the SSL, as shown in fig. 1.14a [61]. This lattice can be viewed as orthogonal aligned dimers, with antiferromagnetic intra-dimer interaction J and inter-dimer interaction J'. The compound $SrCu_2(BO_3)_2$, with Heisenberg like spin $S = 1/2$ Cu ions forming in orthogonal dimers, is well described by this model [61]. It is believed to have a singlet spin liquid state and no magnetic order in zero field. An excellent review of this compound can be found in [61] and references there in. A few unique features are found in this material due to the special nature of the ground state of the SSL.

Some of these features reflect the uniqueness of the quantum spin liquid state. One main character is the unusual gapped excitations [63]. As shown in fig. 1.14a, the ground state is a spin singlet that results from dimers [63]

$$| s\rangle = \frac{|\uparrow\downarrow\rangle - |\downarrow\uparrow\rangle}{\sqrt{2}} \tag{1.55}$$

with the total spin $S = 0$, and there are three excited triplet states

$$| t_1\rangle = |\uparrow\uparrow\rangle, \quad | t_0\rangle = \frac{|\uparrow\downarrow\rangle + |\downarrow\uparrow\rangle}{\sqrt{2}}, \quad \text{and} \quad | t_{-1}\rangle = |\downarrow\downarrow\rangle \tag{1.56}$$

with the total spin $S = 1$. The total spin change from the singlet ground state to the excited triplet states is $\Delta S = 1$, and in this view, this excitation is still a magnon excitation ($S = 1$) [65], which is fundamentally different from the spinon excitation ($S = 1/2$) we have discussed earlier in one dimensional spin chains. However, this $S = 1$ magnon excitation also differs significantly from a classical spin wave excitation in traditional magnets. Importantly, this gapped excitation can be realized in the spin liquid ground state without necessarily breaking the translational symmetry [61], while the traditional spin wave excitations can only be found in the magnetic ordered state, and are usually gapless in the absence of anisotropy. Another peculiar feature is the dome order induced by magnetic fields. As the applied magnetic field increases, the degeneracy of the three excited triplet states will be lifted because of the Zeeman interaction $-g\mu_B S$ [63]. The state energy of $| t_1\rangle$ with $S^z = 1$ will be lowered in fields and suppressed to zero at the critical fields B_{c1} and B_{c2}. The gap size is determined by the intra-dimer interaction with $\Delta \sim J$, which

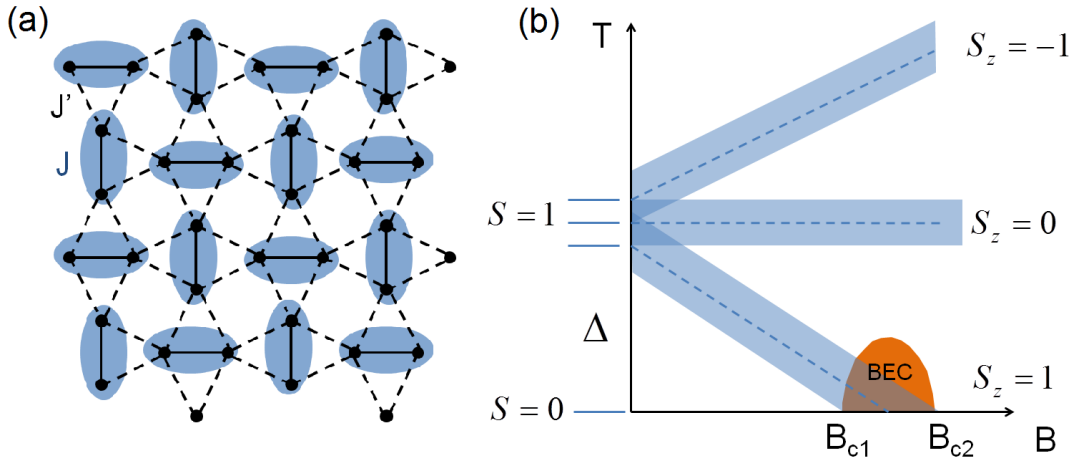

Figure 1.14: (a) A 2D structure with orthogonal dimers, which is topologically equivalent to the original Shastry-Sutherland Lattice (SSL). The solid and dashed lines represent the antiferromagnetic intra-dimer and inter-dimer exchange interaction J and J'. (b) Sketch of the singlet-triplet excitation of the dimers in magnetic fields. The triplet states are separated from the singlet ground state by an excitation gap Δ in zero fields. A Bose-Einstein-Condensation (BEC) state with condensed triplet was induced between the lower and upper critical fields B_{c1} and B_{c2} [63].

is proportional to the critical fields approximately as

$$J \sim (B_{c1} + B_{c2})/2, \tag{1.57}$$

as shown in fig. 1.14b [63]. The colored region with band width d is the dispersion of the excited states which is usually related to the inter-dimer interaction J', and defines the lower and upper critical field where [63]

$$J' \sim (B_{c2} - B_{c1})/2. \tag{1.58}$$

This domed region phase between B_{c1} and B_{c2} could also be viewed as a phase with gradually condensed magnons with bosonic character where $S = 1$, and the two quantum phase transitions at B_{c1} and B_{c2} fall into the Bose-Einstein condensation (BEC) universality class [63].

The gapped excitations and the field induced dome phase are found in other quantum dimer systems too. However, there is another feature of these gapped excitations which is mainly induced by the particular SSL geometry. Since the dimers are orthogonally aligned to each other in the

SSL, the hopping of the triplet between dimers is greatly suppressed, and the triplet excitation is almost localized. This gives an flat dispersion in inelastic neutron scattering experiments [61]. This has been confirmed in the material $SrCu_2(BO_3)_2$, where a small dispersion in the plane was believed to be induced by the Dzyaloshinsky-Moriya (DM) interactions [64]. A remarkable feature due to the locked triplets is the magnetization plateaux in the field dependent magnetization. As the external applied field increases, the density of the triplets changes, and magnetization plateaux exist at certain ratios such as $m = 1/8, 1/4, 1/3$ [61]. It is this localized character that make the SSL significantly different from other dimer systems and allows for the study of many interesting quantum behaviors.

Besides $SrCu_2(BO_3)_2$, the orthogonal aligned dimer SSL is also realized in the rare earth systems TmB_4 [68] and Yb_2Pt_2Pb [66, 67]. However, different from the Heisenberg like $S = 1/2$ spins in $SrCu_2(BO_3)_2$, the magnetic moments in the rare earth materials are usually more like classical Ising spins due to the large moment value and strong anisotropic crystalline electrical field (CEF) effect.

1.6 Scope of this thesis

In this thesis, three typical compounds are studied, leading to the understanding of the quantum phase transitions from different perspectives.

Chapter 3 : Yb_3Pt_4 Most of the heavy fermion systems are studied in the strong coupling limit where the Kondo effect plays an important role. non-Fermi liquid behaviors have been observed near such QCPs. The newly discovered Kondo breakdown energy scale, the T^* line in $YbRh_2Si_2$ near the AF-QCP, has also attracted special interest. It will be interesting to see if this critical behavior is in general induced by the delocalization of the f moments or if it is from the fluctuations of the order parameter only. We have chosen a new Yb-based antiferromagnet Yb_3Pt_4 as local moment version of $YbRh_2Si_2$ where the Kondo effect is negligibly small. Different magnetic properties are measured near the field induced critical point, and a global phase diagram was compared to that of $YbRh_2Si_2$.

Chapter 4 : YFe_2Al_{10} Fermi liquid theory is usually invalid near the QCP, due to the strong critical fluctuations, and scaling provides a powerful description near the critical region. It is rare to find a system where a 'naive' scaling that assumes the existence of hyperscaling can be fully worked out. We will show that such a self-consistent scaling of the specific heat and magnetic

susceptibility has been observed in the $3d$ electron compound YFe_2Al_{10}. The increase of the resistivity at low temperature may suggest that this material may be close to an itinerant-localization transition, such as a metal-insulator transition.

Chapter 5 : $\mathbf{Yb_2Pt_2Pb}$ It has been proposed that the Yb ions in Yb_2Pt_2Pb crystallize in a SSL with orthogonal aligned dimers in the 2D ab plane. Magnetization plateaux and a dome like ordered phase have been observed in magnetic fields. Moreover, a spinon like excitation has been observed in neutron scattering experiments, indicating a spin chain like structure along the crystalline c direction. It thus interesting to see whether the one dimensional Luttinger liquid physics or the 2D SSL physics with frustrated dimers plays a more important role in this low dimensional quantum magnetic system.

Chapter 2

Experimental Techniques

In this chapter, we will briefly describe how our samples are prepared, and how their magnetic properties are characterized, in order to give a general context for the data we are going to show in later chapters. We will first introduce the flux growth technique, which is the way that all three materials studied in this thesis are synthesized. Then we will introduce the thermal property measurement methods such as specific heat, magnetization and magnetocaloric effect. Neutron scattering is a well developed and powerful technique for studying correlated materials, and it will also be briefly discussed in this chapter.

2.1 Crystal Synthesis

2.1.1 Flux Growth Method

Quantum criticality has attracted a lot of attention in the research of condensed matter physics in last decades. Unusual physical properties like the non-Fermi liquid behaviors and various emergent phases are found near the quantum critical points (QCPs). In quantum critical systems, interactions are usually very complex, and subtle disorder or impurities can greatly affect the true ground state, masking the intrinsic properties of the material. This makes measurements on high quality single crystal samples essential for the accurate study of quantum critical behaviors. In addition, measurements on single crystals give information about the crystal anisotropy, which is crucial for understanding different magnetic interactions. Also, neutron scattering experiments on single crystals provides much more detailed information in the momentum energy ($Q-E$) space than on polycrystalline samples, which helps us to determine the full effective Hamiltonian.

Various methods including Bridgman furnace, Czochralski puller, and floating zone techniques are employed to grow single crystals[69]. However, many of these methods are limited to congruently melting compounds, and the starting composition needs to be very close to the desired product. The mixture is then heated above the melting temperature of this congruently melting point before the growth of the crystals. Sometimes this melting temperature can be very high, and it may exceed the working temperatures of the available furnaces.

One way to avoid some of these problems is to grow the crystals from metallic fluxes. A great advantage of the flux technique is that it enables the growth of high quality single crystals at relatively low temperatures, in a clean enclosed environment. The flux method is widely used in material science and condensed matter physics, and it has been explained in many excellent reviews [70, 71, 72]. In flux growth methods, crystals are grown from metallic solutions, like the growth of sugar crystals from a saturated sugar water solution. All the starting materials were first mixed together and then sealed in argon filled quartz tubes, as shown in fig. 2.1a. These quartz tubes were then heated in the high temperature furnace (fig. 2.1b). To make sure all the starting materials are dissolved into the liquid flux, the quartz tubes usually were kept at high temperatures for a few hours before a slow cool down to the lower temperatures where growth occurs. By controlling the cooling rate in different temperature ranges, different compounds were grown according to their phase diagrams. Many times, to get one single pure phase, the mixture was quenched from high temperatures, and the flux was subsequently removed by the centrifuge (fig. 2.1c), with the crystals remaining inside the growth crucibles (fig. 2.1d).

2.1.2 Growth of Yb_3Pt_4 and Yb_2Pt_2Pb

One major difficulty for the growth of Platinum Pt compounds is their very high melting points. In the case of the binary compound Yb_3Pt_4, the melting temperature T_c is $\sim$ 1700^0C (fig. 2.2), which is higher than the maximum working temperature for the quartz tubes ($\sim$ 1200^0C) and the maximum temperature for furnaces with SiC heating elements ($\sim$ 1500^0C). Also considering the huge vapor pressure of Yb at high temperature, it is almost impossible to grow Yb_3Pt_4 single crystals from a pure binary starting point. What we need to do is to find another metallic flux to lower the melting point. By checking the Yb - Pb and Pt - Pb phase diagrams (fig. 2.3), one can see that the melting temperatures of both Pt and Yb are greatly reduced in presence of lead. This gives a wide temperature range that is accessible with the furnace, while both Yb and Pt can remain in the liquid phase (as indicated

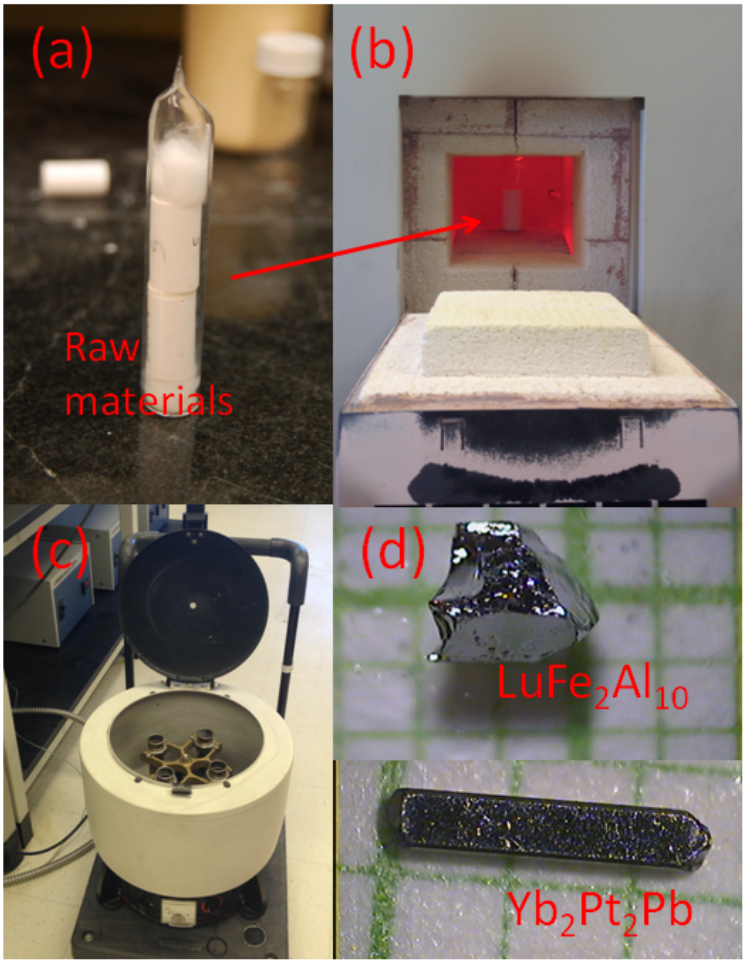

Figure 2.1: (a) A sealed quartz tube with raw starting materials contained in alumina crucibles. (b) High temperature furnaces with SiC heating elements, which can be heated up to $\sim 1500^0$C. (c) The mixture was quenched at high temperatures, and the metallic flux was removed by the centrifuge. (d) Some single crystals ($LuFe_2Al_{10}$ and Yb_2Pt_2Pb as marked) grown from the flux method. (Photos are courtesy of Akshat Puri.)

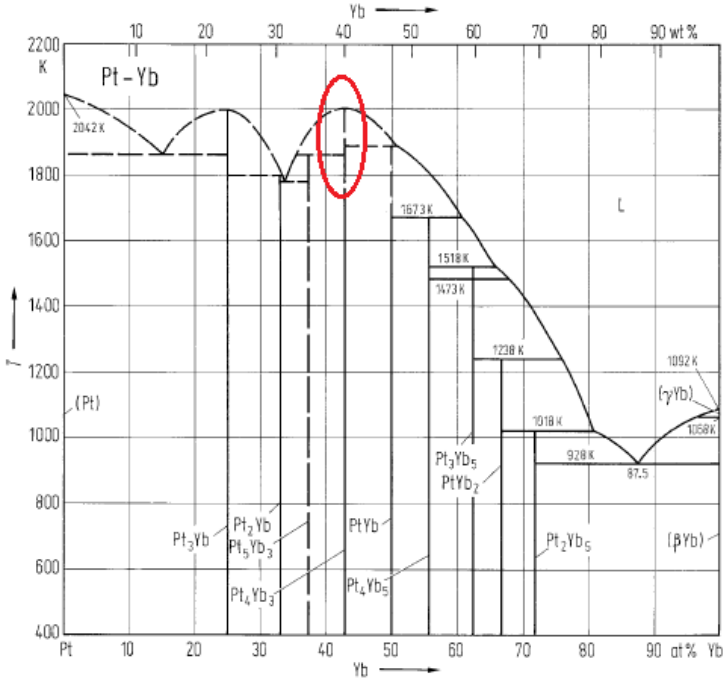

Figure 2.2: Yb - Pt binary phase diagram. The melting temperature of Yb_3Pt_4 is very high $\sim 1700^0$C, which is higher than the maximum working temperature ($T_{max} \approx 1500^0$C) of the furnace.

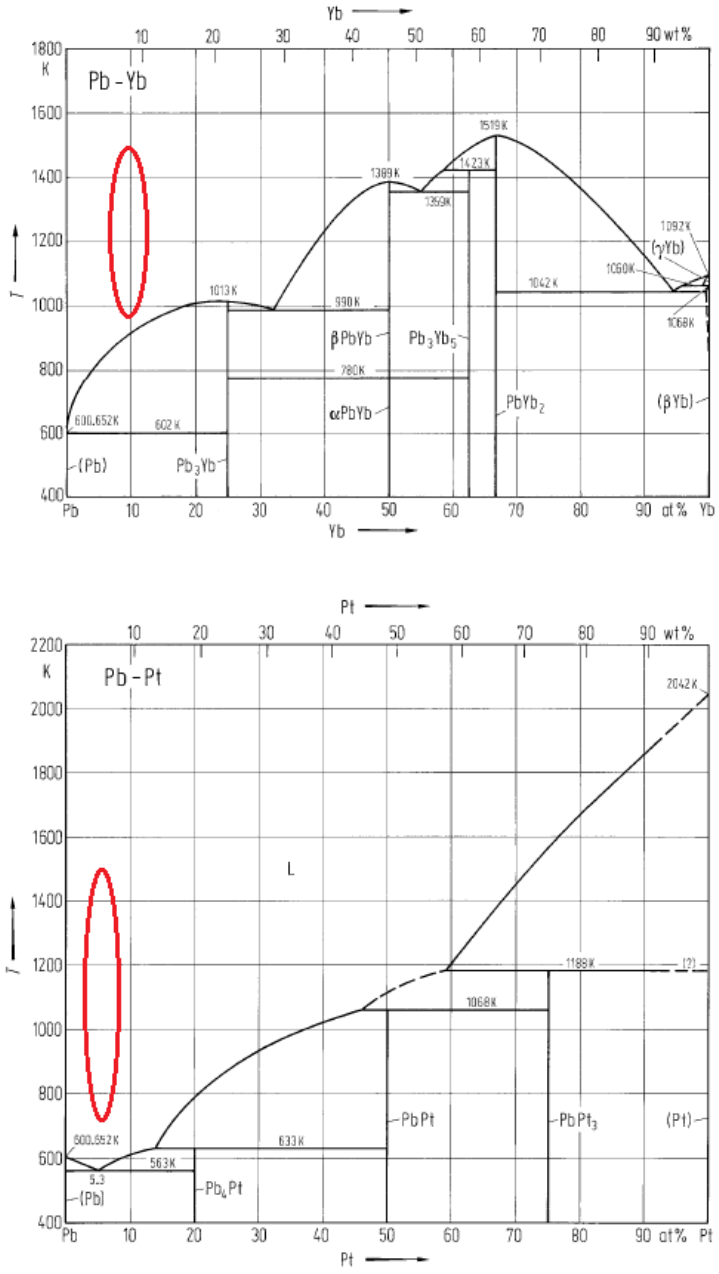

Figure 2.3: Above: Yb - Pb binary phase diagram. Below: Pt - Pb binary phase diagram. The melting point of Pt is greatly reduced by lead flux, and gives a wide temperature range that is accessible with the furnace. With the starting composition Yb:Pt:Pb=9:3.5:87.5, both Yb and Pt remain in liquid solution down to temperature as low as about 900 K ($\sim 600^0$C), as indicated by the red circles.

by the red circles). By choosing the right compositions of the mixture, Yb_3Pt_4 single crystals were successfully grown at about 800^0.

The refined recipe for growing Yb_3Pt_4 was found to be Yb : Pt : Pb = 9 : 3.5 : 87.5 [73, 74, 75]. The starting mixture with pure Yb, Pt, and Pb was placed in alumina crucibles, sealed in evacuated quartz tubes and heated to 1200^0C. After staying at the highest temperature for 4 hours, it was slowly cooled down to 800^0C over about 100 hours. The whole tube was removed from the furnace and spun in the centrifuge to remove the liquid lead flux, leaving long bar shaped single crystals (fig. 2.1d).

Since the exact ternary phase diagram of Yb-Pt-Pb is unknown, the growth of Yb_2Pt_2Pb is based on the analysis of the two binary phase diagrams. The new and refined recipe for the growth of Yb_2Pt_2Pb was found to be similar to the growth of Yb_3Pt_4 with the same starting ratio: Yb : Pt : Pb = 9 : 3.5 : 87.5. However, the growth temperature for Yb_2Pt_2Pb is much lower, which turns out to be between $800^0 \sim 600^0$C at this composition [66, 76]. Thus, by using separate temperature profiles, both Yb_3Pt_4 and Yb_2Pt_2Pb single crystals can be grown from lead flux.

2.1.3 Growth of Ln(Ln=Y, Lu, Yb)Fe_2Al_{10}

Compared to the growth of Yb_3Pt_4 and Yb_2Pt_2Pb, the growth of the YFe_2Al_{10} family of compounds is relatively simple. Since aluminum (Al) itself has a low melting point ($\sim 660^0$C), it could be used as a natural self-flux. Based on the reported Y-Fe-Al ternary isothermal section at 500^0C [77], YFe_2Al_{10} is very likely to be a congruent melting compound, with a melting temperature higher than 500^0C (fig. 2.4). By starting from the ratio of the pure materials Y : Fe : Al = 4 : 8 : 88, YFe_2Al_{10} single crystals were found to form around 960^0C [78]. By spinning the crucible in the centrifuge around this temperature, the aluminum flux was successfully removed. Similar compounds of this family such as $LuFe_2Al_{10}$ and $YbFe_2Al_{10}$ were also grown from Al flux in a similar way, just with slightly different starting ratios. The only thing we need to concern ourselves with is the two main competing binary phases $LnAl_3$ and Fe_4Al_{13}, as we can see from fig. 2.4. Both are congruently melting compounds. The melting temperature of $LnAl_3$ is slightly different for different cases depending on Ln=Y, Lu, Yb, and we have to vary the starting ratio of Ln:Fe accordingly. We found that large shiny $LuFe_2Al_{10}$ crystals could be grown from the composition Lu : Fe : Al = 3 : 5 : 92, and $YbFe_2Al_{10}$ single crystals could be grown with the ratio Yb : Fe : Al = 5 : 3 : 92. The magnetic properties of this family of compounds are reported later in chapter 4.

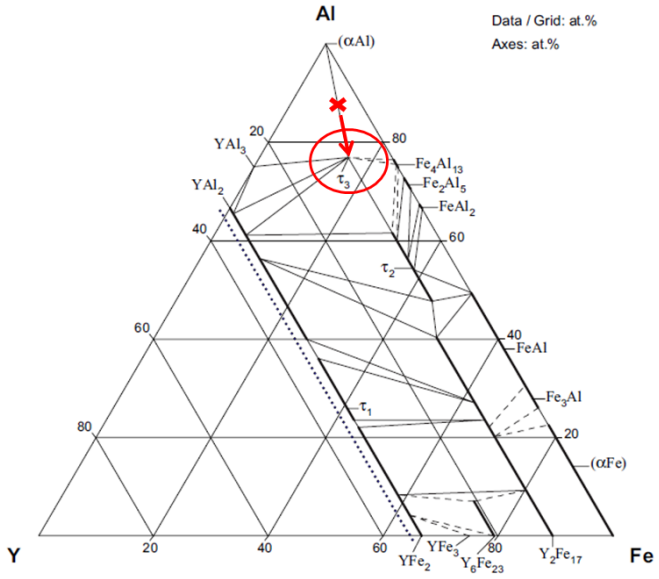

Figure 2.4: Y-Fe-Al isothermal section at 500^0C [77]. The red cross indicates the starting composition ratio with Y:Fe:Al=4:8:88. τ_3 is the desired ternary compound YFe_2Al_{10} as marked by the red circle.

2.2 Measurement Methods

2.2.1 Resistivity

Resistivity measurements were performed using the standard four wire technique. Ideal for resistivity measurements are either the long bar or needle like samples. Shown in fig. 2.5a is a typical resistivity set up of two needle shaped single crystals on the Dilution Refrigerator (DR) probe. Four pieces of Platinum wires (Diameter=0.001 inch) were attached to the sample using silver epoxy. The contact resistance is usually around $\sim 1-2\Omega$. Most of the resistivity data shown later in this thesis were taken using the AC transport option using the commercial Quantum Design Physical Property Measurement System (PPMS) with excitation currents from 0.1 to 1 mA, at temperatures down to 0.1 K, and in fields up to 14 T. A little GE-varnish was used to attach the sample to the resistivity puck, which helps to improve the thermal contact between the sample and the puck for low temperature measurements. Some examples of resistivity curves measured on Yb_2Pt_2Pb single crystals with field and current along different directions are shown in fig. 2.5b. The domed phase is marked by the dashed lines in the figure. No significant anisotropic behaviors were observed down to 0.5 K for field parallel ($B \parallel j$) and perpendicular

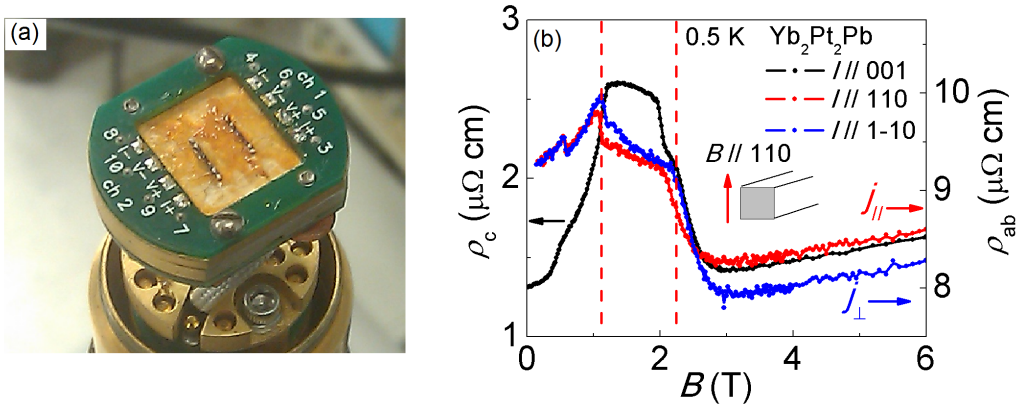

Figure 2.5: (a) A typical four-wire resistance set up on the Dilution Refrigerator (DR) puck. (b) A sample resistivity curve measured on the Yb_2Pt_2Pb single crystals with field and current along different directions.

($B \perp j$) to the current j direction, indicating that this is not a nematic phase as observed in the metallic ruthenate $Sr_3Ru_2O_7$ [80].

The measurement of resistance is also central to many other techniques. As we are going to introduce below, it is necessary for experiments including specific heat, magnetocaloric effect, and Hall sensor magnetometer. The differences are that, in those measurements, the resistance is measured and then transformed to some other physical properties of the sample.

2.2.2 Specific Heat

Field and temperature dependent specific heats were measured using the Quantum Design Physical Property Measurement System (PPMS) at temperatures down to 50 mK, and in magnetic fields up to 14 T. The thermal relaxation method was used in the specific heat measurements. Shown in fig. 2.6a is a picture of a specific heat puck with a YFe_2Al_{10} crystal mounted on the platform. On the back, there are two tiny objects. The black one on the right hand side is the heater, while the one on the left hand side is an additional thermometer, as marked by the red circles in fig. 2.6b. During a specific heat measurement, the system was first stabilized at an initial temperature, and then a heat pulse was given by the heater to make a rise in the sample temperature. After this heat pulse, the heater power was terminated, and the sample was allowed to relax back towards the initial puck temperature. The time dependent heater power and the thermal resistance of the thermometer are plotted in fig. 2.7a. This thermal resistance was then calibrated to the

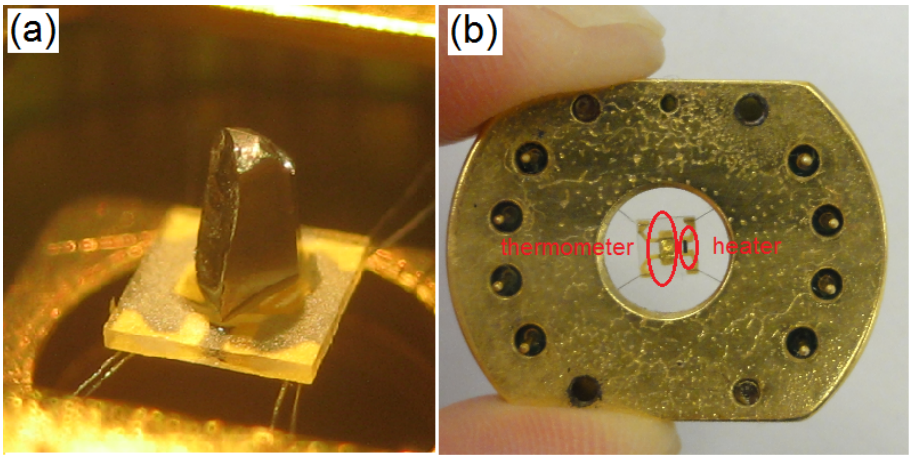

Figure 2.6: (a) A specific heat puck with an YFe_2Al_{10} crystal mounted on the platform. We can see the wires go below the platform, which are connected to the thermometer and heater under the platform respectively. (b) The back of a specific heat puck. The two pieces on the back of the platform as marked by the red circles are the thermometer and heater.

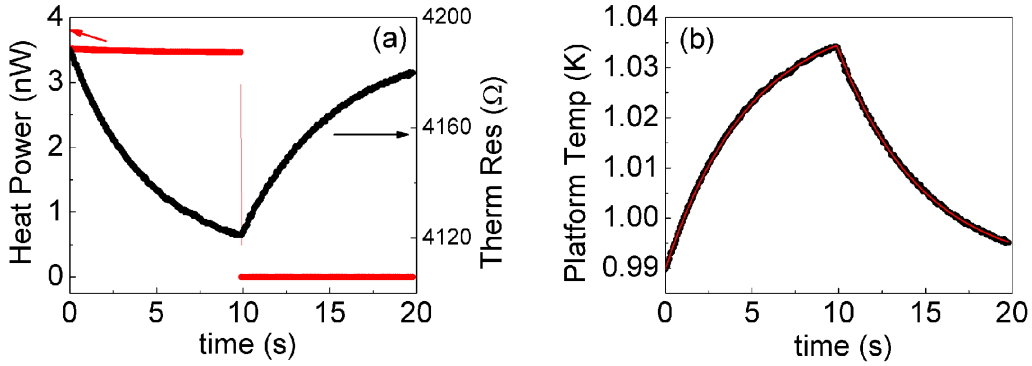

Figure 2.7: (a) Time dependent thermal power (red) and thermal resistances (black) during a single specific heat measurement. (b) Calibrated platform temperature based on the thermal resistance shown in (a). The red line is the numerical fitting to the heat transport function. [79]

platform temperature as shown in fig. 2.7b. Thus, the sample temperature during the whole heating and cooling process was monitored accurately by the thermometer, and the raw data were fitted numerically with the heat transport function (red line in fig. 2.7b)

$$P = C_P \frac{dT_P}{dt} + K_g(T_P - T_c) + K_w(T_P - T_B), \tag{2.1}$$

$$0 = C_c \frac{dT_c}{dt} + K_w(T_P - T_B). \tag{2.2}$$

to give the values of the sample specific heat C_p, addenda specific heat, thermal coupling, thermal time constants and so on [79]. Here P is the thermal power produced by the heater, and T_c, T_P and T_B are the temperatures of the sample, platform and thermal bath respectively, while K_g and K_w are the thermal conductances as indicated in fig. 2.8a [74, 79]. One crucial step in a good specific heat measurement is that the sample temperature should be monitored very accurately during the whole process. As we can see from fig. 2.7, the thermometer resistance changed about 50Ω for a $\Delta T \sim 0.04$ K change of the platform temperature. Usually, the thermal resistance can be measured with an accuracy of ±1Ω, and this means that the temperature variance could be easily recorded with an accuracy of $\Delta T \sim \pm 0.001$ K. By knowing this fact, one can use the same specific heat set up to measure another very interesting property of the material, the magnetocaloric effect (MCE).

2.2.3 Magnetocaloric Effect (MCE)

The magnetocaloric effect (MCE) Γ is observed when a magnetic material is put in a changing magnetic field, where it will heat up or cool down [81, 82, 83, 84]. Since MCE is a magneto-thermodynamic phenomenon, it reflects the basic thermodynamic properties such as entropy, magnetization, and specific heat of the material according to:

$$\Gamma = \frac{dT}{dB} = \frac{\partial S/\partial B}{\partial S/\partial T} = -\frac{\partial M/\partial T}{\partial S/\partial T} = -\frac{\partial M/\partial T}{C/T}, \tag{2.3}$$

and it can be determined indirectly using the measured specific heat and magnetization in different fields and temperatures. This MCE ratio has been proposed to be equivalent to the magnetic Grüneisen ratio, which has been shown to be divergent at QCPs [93, 94]. On the other hand, this effect could also be directly studied by measuring the field dependent temperature $T \sim B$ curve. This is usually done in materials near a phase transition where a giant entropy change ΔS is involved [85]. Interestingly, MCE has become a unique

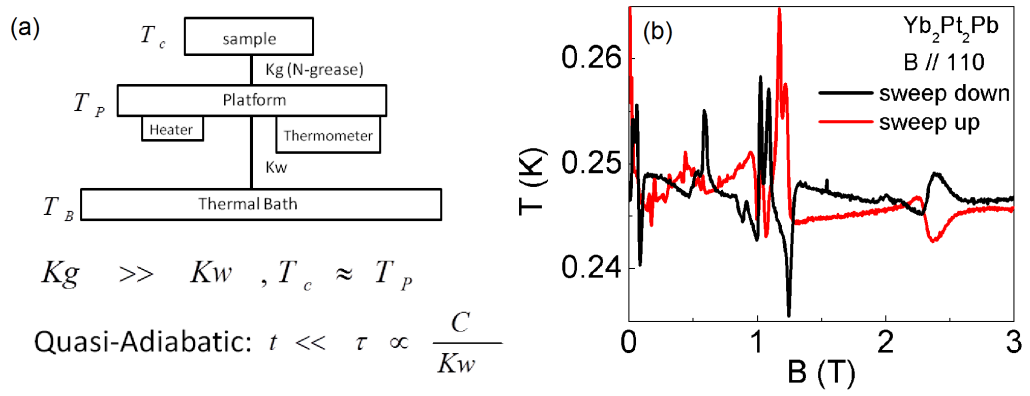

Figure 2.8: (a) Sketch of the MCE technique using the specific heat set up. T_c, T_P and T_B are the temperatures of the sample, platform and thermal bath respectively, while K_g and K_w are the thermal conductances as indicated. (b) A sample $T \sim B$ MCE curve of the Yb_2Pt_2Pb single crystal around 0.25 K with field along the 110 direction using this method. (In the courtesy of Moosung Kim. [67])

probe to study the low temperature field phase transitions in many quantum critical magnetic materials [86, 87, 89, 90, 91, 92, 126].

With the same set up as shown in fig.2.6 for a specific heat measurement, we can measure the MCE using the resistivity option in PPMS. This technique was initially introduced into our lab by Yuri Janssen. It works very well and is very efficient for studying the low temperature phase transitions in other magnetic materials [95, 97]. The sample was first mounted on a specific heat puck as in a normal specific heat measurement, but with a little more N-grease to improve the thermal contact. Then, it was cooled down to low temperatures in high vacuum. After the whole system was stabilized at the desired temperature, an additional magnetic field was applied, which was swept up and down through the field induced magnetic phase transitions. During the process of increasing or decreasing field, the sample temperature would increase or decrease. This is reflected by the resistance change of the thermometer, which could be accurately measured. Since the resistance of the thermometer has already been calibrated with temperature in different fields, we could use the calibration table to extract real sample temperatures in different magnetic fields. This gives us an in-situ temperature field ($T \sim B$) relation across the phase transitions.

The primary thing we need to be concerned about here is the heat relaxation from the sample to the environment heat bath. Usually, the thermal

contact between the sample and the platform through the N-grease is very good, and we assume that $T_c \approx T_P$. Since the experiment was performed in high vacuum, the only thermal leak from the platform to the thermal bath is then through the thin wires (fig. 2.6b), which have very low thermal conductivities at low temperatures (about 10^{-7} W/K at 1.0 K). By choosing a sample of the right size, we can always make the measuring time t much smaller than the decay time τ, which depends on the specific heat C and wire thermal conductance K_w as $\tau \sim C/K_w$. Thus the whole process can be assumed to be quasi-adiabatic. By comparing the hysteresis between increasing fields and decreasing fields, one can also distinguish first order phase transitions from second order continuous phase transitions. Shown in fig. 2.8b is an example T vs B MCE curve of the Yb_2Pt_2Pb single crystal around 0.25 K with field along the (110) direction [67]. Strong anomalies around 1.25 T clearly indicate a first order phase transition. By following a single curve with field sweep up (or sweep down), the symmetry of the temperature increase or decrease around 1.25 T and 2.3 T suggests an intermediate ordered phase with reduced entropy, since the material releases heat when it enters this phase and absorbs heat when it leaves this intermediate phase [97]. A relative entropy change could also be estimated at the critical points by the slope change across the phase transitions [75, 92].

2.2.4 Hall Sensor Magnetometer

Most of the magnetic properties reported in this thesis were measured using the commercial Quantum Design Magnetic Property Measurement System (MPMS) with superconducting quantum interference device (SQUID), in magnetic fields up to 7 T at temperatures from 1.8 K to 400 K. However, for many magnetic materials that we are interested in, magnetic transitions may occur at much lower temperatures than 1.8 K. Although some other properties like magnetoresistivity, specific heat and MCE can be measured down to 0.1 K, they usually give only indirect information about the magnetic properties below 1.8 K. For many cases, knowing the actual magnetization at lower temperatures is crucial. To solve this problem, we have used a Hall sensor as a small dc magnetometer, and it turns out to work very well down to temperature as low as 0.2 K in fields up to several Tesla. This work was done in collaboration with Neil Dilley from Quantum Designs and Andrea Candini from Università di Bologna, Italy [98, 99, 100].

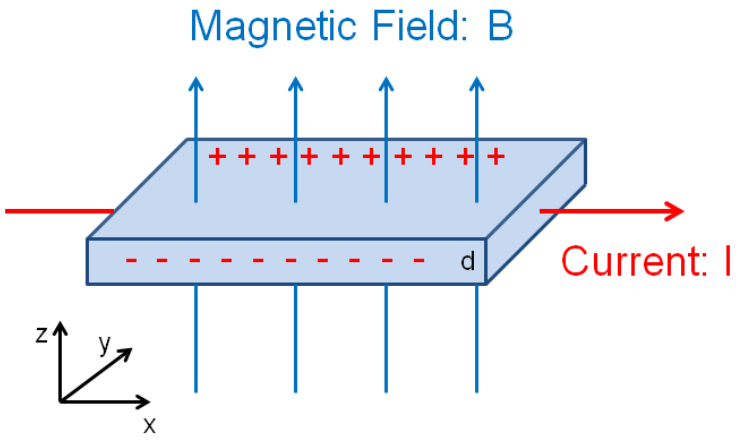

Figure 2.9: Schematic view of the Hall Effect. The Hall voltage comes from the Lorentz force experienced by the charges moving in magnetic fields applied perpendicular to their motion.

Hall Effect

Hall effect sensors measure magnetic fields based on the classical Hall effect discovered by Edwin H. Hall in 1879. The Hall effect is caused by the Lorentz force that is experienced by the charges moving in magnetic fields perpendicular to their motion. Considering the carriers moving in a uniform conducting material with thickness d, the path of these carriers will be deflected in the presence of a perpendicular magnetic field B, and charges accumulate on the two sides that are transverse to the current flow. The accumulation of the charges generates a transverse Hall voltage, as shown in fig. 2.9. The magnitude of the Hall voltage V_H can be expressed as

$$V_H = R_H I \times B/d, \tag{2.4}$$

where R_H is the Hall coefficient. For two dimensional electron systems (2DES), $R_H = 1/ne$ with n being the two dimensional carrier density and e is the electron charge ($\simeq 1.6 \times 10^{-19} C$).

For a Hall effect sensor, the carrier density n and the dimension d are already known, and the Hall voltage is simply proportional to the magnetic flux. This magnetic flux could be generated by an external magnetic field, in which case the Hall effect sensor is used to calibrate the magnetic fields. Alternatively, the magnetic flux may come from the sample magnetization itself, and in this case, Hall effect sensors could be used as magnetometers.

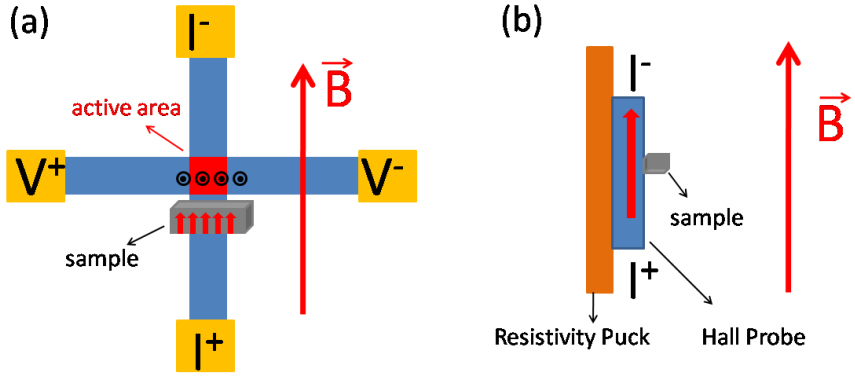

Figure 2.10: Schematic view of an experimental Hall sensor configuration. (a) Top view of the Hall probe. Red region is the active area, and the magnetic sample is placed close to it. (b)Side view of the Hall probe, which is attached to a resistivity puck. The external magnetic field B is always parallel to the driven current in order to minimize the linear background from the applied external field.

Devices and Setup

Although the Hall effect has been known for more than one hundred years, the first application of the Hall effect in a device was only realized in the 1950s. Interest has continued in subsequent years, assisted by progress in microfabrication and the growth of high mobility two dimensional electron semiconductor heterostructures. GaAs/AlGaAs heterostructures are considered to have better performances at low temperatures, and these are the ones we used in this thesis research [99, 100]. A typical Hall sensor is shown in fig. 2.10. There are four terminals with the current I running through along the longitudinal direction, while the Hall voltage V_H is measured across the perpendicular transverse direction. The experiment can be performed as a standard four wire resistivity measurement.

With this set up, what we measured is the Hall resistance

$$R = V_H/I = R_H/d * B. \tag{2.5}$$

Since the dimensional factor d and Hall coefficient R_H are already known and could be assumed as a fixed constants, the output Hall resistance is then directly proportional to the external magnetic flux $\mathbf{B}$. There are two possible contributions to this total magnetic flux: $\mathbf{B} = \mathbf{B}_{ext} + \mathbf{B}_{samp}$. The first term

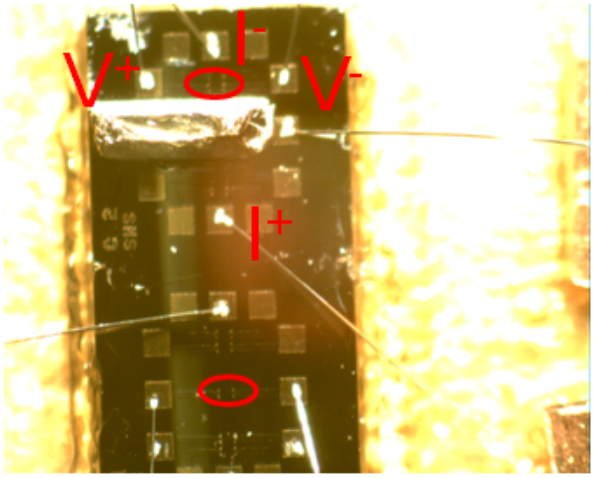

Figure 2.11: Wiring of the actual Hall probe that we are using. There are two panels, and each panel is combined with five active regions. However, we only used one of them. The red circled area is the active region. An empty sensor with no sample was used as the reference for the subtraction of background.

is the external magnetic field B_{ext} generated by the magnet, and the second term is the one induced by the magnetic sample $\mathbf{B}_{samp}$, which is taken to be proportional to the sample magnetization M. In order to separate the sample signal from the background caused by the external field, two methods were applied.

The first one is to minimize the effect of the external field by aligning the Hall sensor in such a way that the current flow is parallel to the external magnetic field B, as indicated in fig. 2.10. From equation 2.5, we can see that in this configuration only the perpendicular component of the external field contributes to the Hall voltage. The linear background is greatly reduced with this configuration in fig. 2.10. In addition, this minimizes the quantum oscillation of the 2D electron gas at very low temperatures.

The second way is to measure an empty probe which works as a reference channel. As shown in fig. 2.11, another clean Hall sensor without any sample was measured at the the same time as the sample, and the data of the reference channel were subtracted from the sample bridge.

By combining these two methods, a clean signal that originated just from the sample was isolated. Plotted in fig. 2.12a is an example of the measured Hall resistance of Yb_3Pt_4 single crystals. The external magnetic field is parallel to the driven current I and along the (110) crystal direction. The cusp shaped feature indicates the antiferromagnetic (AF) phase transition, which could be clearly seen at low fields, shifting to lower temperatures with increasing fields.

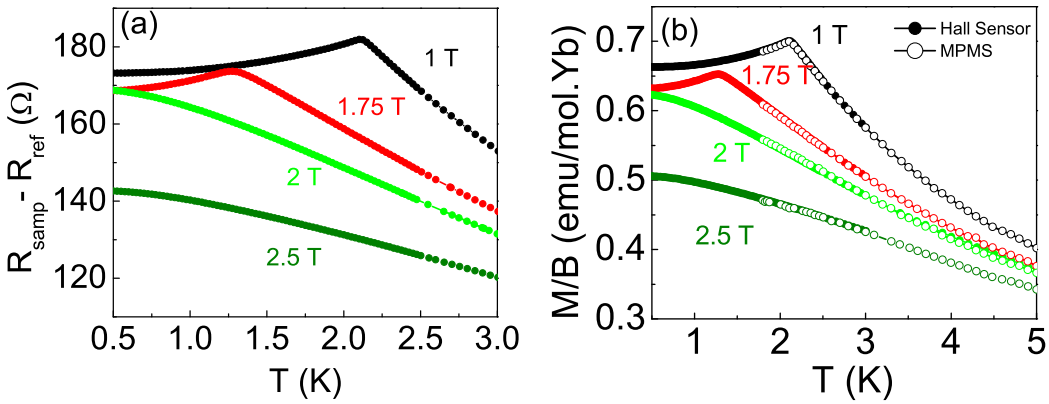

Figure 2.12: (a) Measured Hall resistance of Yb_3Pt_4 as a function of temperature in different magnetic fields. (b) Calibration of the raw Hall resistance to absolute magnetization. Solid circles are the data measured using the Hall sensor magnetometer, and the empty circles are the results measured in MPMS on the same Yb_3Pt_4 single crystal. These two data sets match each other very well in the overlap region from 1.8 K to 3.0 K.

No magnetic phase transition was observed down to 0.5 K above the critical field of 2.0 T. These data are all taken in the commercial PPMS using the dc resistivity option. With the combination of the ^{3}He or Dilution Refrigerator (DR) options, one can easily measure the magnetization well below 1.8 K, the lowest measurement temperature of the standard MPMS magnetometer.

Calibration to Magnetization

To calibrate the measured Hall resistance to the actual sample magnetization, a few things need to be considered. One difficulty is to relate the geometrical shape of the sample to the actual flux detected by the sensor. For micro-size crystals or nano-materials, this is rather difficult, since the magnetic flux induced by the samples may not be spatially uniform near the Hall sensor active region. However, in our case, the sample is more like a regular shaped magnetic bar with the length much larger than the actual Hall sensor active area. In this case, we can assume that the magnetic flux around the small Hall sensor region is roughly homogenous, and the effects caused by the sample edges can be neglected. To get the absolute magnetization, we scaled the data in fig. 2.12a to the magnetization measured on the same sample in MPMS. We can see from fig. 2.12b that both data sets are consistent with each other over the overlapping temperature region from 1.8 K to 3 K. This allows us

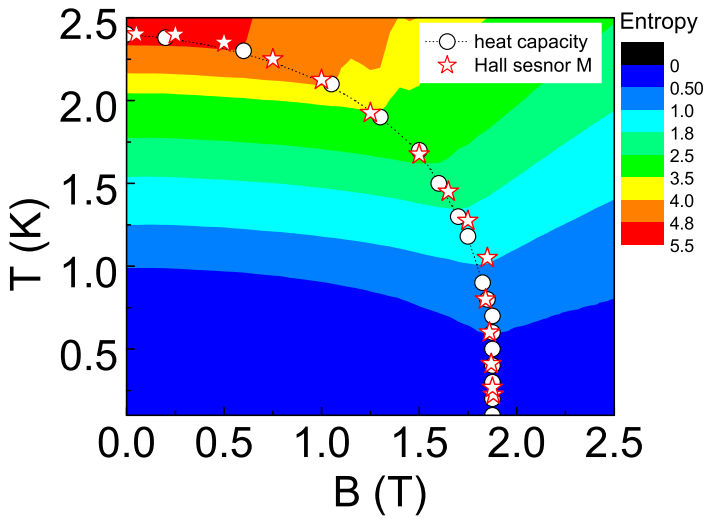

Figure 2.13: Temperature - Field ($B - T$) phase diagram of the sample Yb_3Pt_4. Stars are the phase transition line measured using the Hall sensor magnetometer, and open circles are the phase line extracted from specific heat measurements. The lines in the colored contour plot are the equal entropy lines that correspond to the MCE measurements.

to extract the absolute magnetization values of Yb_3Pt_4 and the magnetic phase transition line at lower temperatures. As shown in fig. 2.13, the field temperature phase line extracted from the magnetization measurements using the Hall sensor magnetometer agrees well with the one extracted from specific heat measurements.

2.2.5 Neutron Scattering Techniques

Neutron scattering is a well developed technique for studying crystallography and dynamics in condensed matter physics and material science. Neutron scattering theory can be found in books and many lecture notes [55, 101, 102, 103, 105]. There are two reasons that neutron scattering techniques are very important in the research of strongly correlated systems. The first is due to the basic properties of neutrons, which carry zero charge but have nonzero magnetic moments. The neutral charge allows neutrons to penetrate deeply into the sample, and they interact with the nucleus instead of the electron cloud, as in X-ray experiments. More importantly, the nonzero magnetic dipole of neutrons makes them sensitive to the magnetic moment of the unpaired electrons in the the sample, and so the neutrons can be used as a unique probe for investigating magnetic structures. The second reason that neutron scattering is quite important is that the neutron energies available at neutron scattering facilities are close to many excitation energy scales in the condensed matter physics, like the phonon excitations in crystals, spin waves in ordered magnets and such. These make neutron scattering well suited for the study of magnetic order and spin-spin correlations.

The master formula of the magnetic scattering cross section of unpolarized neutrons is [104]

$$\frac{d^2\sigma}{d\Omega d\omega} = (r_m)^2 \frac{k_f}{k_i} e^{-2W} F^2(Q) \sum_{\alpha,\beta} (\delta_{\alpha\beta} - \frac{Q_\alpha Q_\beta}{Q^2}) \frac{1}{(2\mu_B)^2} S^{\alpha\beta}(Q,\omega), \tag{2.6}$$

where r_m gives the magnetic scattering length with

$$r_m = -2\mu_B \frac{2m}{\hbar^2} \mu_n = -5.391 \times 10^{-13} cm. \tag{2.7}$$

Here, k_i and k_f are the wave vectors of the incoming and outgoing neutrons. The scattering is corrected by the Debye-Waller factor e^{-2W} for thermal vibrations. $F^2(Q)$ is the magnetic form factor that takes into account that the scattering is spatially extended over a length scale that decreases with increasing the transferred momentum Q. The term $\delta_{\alpha\beta} - Q_\alpha Q_\beta / Q^2$ enforces

that only magnetic components perpendicular to the scattering vector Q contribute to the scattering cross section. The magnetic scattering function is

$$S^{\alpha\beta}(Q,\omega) = \sum_{j,j'} e^{iQ\cdot(R_j - R_{j'})} \sum_{\lambda,\lambda'} p_\lambda \langle\lambda|\hat{S}^\alpha_{j'}|\lambda'\rangle\langle\lambda'|\hat{S}^\beta_j|\lambda\rangle\delta(\hbar\omega + E_\lambda - E_{\lambda'}). \quad (2.8)$$

For elastic scattering without energy transfer, the scattering function $S^{\alpha\beta}(Q,\omega)$ can be simplified to [101]

$$S^{\alpha\beta}(Q,\omega) = \sum_l e^{iQ\cdot l}\langle\hat{S}^\alpha_0\hat{S}^\beta_l\rangle\delta(\omega), \quad (2.9)$$

where $l = R_j - R_{j'}$ is the distance between the two ions at R_j and $R_{j'}$. For a classical, non-ordered paramagnet, there are no correlations between spins S_i and S_j at different sites, and the spin matrix element is time independent, thus for $l \neq 0$,

$$\langle\hat{S}^\alpha_0\hat{S}^\beta_l\rangle = \langle\hat{S}^\alpha_0\rangle\langle\hat{S}^\beta_l\rangle = 0. \quad (2.10)$$

The only non-zero term is when $\alpha = \beta$ at $l = 0$, which equals to [101]

$$\langle\hat{S}^\alpha_0\hat{S}^\beta_l\rangle = \delta_{\alpha\beta}\langle\hat{S}^\alpha_0\rangle^2 = \frac{1}{3}S(S+1). \quad (2.11)$$

This gives isotropic magnetic scattering, which is proportional to the value of the magnetic moment S in neutron scattering. However, in a magnetically ordered state, the spins correlations are not zero, and the magnetic scattering is now wave vector dependent. The magnetic diffraction peaks can be represented by the propagation vector τ in addition to the original translational vector of the lattice. In a ferromagnetic case, the propagation vector $\tau = 0$, and elastic scattering appears at the same wave vectors as the nuclear diffraction peaks, while the peak intensity is determined by the magnetic moment direction with respect to the transferred momentum Q. For antiferromagnetic order, the propagation vector τ can have nonzero values, and this usually gives new magnetic peaks in addition to nuclear peaks.

For inelastic scattering, spin wave excitations are usually observed in the magnetic ordered states due to the breaking of the translation symmetry. A more interesting question was raised by the study of the strongly correlated systems like the low dimensional or strongly frustrated quantum magnets. Spin liquid ground states can be observed in these materials, where translational symmetry was not broken when approaching the lowest temperature. The question is whether one could distinguish these dynamically correlated quantum states from the conventional paramagnets when static order is absent in both. Because neutrons can actually probe the spin-spin correlations,

even in the absence of static order, magnetic neutron scattering does show significant differences. For example, pinch point scattering with a particular Q dependence that comes from the spin ice rule on the magnetic clusters has been observed in the Kagome ice [106], and also cluster ring like scattering was observed in the spinel $ZnCr_2O_4$ with the pyrochlore lattice [107]. Exotic excitations like spinons with continuum dispersions were observed low dimensional spin chains or spin ladder materials [54, 55].

Neutron Sources

Neutron scattering experiments were performed at two neutron sources located at the National Institute of Standards and Technology (NIST) Center for Neutron Research in Gaithersburg, Maryland, and at the Spallation Neutron Source (SNS) at Oak Ridge National Lab in Tennessee. There are two kinds of neutron sources for neutron scattering studies. The one at NIST, NCNR is a reactor neutron source, which uses a controlled fission process to produce a steady flux of neutrons. Neutrons can also be generated by spallation neutron sources like the one in Oak Ridge National Lab, in which high energy proton pulses are fired into a heavy metal target, resulting in pulses of neutrons.

The reactor sources have the advantage of stable time independent flux with higher time averaged intensity. However, spallation neutron sources have the highest peak flux, which offer significant advantages in measurements using time-of-flight (TOF) methods. Here we briefly describe several different instruments employed in this thesis. Further information can be found in the references [101, 102, 108].

Triple Axis Spectrometer

The triple axis spectrometer was first developed by Bertram Brockhouse at the NRX research reactor at the Chalk River Laboratory in Canada. It is well suited to reactor sources with continuous stable neutron flux. The one used in this thesis is the Double Focusing Thermal Triple-Axis Spectrometer (BT-7) located at NCNR, NIST. A schematic view of a triple axis spectrometer is shown in fig. 2.14. The 'triple axis' corresponds to the three axes of the monochrometer, the sample, and the analyzer. A single crystal monochromator selects a particular wavelength defined by the Bragg relation from the white neutron beam produced by the source. This determines the energy of the incoming neutrons by fixing the rotation angle θ_M. This monochromatic beam is then scattered by the sample, and the sample orientation can be alternated by rotation of the angle θ_S. After scattering from the sample, the neutrons may not just change their momentum but

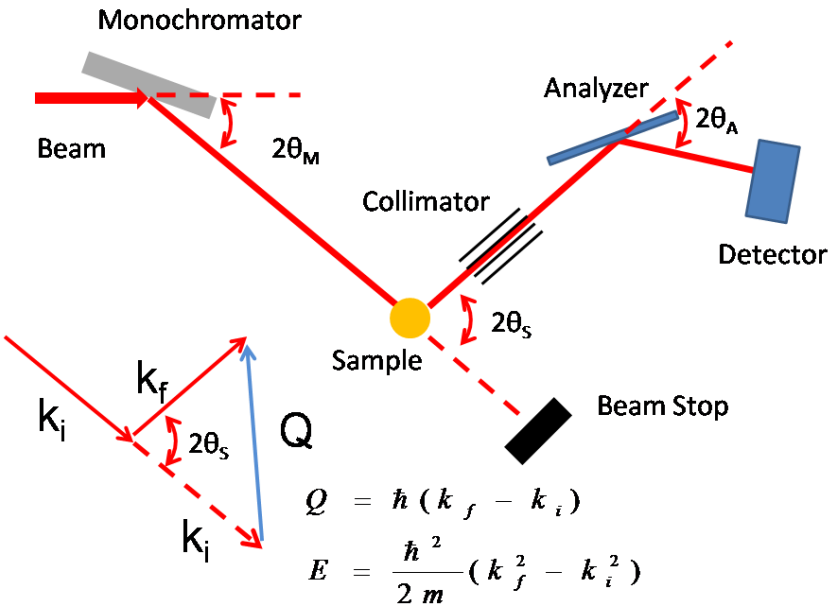

Figure 2.14: Schematic view of a typical triple axis spectrometer with the scattering triangle shown on the lower left corner.

also their out-going energy. The analyzer performs a similar function as the monochrometer, defining the final energy of the scattered beam using Bragg reflection by changing angle θ_A. Only neutrons with particular selected energies can be counted by the detectors.

The wave vectors of the incoming (k_i) and final (k_f) neutron beams determine the transferred wave vector Q and energy E based on the momentum and energy conservation laws

$$Q = \hbar(k_i - k_f), \tag{2.12}$$

$$E = E_i - E_f = \frac{\hbar^2}{2m}(k_i^2 - k_f^2). \tag{2.13}$$

These are in turn connected to the three independent rotation angles θ_M, θ_S and θ_A. Variation of these angles allows measurements of the scattering function at any point in momentum and energy space using triple axis spectrometers.

Time of Flight (TOF) Chopper Spectrometer

In the TOF technique, the incident neutron beam is chopped to create a pulsed monochromatic beam using mechanical choppers instead of the single crystal monochromator in the triple axis spectrometer. The rotating speed of the monochromating choppers selects the neutron velocity v_i. In a TOF spectrometer, the time that it takes the pulsed neutrons to travel from the chopper to the sample is measured. After scattering from the sample, the neutron energy changes, and thus the velocity of the neutron beam is modified. By recording both the positions and time delays of the neutrons as they arrive at the detectors, the momentum and energy transfers can be calculated. As shown in fig. 2.15, the distance R_i from the chopper to the sample and R_f from the sample to the detector could be accurately measured. By recording the arrival time t at the detector, the final velocity of the scattered neutrons is then determined according to

$$t = \frac{R_i}{v_i} + \frac{R_f}{v_f} \Rightarrow v_f = \frac{R_f}{t - R_i/v_i}. \tag{2.14}$$

Based on the energy conservation law (equation 2.4), the energy transfer can be calculated as

$$E = E_i - E_f = \frac{1}{2}mv_i^2 - \frac{1}{2}m(\frac{R_f}{t - R_i/v_i})^2. \tag{2.15}$$

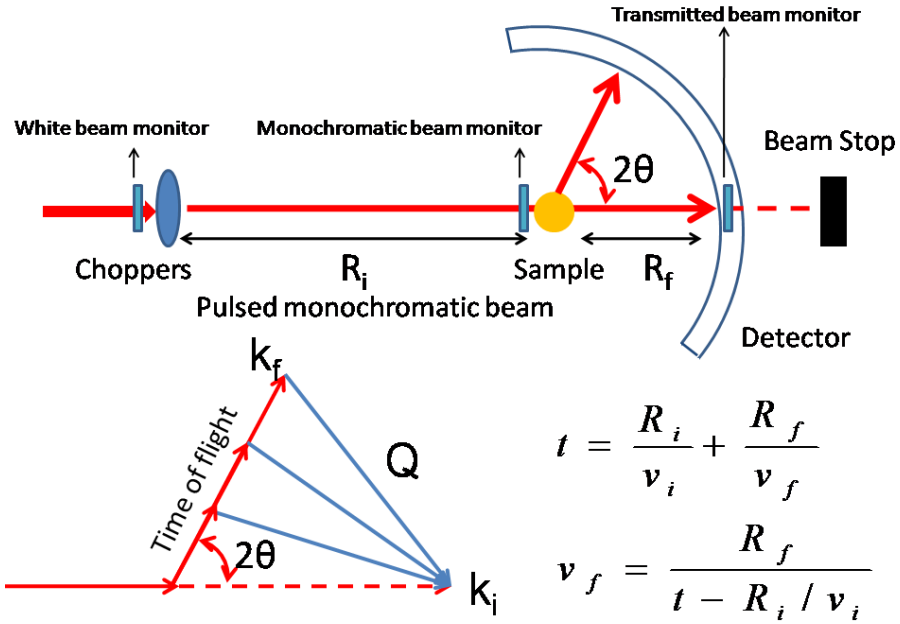

Figure 2.15: Schematic view of a generic time of flight (TOF) chopper spectrometer. Different from the triple axis spectrometer, the incoming neutron velocity was selected by the monochromatic choppers. In the scattering triangle, the scattering vector Q varies with the time of flight, and the transverse energy E is measured through the recording of the time of flight t.

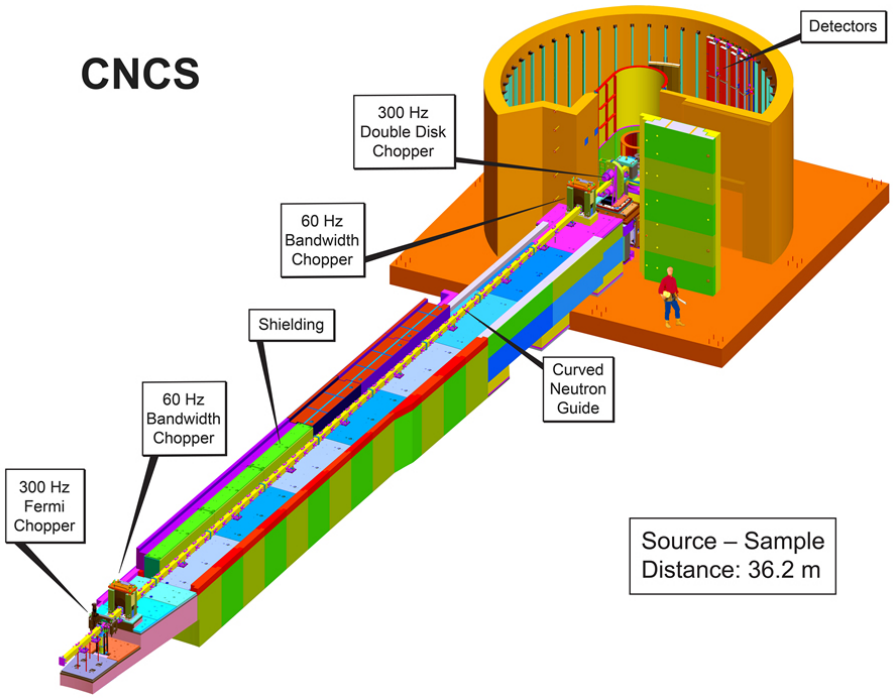

Figure 2.16: Schematic view of the design of the Cold Neutron Chopper Spectrometer (CNCS) at the Spallation Neutron Source (SNS), Oak Ridge[110].

The momentum transfer Q is determined by the initial wave vector k_i and the final wave vector k_f. The initial wave vector k_i is already known, however, k_f depends on the final energy E_f and the scattering angle of the arriving neutrons, as shown on the scattering triangle in fig. 2.15. We can see that the transferred wave vector Q is now coupled to the energy transfer E. This is different from the triple axis spectrometer, where only one point in the momentum energy $(Q - E)$ space is measured at each time, where in TOF spectroscopy a two dimensional array of detectors covering a big range of momentum and energy $(Q - E)$ is used in TOF spectrometers. This is very efficient for the study of the excitations over a wide range of momentum Q space.

TOF techniques can also be used at continuous flux neutron sources, however, choppers are needed first to provide the pulsed beams for the monochromating choppers, as for the Disk Chopper Spectrometer (DCS) at NCNR, NIST [109]. Compared to the reactor sources, the pulsed spallation neutron sources are naturally more suited for the TOF technique. Shown in fig. 2.16 is the schematic view of the Cold Neutron Chopper Spectrometer (CNCS) at SNS, Oak Ridge [110].

Neutron experiments in this thesis using TOF spectrometers were performed at DCS, (NCNR, NIST) and CNCS, (SNS, Oak Ridge). Both experiments on oriented arrays of Yb_2Pt_2Pb single crystals were performed in the [H, H, L] scattering plane with magnetic field applied along the (1,-1,0) crystal direction. Since CNCS was built at the Spallation Neutron Source, the maximum flux intensity is higher than the one at DCS. In addition to the difference in the flux intensity between DCS and CNCS, the detectors in CNCS are also different. For DCS, the spectrometer detectors are long arrays of ^{3}He tubes, and only horizontal positions of the arriving neutrons are recorded. However, in CNCS, the tubes are also sensitive along the vertical direction, and detect neutrons at angles as large as $\pm 16^0$ above and below the horizontal scattering plane [111].

Chapter 3

Magnetic field tuning of the antiferromagnet Yb_3Pt_4

This chapter presents the magnetic properties and phase diagram of the antiferromagnet Yb_3Pt_4. Yb_3Pt_4 orders antiferromagnetically at 2.4 K in zero field, and the magnetic order can be gradually suppressed to $T \rightarrow 0$ at the critical field B=1.9T for field applied in the ab plane. The purpose of these experiments was to observe how the magnetic properties would evolve through the magnetic critical points. We first present measurements of the specific heat, magnetization, magnetocaloric effect and magnetic neutron diffraction. The field temperature (B-T) phase diagram based on these experiments was established, and the $T = 0$ phase transition turns out to be a first order critical end point (CEP). For further investigation of the nature of the CEP, we measured the electrical resistivity ρ down to 0.1 K in magnetic fields. No non Fermi-Liquid (nFL) was observed, and the magnetoresistivity was dominated by the scattering of conventional quasiparticles from paramagnetic fluctuations of Yb local moments. Based on these experiments, we conclude that in contrast to heavy fermions like $YbRh_2Si_2$, Yb_3Pt_4 represents an extremely simple regime of f-electron behavior where the Yb moments and conduction electrons are almost decoupled, where Kondo physics plays little role.

3.1 Introduction

Materials where magnetic order can be suppressed to low or even vanishing temperatures have proven to be rich sources of new physics. In different families of compounds, based both on transition metal and rare earth moments, the relative weakness or absence of competing magnetic phases makes it possible to observe new types of ordered states, most notably superconductivity [28, 29] and quasi-ordered phases such as 'spin nematics' [80], that would normally be obscured. The magnetic excitations are greatly modified when the onset of magnetic order occurs at low temperatures, due to the importance of quantum mechanical fluctuations between the ordered and disordered states, leading to their characteristic E/T scaling [16, 17] and to unusual temperature divergencies in the specific heat and magnetic susceptibility [10, 12, 112, 113, 114, 115]. It is a matter of continuing debate as to how these fluctuations enable or destabilize novel orders, for instance whether they provide a pairing mechanism for unconventional superconductors [116].

Very few compounds form with magnetic order restricted to zero temperature, and in most cases it is necessary to use pressures, compositions, or magnetic fields to tune the ordering temperature to $T = 0$ to form a quantum critical point (QCP) if magnetic order is continuous, or a quantum critical end point (QCEP) if the magnetic transition becomes first order. It is well appreciated that quantum critical compounds are exquisitely sensitive to disorder, and it has been established that even modest amounts of disorder can change the order of magnetic transitions if the transition temperature is sufficiently low [7, 8, 117]. Pressure tuning of magnetic transitions has an appealing simplicity, since it largely avoids these concerns about disorder, but experimental access is somewhat limited, due to the bulky equipment needed for high pressure measurements. Thermodynamic measurements are especially problematic at high pressures, although they are of particular value for understanding how cooperative phases are stabilized at the lowest temperatures. For these reasons, magnetic field tuning of magnetic transitions is increasingly attractive, although it has been noted that the quantum criticality induced by field and pressure within a single material may not be identical [118, 119, 120].

Magnetic fields affect the stability of magnetic order at two different levels. First, fields can destabilize the magnetic structure, selected by the system as the lowest energy configuration for $T \to 0$ in zero field. This is effected by the suppression of critical fluctuations, hampering the establishment of long-ranged and long lived magnetic correlations that can lead to magnetic order itself. Second, magnetic fields can change the properties of individual magnetic

moments as well, resulting in Zeeman splitting of the states of the crystalline electric field manifold, and in some cases by the suppression of moment compensation by the Kondo effect. Both effects are expected to be important for heavy fermion compounds, where two limiting behaviors can be identified. In one case, magnetic order emerges at T_N from a paramagnetic state where the moments are highly localized, having only a weak exchange coupling to the conduction electron states whose energy scale $k_B T_0 \leq k_B T_N$. Alternatively, the crystal field states can be extensively broadened via hybridization, possibly to the point that the localized character can be considered minimal or absent when magnetic order occurs at $k_B T_N \leq k_B T_0$.

Field tuning experiments have been extensively pursued in complex systems like $CeCu_{6-x}Au_x$ [118] and $YbRh_2Si_2$ [121], where the antiferromagnetic phase line remains continuous as $T_N \rightarrow 0$ at a quantum critical field B_{QCP}. It is evident here that not only does the magnetic order evolve with field, but also the underlying electronic structure can itself be critical at or near B_{QCP} [10, 122]. We present here an experimental study of the field-temperature phase diagram of the heavy fermion antiferromagnet Yb_3Pt_4. Yb_3Pt_4 orders antiferromagnetically at a Néel temperature $T_N = 2.4$ K [73]. While Yb_3Pt_4 is metallic, magnetic order develops directly from a paramagnetic state where the fluctuating moments correspond to the ground doublet of the crystal field split Yb^{3+} ion, with no indication of any Kondo effect. We will argue here that the relative simplicity of the antiferromagnetic order in Yb_3Pt_4 allows us to explore the field tuning of antiferromagnetic order without the complexities of electronic delocalization that are found in systems like $YbRh_2Si_2$.

3.2 Experimental Details

Single crystals of Yb_3Pt_4 were grown from lead flux (fig. 3.1(a)), and powder x-ray diffraction measurements were used to verify the rhombohedral Pu_3Pd_4 structure type [73, 75]. The field B and temperature T dependent dc magnetization $M(B,T)$ and ac magnetic susceptibility χ'_{ac} was measured using a Quantum Design Magnetic Properties Measurement System (MPMS) for temperatures above 1.8 K, and at lower temperatures using a Hall sensor-based technique that was calibrated to the MPMS data above 1.8 K [98, 99, 100]. The specific heat was measured for temperatures that ranged from 0.1 K to 4 K, and in fields as large as 3 T using a Quantum Design Physical Property Measurement System (PPMS), equipped with ^{3}He and dilution refrigerator inserts. Measurements of the magnetocaloric effect (MCE) were performed in high vacuum using the PPMS ^{3}He specific heat puck where the sample was

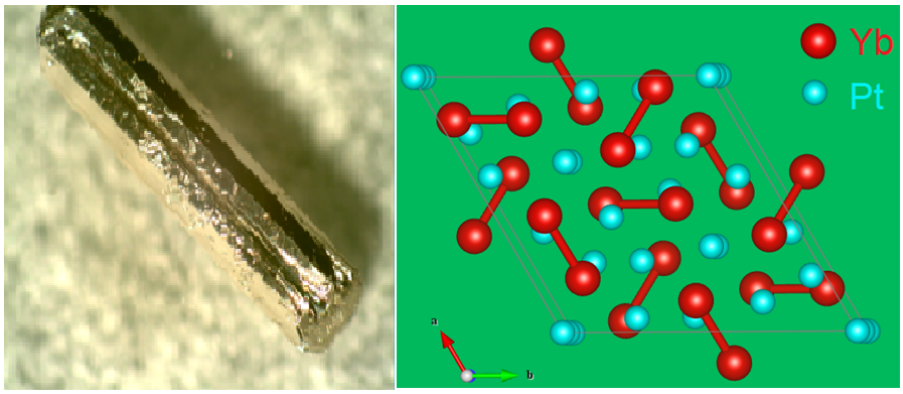

Figure 3.1: (a) A Yb_3Pt_4 single crystal grown from lead flux. The long axis is the c axis. (b) Unit cell of the crystal structure of Yb_3Pt_4. The red solid lines indicate the shortest bond between the nearest neighbor Yb atoms. [75]

heat sunk to a calibrated resistive thermometer. By sweeping the magnetic field up and down at $\sim 20 - 50$ Oe/sec, the sample temperature variation can be obtained by measuring the thermometer resistance at different fixed bath temperatures. Because the thermal link between the sample platform and calorimeter frame is very weak, about 1.7×10^{-7} W/K at $T = 1.0$ K for this case, the estimated relaxation time for a big Yb_3Pt_4 sample of about 17 mg used in MCE measurements could be as large as 300 sec. Since the thermometer resistance can be measured in less than one second, the heat leak during this measuring time is negligible, and it is assumed that these experiments are carried out in the quasiadiabatic limit. Neutron diffraction was carried out on a 65 mg single crystal of Yb_3Pt_4 at the NIST Center for Neutron Research using the BT- 7 double focusing triple-axis spectrometer with the neutron wavelength $\lambda = 2.47$ $\mathring{A}$. Since the anisotropy within the easy ab plane is very small, the field direction within the ab plane is not specified.

3.3 Crystal and Magnetic Structure

X-ray diffraction shows that Yb_3Pt_4 crystallizes in the reported rhombohedral Pu_3Pd_4-type of structure [124], which has 18 Yb atoms per unit cell, all with the same site symmetry, and 24 Pt atoms per unit cell, with three different site symmetries fig. (3.1(b)). In zero field, Yb_3Pt_4 orders antiferromagnetically at the Néel temperature $T_N = 2.4$ K [73] and the magnetic structure was determined from neutron diffraction measurements using representation analysis fig. (3.2) [75]. The fundamental building block of this $q = 0$

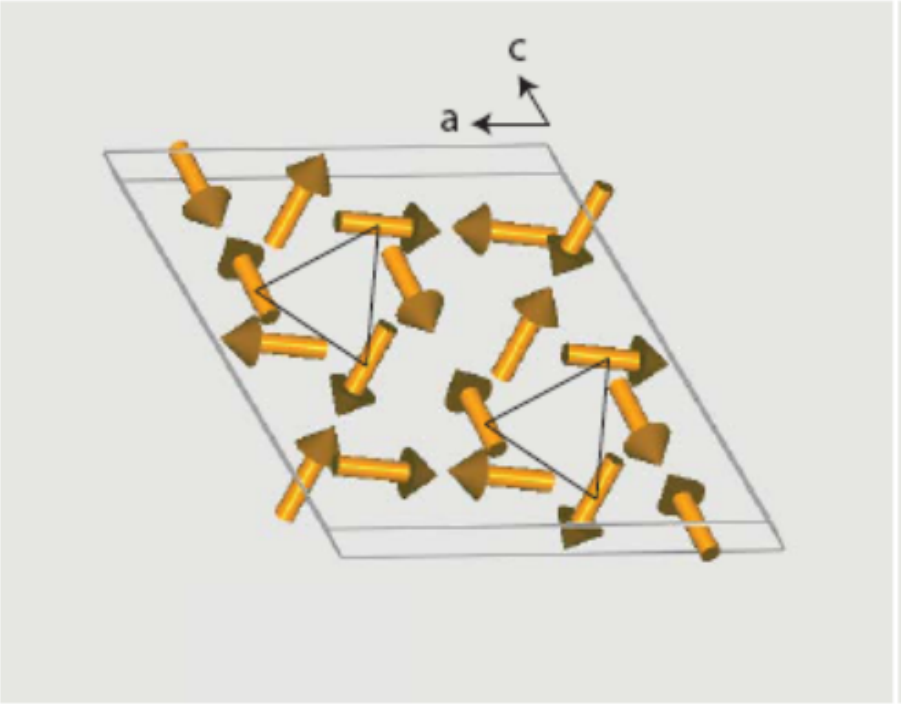

Figure 3.2: (a) Magnetic structure of Yb_3Pt_4 in zero field antiferromagnetic ordered state below 2.4 K. The arrows indicate the Yb magnetic moments. (Figure is courtesy of Yuri Janssen [75].)

antiferromagnetic structure is a triad of Yb moments, each rotated 120 degrees with respect to each other. Each triad is matched by a reflected triad to form octahedra, which are stacked in a staggered fashion along the c-axis to form the overall magnetic structure.

3.4 Magnetic and Thermal Properties

3.4.1 Crystalline Electrical Field (CEF)

Magnetization measurements indicate that the hard axis is along the c-axis, and the easy axis lies in the ab plane. The magnetic anisotropy is weak inside the ab plane, with $\chi_{[110]}/\chi_{[100]} \simeq 1.07$. It is much bigger between the ab plane and c axis, with $\chi_{\rm ab}/\chi_{\rm c} \simeq 6$ at low temperatures. There is significant evidence that the Yb moments in Yb_3Pt_4 are spatially localized over much of the range of experimental temperatures, and so their f electrons are excluded from the metallic Fermi surface. The magnetic susceptibilities for fields along both the c axis and in the ab plane are in agreement with Curie-Weiss expressions above $\simeq$ 150 K, giving a paramagnetic moment about 4.24 μ_B/Yb, as expected for trivalent Yb [73]. A pronounced anomaly in the zero field specific heat C is well described by a Schottky expression involving four crystal-field-split doublets, just as expected for Yb^{3+} in a crystal symmetry that is lower than cubic. Inelastic neutron scattering measurements confirm that there are four magnetic doublets that are well separated in energy, and since the first excited state is $\simeq$ 7.5 meV ($\sim$ 87 K) above the ground state fig. 3.3(a) [75], this ground doublet dominates the magnetic properties of Yb_3Pt_4 at low temperatures. Antiferromagnetic order occurs in Yb_3Pt_4 at 2.4 K, signalled by a mean field peak in the specific heat fig. 3.3(b) [73]. The entropy reaches $\sim$ 0.8 Rln2 at $T_{\rm N}$, confirming that the doublet moment orders with a minimum of critical fluctuations or with appreciable suppression of the ordering moment via the Kondo effect. Triple axis spectroscopy was used to show that the temperature evolution of the spin waves in the antiferromagnetic state [123] is similar to that of the magnetic order parameter, suggesting that the spin waves are conventional and arise from the action of the exchange coupling on the crystal field split single ion states.

3.4.2 Low Temperature Specific Heat

We have measured the magnetic and electronic specific heat $C_{\rm M}$ of Yb_3Pt_4 with different values of the magnetic field B in the ab plane at low temperatures, as shown in fig. (3.4(a)). Since the magnetic anisotropy inside the ab plane

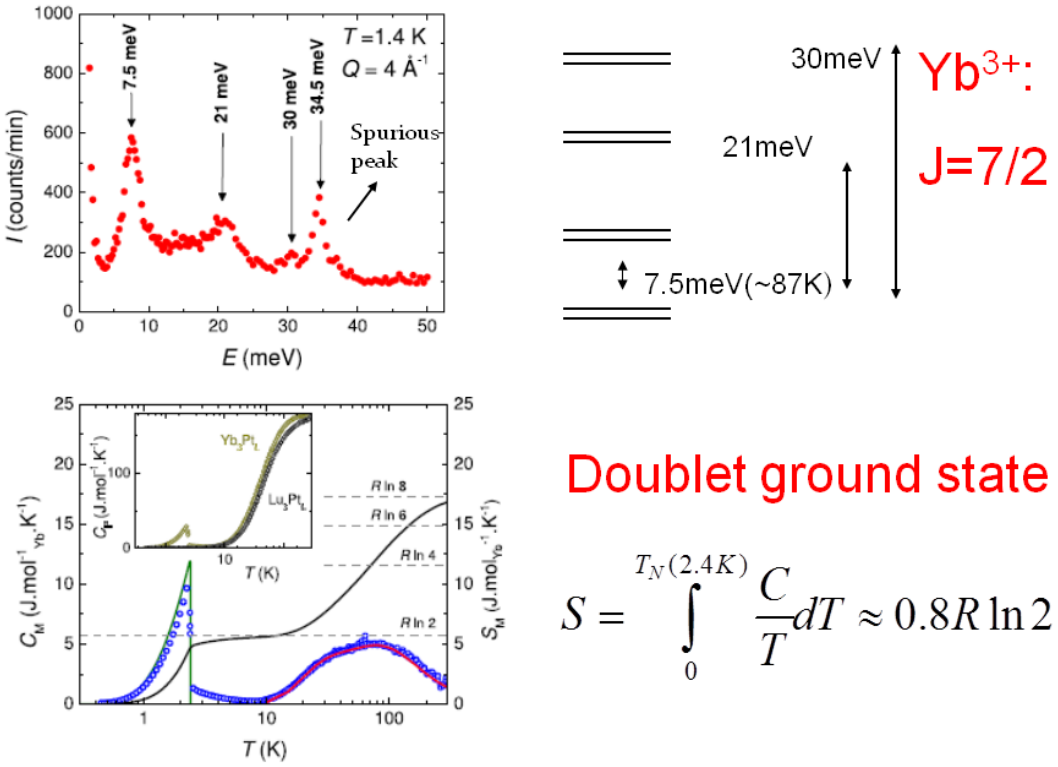

Figure 3.3: (a)Inelastic neutron scattering of Yb_3Pt_4 powder samples. The arrows at peaks around 7.5 meV, 21 meV and 30 meV indicate different Yb^{3+} crystal field energy levels. The last peak at 34.5 meV is a spurious peak that comes from the instrument. (b)Magnetic specific heat of Yb_3Pt_4 in zero field (blue circles), found by subtracting the lattice contribution estimated from Lu_3Pt_4 specific heat data from the measured specific heat. The red curve is the fitting based on the crystalline electrical field configuration indicated above. The black line is the entropy calculated from the magnetic specific heat. The green line is the fit to the mean field expression of the specific heat at the magnetic phase transition. Inset: Measured zero field specific heat of Yb_3Pt_4 (dark yellow circles) and the nonmagnetic counterpart (black circles). [75]

is very small, we do not specify the magnetic field direction inside the ab plane for all the experiments presented here and below. In low fields, the specific heat jump at T_N has a triangular shape evocative of a mean-field transition. T_N decreases with increasing field, while the magnitude of the ordering anomaly decreases and eventually becomes undetectable for fields greater than $\simeq 1.75$ T, where $T_N < 1.2$ K. While these data may suggest that the antiferromagnetic phase line $T_N(B)$ terminates at a critical endpoint with $T_N = 1.2$ K, $B = 1.75$ T, it is also possible that the phase line simply becomes very steep as $T_N \to 0$. To distinguish between these two possibilities, field scans of the specific heat $C_M(B)$ were performed at different fixed temperatures (fig. 3.4(b)). Very different behaviors were found above and below 1.2 K. For $T \geq 1.2$ K, there is a step in $C_M(B)$ as the field transits the phase line $T_N(B)$, reminiscent of the step that is found in $C_M(T)$ when increasing temperature is used to suppress antiferromagnetic order in a fixed magnetic field (fig. 3.4(a)). This step evolves into a broad peak centered at $T_N(B)$ for $T \leq 1.2$ K, whose magnitude decreases and becomes very small at the lowest temperatures (fig. 3.4(c)). There is no measurable change in the field at which the peak in $C_M(B)$ occurs for any temperature below $\simeq 0.9$ K, indicating that within the accuracy of our measurements the antiferromagnetic phase line becomes vertical in the $B - T$ plane as $T_N \to 0$ for the magnetic field $B_0 = 1.85$ T. The full antiferromagnetic phase line $T_N(B)$ determined from field sweeps of the specific heat C is presented in fig. 3.4(d). The phase line abruptly deviates from this behavior as the field approaches 1.85 T, and since its final approach to the $T = 0$ axis cannot be described by any power law, quantum criticality is ultimately avoided in field tuned Yb_3Pt_4.

3.4.3 Magnetization

A more detailed picture of the antiferromagnetic phase transition is revealed by the magnetization measurements. The temperature dependencies of the magnetization M/B were measured in different fixed fields B (fig. 3.5(a)), displaying distinct cusps at T_N. As we found in the specific heat measurements, T_N is driven to lower temperatures by the application of magnetic fields B, and the values of $T_N(B)$ agree very well between the two measurements (fig. 3.4(d)). The ordering anomaly in $M(T)/B$ broadens and is no longer observed above 0.5 K for $B \geq 1.85$ T. Given the vertical nature of the phase line $T_N(B)$ revealed by the specific heat measurements, we turn to field sweeps of the magnetization $M(B)$ to clarify the phase behavior at the lowest temperatures. Fig. 3.5(b) shows that $M(B)$ is initially linear in field, but deviates from this initial slope near the field-driven transition at 1.85 T before becoming linear again with a much smaller slope at the highest fields. With decreasing

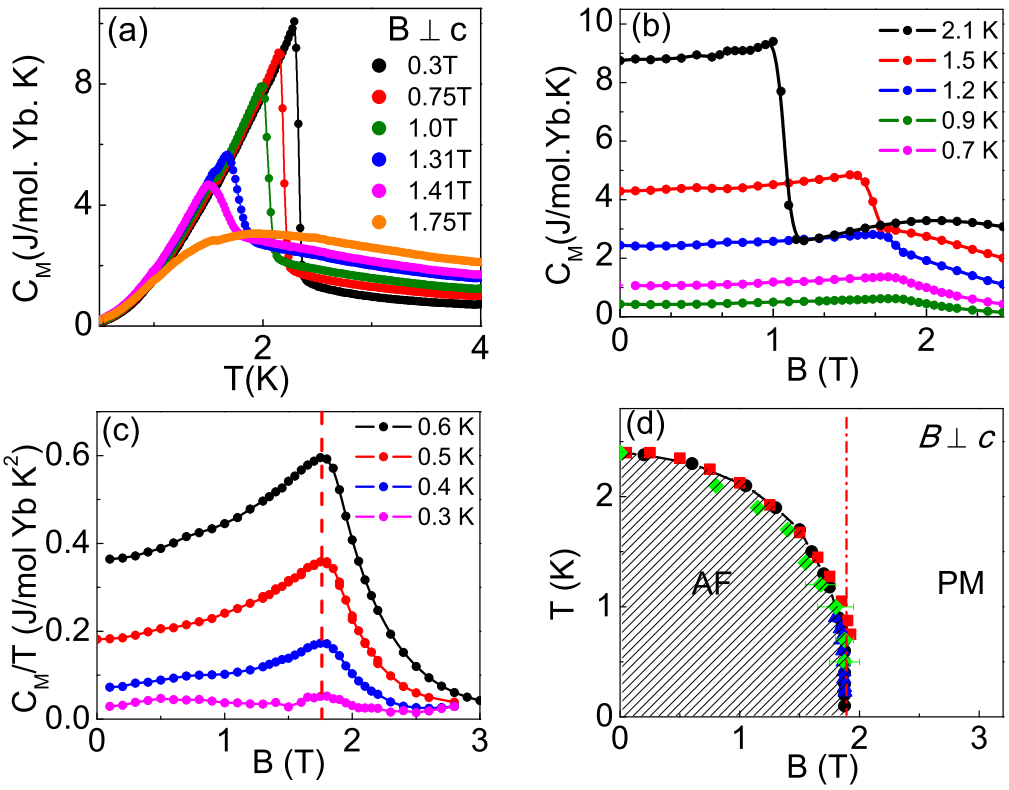

Figure 3.4: (a) Temperature dependencies of the magnetic specific heat $C_{\rm M}$ in different magnetic fields as indicated. (b) Field dependencies of $C_{\rm M}$ at different fixed temperatures, as indicated. (c) Field dependencies of $C_{\rm M}/T$ at fixed temperatures below 0.7 K, as indicated. Dashed line shows that the phase line $T_{\rm N}(B)$ becomes field independent for $T_{\rm N} \leq 0.9$ K. (d)Antiferromagnetic order is found in the shaded area of the field -temperature phase diagram of Yb_3Pt_4, where the phase boundary $T_{\rm N}(B)$ is determined from field scans of the specific heat $C_{\rm M}$ (●), from the temperature dependencies of the magnetization M, carried out in different fixed fields (■), from the field dependencies of the magnetization M, carried out at different fixed temperatures (▲), and from the magnetic intensity of the (110) Bragg peak, measured in a neutron diffraction experiment for different fixed temperatures and fields (♦). Error bars indicate the width of the moment step in the neutron diffraction experiment. Vertical dash - dot line indicates the 1.85 T field at which $T_{\rm N} \to 0$. The magnetic field in (a)-(d) is perpendicular to the c axis. Solid lines in (a)-(d) are guides for the eye.

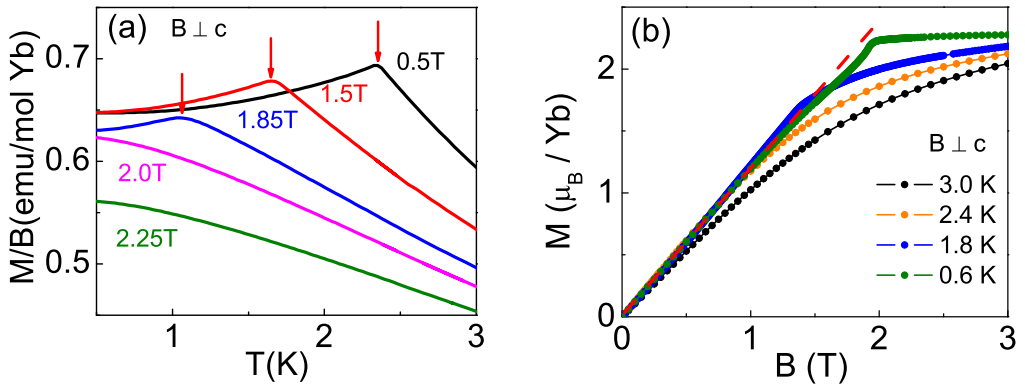

Figure 3.5: (a) Temperature dependencies of the magnetization M divided by different measuring fields B, as indicated. The arrows indicate the antiferromagnetic transitions in each field. (b) Field dependencies of M at indicated temperatures. Dashed line indicates the departures from linear extrapolations of low field $M(B)$.

temperature (fig. 3.6(a)), this slope change becomes sharper, suggesting that the associated differential susceptibility $\chi(B) = dM/dB$ is becoming very large at $T_N(B)$. Indeed, fig. 3.6(b) shows that there is a distinct peak in $\chi(B)$ that becomes sharper and increases strongly in magnitude as the temperature decreases. We emphasize that no hysteresis is observed between measurements performed with increasing and decreasing fields, at any field or temperature. Figure 3.7 shows that the maximum value of the susceptibility χ at $T_N(B)$ initially increases according to a power law $\chi \sim T^{-1/2}$, but saturates below $\simeq 0.35$ K. We considered the possibility that experimental factors may play a role in this saturation, for instance the degree of thermal sinking of the sample on the Hall sensor, found to be appreciable below $\simeq 0.15$ K, as well the precision of the $M(B)$ measurement itself, which limits the degree of divergence possible in $\chi(B)$, obtained by numerically differentiating $M(B)$. These effects are minimal above 0.2 K, where the saturation of the power law divergence of $\chi(T)$ primarily reflects a broadening of the antiferromagnetic transition, due either to disorder in the sample or alternatively by thermal or quantum fluctuations.

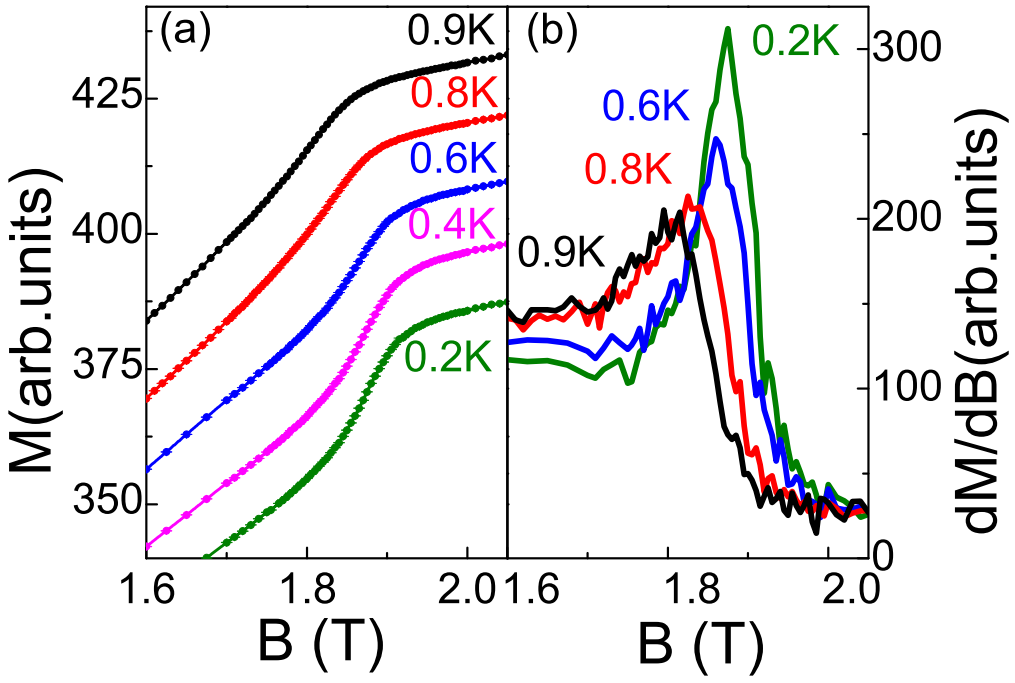

Figure 3.6: (a) Field dependencies of M at indicated temperatures below 1.0 K. Each magnetization curve above 0.2 K is shifted up by 10 to make the plot clearer. (b) The numerical derivative $\chi = dM/dB$ of the data in (b).

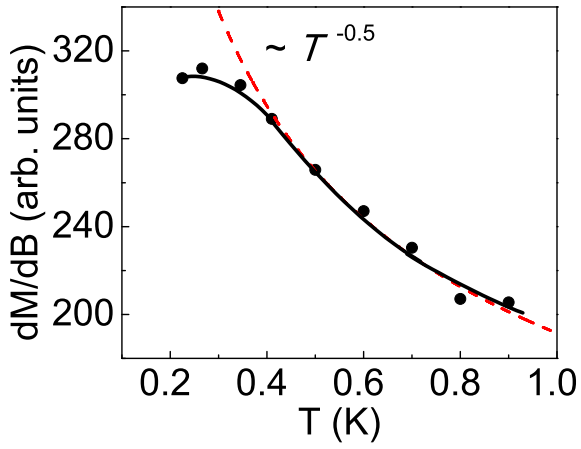

Figure 3.7: Temperature dependence of the maximum value of $\chi = dM/dB$. The dashed line is the fit to $\chi \simeq T^{-0.5}$, while the solid line is guide for the eye that emphasizes the saturation of χ for $T \leq 0.35$ K.

3.4.4 Magnetic Neutron Diffraction

The most direct information about the evolution of antiferromagnetic order with field and temperature comes from neutron diffraction measurements. We previously showed that the magnitude of the magnetic part of the (110) Bragg peak in zero magnetic field obeys a mean field temperature dependence, consistent with the mean field character of the specific heat near T_N [75]. Fig. 3.8(a) confirms that magnetic field decreases the magnitude of the order parameter, and for temperatures larger than $\simeq 1.2$ K, it drops smoothly to zero along the antiferromagnetic phase line. We have added these critical fields and temperatures to the phase diagram in fig. 3.4(d), showing that they are in good agreement with values for $T_N(B)$ obtained from specific heat and magnetization measurements. For $T \leq 1.2$ K, there is a distinct broadening of the transition, and at the lowest temperatures there is a pronounced step in the moment $\Delta M \simeq 0.2\mu_B$/Yb centered at the critical field $B_0 = 1.85$ T. Like the step in $M(B)$, the breadth of the step in the ordered moment remains considerable, even at the lowest temperatures. Fig. 3.8(b) shows that the transition widths found in the two experiments are very similar, $\simeq 0.25$ T.

3.4.5 Magnetocaloric Effect (MCE)

The picture that emerges from the specific heat, magnetization, and neutron diffraction experiments is that the antiferromagnetic phase transition is continuous and mean-field like in low fields, but when magnetic fields suppress T_N to values less than $\simeq$ 1.2 K, the broadened steps in the moment suggest that the transition may develop a first-order character. To test this hypothesis, we have carried out measurements of the magnetocaloric effect (MCE) to determine if a latent heat is associated with the antiferromagnetic transition along the vertical part of the phase line, i.e. when $T_N \leq 1.2$ K. The MCE is the temperature change of a material when a magnetic field is changed adiabatically [81, 82, 83, 84], and it has been used to be a practical and sensitive way to detect latent heat at magnetic phase transitions and to study the quantum criticality in various correlated electron systems [86, 87, 89, 90, 91, 92, 126]. The results of MCE are shown in fig. 3.9(a), where the solid line represents the sample temperature T, measured as the magnetic field is scanned. A clear increase in the slope dT/dB is observed as the antiferromagnetic phase is excited at $T_N(B)$, but there is no discontinuity or jump in $T(B)$ anywhere along the phase line, either for $T_N \geq 1.2$ K where the transition is definitively continuous, or at lower values where the nature of the transition is more ambiguous. We note that no differences are found along the phase line between increasing and decreasing

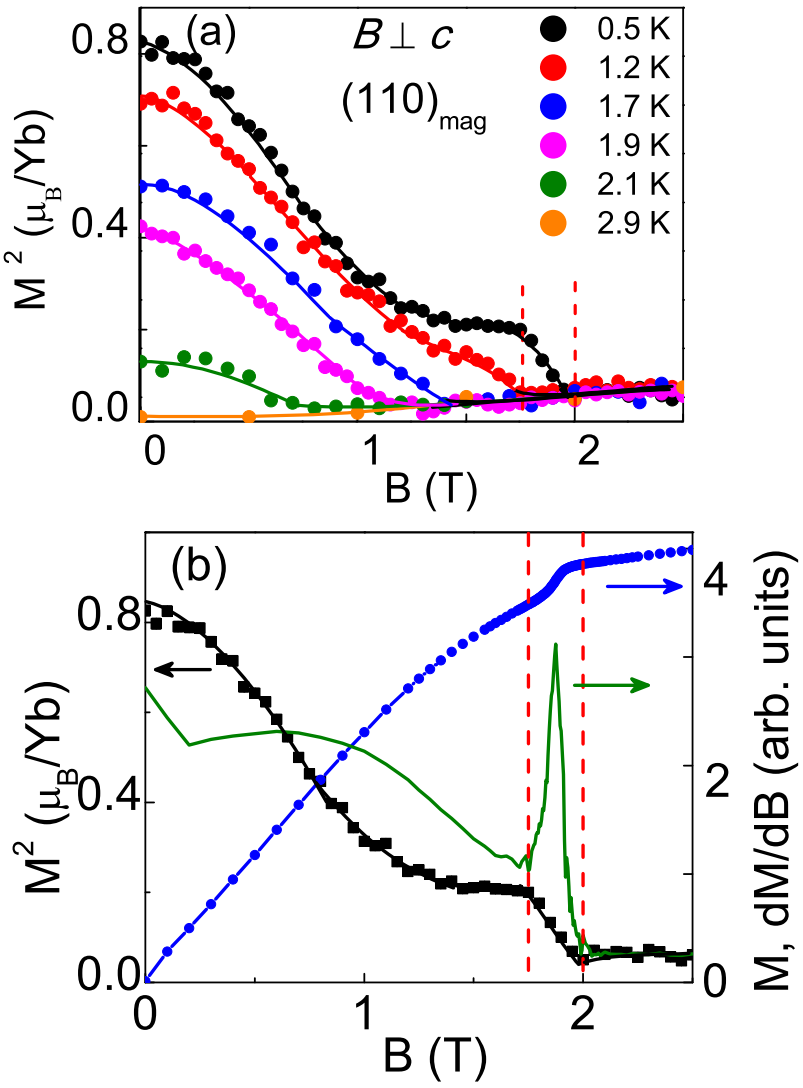

Figure 3.8: (a)Field dependencies of the (110) magnetic Bragg peak intensity at different temperatures, as indicated. Solid lines are guides for the eye. (b) The magnetization(•), and differential magnetic susceptibility (solid line) at 0.2 K plotted together with the (110) magnetic peak intensity at 0.5 K (■). Vertical dashed lines delineate the range of fields where there are similar width steps in the Yb moment measured both by neutrons and by dc magnetization measurements. The magnetic field in both experiments is perpendicular to c axis.

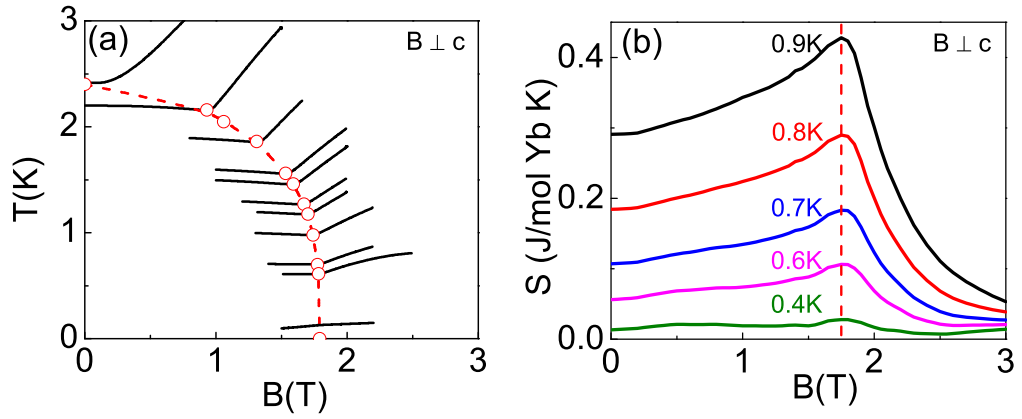

Figure 3.9: (a) The effect of magnetic fields perpendicular to the c axis on different initial sample temperatures. The dashed line indicates the antiferromagnetic transition $T_{\rm N}(B)$. (b) Entropy S calculated from specific heat $C_{\rm M}$ at different temperatures. Dashed line indicates that the maximum entropy occurs along the field independent antiferromagnetic phase line $T_{\rm N}(B)$.

field sweeps. To verify the adiabatic condition in the MCE measurements, we also calculate the entropy from the specific heat we showed earlier. If the MCE were carried in the adiabatic limit, each MCE curve should also be an equal entropy line. As shown in fig. 3.10, the MCE curves does show a trend that is very similar to the one we have calculated. Thus we believe that the MCE measurements were performed close to the adiabatic limit at low temperatures. Since the MCE measurements find that no latent heat is associated with the antiferromagnetic phase line in Yb_3Pt_4, we conclude that the transition is continuous for all nonzero values of $T_{\rm N}$.

Since the MCE experiments approximate the adiabatic condition, the slope differences at $T_{\rm N}(B)$ found in fig. 3.9(a) imply that the antiferromagnetic and paramagnetic states have different entropies, and that the difference between their respective entropies ΔS becomes increasingly small with reduced temperature. This conclusion is supported by the field dependence of the entropy S, extracted from specific heat measurements (fig. 3.9(b)), where we see a broad maximum in S at $T_{\rm N}$ with a magnitude that decreases with decreasing temperature. Despite the steps observed in $M(B)$ and neutron diffraction experiments for $T \leq 1.2$ K, the MCE measurements apparently rule out a first order antiferromagnetic transition in Yb_3Pt_4 for nonzero $T_{\rm N}$. Does this argument extend to $T_{\rm N} = 0$? The $Clausius - Clapeyron$ equation relates

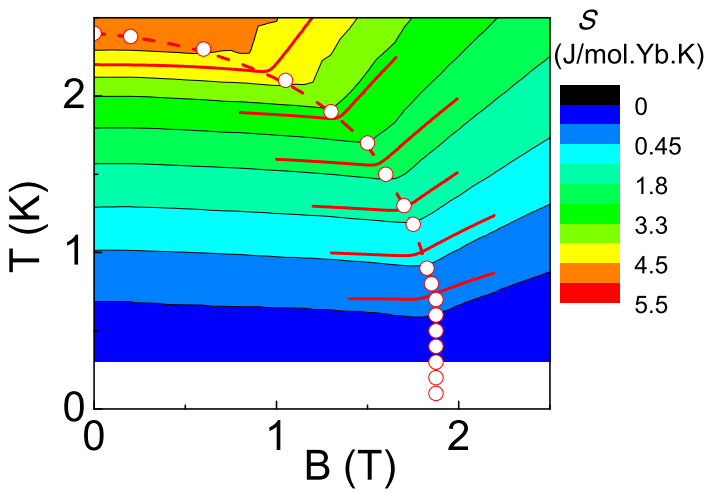

Figure 3.10: (a) Contour plot of the calculated entropy S from specific heat C_{M}. The black solid lines are the equal entropy lines from calculation. The red lines are the measured MCE curves. The empty circles ($\circ$) are the $B-T$ phase boundary determined from the field dependent specific heat. The dashed line is a guide for the eyes.

the slope of the antiferromagnetic phase line dT_N/dB to the differences between the magnetizations and entropies of the antiferromagnetic and paramagnetic phases at $T = 0$:

$$\frac{dT_N}{dB} = -\frac{\Delta M}{\Delta S}. \tag{3.1}$$

The third law of thermodynamics requires that $\Delta S = 0$ for $T = 0$, and the vertical nature of the phase line T_N at the critical field B_0 implies that $dT_N/dB \to -\infty$ for $T_N = 0$. The *Clausius−Clapeyron* equation is satisfied at $T_N = 0$ when the transition is between two states with different magnetizations, i.e. $\Delta M \neq 0$, as we have seen in both the magnetization and neutron diffraction measurements. Our conclusion is that the antiferromagnetic phase line $T_N(B)$ in Yb_3Pt_4 is continuous at all nonzero temperatures, but terminates in a $T = 0$ first order transition at a critical field $B_0 = 1.85$ T.

3.4.6 Magnetic Phase Diagram and Critical End Point (CEP)

Our current understanding is that there is no universal path by which magnetic fields suppress antiferromagnetic order to zero temperature in heavy fermion compounds, and the schematic phase diagrams presented in fig. 3.11 seek to categorize the simplest possibilities that have been identified by experiments. They are not meant to capture the full complexity of heavy fermion compounds, which may pass through a multiplicity of different structures en route to the collapse of magnetic order [12], but rather to focus on the final phase line that separates magnetic order from the paramagnetic state. To our knowledge, all heavy fermion antiferromagnets order via a continuous transition in zero field. Fig. 3.11(a) depicts the situation found in systems like $YbRh_2Si_2$ [121], YbPtIn [125], $CeCu_{6-x}Au_x$ [118], and $CeIn_{3-x}Sn_x$ [126], where the antiferromagnetic phase line remains continuous as $T_N \to 0$ at a quantum critical field B_{QCP}. Bulk properties such as the magnetization scale as functions of T and $(B - B_{QCP})$ [40, 121], and the magnetic Grüneisen parameter diverges as well for $T = 0$ and $B = B_{QCP}$ [93, 94]. Given that all experiments have a lower temperature limit, it is fair to say that it is not known in any compound whether the antiferromagnetic phase line is continuous to $T_N = 0$. However, it is evident that the scaling associated with the quantum critical point at $T_N = 0$ and $B = B_{QCP}$ dominates many of the measured quantities over a wide range of fields and temperatures.

A very different situation is realized when magnetic fields are applied to conventional antiferromagnets such as rare earth aluminum garnets and $FeCl_2$ [127, 128, 129], which have continuous antiferromagnetic transitions in

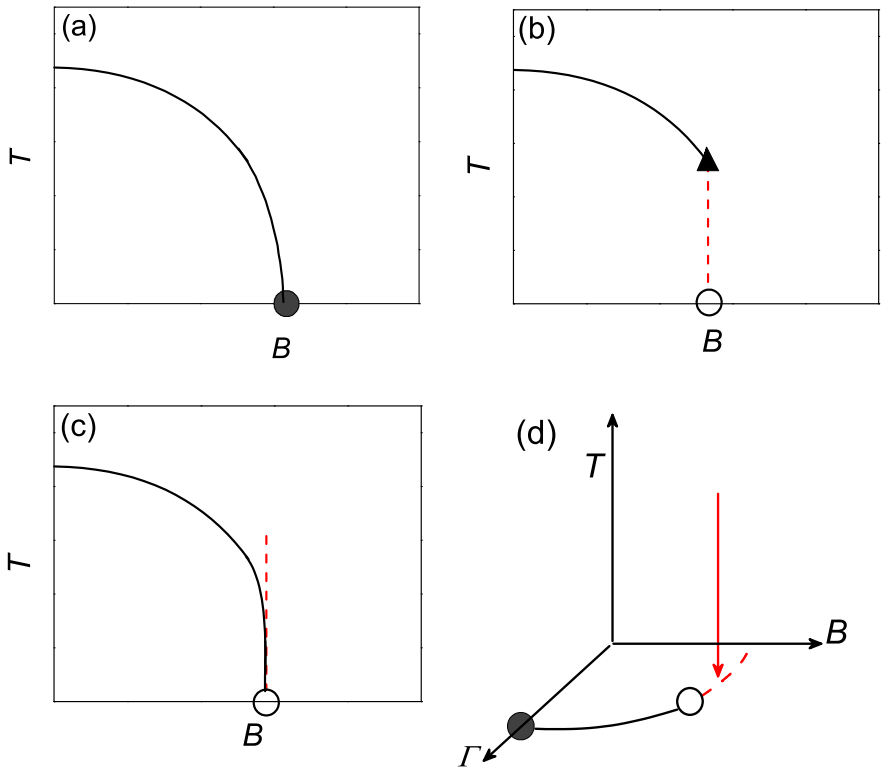

center

Figure 3.11: Schematic phase diagrams for field tuned antiferromagnets. (a) The phase line of a field tuned antiferromagnet remains second order at all fields (solid line), ending at a continuous transition with $T_N = 0$, i.e. a quantum critical point (•). (b) The phase line of a field tuned antiferromagnet is initially second order(solid line), but this phase line terminates at a tricritical point(▲). For smaller values of T_N, the phase line is first order (dashed line), ending at a first order transition where $T_N = 0$, i.e. a quantum critical endpoint (○). (c) An intermediate situation between (a) and (b), where the first order transition line in (b) has shrunk to a single point with $T_N = 0$, a quantum critical endpoint (○). For all nonzero values of T_N, the phase line is continuous but strongly modified from the second order line shown in (a). (d) A three dimensional phase diagram with no magnetic order for $T > 0$ at any value of field or other non-thermal variable Γ, such as pressure. There is a quantum critical endpoint (○) in the $T = 0$ $B - \Gamma$ plane, that separates a first order line (dashed line) from a line of continuous transitions (solid line) that ends in a quantum critical point for $B = 0$ (•). The red vertical arrow indicates the effect of lowering temperature in a metamagnet, defined as a system that has no long-ranged order for $T \neq 0$, but positioned in the $B - \Gamma$ parameter space close to a quantum critical endpoint(○).

zero field (fig. 3.11(b)). Here, the antiferromagnetic phase line is initially second order, but terminates at a tricritical point [130, 131]. Since magnetic order involves a broken symmetry, the phase line must continue to $T_N = 0$, and it does so as a line of first order transitions that terminate at a QCEP. Scaling is found in systems of this type, both of the conventional variety in low and zero fields, but more prominently in the vicinity of the tricritical point [129, 132]. This phase diagram is very similar to the one that was both predicted [7] and experimentally realized [133] in field and pressure tuned metallic ferromagnets where disorder is weak. To our knowledge, the phase diagram in fig. 3.11(b) has been found only in ferromagnetic UGe_2 [134], and not in any antiferromagnetic heavy fermion compounds.

The phase diagram of fig. 3.11(c) represents a situation that is intermediate between figs. 3.11(a) and 3.11(b), in that the line of first order transitions has now shrunk to a single point at $T = 0$, and it is the influence of this point that keeps the lowest temperature part of the phase line from becoming the more conventional second order phase line found in $YbRh_2Si_2$ (fig. 3.11(a)). This is the phase diagram that best describes Yb_3Pt_4, and perhaps as well Yb_5Pt_9 [135], $CeRh_2Si_2$ [136], $YbNiSi_3$ [137, 138] and $CeNiGe_3$ [139]. Here, the phase line is always continuous for $T_N \neq 0$, and no latent heat is found anywhere along the phase line. The phase line superficially resembles the first order phase line of fig. 3.11(b), since it becomes vertical as $T_N \to 0$. The initial stabilization of antiferromagnetic order as a second order transition at $B = 0$ implies the general importance of long wavelength critical fluctuations through much of the $B - T$ plane, and the initial divergence of the susceptibility at the critical field where $\chi(T) \sim T^{-x}$, generally reflects these correlations. Since a true quantum critical point is ultimately avoided in systems described by the phase diagram in fig. 3.11(c), the longest wavelength fluctuations must either be absent, as in disordered systems, or are prohibited in some way from contributing to the physical observances. We hypothesize that their absence is responsible for the breakdown of scaling near the QCEP, and for the general appearance of the phase line, which increasingly resembles a first order phase line, lacking only the latent heat. Ultimately the failure of universality as $T_N \to 0$ causes the antiferromagnetic phase line to terminate in a first order phase transition at zero temperature $T_N = 0$, also known as a quantum critical end point.

The most unimpeded view of the properties of a quantum critical endpoint is found in systems in which no magnetic order is present, at least for $T \neq 0$. The most heavily studied examples of these so-called metamagnetic systems are $CeRu_2Si_2$ and $Sr_3Ru_2O_7$ [140, 141, 142]. The signature of metamagnetism is steps in the magnetization whose breadth decreases with decreasing

temperature. In some cases, a full field-driven first order transition results below a certain onset temperature [143], but for $CeRu_2Si_2$ and $Sr_3Ru_2O_7$ there is no sign of long-ranged magnetic order at any field or temperature. In both cases, there is a pronounced enhancement of the magnetization and specific heat near the critical field, and with reduced temperature the associated magnetic susceptibility begins to diverge as $\chi(T) \sim T^{-x}$ [144]. Instead of a maximum in the specific heat, a dip is found in C at the critical B. Unlike the case of Yb_3Pt_4 where the termination of the nonzero temperature part of the phase line necessitates a true phase transition at $T = 0$, no fine tuning is required for the metamagnets. All that is required is that the metamagnet is sufficiently close to a quantum critical endpoint, accessible by tuning a nonthermal variable such as field angle in $Sr_3Ru_2O_7$ [142], or pressure in either system [95, 145] (fig. 3.11(d)).

Unlike the case of clean ferromagnets, where it is theoretically and experimentally agreed that the phase line is initially continuous at small fields, but ultimately must become first order when the Curie temperature becomes sufficiently small, there is much less theoretical guidance for the range of behaviors that might be possible for antiferromagnets when $T_N \to 0$. There is a continuing need to identify new systems that exemplify the differing phase diagrams that are represented in fig. 3.11. There are significant and intrinsic obstacles that make the search for such systems inherently challenging. One complication is that the suppression of magnetic order can enable the stabilization of competing collective phases, most notably superconductivity, as found in $CeCoIn_5$ [147], $CeRhIn_5$ [204], and $CeCu_2Si_2$ [148]. However interesting and significant, these new phases obscure the part of the phase diagram where antiferromagnetic order vanishes. Similarly, experiments must be conducted at the very lowest temperatures to determine whether the quantum critical scaling is robust, or alternatively if universality fails and the antiferromagnetic transition becomes first order when T_N becomes sufficiently small.

Perhaps the most compelling aspect of the phase diagrams in fig. 3.11 is their potential relationship to the underlying electronic structure. This has been studied extensively in the metamagnets, and in $CeRu_2Si_2$ magnetic fields are thought to drive a continuous evolution of the electronic structure from the $B = 0$ limit where one of the spin polarized Fermi surfaces is favored in field, with the other vanishing at a Lifshitz transition at the metamagnetic field [149]. In contrast to this case where the electrons are always delocalized, a rather different situation is realized in the heavy fermion $YbRh_2Si_2$ [121]. Here the local moment character of the Yb moments is completely quenched near a Kondo temperature T_K that is well in excess of the Néel temperature.

Consequently, antiferromagnetic order must be considered to be a collective instability of the fully hybridized Kondo lattice, and magnetic fields drive a delocalization transition at the critical field $B_{\rm QCP}$ that is akin to a Mott transition, increasing the size of the Fermi surface [150]. Much of the $B-T$ phase diagram is affected by this transition, which coincides at $T=0$ with the antiferromagnetic quantum critical point in pure $YbRh_2Si_2$ [10], but remains a separate transition under Co and Ir doping [122]. In contrast, the antiferromagnetic order that is found at the Néel temperature $T_{\rm N}$ in Yb_3Pt_4 at zero field involves well localized Yb moments that are essentially unaffected by the Kondo effect, which we conclude occurs below a characteristic temperature $T_{\rm K}$ that is smaller than the ordering temperature itself, i.e. $T_{\rm K} \leq T_{\rm N}$ [73, 75]. The antiferromagnetic order is conventional, with a staggered Yb moment that is consistent with a doublet ground state [75], and with spin waves that result from the exchange splitting of this state of the crystal electric field manifold [123]. It is tempting indeed to speculate that the very different natures of the Yb magnetism in $YbRh_2Si_2$ and Yb_3Pt_4 may be responsible for their very different antiferromagnetic phase diagrams, represented in figs 3.11a, and 3.11c, respectively. Lacking a more comprehensive set of well characterized compounds with vanishing Néel temperatures, this association remains for now unproven.

To conclude, we have used measurements of the specific heat, magnetization, neutron diffraction, and magnetocaloric effect to establish the field-temperature phase diagram of the heavy fermion antiferromagnet Yb_3Pt_4. The antiferromagnetic transition is initially continuous in zero field, but magnetic fields applied in the easy ab plane reduce the Néel temperature in Yb_3Pt_4 to zero temperature at a critical field $\simeq 1.85$ T. The antiferromagnetic phase line becomes very steep at low temperatures, and within the accuracy of our measurements becomes independent of field as $T_{\rm N} \to 0$. The appearance of the phase line is suggestive that the antiferromagnetic transition in Yb_3Pt_4 becomes first order, however magnetocaloric effect measurements find no evidence for a latent heat for any value of $T_{\rm N}$. We conclude that the antiferromagnetic transition in Yb_3Pt_4 is continuous, at least for $T_{\rm N} > 0$. A step in the moment is observed at the critical field in both magnetization and magnetic neutron diffraction measurements, and the associated susceptibility $\chi = dM/dB$ at the critical B initially increases with decreasing temperature, i.e. $\chi \sim T^{-1/2}$, signifying that the step width is decreasing. However, the incipient divergence in χ is cutoff below $\simeq 0.35$ K, a behavior familiar from metamagnetic systems like $CeRu_2Si_2$ and $Sr_3Ru_2O_7$. Accordingly, we propose that the low temperature properties of Yb_3Pt_4 are controlled by the quantum critical endpoint that is created when the antiferromagnetic phase

line terminates at zero temperature. These measurements position Yb_3Pt_4 as one of the few antiferromagnets from the heavy fermion class that do not seem to have true quantum critical points, formed when a second order phase transition is suppressed to zero temperature by magnetic field tuning. The field temperature magnetic phase diagram of Yb_3Pt_4 seems to form a link between those of most field-tuned heavy fermions, which are dominated by a quantum critical point, and those of conventional magnetic insulators, where the central features are a tricritical point and a line of first order transitions terminating in a quantum critical end point.

3.5 Localized Moment Behaviors

$YbRh_2Si_2$ exemplifies the full range of phenomena that can be associated with a field-driven QCP [10]. First, the $B = 0$ Néel temperature is only 0.065 K, with a correspondingly small ordered moment $\simeq 10^{-3}\mu_B$/Yb. T_N is suppressed continuously to $T_N = 0$ with a field $B = 0.66$ T [154, 155]. Quantum critical scaling of the field and temperature dependencies of the specific heat C and the magnetization M are reported in the vicinity of the QCP [121]. non-Fermi liquid temperature dependencies are observed near the QCP, such as a diverging specific heat $C/T \simeq$-ln(T), and a linear temperature dependence for the electrical resistivity $\rho(T) = \rho_0 + aT$, observed over several decades in temperature [121, 154]. Fermi liquid behavior is found once the antiferromagnetic order is suppressed by fields $B \geq B_{QCP}$, with $\rho = \rho_0 + A(B)T^2$ and $C = \gamma(B)T$. The Fermi liquid parameters A and γ indicate that the quasiparticle mass is strongly enhanced and even diverges as $B \rightarrow B_{QCP}$ from above, signalling the breakdown of the Fermi liquid itself at the QCP. Associated with this breakdown is an electronic localization transition, where the number of states contained by the Fermi surface changes at or near the QCP [10, 31, 122, 152, 156].

The question that we ask here is what part of this spectrum of quantum critical phenomena survives in a more minimal system, where electronic localization does not occur. Yb_3Pt_4 is an ideal system in which to explore this issue. Metallic Yb_3Pt_4 orders antiferromagnetically at $T_N = 2.4$ K [73], where the mean-field like development of the ordered parameter taken from neutron diffraction measurements results in a T=0 moment of 0.8 μ_B/Yb [75]. Specific heat and inelastic neutron scattering measurements indicate that the antiferromagnetic order develops from Yb moments in a crystal field split doublet ground state that is well separated in energy from the first excited state [123]. The rapid recovery of the magnetic entropy $S(T_N) = 0.8$ Rln2 suggests that there is little evidence that Kondo compensation of the Yb

moments has occurred as $T \to T_N$, indicating that $T_K \leq T_N$. For these reasons, it is believed that the Yb moments in Yb_3Pt_4 are spatially localized, and only weakly coupled to the conduction electrons. Given the apparent irrelevance of Kondo physics to Yb_3Pt_4, it likely that the $4f$-holes of the Yb ions are excluded from the $B = 0$ Fermi surface. The complexity of the unit cell in Yb_3Pt_4 precludes a direct test of this conclusion from electronic structure calculations.

Magnetic fields suppress antiferromagnetic order in Yb_3Pt_4, and we find that $T_N = 0$ for the critical end point (CEP) $B_{CEP} = 1.85$ T. The Clausius - Clapeyron equation is obeyed here, and although the antiferromagnetic phase line intersects the $T = 0$ axis vertically and so cannot be fitted to a power-law as $T_N \to 0$, $T_N(B)$ is continuous for $T_N > 0$ [95], possibly following a mean-field expression. We present here the results of experiments that seek answers to three questions. First, is there non-Fermi liquid behavior near B_{CEP} in Yb_3Pt_4? Measurements of the temperature dependence of the electrical resistivity are expected to be of particular importance in answering this question. Second, does a Fermi liquid state develop once magnetic fields suppress antiferromagnetic order? If so, is there a divergence of the Sommerfeld coefficient γ and the resistivity coefficient A as $B \to B_{CEP}$ that signals the breakdown of this Fermi liquid with the onset of antiferromagnetic order? Finally, is there any suggestion of electronic delocalization in Yb_3Pt_4, or is the coupling between the Yb moments and the conduction electrons always vanishingly small?

Electrical resistivity ρ, specific heat C, magnetic susceptibility χ, and magnetization M measurements were compared to those of similar experiments on $YbRh_2Si_2$, with the intention of providing support for a global phase diagram that relates these two very different systems.

3.5.1 Field and Temperature Dependent Resistivity

Electrical resistivity has proven to be a very sensitive probe of the quantum critical fluctuations in other heavy fermion compounds where antiferromagnetic order can be suppressed to $T = 0$ [12, 157]. The temperature dependence of the $B = 0$ electrical resistivity $\rho(T)$ in Yb_3Pt_4 is shown in fig. 3.12a. $\rho(T)$ drops monotonically from its room temperature value of 127 $\mu\Omega$-cm to 35 $\mu\Omega$-cm at 10 K, confirming that Yb_3Pt_4 is definitively metallic. Given the crystal field scheme deduced from specific heat and inelastic neutron scattering measurements where four doublets are separated by 87 K, 244 K, and 349 K [123], it is likely that the bulge in $\rho(T)$ at intermediate temperatures reflects the depopulation of these crystal field levels with reducing temperature. The onset of antiferromagnetic order is evident from the sharp drop in $\rho(T)$

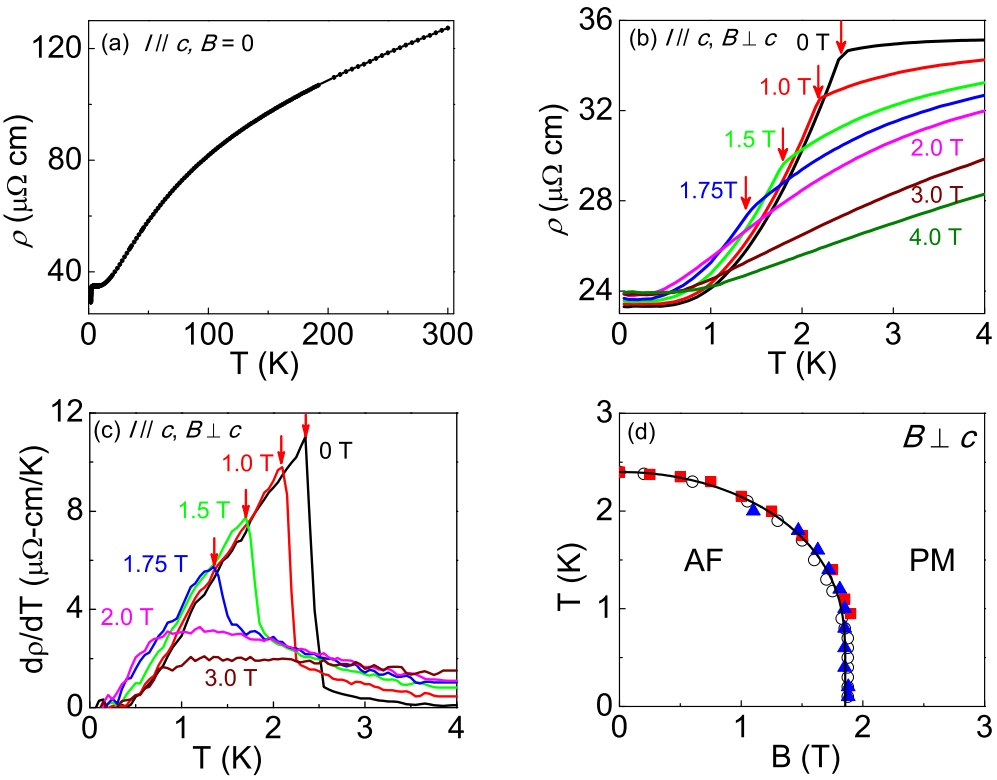

Figure 3.12: (a) Zero field temperature dependence of the electrical resistivity $\rho(T)$ in Yb_3Pt_4. (b) The temperature dependencies of $\rho(T)$ measured in different magnetic fields from 0 T to 4.0 T at low temperatures. The red arrows indicate the antiferromagnetic transitions at each field $B \leq 1.85$ T. (c) The temperature derivative of the electrical resistivity $d\rho/dT$ in different fixed fields, as indicated. Red arrows indicate values of $T_N(B)$, taken from the maxima in $d\rho/dT$. (d) Field - temperature phase diagram of Yb_3Pt_4. The antiferromagnetic ordering temperatures $T_N(B)$ extracted from the temperature(■) and field (▲) dependent resistivities are in good agreement with the phase line determined from specific heat(○) measurements. Solid black line is a fit to a mean-field expression.

at the Néel temperature $T_N = 2.4$ K. Since our primary interest is in the behavior of $\rho(T)$ as magnetic fields suppress T_N to zero, we have repeated the measurements of $\rho(T)$ in different fixed fields B ranging from 0 T to 4 T (fig. 3.12b). As expected, the resistive drop at T_N occurs at lower temperatures with increasing fields, and there is no indication of a resistive anomaly when $B \gtrsim 2$ T. We take $T_N(B)$ from the maximum in the temperature derivative, $d\rho/dT$ (fig. 3.12c), and the result is compared in fig. 3.12(d) to the phase line $T_N(B)$ that was previously determined from specific heat, neutron diffraction, and magnetization measurements [95]. We note that the specific heat measurements place B_{CEP} near 1.9 T, although the other measurements find $B_{CEP} \simeq 1.8 - 1.85$ T. The agreement is very good, especially considering that the experiments were performed on different crystals, and that small uncertainties in the orientation of the field are inevitable. We will take $B_{CEP} = 1.85 \pm 0.05$ T.

Since the phase line is very steep when $T_N \to 0$, measurements of the field dependence of the resistivity at different fixed temperatures are better suited to exploring this part of the $T - B$ phase diagram. As indicated in fig. 3.13a, the magnetoresistance ρ(B) has a sharp peak at $T_N(B)$, most prominent for $T_N \geq 1$ K. At lower temperatures, the peak in $\rho(B)$ evolves into a broadened step, whose magnitude becomes smaller with decreasing temperature. No hysteresis was observed between resistivity measurements obtained with increasing or decreasing fields, even at the lowest temperatures. The values of $T_N(B)$ that are taken from the resistive step have been added to fig. 3.12(d), and we see that the magnetoresistivity data closely track the near-vertical phase line $T_N(B)$ as it approaches the horizontal axis at the critical field $B_{CEP} = 1.85$ T. The width of the field-induced step in $\rho(B)$ decreases with decreasing temperature, and at the lowest temperatures it has a width of $\simeq 0.2$ T. This behavior is reminiscent of the step in the Yb_3Pt_4 moment observed in both magnetization $M(B)$ and neutron diffraction measurements [95]. We previously showed that the step ΔM and the vertical phase line $T_N(B)$ are in agreement with the Clausius-Clapeyron equation, indicating that antiferromagnetic order in Yb_3Pt_4 vanishes at a first order transition or critical endpoint, where $T_N = 0$ and $B = B_{CEP}$. We have compared the magnetization step measured at $T = 0.2$ K to the magnetoresistivity step measured at 0.1 K in fig. 3.13b, and their resemblance is striking. This is our first indication that the magnetization controls the electrical resistivity in Yb_3Pt_4, a finding that we will develop further below.

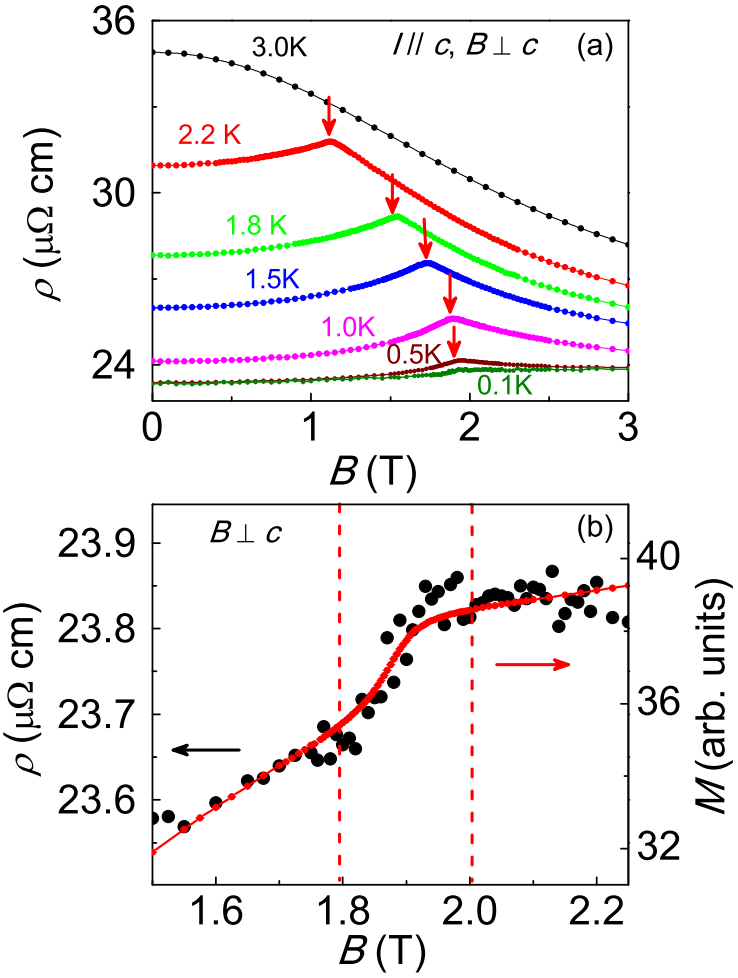

Figure 3.13: (a) Field dependencies of the electrical resistivity ρ measured at different temperatures from 0.1 K to 3.0 K, as indicated. Red arrows indicate the antiferromagnetic transitions. (b) Magnetoresistivity ρ (•, left axis) measured at 0.1 K plotted together with the magnetization (red solid line, right axis) measured at 0.2 K. Vertical dashed lines delineate the step like kink around the critical field ~ 1.85 T.

3.5.2 Spin Disorder Scattering of Local Moments

The suppression of magnetic order in a heavy fermion compound that has been driven to a QCP often results in a normal metallic state that is a Fermi liquid. Here, the electrical resistivity is quadratic in temperature $\rho(T) = \rho_0 + AT^2$, and the coefficient A is often enhanced near the QCP, reflecting the growth of quasiparticle interactions that can culminate in the divergence of the quasiparticle mass at the QCP itself. Accordingly, we have plotted the temperature dependent part of the electrical resistivity $\rho(\mathrm{T}) - \rho_0$, measured in different fixed fields, as a function of T^2 in fig. 3.14a. A quadratic temperature dependence is observed within the antiferromagnetically ordered state, i.e. for $T \leq T_{\mathrm{N}}(B)$. There is only a small variation in the slopes of the curves in fig. 3.14a for the fields $B \leq 1.85$ T where antiferromagnetic order is present. To highlight this point, we have plotted the coefficient $A(B)$ in fig. 3.14b, and within the antiferromagnetic phase $A(B)$ remains roughly constant. We have attempted to extend the Fermi liquid temperature dependence to higher fields $B \geq B_{\mathrm{CEP}}$, but we find that the fit is only valid over an extremely small range of temperatures $T \leq T_{\mathrm{FL}}(B)$ and the minimum measurement temperature 0.3 K. While we report $A(B)$ that is derived from these fits in fig. 3.14b, we feel that there is no convincing evidence that Fermi liquid behavior can be detected in $\rho(T)$, once antiferromagnetic order has been suppressed to zero by either temperature or field.

If the paramagnetic state with $B \geq B_{\mathrm{CEP}}$ is not a Fermi liquid at low temperatures, then what physical processes are responsible for the electrical resistivity once antiferromagnetic order is suppressed? The similar field dependencies of the magnetoresistivity $\rho(B)$ and the magnetization $M(B)$ displayed in fig. 3.13b suggest that spin disorder scattering may dominate. To test this idea, we have combined measurements of $M(B)$(fig. 3.15a), normalized by M_{S}, which is taken to be the value of M for $T = 1.8$ K and $B = 3$ T, with those of the normalized magnetoresistivity $\Delta\rho/\rho(B = 0) = (\rho(B) - \rho(B = 0))/\rho(B = 0)$. The result is presented in fig. 3.15b. The normalized magnetoresistivity obtained at different fixed temperatures collapses as a function of the normalized magnetization, provided that the fields and temperatures of the respective measurements do not place Yb_3Pt_4 within the antiferromagnetic phase, whose boundaries are indicated by arrows in fig. 3.15b. Spin-disorder scattering can be identified by its power-law relation between $\rho(T, B)$ and $M(T, B)$, where $\Delta\rho/\rho(B = 0) \propto (1 - (M/M_{\mathrm{S}})^2)$ [158, 159]. This relationship is confirmed in fig. 3.15c, where a double logarithmic plot of $\Delta\rho/\rho(B = 0)$ is linear with respect to M/M_{S}. The best fit to the scaling region gives a slope of two, as indicated by the red line. Our measurements affirm our proposal that fluctuations in the magnetization

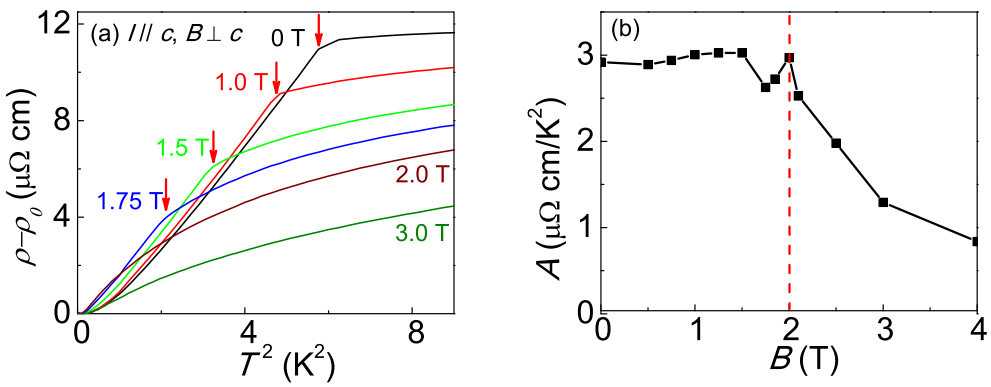

Figure 3.14: (a) The resistivity $\rho - \rho_0$ as a function of T^2 in different magnetic fields as indicated. Red arrows indicate the antiferromagnetic transitions, taken from the maxima in $d\rho/dT$. (b) The coefficient of the quadratic temperature dependence A as a function of magnetic field B. Vertical dashed line indicates the critical field B_{CEP}.

are the primary agent for scattering quasiparticles over a very wide swath of the $B-T$ phase diagram, provided that antiferromagnetic order is not present.

3.5.3 Zeeman Splitting of the Ground Doublets

B/T scaling of the Low Temperature Thermal Properties

A simple scaling analysis reveals the nature of the dominant magnetization fluctuations. Fig. 3.16a shows that the magnetization M collapses when plotted as a function of B/T, but only when B and T are taken from the paramagnetic part of the (T, B) phase diagram (fig. 3.12d). Since fig. 3.15 shows that the magnetoresistivity is a proxy for the magnetization, it is not surprising that it displays B/T scaling too(fig. 3.16b). This scaling fails within the antiferromagnetic phase $T \leq T_N(B)$, where Fermi liquid behavior $\Delta\rho = AT^2$ is observed. The success of the B/T scaling implies that the magnetization fluctuations are simply paramagnetic fluctuations among the crystal field split states of the Yb^{3+} ion. The crystal field split manifold of the $J = 7/2$ Yb^{3+} ions in rhombohedral symmetry consists of four doublets, and inelastic neutron scattering and specific heat measurements indicate that the ground doublet in Yb_3Pt_4 is separated from the first excited level by $80 - 90$ K [75, 123], much larger than the temperature scales probed in the measurements reported here. Practically speaking, we can safely ignore

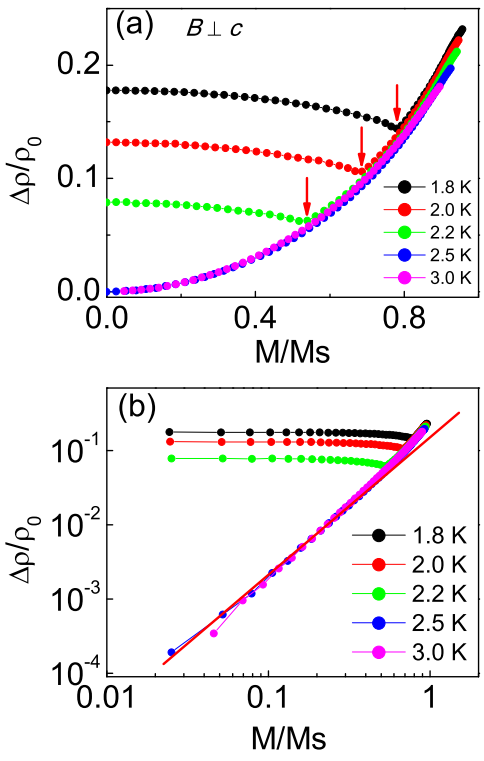

Figure 3.15: (a) Plot of the normalized magnetoresistivities as functions of the normalized magnetizations M/M_{S} measured at different temperatures, where $\Delta\rho(B) = \rho(B) - \rho(B = 0)$, and M_{S} is the saturation magnetization defined in the text. The red arrows indicate the onset of antiferromagnetic order for each curve, highlighting that this relationship fails within the antiferromagnetic phase. (b) The data from (a) collapse onto a single curve with a slope of 2, as indicated by the red line.

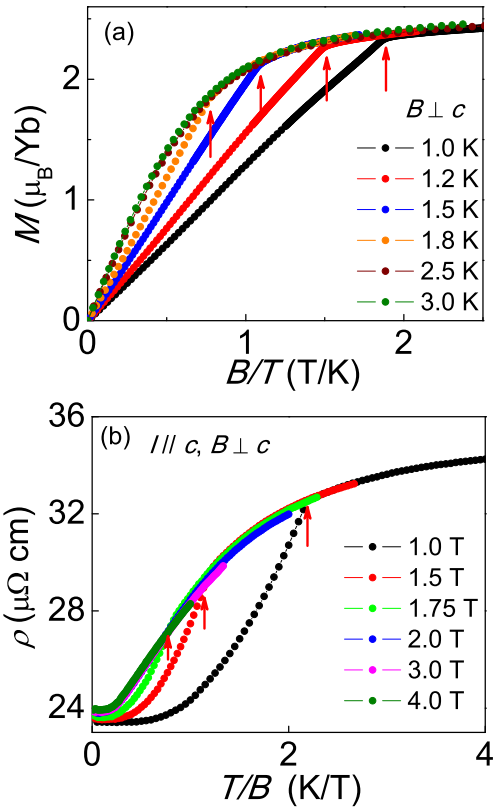

Figure 3.16: (a) Field dependencies of the magnetization M were measured at different temperatures, and then plotted as functions of B/T. (b) The temperature dependencies of the electrical resistivity ρ were measured in different magnetic fields from 1.0 T to 4.0 T, and then plotted as functions of T/B. Red arrows indicate the onset of antiferromagnetic order, showing that the resistivity data collapse onto a single curve in the paramagnetic phase.

the excited states, and so the field and temperature dependencies of the magnetization M reflect the two-fold degeneracy of the ground doublet, lifted by Zeeman splitting in field.

The paramagnetic nature of the magnetic fluctuations also leads to B/T scaling in the measured specific heat $C_{\rm P}$. The field dependence of $C_{\rm P}$ is plotted in fig. 3.17a for different fixed temperatures between 0.7 K and 2.3 K, and at lower temperatures in fig. 3.17b, where the field dependencies of $C_{\rm P}(B)$ are presented for 1.9 K$\geq T \geq$ 0.3 K. For each temperature, $C_{\rm P}$ falls on an apparently universal function of B/T above a characteristic value of B/T marked by red arrows. Fig. 3.17a shows the fields separating the scaling and nonscaling parts of the $C_{\rm P}(B)$ curves, and the resulting curve closely resembles the phase line $T_{\rm N}(B)$ in fig. 3.12d. Like the magnetization M, the B/T scaling evident in $C_{\rm P}$ betrays an underlying energy spectrum that has only two states. Accordingly, fig. 3.17a shows that $C_{\rm M}$ is well described in the paramagnetic phase by a Schottky expression, where the Zeeman splitting of the states $\Delta = g\mu_{\rm B}B$ with $g = 2.5$.

The B/T scaling that we have demonstrated in the field and temperature dependent resistivity ρ, magnetization M, and specific heat C suggests that the predominant magnetic fluctuations that are present for $T \geq T_{\rm N}(B)$, and in the $T = 0$ paramagnetic phase where B exceeds the critical value of 1.85 T, are incoherent fluctuations of the Yb moments within their Zeeman split doublet ground state. Within the accuracy of our measurement, this single ion behavior extends to $T_{\rm N}$ itself, implying that critical fluctuations play a negligible role in Yb_3Pt_4. If this conclusion is correct, then the magnitude of the gap Δ between the Zeeman split ground state doublet of the Yb ions should provide the only energy scale for the paramagnetic part of the Yb_3Pt_4 phase diagram. The importance of this energy scale near field-driven QCPs has recently been emphasized [160].

Crossover Behaviors in Magnetic Susceptibility

The Zeeman gap Δ may be determined, in principle, from analyses of the magnetization M, resistivity ρ, and specific heat $C_{\rm P}$. The temperature derivative of the magnetization $\Delta M/\Delta T$ can be calculated from magnetization isotherms $M(B)$, measured at temperatures differing by $\Delta T = 0.05$ K according to $-dM/dT \simeq -\Delta M/\Delta T = -[(M(T + \Delta T, B) - M(T - \Delta T, B)]/(2\Delta T)$. This procedure is repeated for a wide range of fields B, and the result is plotted in fig. 3.18a. We restrict ourselves here to temperatures $T \geq T_{\rm N}$. The field dependence of -$\Delta M/\Delta T$ displays a distinct maximum at a field $B_{\rm M}$ that moves to higher fields with increasing temperature. The temperatures $T_{\rm M}$ and fields $B_{\rm M}$ of the maxima in $-\Delta B/\Delta T$ are plotted in

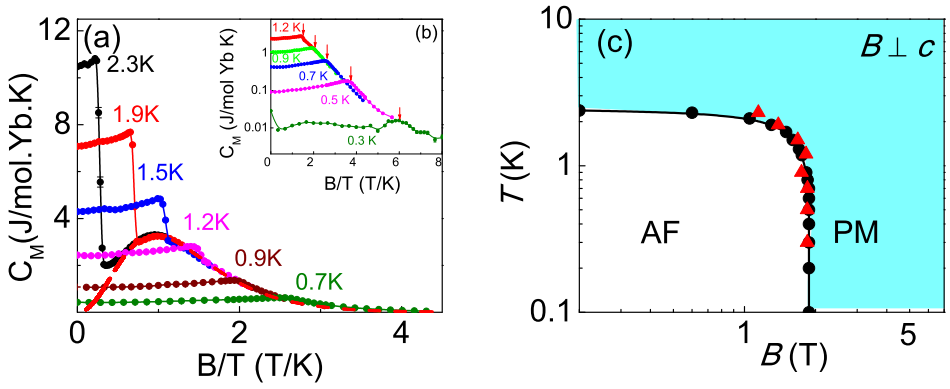

Figure 3.17: (a) The field dependencies of the specific heat $C_{\rm P}$ were obtained at different fixed temperatures, and were then plotted as functions of B/T. The red arrows indicate the onset of antiferromagnetic order, and the red line is the Schottky expression for the specific heat of a two level system with $g = 2.5$. (b) An expanded view of the field dependencies of the specific heat $C_{\rm P}$ measured from 0.3 K to 1.9 K. The red arrows indicate the onset of antiferromagnetic order. (c) The lowest temperature where B/T scaling was observed in the specific heat $C_{\rm P}$ (red triangles) is virtually indistinguishable from the antiferromagnetic phase line $T_{\rm N}(B)$ (black circles) previously determined from specific heat measurements. The B/T scaling is seen in the shaded region that extends over a very wide range of fields and temperatures where antiferromagnetic order is absent.

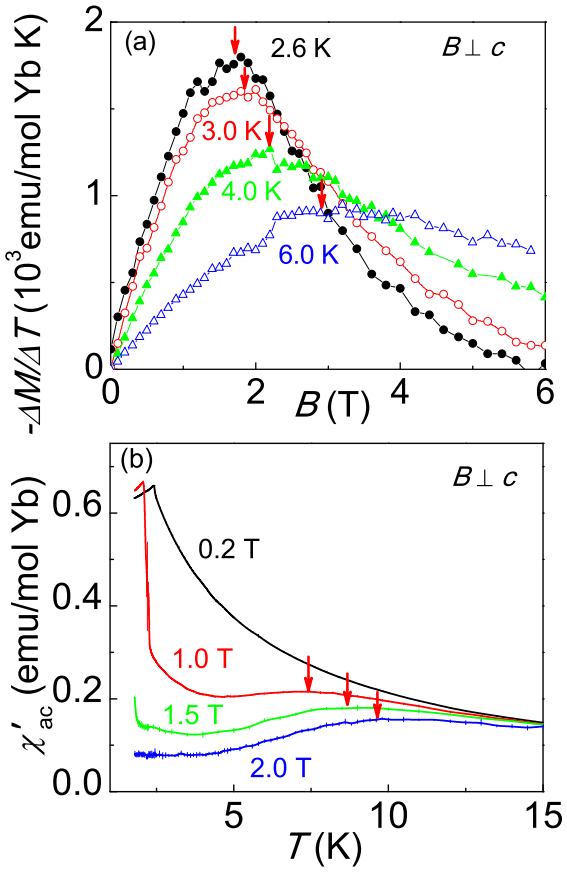

Figure 3.18: (a)$-\Delta M/\Delta T$ *vs* B calculated as described in the text, for different fixed temperatures. (b) The temperature dependencies of the real part of the ac magnetic susceptibility χ'_{ac}, measured at different fields. The red arrows in (a) and (b) mark the positions of maxima.

fig. 3.19d, where they are shown to be linearly related.

ac magnetic susceptibility measurements provide complementary information, since χ'_{ac} is defined as the field derivative of the magnetization, measured as a function of temperature in different fixed dc fields (fig. 3.18b). When the dc magnetic fields are small, a sharp ordering anomaly is observed at $T_{\rm N}$, which passes out of our experimental temperature window $T \geq 1.8$ K for $B \geq 1$ T. In the paramagnetic state at higher fields, χ'_{ac} also has a maximum at $T_{\chi'}$, which moves to larger temperatures with increasing fields. fig. 3.18 shows that, like $T_{\chi'}(B)$, $T_{\rm M}(B)$ increases linearly with magnetic field, at least for the limited range of fields where the magnetization and ac susceptibility measurements overlap. Intriguingly, the peak in χ'_{ac} is not driven to $T = 0$ as $B \to 0$, but instead occurs at $\simeq 4.6$ K when $B = 0$.

Inflection Points in the Field Dependent Resistivity

Since the resistivity and the magnetization are related for paramagnetic Yb_3Pt_4, it follows that the field derivative of the resistivity $d\rho/dB$ will also have a peak that mirrors that of $\chi'_{ac} = dM/dH$. The magnetoresistance of Yb_3Pt_4 was measured for temperatures $T \geq T_{\rm N}$, as shown in fig. 3.19a. The corresponding field derivative $d\rho/dB$ was determined numerically, and it is plotted in fig. 3.19b. A negative maximum is found for $d\rho/dB$ that moves to larger fields with increased temperature. The fields B_ρ and temperatures T_ρ where $-d\rho/dT$ has its maximum should correspond to the fields $B_{\rm M}$ and temperatures $T_{\rm M}$ where $-\Delta M/\Delta T$ has its maximum. Fig. 3.19d confirms that T_ρ and $T_{\rm M}$ are identical, within the accuracy of our analyses. The peak in $-d\rho/dT$ broadens markedly with increasingly temperature, and although the onset of antiferromagnetic order prohibits a direct measurement, its full-width, half-maximum (FWHM)(fig. 3.19c) extrapolates approximately to zero as $B \to 0$.

Schottky Effect in the High Temperature Specific Heat

The effect of Zeeman splitting on the ground doublet is most obvious in measurements of the temperature dependent specific heat $C_{\rm P}$, carried out in different fixed fields (fig. 3.20a). We separate $C_{\rm P}$ into two parts: $C_{\rm P} = C_{\rm M} + C_{\rm Ph}$. $C_{\rm Ph}$ is the contribution from the phonons, and we approximate this term by the specific heat measured in nonmagnetic but isostructural Lu_3Pt_4 (fig. 3.20a). C_{Ph} is taken to be field independent. $C_{\rm M}$ is the magnetic and electronic contribution to the specific heat, and we take $C_{\rm M} = \gamma(B)T + C_{\rm Schottky}$. $C_{\rm P} - C_{\rm Ph} - \gamma T$ is plotted in fig. 3.20b, and indeed it consists of a peak that broadens and moves to higher temperatures with increasing field,

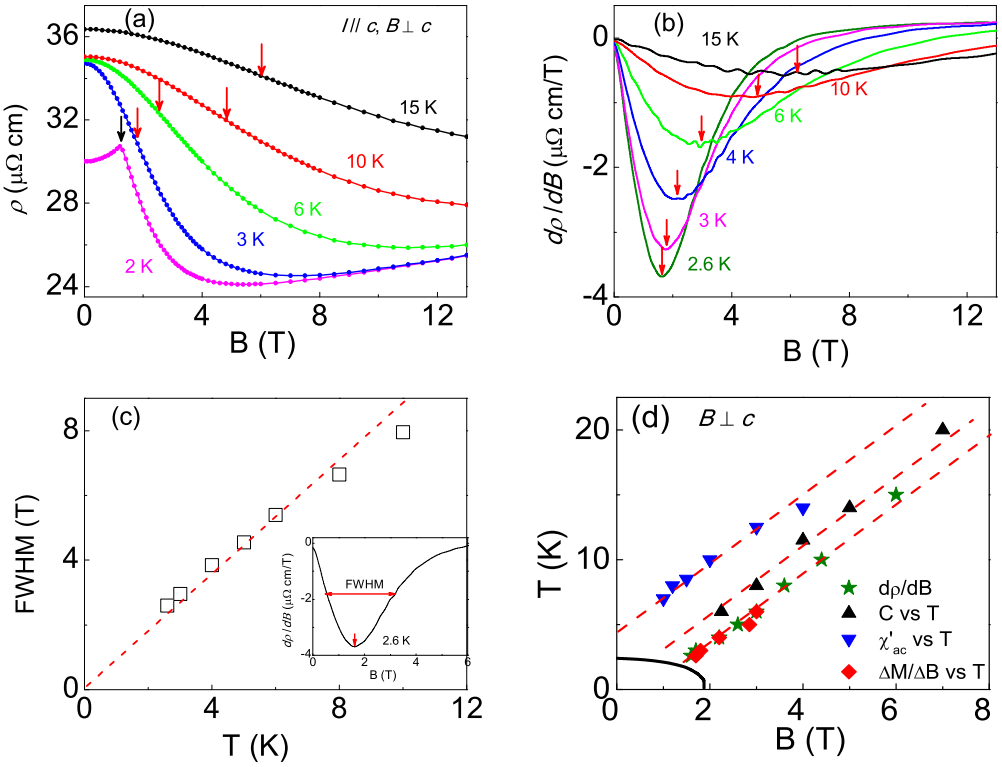

Figure 3.19: (a) Magnetic field dependencies of the electrical resistivity $\rho(B)$ measured at different fixed temperatures, as indicated. The black arrow indicates the antiferromagnetic transition, and red arrows indicate the position of the negative peak in $d\rho/dB$ (b). (c) The full width at half maximum(FWHM) of the $d\rho/dB$ peak decreases linearly with decreasing temperature, and within the accuracy of our analysis extrapolates to zero for $T \to 0$ (red dashed line). Inset: The FWHM is defined as the crossover width at half maximum (as indicated by the red horizontal arrow) of the $d\rho/dB$ peak, demonstrated here for $T = 2.6$ K. (d) The field dependencies of the crossover temperatures determined from $-\Delta M/\Delta T$ ($T_{\rm M}$, red diamonds)), ac magnetic susceptibility (T_χ, blue triangles), $d\rho/dB$(T_ρ, green stars), and the Zeeman energy $T_\Delta = \Delta/k_{\rm B}$ (black triangles) determined from the high temperature specific heat measurement. Solid line is the antiferromagnetic phase boundary $T_{\rm N}$(B) taken from fig. 3.12d. The dashed red lines are guides for the eye, indicating that the three different temperature scales have the same slope($\Delta T/\Delta B \simeq 2.6$ K/T).

much as we would expect for a Schottky contribution to the specific heat. Accordingly, we have fit $C_{\rm P} - C_{\rm Ph} = \gamma(B)T + C_{\rm Schottky}$, where $C_{\rm Schottky}$ is the Schottky expression for two levels with equal degeneracy, separated by a gap $\Delta(B)$. The quality of these fits for fields from 2.25 T to 7 T is demonstrated in fig. 3.20b. The Sommerfeld coefficient $\gamma(B)$ is approximately 40 mJ/mol-K^2 for $B = 0$, and the minimal field dependence that is displayed in fig. 3.20c likely reflects the inherent accuracy of our fits. γ is always small, consistent with the apparent absence of any Kondo physics in Yb_3Pt_4, and there is no evidence for any divergence of γ at $B_{\rm CEP}$, in agreement with similar results on the resistivity coefficient A (fig. 3.14b).

Fig. 3.20b shows that $C_{\rm M} = C_{\rm P} - \gamma T - C_{\rm Ph}$ is well fitted by the Schottky expression for fields from 2.25 T to 7 T, and the field dependence of the temperature scale $T_\Delta = \Delta/k_{\rm B}$ that results from these fits has been added to fig. 3.19d. As expected, T_Δ increases linearly with field. While the temperature scales $T_{\rm M}$, $T_{\chi'}$, T_ρ, and T_Δ are not all identical, in each case we find that their slopes $\Delta T/\Delta B \simeq 2.6$ K/T (fig. 3.19d), which is also consistent with the value $g = 2.5$ found in the scaling of the specific heat at very low temperatures (fig. 3.17a). It is tempting to believe that all these scales originate with the Zeeman splitting of the Yb doublet ground state.

3.6 Discussion and Conclusion

Our measurements suggest that Yb_3Pt_4 is a particularly simple system. Throughout the paramagnetic phase $T \geq T_{\rm N}$ and $B \geq B_{\rm CEP}$, the magnetic and electronic specific heat $C_{\rm M}(T, B)$, the magnetization $M(T, B)$, and even the resistivity $\rho(T, B)$ are all dominated by strong magnetic fluctuations, where the only characteristic energy scale results from the Zeeman splitting of an energetically isolated, Yb doublet ground state. These single ion, paramagnetic fluctuations extend down to $T_{\rm N}(B)$ itself, indicating that critical fluctuations are always very weak. This may reflect the fact that the Néel state vanishes at $B_{\rm CEP} = 1.85$ T in a field-driven critical end point, much as is found for antiferromagnetic insulators [127, 128, 129]. Quantum critical fluctuations are still possible, in principle, if this transition is weakly first order. We speculate that the absence of these quantum critical fluctuations in Yb_3Pt_4 may result from an inherent mean-field like character that is evident in the phase line T_N(B), from the B=0 order parameter found in neutron diffraction measurements [75],and in the appearance of the specific heat transition itself [95, 96]. The highly localized character of the moments in Yb_3Pt_4 prohibits the sorts of quantum critical fluctuations between states with different Fermi surface volumes that were reported in $YbRh_2Si_2$, suggesting

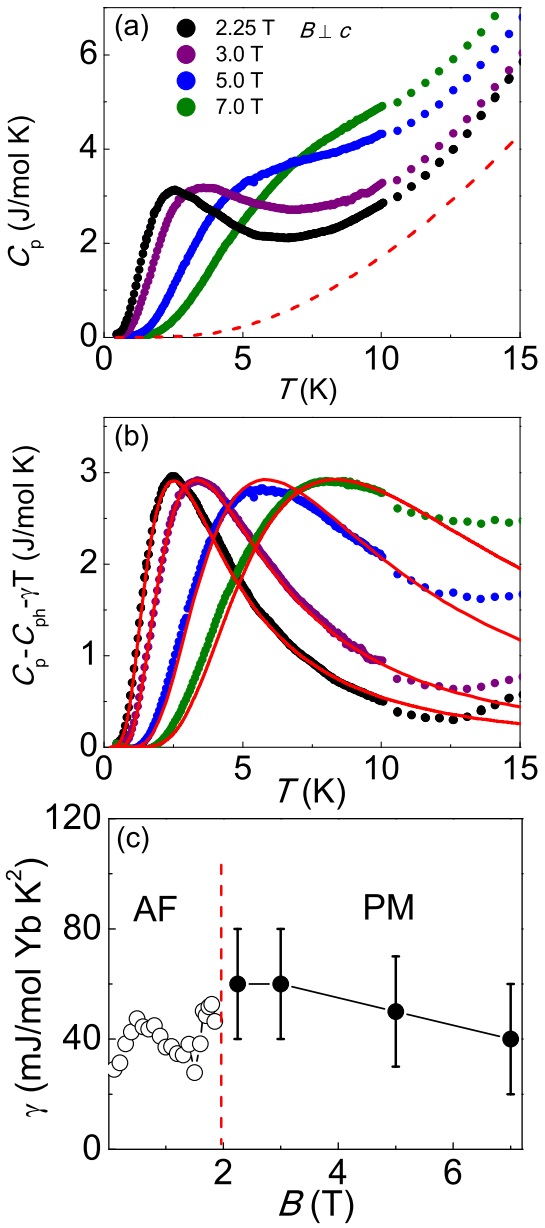

Figure 3.20: Temperature dependencies of the specific heat $C_{\rm P}$, measured at different fields. The red dashed line is the measured $B = 0$ specific heat of the isostructural and nonmagnetic analog compound Lu_3Pt_4, which gives an estimate of the phonon contribution to the specific heat (see text). (b) The temperature dependencies of the specific heat after subtraction of the phonon contribution $C_{\rm Ph}$ and the electronic contribution $\gamma(B)T$. The solid lines are fits to the Schottky expression, described in the text. (c) The Sommerfeld coefficient γ that was obtained from the fits in (b) is almost field independent. Vertical dashed line indicates $B_{\rm CEP} = 1.9$ T, where antiferromagnetic order vanishes.

that they may be a larger part of the quantum critical fluctuations of the more hybridized heavy fermions than was previously appreciated.

Yb_3Pt_4 is a metal, and the near-constancy of the Sommerfeld coefficient for fields both larger and smaller than $B_{\rm CEP}$ suggests that there is a Fermi liquid state that underlies both the antiferromagnetic and paramagnetic phases in Yb_3Pt_4. The T^2 temperature dependence of the electrical resistivity is only observed when antiferromagnetic order disables the paramagnetic fluctuations, suppressing the spin-disorder scattering that otherwise obscures the Fermi liquid component of the resistivity. The smallness of the Sommerfeld coefficient indicates that the exchange coupling of the conduction electrons to the Yb moments is weak, and that the quasiparticle mass enhancement is minimal.

It is fair to say that the Fermi liquid in Yb_3Pt_4 simply coexists with the Yb moments, and that it is almost unaffected by the onset of antiferromagnetic order. Yb_3Pt_4 seems to have much more in common with elemental rare earth metals like Gd or Dy, where magnetic order occurs well above the extremely low or even vanishing temperature scales where Kondo physics could play a role, than heavy fermions like $YbRh_2Si_2$, where the Kondo effect is largely complete by the time magnetic order is established.

Our measurements provide definitive answers to the questions that we posed earlier.

• Is non-Fermi liquid behavior found near the $T_{\rm N} = 0$, $B = B_{\rm CEP} = 1.85$ T critical endpoint? Given the first order character of this transition, quantum critical fluctuations are weak, at best. We have shown that paramagnetic fluctuations of individual Yb moments dominate all measured quantities down to the antiferromagnetic phase line itself. non-Fermi liquid behaviors such as $\Delta\rho = BT^{1+\delta}$ are entirely absent near $B_{\rm CEP}$.

•Is a heavy Fermi liquid found once magnetic fields suppress antiferromagnetic order? A Fermi liquid underlies both the antiferromagnetic and paramagnetic phases of Yb_3Pt_4, but the Sommerfeld coefficient is small in both, signalling a small quasiparticle mass enhancement. There is no sign of Fermi liquid breakdown in paramagnetic Yb_3Pt_4, signalled in other systems by divergencies of the Sommerfeld coefficient γ or the resistivity coefficient A as the field approaches $B_{\rm CEP}$ from above.

•Is there any indication of electronic delocalization in Yb_3Pt_4? Yb_3Pt_4 appears to be an extreme case of moment localization. Outside the range of fields and temperatures where antiferromagnetic order is stable, the electrical resistivity, magnetization, and specific heat all display the B/T scaling that is expected for decoupled and fully incoherent magnetic moments, where the spacing between the underlying energy levels increases linearly with magnetic field. The ubiquity of B/T scaling suggests that these levels originate with the well-

separated doublet ground state in Yb_3Pt_4, which is Zeeman split in field. This single ion behavior dominates in the absence of antiferromagnetic order, suggesting that the Yb moments are always localized, seemingly ruling out the possibility of electronic delocalization and an expansion of the Fermi surface at T_N, as is found in systems like $YbRh_2Si_2$.

It is interesting to consider how the rather minimal physics of localized Yb_3Pt_4 might be connected to the rich physics that is found in heavy fermions with bona fide QCPs. Is there a generalized $T = 0$ phase diagram that can accommodate both? We present a phase diagram in fig. 3.21 that proposes just such a connection. Since this proposed phase diagram is based largely on experimental results in Yb_3Pt_4, further experimental investigation will be required to establish whether it may have more universal application. One axis of this phase diagram is inspired by the Doniach phase diagram [36], and represents the degree of hybridization Γ between the moment-bearing f-electrons and conduction electrons. Applied pressure increases Γ for Ce compounds, but decreases Γ for Yb compounds [161, 162]. The Doniach argument associates magnetic order arising from the Rudermann-Kittel-Kasuya-Yosida (RKKY) interaction with weak hybridization, although the increasing influence of Kondo physics ultimately leads to its suppression at a QCP for a critical value of $\Gamma = \Gamma_{QCP}$. The second axis of this $T = 0$ phase diagram is magnetic field, which generally suppresses antiferromagnetic order. Antiferromagnetic order is stable at $T = 0$ when $B \leq B_N(\Gamma)$ and for $B = 0$, when $\Gamma \leq \Gamma_{QCP}$.

The persistence of field-temperature scaling for compounds that are tuned to the vicinity of the ($B = 0$, $\Gamma = \Gamma_{QCP}$) QCP suggests that the phase line $B_N(\Gamma)$ is second order for an appreciable range of the hybridization parameter Γ, terminating for $B = 0$ at $\Gamma = \Gamma_{QCP}$ [121]. $YbRh_2Si_2$ forms very close to Γ_{QCP}, and the fragility of its antiferromagnetic state is evident from both the tiny ordered moment [163] and by the small amounts of doping that are required to drive $T_N \to 0$ [121, 164]. Larger chemical pressures are responsible for the absence of antiferromagnetic order in $YbIr_2Si_2$, which can be restored by the subsequent application of hydrostatic pressure [165]. High pressures are expected to stabilize antiferromagnetic order at progressively higher fields, an effect that is reproduced by Co-doping in $Yb(Rh_{1-x},Co_x)_2Si_2$ [122]. A different behavior is found in compounds like Yb_3Pt_4, where the exchange coupling Γ is very small ($\Gamma \to 0$) and the field-driven phase transition $T_N = 0$ is first order. The magnetic fields required to suppress antiferromagnetic order to $T_N = 0$ form a line of $T = 0$ transitions that emanate from a tricritical point with Γ_{TCP} that separates this first order part of the $B_N(\Gamma)$ phase line with $\Gamma \to 0$ from the continuous regime with $\Gamma \to \Gamma_{QCP}$ [166, 167]. There is some initial

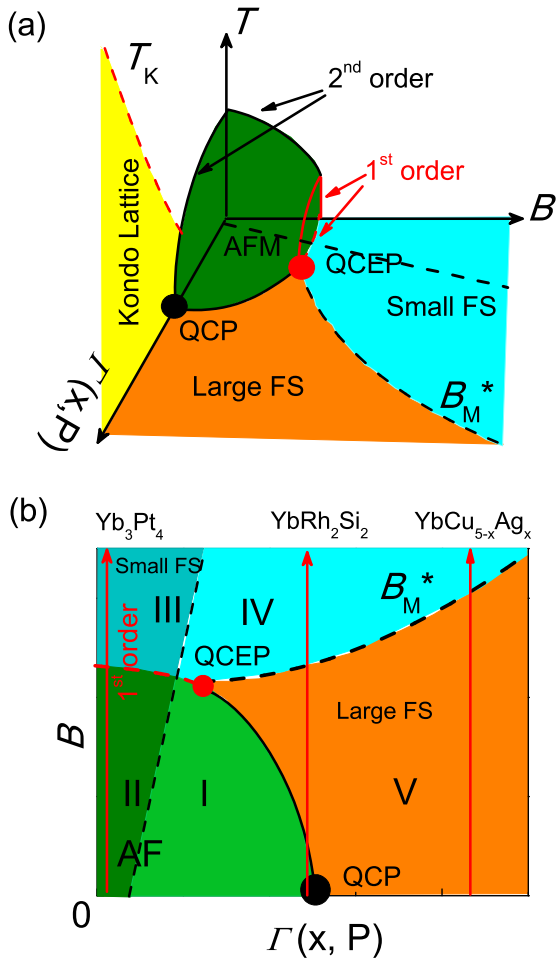

Figure 3.21: Field B - hybridization Γ phase diagram for $T \neq 0$ (a) and $T = 0$ (b). The antiferromagnetic phase line $B_{\rm N}(\Gamma)$ has a continuous region that terminates for $B = 0$, $\Gamma = \Gamma_{\rm QCP}$ (solid line) and a first order part (dashed line) that terminates at $\Gamma \rightarrow 0$, $B_{\rm CEP}$, separated by a tricritical point (White circle, $\Gamma = \Gamma_{\rm TCP}$). Regions I and II are antiferromagnetically ordered, regions III,IV, and V are not. Dashed line $B_{\rm C}(\Gamma)$ separates regions II and III, having localized Yb moments, from Regions I, IV, and V, where there are differing degrees of electronic localization (see text). The line $B_{\rm M}(\Gamma)$ separates regions IV (light mass Fermi liquid) from region V (heavy mass Fermi liquid). It is not known where $B_{\rm M}(\Gamma)$ intersects the antiferromagnetic phase line $B_{\rm N}(\Gamma)$ (dashed line). The evolution of the $T = 0$ states with increasing Γ (decreasing pressure) from local moment AF magnets (Yb_3Pt_4) to HF AF quantum critical compound ($YbRh_2Si_2$) to mixed valence compounds ($YbCu_{5-x}Ag_x$), as indicated by vertical arrows.

evidence that the antiferromagnetic ground state is achieved via a first-order transition in Co-doped $YbRh_2Si_2$ [168], suggesting that it may be possible to span this tricritical point with an appropriate combination of magnetic fields and chemical pressure.

Very different types of electronic behaviors are found in the different regimes of this $T = 0$ phase diagram. All these f-electron based compounds start with the same high temperature state, where spatially localized moments fluctuate independently and are essentially decoupled from the conduction electrons. With lowered temperature, magnetic order and Kondo compensation compete to determine the final $T = 0$ state. In systems like Yb_3Pt_4, T_N is larger than T_K, and so the ground state is magnetic order of spatially localized moments, where the related f-electrons or holes are excluded from the Fermi surface. Magnetic fields suppress the $T = 0$ antiferromagnetic order in Yb_3Pt_4, and the robust B/T scaling in the paramagnetic regime indicates that the localized moments persist, creating a paramagnetic state that is stable even for $T = 0$. In $YbRh_2Si_2$, T_K is much larger than T_N. Here, the Yb-based f-holes and the conduction electrons are strongly entangled, with both contributing to the Fermi surface of the $T = 0, B = 0$ ordered state. Here, too, magnetic fields suppress antiferromagnetic order [155], but the transition in $YbRh_2Si_2$ is accompanied by an expansion of the Fermi surface that produces a heavy Fermi liquid [31, 160]. A second transition or crossover is found at $B_M \simeq 10$ T [169], which is accompanied by a broadened step in the magnetization and a step like reduction in the Sommerfeld constant, suggesting the formation of a new Fermi liquid with substantially reduced quasiparticle mass and interactions [170]. High pressure measurements on $YbRh_2Si_2$ find that B_M decreases with increasing pressure (decreasing Γ) as indicated in fig. 3.21. This general trend has been reported as well in a number of different heavy fermion and mixed valence compounds [171]. The exact nature of the transition or crossover at B_M remains uncertain. de Haas - van Alphen measurements [172] support the proposal that a Lifshitz transition occurs in $YbRh_2Si_2$ at $\simeq$10 T, where the majority spin sheet of the Fermi surface vanishes to produce a more weakly correlated Fermi liquid [173]. Electronic structure calculations suggest instead a gradual crossover that is driven by Zeeman splitting of the quasiparticle states, a process that redistributes spectral weight among bands with different masses, while leaving the number of states contained by the Fermi surface unchanged between the light and heavy Fermi liquid states [174]. Neither scenario suggests that there is an actual localization of the f-holes at $B_M \simeq 10$ T.

The complete destruction of the heavy fermion state is projected to occur at a much higher field B_C [173], resulting in a high field state where the

Yb moments and the conduction electrons are decoupled. The definitive absence of heavy fermion character in Yb_3Pt_4, where the Yb moments and the conduction electrons are nearly decoupled, prompts our suggestion that a smaller field is required to suppress the heavy fermion state as Γ decreases, ultimately producing a $B = 0$ state with $\Gamma \leq \Gamma_{\rm LOC}$ where moments are always localized. We note that such a transition has been observed in $YbRh_2Si_2$, where a pressure $P \simeq 10$ GPa causes the $B = 0$ ordering transition become first order [175], and the ordered Yb moment increases dramatically from 0.02 μ_B/Yb at 1 bar [163] to $\sim 1.9\mu_B$/Yb at 16.5 GPa [175]. The latter value is similar to the $B = 0$ moment found in Yb_3Pt_4, which is in turn close to the expected value for a Yb doublet ground state when $T_{\rm K} \to 0$, signalling that the Yb moments have become largely decoupled from the conduction electrons. These data suggest that $B_{\rm C}(\Gamma)$ intersects the $B = 0$ axis at $\Gamma_{\rm LOC} \leq \Gamma_{\rm TCP}$. Understanding how the $B_{\rm C}(\Gamma)$ line passes through the antiferromagnetic phase and connects to a $B = 0$ moment localization transition will require challenging new measurements that use high pressures or chemical pressure to drive localization, with the subsequent addition of magnetic fields to drive the resulting $T = 0$ transition towards the $B_{\rm N}(\Gamma)$ phase line itself.

Chapter 4

Quantum Criticality in the Family of Compounds Ln(Ln=Y, Lu, Yb)Fe_2Al_{10}

Quantum criticality has been studied in various systems, however, it is rare that the observed scaling can be unified with a critical free energy, or where the resulting exponents form the basis for bona fide QC universality classes. This chapter presents the magnetic properties including specific heat C, magnetization M and electrical resistivity ρ of the 3d-electron based compounds YFe_2Al_{10} , $LuFe_2Al_{10}$ and $YbFe_2Al_{10}$. non Fermi Liquid (nFL) behaviors with strong divergencies in magnetic susceptibility ($\chi \sim T^{-\gamma}, \gamma \approx 1.4$) and specific heat ($C_M/T \sim -logT$) were observed in YFe_2Al_{10} , indicating that it may be located very close to a QCP at $B = 0$ and $T = 0$. Universal scaling behaviors of magnetic susceptibility $d\chi/dT = B^{-1.4}\phi(T/B^{0.6})$ and specific heat $\Delta C_M/T = \varphi(T/B^{0.6})$ were seen over more than three decades of $T/B^{0.6}$. A detailed scaling analysis based on the critical free energy found that the spatial dimension d is equal to the dynamic exponent z at this QCP. Further study suggests that this may not be a magnetic QCP, and different possibilities for the nature of this QCP are also discussed.

4.1 Introduction

Observation of universality and critical scaling behaviors is a big triumph in understanding classic phase transitions [1, 2, 3, 4]. Since the correlation length goes to infinity at the critical point, the critical properties of the system are independent of the dynamical microscopic details. It was known from the scaling theory that every critical point is characterized by a universal class with a set of critical scaling exponents [1, 2, 3, 4]. Different from the classical phase transitions, a quantum phase transition refers to a continuous transition that occurs at zero temperature, where both the correlation length and time scales diverge [24]. Thus in addition to the length scale, a characteristic energy scale of the system will also vanish at such a $T = 0$ QCP [24]. A direct consequence is that the dynamical components play an important role in quantum phase transitions, and quantum critical scaling differs from its classical counterpart in that the spatial dimension d is replaced by an effective dimension $d + z$, where z is the dynamical critical exponent [11, 24]. Quantum criticality has been studied in various systems [10, 11, 12, 21, 32], however it is rare that the observed scaling can be unified with a critical free energy, assuming the existence of hyperscaling [20, 32].

We report here our experimental evidence that YFe_2Al_{10} is one of the few materials of this class. Disorder effects are not decisive in single crystals of this compound, which are stoichiometric with a high degree of crystalline perfection [78, 210]. The magnetism derives entirely from the 3d-electrons contributed by the Fe, all of which appear to be delocalized as $T \to 0$. All the measured quantities in YFe_2Al_{10} are dominated by the QC fluctuations associated with a $B = 0$, $T = 0$ QCP, although there is no indication of any static order above 0.05 K [78]. The complete range of magnetic and thermal measurements are accessible in this system, holding the promise of a full description of the quantum criticality.

4.1.1 Experimental Details

Faceted single crystals of the compound YFe_2Al_{10} with typical dimensions about 3 mm were synthesized using aluminum (Al) metal flux [78, 210]. High precision measurements of the magnetization M and the ac susceptibility χ' were carried out using a Quantum Design Magnetic Phenomena Measurement System (MPMS). Measurements of the specific heat C_P were carried out in a Quantum Design Physical Property Measurement System (PPMS) using the relaxation method. The magnetic and electronic part of the specific heat C_M was determined from the measured specific heat C_P by subtracting specific heat measurements obtained from a single crystal of YRu_2Al_{10}, after

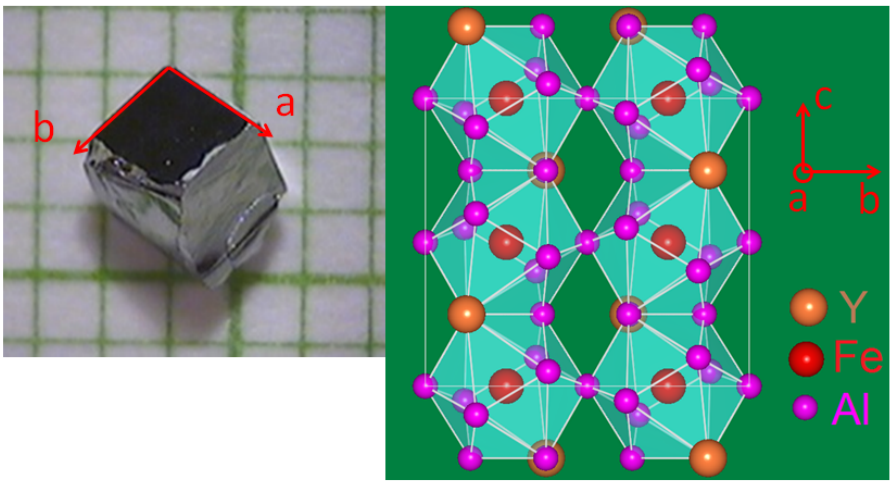

Figure 4.1: Left: A block shaped YFe_2Al_{10} single crystal grow from the Al flux with the principal axis a and b as indicated. Right: Crystal structure of YFe_2Al_{10} . The Fe atoms are sitting in the center of polyhedra like cages made from Al and Y atoms. [78, 210]

scaling the temperature by the ratio of the Debye temperatures θ_D where θ_D(YFe_2Al_{10})=1.03 $\theta_D(YRu_2Al_{10})$ [78]. The resistivity was measured in the PPMS using the AC transport option on the ^{3}He probe. The MCE ratio was extracted indirectly from the magnetic susceptibility and specific heat measurements.

4.1.2 Crystal Structure of YFe_2Al_{10}

Single crystal x-ray diffraction measurements confirm previous reports [219] that YFe_2Al_{10} forms in an orthorhombic $YbFe_2Al_{10}$ type structure with the space group Cmcm (63). In this structure, each Fe atom is surrounded by ten Al and two Y atoms, and the crystal structure can be viewed as connected polyhedral cages made of Y and Al atoms with Fe atoms sitting in the center, as shown in fig. 4.1. These cages are connected in the ac plane by sharing edges, while they were linked by a shared Al atom at the corner along the b direction. The lattice parameters for YFe_2Al_{10} are $a = 8.9654(2)$Å, $b = 10.1578(3)$Å, $c = 9.0110(3)$Å , and $V = 820.6$Å^3. We obtained a refinement factor R1=0.0164 [78, 210] that permits no more than 1% variation in site occupancy, ruling out the considerable Fe/Al site interchange characteristic of the Fe-rich members of the YFe_xAl_{12-x} family [221]. Direct inspection by optical microscopy of polished cross-sections of YFe_2Al_{10} crystals found no evidence for

contaminant phases, beyond small inclusions of Al flux. Energy dispersive x-ray (EDX) analysis found that there were no variations in the nominal Y-Fe-Al stoichiometry at different locations in the crystals, within the 1-2 % accuracy of EDX [78]. These direct investigations, as well as the overall uniformity of experimental results among different crystals from different batches argue strongly that our YFe_2Al_{10} crystals are of excellent quality.

4.2 Magnetic Properties of YFe_2Al_{10}

4.2.1 Magnetic susceptibility

The intrinsically magnetic character of YFe_2Al_{10} is evident from measurements of the field and temperature dependent magnetic susceptibility. Shown in fig. 4.2(a) is the temperature dependent ac magnetic susceptibility measured in an ac field $B_{ac} = 4.17$ Oe applied both along and perpendicular to the crystal b direction [78]. The magnetic susceptibility continues to increase with decreasing temperature, and a strong divergence with $\chi \sim T^{-1.4}$ was observed for the $B \perp b$ direction at low temperatures. However, for the field in the $B \| b$ direction, the magnetic susceptibility is less divergent, and trend toward saturation was observed below about 10 K.

For temperatures above 30 K, the ac magnetic susceptibility was fitted to the Curie-Weiss expression $\chi_{ac} = \chi_0 + C/(T - \theta)$, where χ_0 is the temperature independent background, θ is the Curie-Weiss temperature, and C is the Curie constant, as shown in fig. 4.2(b) [78]. The fitting gives similar effective moments for fields along different directions, with magnitudes $0.41\mu_B$/Fe ($B \| b$) and $0.45\mu_B$/Fe ($B \perp b$), and Curie-Weiss temperature -24 K ($B \| b$) and -28 K ($B \perp b$) [78]. However, the temperature independent background χ_0 is very different for different field directions with $\chi_0 \sim 2.5 \times 10^{-4}$emu/mol.Fe for $B \| b$, which is almost 100 times larger than χ_0 for $B \perp b$. The Curie law can be extended to temperatures as high as 750 K (inset of fig. 4.2(b)) [78]. The negative Curie-Weiss temperature indicates antiferromagnetic interactions, although no magnetic order was observed down to 1.8 K in the magnetic susceptibility measurements. The fluctuation moments determined from the Curie law are much smaller than the ones expected from Fe local moments. One possibility that would explain the origin of the tiny effective moments is that the measured magnetic susceptibility comes from some kind of local moment magnetic impurities.

However, we will show that the impurity scenario does not account for many of the observations. One important aspect is the observed strong anisotropy of the magnetic susceptibility measured in different field directions.

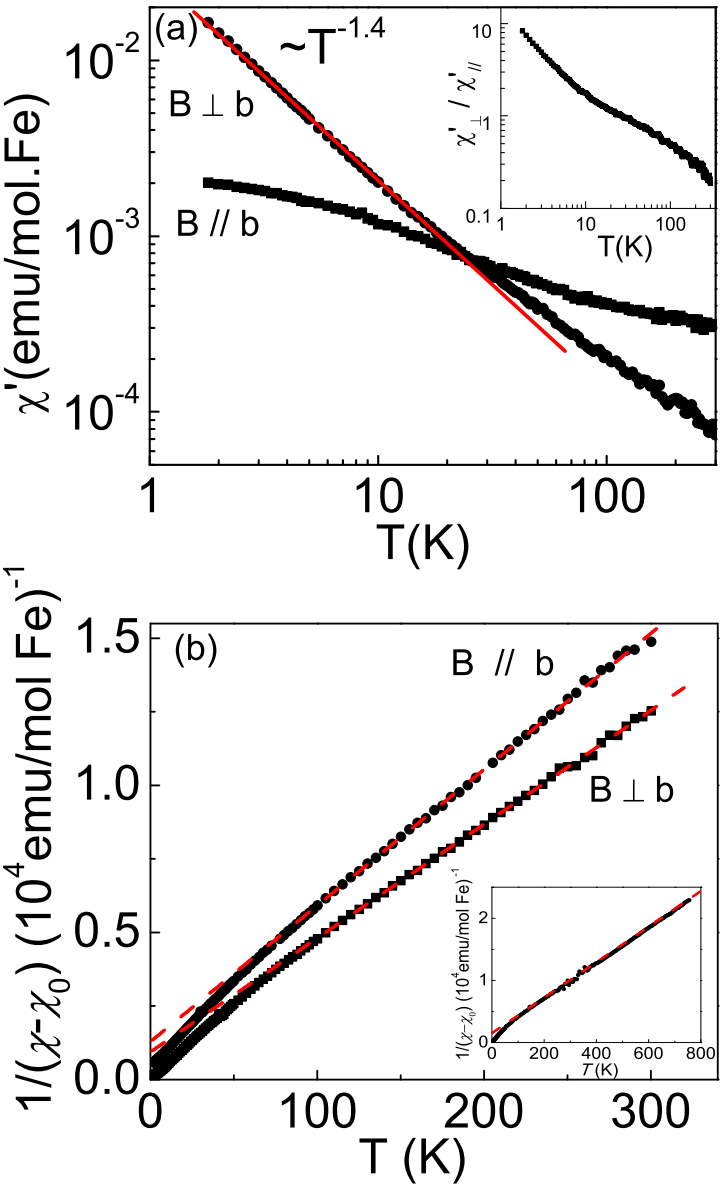

Figure 4.2: (a)Temperature dependencies of ac susceptibility with the ac field B_{ac} = 4.17 Oe applied both parallel and perpendicular to the b axis, as indicated. Inset: The ratio of the ac susceptibility along two different directions. (b) The inverse of the temperature-dependent parts of the susceptibility display Curie-law temperature dependencies (red dashed lines) for $B \perp b$ and $B \parallel b$. The inset shows that the Curie law extends up to 750 K in a crystal with indefinite orientation. [78]

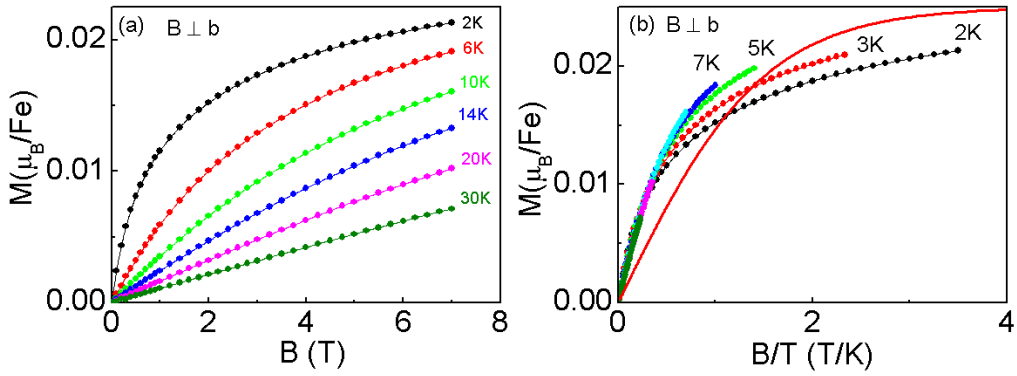

Figure 4.3: (a) Magnetization M as a function of field $B \perp b$, at indicated temperatures. (b) Data from (a), plotted as functions of B/T. Solid line is the $S = 1/2$ Brillouin function, with a scaled magnitude. [78]

Shown in fig. 4.2(a) (inset) is the ratio of the ac magnetic susceptibilities ($\chi'_{B\perp b}/\chi'_{B\parallel b}$) for field along the two different directions. We can see that $\chi'_{B\perp b}$ is almost one order larger than $\chi'_{B\parallel b}$ at low temperatures ($\chi'_{B\perp b}/\chi'_{B\parallel b} \sim 10$ at $T = 1.8$K) [78]. However, with increasing temperature, $\chi'_{B\perp b}$ becomes much weaker and $\chi'_{B\perp b}/\chi'_{B\parallel b} \sim 0.2$ at temperature around 300 K. This particular anisotropy is very hard to understand with scenarios of contamination from local moment impurities, which are more likely to give isotropic behaviors. In addition, for impurity models, magnetic susceptibility with fields along the divergent direction ($B \perp b$) should always have larger magnitude over the whole temperature range, and not just at low temperatures as we find here.

Another very important observation comes from the scaling behaviors of the magnetic field dependent magnetization. Shown in fig. 4.3(a) is the magnetization measured with the field perpendicular to the b direction at different temperatures from 2 K to 30 K [78]. The magnetization M is linear with field B at higher temperatures. However, at lower temperatures, the nonlinearity becomes more and more significant at small fields. Assuming the magnetization measured here comes from isolated paramagnetic impurities, the overall field and temperature dependent behaviors should obey the Brillouin function. We have plotted the isotherms of the field dependent magnetization M as functions of B/T in fig. 4.3(b) [78]. The red solid line is the scaled Brillouin function assuming $S = 1/2$. The magnetization curves do not collapse to a universal function of B/T, and the overall curve can hardly be explained by the Brillouin function. These observations rule out the possibility that contamination from localized moment impurities is responsible

for the measured magnetization. The strong divergence for field perpendicular to the b direction and the strong anisotropy indicates that the low temperature magnetic susceptibility may be dominated by critical fluctuations residing in the ac plane [78].

4.2.2 Specific heat

Further evidence for these critical fluctuations comes from the low-temperature specific heat C. Shown in fig. 4.4a is the measured specific heat of YFe_2Al_{10} in zero field from 0.4 K up to 30 K [78]. To separate the contributions from phonons, the specific heat of the nonmagnetic but isostructural compound YRu_2Al_{10} was measured [78]. Considering that $4d$ Ru atoms are heavier than the $3d$ iron (Fe) atoms, the Debye temperatures of these two compounds are slightly different. However, the overall trends of the two specific heat are very similar. By correcting these slight differences in the Debye temperature $\theta_D(YFe_2Al_{10}) = 1.03\theta_D(YRu_2Al_{10})$, the specific heat of YRu_2Al_{10} was rescaled as shown in fig. 4.4a [78]. This re-scaled specific heat was then used as the estimated phonon contribution, and was subtracted from the as measured YFe_2Al_{10} data. The magnetic specific heat C_M/T that was isolated by this procedure is plotted in fig. 4.4b [78]. For temperature above about 10 K, the magnetic specific heat C_M/T is almost constant, indicating Fermi liquid (FL) behavior with the Sommerfeld coefficient $\gamma \simeq 9$ mJ/mol.Fe.K^2. Comparing to the one found in the nonmagnetic compound YRu_2Al_{10}($\gamma \simeq 3$ mJ/mol.Ru.K^2), we conclude that the effective quasiparticle mass is significantly enhanced in the FL state of YFe_2Al_{10} [78].

Below 10 K, the Sommerfeld coefficient of YFe_2Al_{10} increases monotonically to about 50 mJ/mol.Fe.K^2 around 0.1 K. As shown in fig. 4.5, the zero field specific heat follows a power law as $C_M/T \sim T^{-0.5}$ below about 10 K [78]. However, a kink was observed at ~ 0.4 K, and the measured zero field specific heat deviates from this power law below that temperature. A weak maximum was also seen at about 0.1 K, which may come from the effect of the nuclear Schottky effect of the ^{27}Al nucleus. No clear evidence of any magnetic ordering was observed down to the lowest temperature.

We have considered that there may be some contribution in the as-measured zero field specific heat other than the singular part caused by the critical fluctuations. As was already indicated from the field dependent magnetization, the critical fluctuations are suppressed in high fields. The specific heat measured in a sufficiently high field could be used as the non-critical background. We have measured $C_M(T)$ for $B = 4$ T, and subtracted it from the $B = 0$ specific heat C_P to isolate $\Delta C_M/T = C_P/T - C_P(B = 4T)/T$ (fig. 4.5). The kink at 0.4 K disappears in the semi-log plot, and at lower

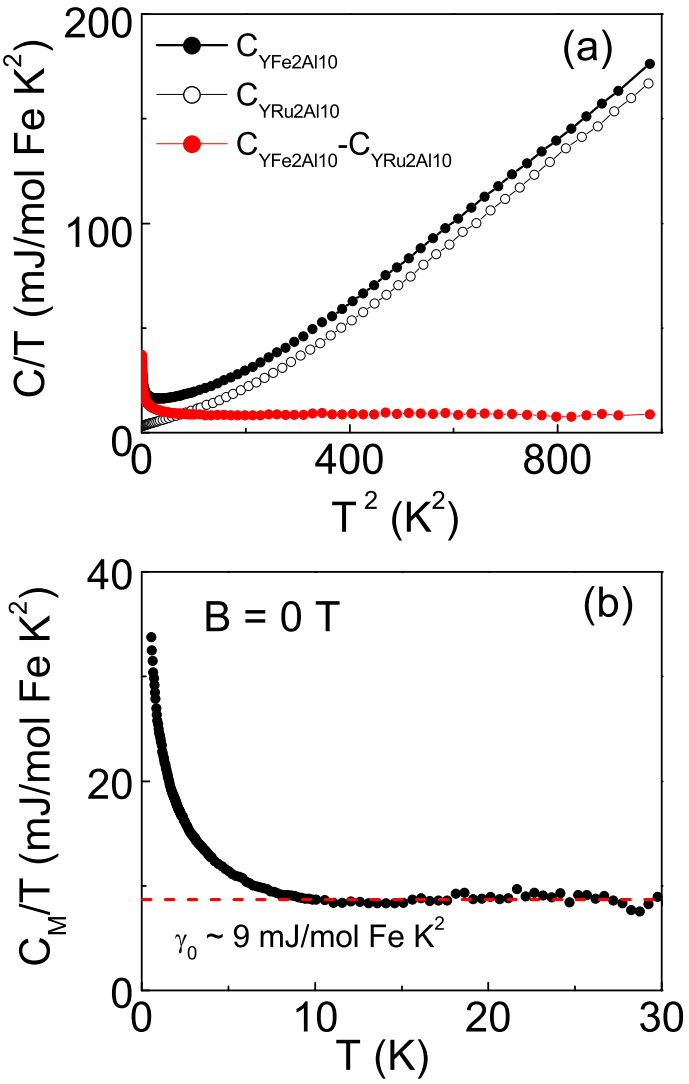

Figure 4.4: (a) As-measured specific heat C/T for YFe_2Al_{10} (•) and the rescaled specific heat of YRu_2Al_{10} (○). The red solid circles (•) are the extract magnetic contribution to the specific heat of YFe_2Al_{10} . Details explained in the text. (b) Magnetic contribution of the specific heat C_M/T for YFe_2Al_{10} . Red dashed line indicates Sommerfeld coefficient $\gamma \sim 9$ mJ/mol Fe K^2. [78]

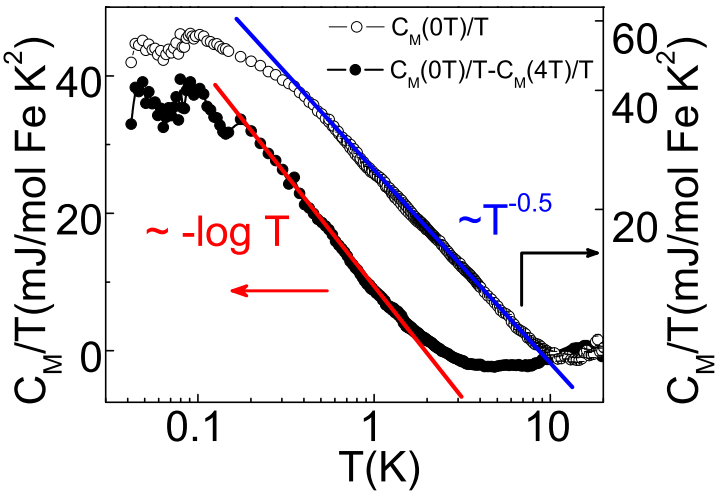

Figure 4.5: Log-log plot (○) of the zero field specific heat and the semi-log plot (●) of the subtract specific heat $C_M(0T)/T - C_M(4T)/T$ as a function of temperature T.

temperatures, the subtracted specific heat can be described as a logarithmic divergence $\Delta C_M/T \sim -logT$.

We are not trying to argue which of the two expressions for the divergent specific heat is better. The power law describes the high temperature data better, while the logarithmic divergence is more suited to the lowest temperature data. We will see below that the logarithmic divergence is more consistent with the scaling behaviors than the power law.

4.3 Quantum Critical Scaling in YFe_2Al_{10}

4.3.1 Scaling of the Magnetic Susceptibility

Since YFe_2Al_{10} may be located close to a QCP at $B = 0$, magnetic field is a tuning parameter that suppresses the critical fluctuations and tunes the system away from the quantum critical region, just as been observed in the heavy fermion materials [10, 11, 12, 21, 32]. Thus, it will be very interesting to know if there is any universal behavior that may link the critical behaviors observed in the magnetization, and specific heat measurements. A detailed study of field tuned magnetic behaviors in YFe_2Al_{10} is presented here.

The field and temperature dependencies of the magnetic susceptibility demonstrate that the most divergent magnetic response is found at the lowest

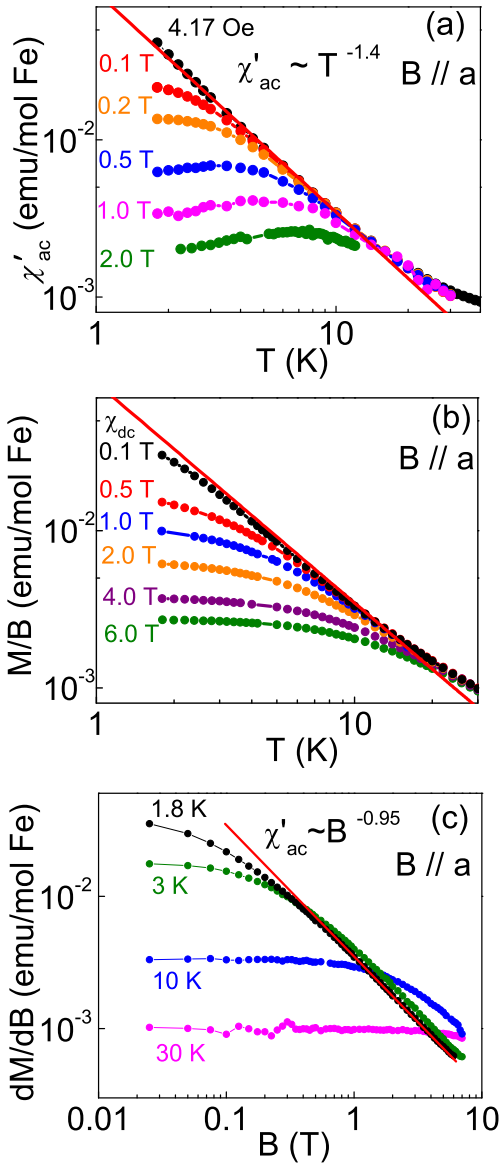

Figure 4.6: (a)Temperature dependent ac magnetic susceptibility χ' measured in different dc fields from 0 T to 2.0 T with $B_{\rm ac} = 4.17$ Oe. The red line is a fit as $\chi'(T) \sim T^{-\gamma}$ for temperature $T < 10$ K, where $\gamma = 1.4$. (b) Temperature dependent dc susceptibility M/B measured in fields up to 6.0 T. The red line is the same fit as shown above in fig.1a. (c) Field dependence of the magnetic susceptibility χ' at different temperatures as indicated. The red line indicates the magnetic susceptibility decreases as a function of $\chi'(B) \sim B^{-0.95}$ at 1.8 K. All the measurements here were performed with magnetic fields along the a axis.

fields and temperatures. Strong anisotropy was observed with magnetic field along different principal crystal axes. The most divergent direction we found is with field along the crystal a direction. The magnetization data shown in fig. 4.3 were obtained in fields in the ac plane ($B \perp b$), and all the magnetization data shown here and below are with field along the most divergent crystal a axis. Due to some weak anisotropy in the ac plane, the fitted critical exponents γ for ($B \| a$) are slightly different from those with $B \perp b$. The temperature dependence of the ac susceptibility $\chi' = dM/dB$ was measured for different fixed fields $B \| a$-axis up to 2.0 T (fig. 4.6a). At the lowest fields, χ' increases monotonically and approaches the power law divergence of $\chi' \sim T^{-1.4}$, with the measured ac field $B_{ac} = 4.17$ Oe. With increasing field, there is a saturation of χ' as $T \to 0$, signalling that the critical divergence is increasingly suppressed by the magnetic field to create a new Fermi liquid state where the magnetization depends only weakly on temperature. The dc susceptibility $\chi = M/B$ displays very similar behavior as shown in fig. 4.6b. The strong temperature divergence at low fields is significantly suppressed with increasing field, and the magnetic susceptibility flattens at low temperatures when field is as high as $B = 6.0$ T.

The magnetic field dependence of χ' at different temperatures is presented for different temperatures in fig. 4.6c. dM/dB decreases strongly with increasing field at the lowest measured temperature 1.8 K, and a strong divergence with $\chi' \sim B^{-0.95}$ was found in the high field region. The power law dependencies found in both the field and temperature dependent magnetic susceptibilities indicate that high temperatures have the similar qualitative effect on dM/dB as high fields. In both cases, the divergencies that are observed at the lowest fields and temperatures are suppressed in favor of high field and high temperature states where the susceptibility is insensitive to either field or temperature, much like the Pauli susceptibility found in a normal Fermi liquid. Fig. 4.6 demonstrates that the dc and ac susceptibilities in YFe_2Al_{10} are increasingly divergent with decreasing field and temperature. This is consistent with the assumption that this system may be approaching the QCP that occurs at or near $B = 0$ and $T = 0$. Our measurements of the magnetic susceptibility reveal that field and temperature play dual roles in suppressing the quantum critical behavior that is evident in YFe_2Al_{10} , suggesting field-temperature scaling.

Here we start from the scaling of the temperature derivative of the magnetic susceptibility. One advantage of this is that it omits the noncritical contribution from the temperature independent susceptibility χ_0. On the other hand, this analysis involves numerical differentiation of the magnetization data, demanding excellent quality data. For dc magnetization measurements, high quality data were taken in the field as large as 6.0 T. The ac magnetic

susceptibility becomes too noisy to be measured reliably in fields higher than 2.0 T. The final scaling of the ac susceptibility was performed in fields up to 1.0 T.

Figure 4.7 shows that both ac magnetic susceptibility $\chi' = dM/dB$ and dc magnetic susceptibility $\chi = M/B$ collapse in a similar way as

$$-\frac{d\chi}{dT}B^{1.4} = \phi(\frac{T}{B^{0.6}}) \tag{4.1}$$

with the same scaling exponents. The overall scaling is excellent extending over more than three decades of the scaling variable $T/B^{0.6}$, for temperatures 1.8 K$\leq T \leq$ 30 K and for fields up to 6.0 T in the dc susceptibility and 1.0 T in the ac susceptibility. A broad maximum was observed in both of the scaled ac and dc magnetic susceptibilities, which is the crossover from the quantum critical region where $T \gg B$ to the Fermi liquid like state where $T \ll B$. Shown in fig. 4.7a and fig. 4.7c are the log-log plot of the scaling curves, and in fig. 4.7b and fig. 4.7d the semi-log plots, emphasizing the quality of the scaling in the Fermi liquid region (small $T/B^{0.6}$). The red solid lines are the fits based on a scaling function that will be explained in section 4.6. Also it has been argued in [176, 177] that, for single impurity models, the scaling dimension Δ must be less than one for the scaling variable B/T^{Δ}. The scaling function we found above with $\Delta = 1/0.6 \simeq 1.6$ clearly violates any impurity theory, and suggests that nonlocal critical fluctuations are important in YFe_2Al_{10} .

4.3.2 Scaling of the Specific Heat

The specific heat C_M is also dominated by the same quantum critical fluctuations at low temperatures and fields, where the B=0 specific heat C_M/T increases strongly below 10 K (fig. 4.5). A comparison of double log and semi-log plots indicates that either a power law $C_M/T \sim T^{-0.5}$, as we previously reported [78], or a logarithmic temperature dependence $C_M/T \sim -logT$ describe the data equally well. As we will see below, the latter is consistent with the field and temperature scaling, while the former is not.

Like the magnetic susceptibility, magnetic fields suppress the $B = 0$ divergence in the specific heat, and lead to a low temperature saturation of C_M/T (fig. 4.8a). This suggests that a heavy Fermi liquid state is found at high fields, as seen in f electron heavy fermion compounds [10, 12, 21, 32]. We will use this universal behavior to propose a specific function of the free energy in the next section. We have shown that the magnetic susceptibility scales as $T/B^{0.6}$. Since magnetization M is related to the entropy S through the Maxwell relation $dM/dT = dS/dB$, the specific heat should also scale

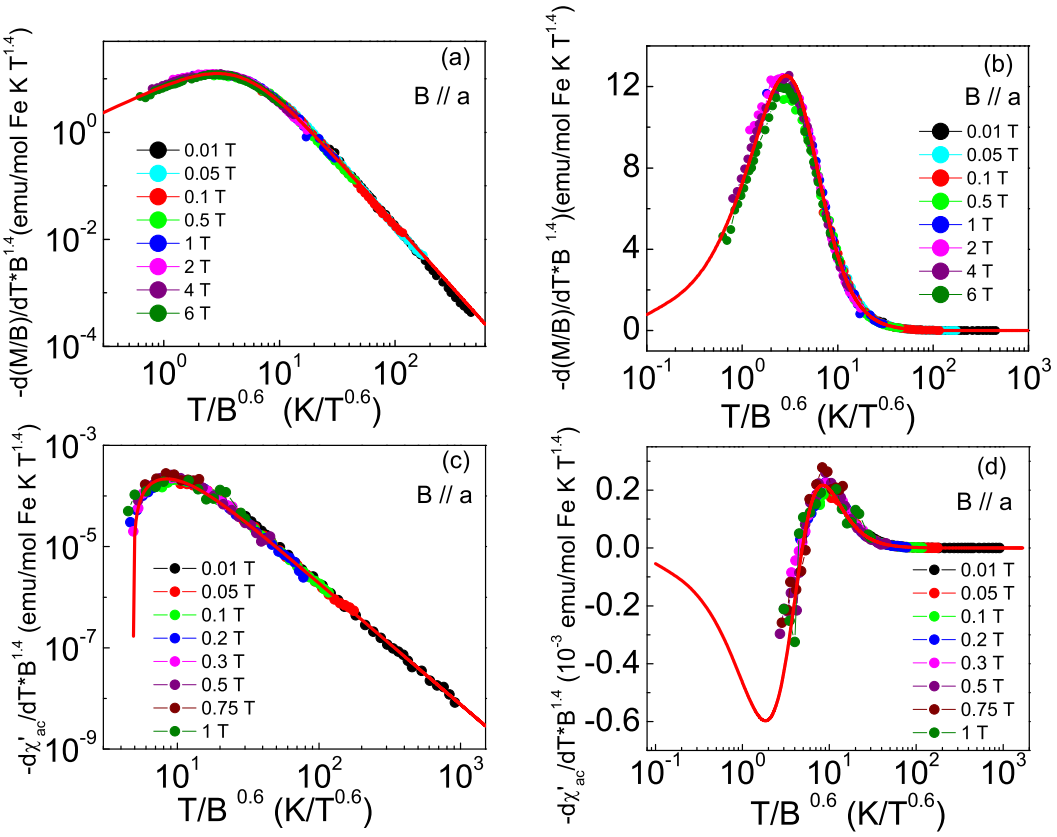

Figure 4.7: Scaling observed for the dc and ac magnetic susceptibility over several decades of the scaling variable $T/B^{0.6}$. The red line is the fitting based on the proposed scaling function of the magnetization, as explained in the later sections. (a), and (c) are the log-log plot of the dc and ac magnetic susceptibility, while (b) and (d) are the semi-log plot of the same data in (a) and (c).

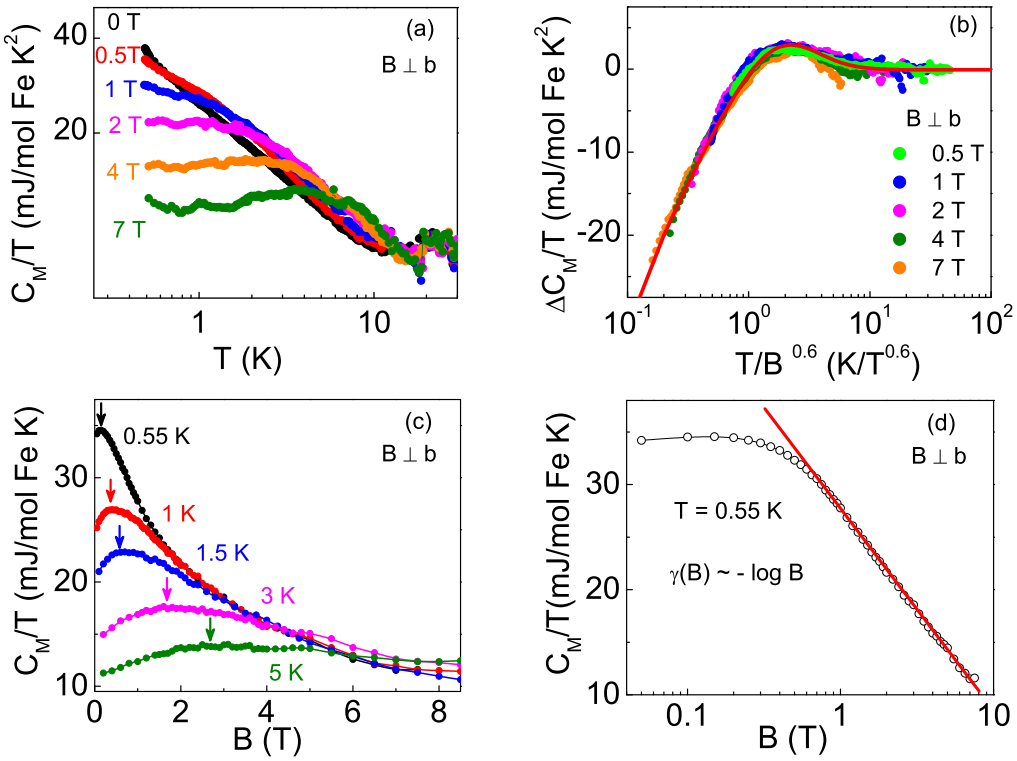

Figure 4.8: (a)Temperature dependent specific heat measured in different magnetic fields (0 T $\leqslant B \leqslant$ 7.0 T) perpendicular to the b axis. (b)Scaling of the field dependent specific heat ($\Delta C_{\rm M}/T = (C(B,T) - C(0,T))/T$) as a function of $T/B^{0.6}$ in the field and temperature range with 0.4 K$< T <$ 10 K and 0 T$< B \leqslant$ 7 T. Red line is the fitting based on the proposed scaling function of the free energy as described in the later sections. (c) Field dependent specific heat measured in different temperature from 0.5 K to 5 K. The arrows indicates crossovers from the quantum critical region to the high field Fermi liquid state. (d) A logarithmic decrease of the specific heat was observed at 0.55 K in high fields from about 1 T to 9 T.

as a function of $T/B^{0.6}$. An excellent scaling collapse is indeed found for the specific heat. As shown in fig. 4.8b, the field dependent specific heat $\Delta C_M/T = C_M(B,T)/T - C_M(0,T)/T$ performed in different fixed fields B describe a universal function of the same scaling variable $T/B^{0.6}$ as

$$\frac{\Delta C_M}{T} = \varphi(\frac{T}{B^{0.6}}). \tag{4.2}$$

This scaling is just as we expected from the scaling of the susceptibility, described above in equation 4.1. From the scaling curve, we can see that $\Delta C_M/T$ approaches a constant value for $T/B^{0.6} \gg 1$, implying that the Fermi liquid state emerges from the quantum critical fluctuations in the high field low temperature region when $k_B T \ll g\mu_B B$. Between these two limiting regions, crossover behaviors as the broad maximum in the specific heat are observed (fig. 4.8b and c), similar to what we see in the magnetic susceptibility. In the field dependent C_M/T (fig. 4.8c), the peak position of these maxima increase with increasing temperature (as marked by the arrows), and the peak shape itself becomes more broad. These peak positions follow the same field dependence found in the magnetic susceptibility measurements, as expected from the scaling. At our lowest temperature, 0.55 K, we see that there is a logarithmic field divergence $C_M/T \sim -logB$, for about 1.0 T$\leq B \leq$ 9 T (fig. 4.8d). This is also as expected from the scaling analysis that we will discuss in section 4.6.

4.3.3 Field Temperature Phase Diagram

Although no static order has been observed in YFe_2Al_{10} on the measured temperature and field ranges, we do see crossover behaviors in different measurements. We have defined here the crossover values $T^*(B)$ as the field dependent temperatures where dM/dB, dM/dT and C/T vs B are maximized. Although the absolute values of $T^*(B)$ determined from different experiments are different, they all follow the same field and temperature relation, that is $T^* \propto B^{0.6}$, just as expected from the scaling variable $x = T/B^{0.6}$. The crossover lines determined from the ac susceptibility dM/dB and specific heat C/T vs B are re-scaled to the $T^*(B)$ value from the dc magnetization dM/dT and plotted together in fig. 4.9. Fermi liquid behavior like $\Delta C_M/T \simeq \gamma$, where $\gamma \simeq$ const, and $\chi \simeq$ const is found when $T \ll T^*(B)$, i.e. for low temperatures and high fields. Conversely, quantum critical fluctuations dominate in low fields when $T \gg T^*(B)$, and at increasingly high temperatures as the field is increased. The excellent scaling collapses found from susceptibility and specific heat experiments are valid over the complete range of fields and temperatures

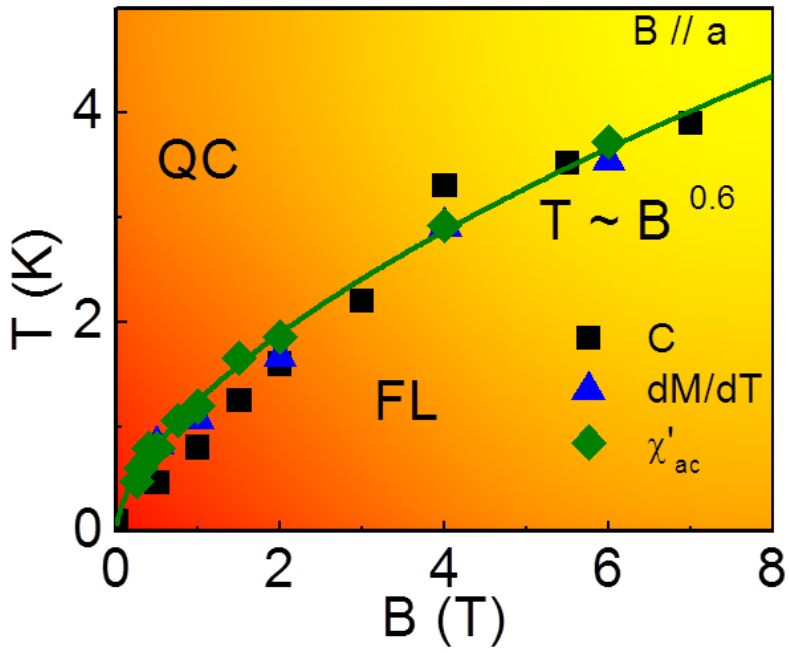

Figure 4.9: Field temperature ($B-T$) phase diagram of YFe_2Al_{10} with field B along the a direction. The crossover lines are defined through the peak position of $C_M(B,T)/T$ (■), dc magnetization $-dM/dT$ (▲), and ac magnetic susceptibility χ' (♦).

represented in fig. 4.9, suggesting that a crossover function might be found that would connect the Fermi liquid and quantum critical regimes of YFe_2Al_{10} .

Up to now, we have shown that all the dc, ac magnetic susceptibility and specific heat data display well behaved scaling over several decades of the scaling variable $T/B^{0.6}$, supporting the idea that the QCP is located at $T = 0$, and $B = 0$ (fig. 4.9). The observed scaling functions of equation 4.1 and 4.2 are re-examined below using a consistent quantum critical scaling analysis.

4.4 The Scaling Analysis in YFe_2Al_{10}

4.4.1 Free Energy and Magnetization

Experimentally the specific heat and magnetic susceptibility are two independent measurements, but they are related to the same free energy, where $\chi' = -\partial^2 F/\partial B^2$, and $C/T = -\partial^2 F/\partial T^2$. The scaling observed in both magnetic susceptibility and specific heat implies that the free energy which is

responsible to the the low temperature properties should also be scalable.

We assume the generic form for the singular part of the free energy F as introduced in chapter 1 (equation 1.24),

$$F(B,T) = T^{\frac{d+z}{z}} f_F(\frac{B}{T^{y_b/z}}) = B^{\frac{d+z}{y_b}} \tilde{f}_F(\frac{T}{B^{z/y_b}}). \tag{4.3}$$

where y_b is the scaling exponent related to the field B. With this assumption for the free energy, we can now express all the other thermodynamic properties as functions of T and B. The magnetization $M = \partial F/\partial B$, is determined by taking the derivative of the free energy (4.3),

$$M = B^{(d+z)/y_b - 1} f_M \left(\frac{T}{B^{z/y_b}} \right), \tag{4.4}$$

where the scaling function f_M is related to the original scaling function of the free energy $\tilde{f}_F$ by

$$f_M(x) = (d+z)/y_b \tilde{f}_F(x) - z/y_b x \tilde{f}'_F(x).$$

It follows that the scaling function for the dc magnetic susceptibility can be written as

$$\chi_{dc} = M/B = M = B^{(d+z)/y_b - 2} f_M \left(\frac{T}{B^{z/y_b}} \right). \tag{4.5}$$

The measured dc susceptibility contains a very small temperature independent component χ_0 that is not critical. By taking the temperature derivative of both sides of equation 4.5, we can isolate the temperature dependent part of χ_{dc}, which has the scaling behavior

$$d\chi_{dc}/dT = B^{d/y_b - 2} \psi(\frac{T}{B^{z/y_b}}), \tag{4.6}$$

Here, the scaling function $\psi(x)$ is related to $\tilde{f}_F(x)$ as

$$\psi(x) = f'_M(x),$$

where $f'_M(x) = \partial f_M(x)/\partial x$ is the derivative respect to the variable $x = T/B^{z/y_b}$. Similarly, we find that the scaling form of the ac magnetic susceptibility is

$$\chi_{ac} = dM/dB = B^{(d+z)/y_b - 2} f_\chi(\frac{T}{B^{z/y_b}}), \tag{4.7}$$

with

$$f_\chi(x) = ((d+z)/y_b - 1)f_M(x) - z/y_b x f'_M(x),$$

and also

$$d\chi_{ac}/dT = B^{d/y_b-2}\phi(\frac{T}{B^{z/y_b}}), \tag{4.8}$$

where $\phi(x)$ is related to $f_\chi(x)$ as

$$\phi(x) = f'_\chi(x).$$

These scaling expressions can be directly tested using measurements of the field and temperature dependencies of the ac and dc magnetic susceptibilities, as shown in fig. 4.7. Both the dc and ac magnetic susceptibilities undergo excellent scaling collapses over almost four decades of the scaling parameter $T/B^{z/y_b}$. By comparing the scaled data in fig. 4.7 directly to relations 4.6 and 4.8, we determined that the scaling exponents $(d+z)/z$ and y_b/z have the values

$$\begin{cases} d/y_b - 2 \simeq -1.4 \\ \\ z/y_b \simeq 0.59 \end{cases}$$

This gives

$$\begin{cases} d/y_b \simeq z/y_b \simeq 0.59 \\ \\ d \simeq z \end{cases} \tag{4.9}$$

Relation 4.9 indicates the spatial dimension d is equal to the dynamical dimension z in YFe_2Al_{10} .

Now we derive the limiting critical behaviors using relation 4.9. For the $T \to 0$ field dependent magnetic susceptibility, equation 4.7 implies that

$$\chi_{ac} \to B^{-((d+z)/y_b-2)} f_\chi(0)$$

in the $T \to 0$ limit. Taking $f_\chi(0) \sim$ const, we have

$$\chi_{ac} \sim B^{-((d+z)/y_b-2)} = B^{-0.82}.$$

This value is just a little smaller than the one that we observed at 1.8 K, where $\chi_{ac} \sim B^{-0.95}$. However, we can see from fig. 4.6c that there is still some temperature dependence in high fields. This means that 1.8 K is not low enough temperature to fully reach the Fermi liquid state. The scaling analysis suggests that this critical exponent should approach 0.82 if we could measure the field dependent magnetic susceptibility at much lower temperatures.

We rewrite equation 4.8 as

$$\chi_{ac} = dM/dB = M = T^{(d+z)/z-2y_b/z}\tilde{\phi}(\frac{B}{T^{y_b/z}}). \tag{4.10}$$

and for the temperature dependence of $\chi(T)$ at $B \to 0$,

$$\chi_{ac} \to T^{(d+z)/z-2y_b/z}\tilde{\phi}(0).$$

Assuming that $\tilde{\phi}(0)$ has a constant value, then the $B = 0$ temperature divergence is found as

$$\chi_{ac} \propto T^{(d+z)/z-2y_b/z} = T^{-\gamma}.$$

Using the relation that $d = z$, and $d/y_b = 0.59$, we find that

$$\gamma = 2y_b/z - (d+z)/z = 1.4 \tag{4.11}$$

This is just what we observed in fig. 4.6a.

4.4.2 Scaling Function and Crossover Behaviors

Two observations prompted our adoption in YFe_2Al_{10} of a free energy that can be written as a function of $x = T/B^{z/y_b}$. First, we observed that, for $x \gg 1$ where $T \gg B$, the magnetization diverges as power law with decreasing temperature, and this implies that $f_M(x) \sim x^{-\gamma}$. However, in the other limit for $x \ll 1$ where $T \ll B$, the loss of temperature dependence in the magnetic susceptibility and specific heat C_M/T suggests that the system becomes Fermi liquid like, where $f_M(x)$ should be expandable as a power of x^2. Inspired by the scaling function proposed for β-$YbAlB_4$ in [20], we write the asymptotic behaviors of $f_M(x)$ as follows:

$$f_M(x) \propto \begin{cases} x^{-\gamma} & T \gg B, \text{ non-Fermi liquid} \\ \text{const} + O(x^2) & T \ll B, \text{ Fermi liquid.} \end{cases} \tag{4.12}$$

We will show that a specific function

$$f_M(x) = c(a^2 + x^2)^{-\gamma/2} \tag{4.13}$$

reproduces the limiting behaviors that we expect for large and small x, and as well leads to other functions that describe the specific heat and magnetization for intermediate values of x. We begin by writing the magnetization in terms

of this scaling function:

$$M = B^{(d+z)/y_b - 1} c(a^2 + x^2)^{-\gamma/2}. \tag{4.14}$$

The corresponding scaling functions for $d\chi_{dc}/dT$, and $d\chi_{ac}/dT$ are easily determined, and they are given by

$$\frac{d\chi_{dc}}{dT} = B^{d/y_b - 2}\psi(x) = -c\gamma B^{d/y_b - 2} x(a^2 + x^2)^{-\gamma/2-1}, \tag{4.15}$$

and

$$\frac{d\chi_{ac}}{dT} = B^{d/y_b - 2}\phi(x) = -c\gamma B^{d/y_b - 2} x(a^2 + x^2)^{-\gamma/2-2}(x^2 - a^2). \tag{4.16}$$

Here, a and c are the fitting parameters, and γ is the temperature dependent exponent of the magnetic susceptibility, as defined above. These scaling functions are compared to the scaled ac and dc magnetic susceptibilities in fig. 4.7 (red line). The agreement is excellent, and the fitting parameters are $a = 4.6, c = 1300$, and $\gamma = 1.4$.

As we have discussed above, the broad maximum observed in fig. 4.7 indicates the crossover from the quantum critical region to the heavy Fermi liquid state in high fields. Here, we are going to show that the crossover behaviors are quantitatively explained by the scaling function 4.14. The position of the peak in the magnetization dM/dT curve can be computed from the scaling function as

$$\frac{d}{dT}\left(\frac{dM}{dT}\right) = 0,$$

which gives that

$$T^*_{dc}/B^{z/y_b} = x = \sqrt{a^2/(\gamma + 1)} = 3. \tag{4.17}$$

A similar relation can also be worked out for the ac magnetic susceptibility χ_{ac}, although the overall quality of the data is less good than that of χ_{dc}, especially above 2 T. Unlike the dc magnetic susceptibility, the scaling curve of the ac magnetic susceptibility indicates that $d\chi_{ac}/dT$ approaches zero when $x = a$, and for smaller x, $d\chi_{ac}/dT$ becomes negative. This simply means that a peak appears in the ac susceptibility itself, and the peak positions would shift in fields like the scaling parameter:

$$T^*_{ac}/B^{z/y_b} = x = a = 4.6. \tag{4.18}$$

The peak and its field dependence is presented in fig. 4.10. The peak positions

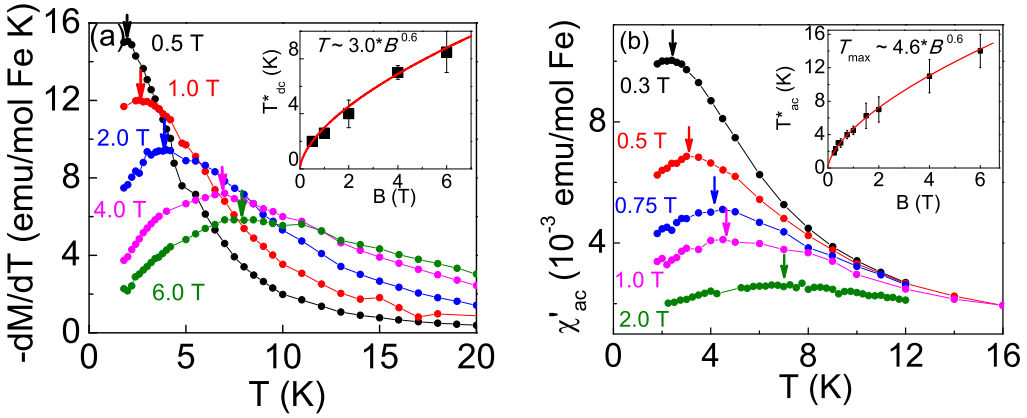

Figure 4.10: (a)Plots of $-dM/dT$ as a function of T in different fixed fields B. There are peaks in the temperature dependencies of dM/dT (a) and also in χ_{ac}=dM/dH (b) that shift to higher temperatures with increasing field, as indicated by the arrows. Inset: Peak position T^*_{dc} plotted as a function of B follows the scaling function 4.17 with $a = 4.6$, and $\gamma = 1.4$. (b) Plots of the temperature dependent ac magnetic susceptibility $\chi_{ac} = dM/dB$ in different magnetic fields B. Inset: Peak position T^*_{ac} plotted as a function of B follows the scaling function 4.18 with $a = 4.6$.

extracted from $-dM/dT$ and from the ac magnetic susceptibility χ_{ac} agree well with the predictions of equation 4.17 and 4.18, as indicated by the red lines in the insets of fig. 4.10a and fig. 4.10b.

4.4.3 Field Dependent Specific Heat

Our adoption of expressions 4.3, 4.12, and 4.13 for the free energy and magnetization lead to a satisfactory description of the magnetization data over a wide range of fields and temperatures. In principle, if this assumption of the singular part of the free energy indeed captures the quantum criticality of YFe_2Al_{10}, it should also lead to scaling of other measurable thermal quantities, such as the specific heat $C(B,T)$.

Let us start from the free energy, considering only the temperature derivatives. We can write the entropy S as

$$S(B,T) = -\frac{\partial F}{\partial T} = -B^{(d+z)/y_b - z/y_b} f'_F(x). \tag{4.19}$$

By taking another temperature derivative of the entropy S, we obtain the specific heat as

$$\frac{C(B,T)}{T} = \frac{\partial S}{\partial T} = -B^{(d+z)/y_b - 2z/y_b} f_F''(x).$$

Since $B = T^{y_b/z}$, we rewrite the function above as

$$C(B,T)/T = T^{(d+z)/z-2}\tilde{g}_F(\tilde{x}). \tag{4.20}$$

We have defined the scaling function $\tilde{g}_F(\tilde{x}) = -Trf_F''(x)$, where $x = T/B^{z/y_b}$, and $\tilde{x} = B/T^{y_b/z}$. Here, we need to be particularly careful regarding the treatment of the zero field contribution from the free energy F. Since the magnetic susceptibility comes from the field derivative of the free energy, any field independent part will disappear when the field derivatives are taken in equation 4.4. In contrast, the specific heat is the temperature derivative of the free energy, and it will have contributions from both the zero field part and the field dependent parts of the free energy.

We can expand the scaling function 4.20 around $B = 0$ thus $\tilde{x} = 0$ as

$$\frac{C(\tilde{x})}{T} = T^{(d+z)/z-2}\tilde{g}_F(\tilde{x}) = T^{(d+z)/z-2}(\tilde{g}_F(0) + a\tilde{x}\tilde{g}_F'(\tilde{x}) + a\tilde{x}^2\tilde{g}_F''(\tilde{x}) + \ldots) \tag{4.21}$$

$$= T^{(d+z)/z-2}(\tilde{g}_F(0) + \tilde{\varphi}(\tilde{x})) \tag{4.22}$$

In this way, it is possible to separate the zero field contribution

$$C(B=0,T)/T = T^{(d+z)/z-2}\tilde{g}_F(0) \tag{4.23}$$

from the entire specific heat $C(B,T)/T$, while generating a new scaling function $\tilde{\varphi}(\tilde{x})$ that describes only the field-dependent part of the specific heat C

$$C(B,T)/T - C(0,T)/T = T^{(d+z)/z-2}\tilde{\varphi}(\tilde{x}). \tag{4.24}$$

Now, the critical exponent that is related to the divergence of the specific heat $\alpha = 2 - (d+z)/z \sim 0$, so that using the results in relation 4.9, leads to

$$C(B,T)/T - C(0,T)/T = \tilde{\varphi}(\tilde{x}). \tag{4.25}$$

This suggests a particularly simple scaling of the field dependent specific heat for $B \neq 0$ as

$$\Delta C_M/T = C(B,T)/T - C(0,T)/T = \varphi(\frac{T}{B^{z/y_b}}). \tag{4.26}$$

This is just as was experimentally observed, as shown in fig.4.8 for fields as large as 7.0 T and for temperatures up to 10 K.

The scaling of the specific heat also follows from the Maxwell relation, which relates the entropy S to magnetization M directly as

$$\frac{\partial S(B,T)}{\partial B} = \frac{\partial M(B,T)}{\partial T}. \tag{4.27}$$

This implies an underlying relationship between the scaling functions that were separately obtained for the specific heat and the magnetization. By integrating both sides relative to the magnetic field B, one has that

$$\int_0^B \frac{\partial S(B,T)}{\partial B} dB = \int_0^B \frac{\partial M(B,T)}{\partial T} dB. \tag{4.28}$$

Since

$$\int_0^B \frac{\partial S(B,T)}{\partial B} dB = S(B,T) - S(0,T) = \int_0^T (\frac{C(B,T)}{T} - \frac{C(0,T)}{T}) dT, \tag{4.29}$$

and by inserting this in equation 4.28 before taking the temperature derivative on both sides, we find that

$$\frac{\Delta C_M}{T} = \frac{C(B,T)}{T} - \frac{C(0,T)}{T} = \frac{\partial^2}{\partial T^2} \int_0^B M(B,T) dB, \tag{4.30}$$

giving

$$\frac{\Delta C_M}{T} = \frac{\partial^2}{\partial T^2} \int_0^B B^{(2-\alpha)z/y_b - 1} f_M \left(\frac{T}{B^{z/y_b}} \right) dB = \varphi \left(\frac{T}{B^{z/y_b}} \right). \tag{4.31}$$

by inserting in equation 4.4. This scaling is the same as equation 4.26, but now the Maxwell relation allows us to relate the scaling function $\varphi(x)$ directly to the function $f_M(x)$ without knowing the specific form of the free energy. If we take the temperature derivatives before carrying out the integral, then equation above can be simplified as follows:

$$\frac{\Delta C_M}{T} = \varphi \left(\frac{T}{B^{z/y_b}} \right) = \int_0^B B^{-1} f''_M(x) dB, \tag{4.32}$$

where

$$f''_M(x) = \frac{\partial^2}{\partial x^2} f_M(x) = -c\gamma(a^2 + x^2)^{-\gamma/2-1}[1 - (\gamma+2)\frac{x^2}{x^2+a^2}].$$

The integral of the above function has no analytic form for $\gamma = 1.4$. Nonetheless, we can still obtain its limiting behaviors. For the Fermi liquid limit with $k_B T \ll g\mu_B B$, where $x = T/B^{z/y_b} \ll 1$, equation 4.32 can be simplified to the following:

$$\frac{\Delta C_M}{T} \simeq -c\gamma \int_0^B B^{-1}[a^2 - (\gamma/2+1)x^2]dB \simeq -ca^2\gamma logB + O(T^2). \quad (4.33)$$

This indicates that the specific heat measured at fixed low temperatures decreases logarithmically in high fields. This was experimentally demonstrated in fig. 4.8d. The second term of the order $O(T^2)$ suggests that the temperature dependent part is very weak for $T \ll B$, confirming that Fermi liquid behavior is regained in high fields at low temperatures.

Now, let's turn to the non-Fermi liquid limit as $B \ll T$, with $x \gg 1$. Here equation 4.32 becomes

$$\frac{\Delta C_M}{T} \simeq c\gamma(\gamma+1) \int_0^B B^{-1} x^{-\gamma-2} dB \backsimeq c\gamma(\gamma+1) B^2 T^{-\gamma}. \quad (4.34)$$

Equation 4.34 suggests an increase of the specific heat in small fields before the logarithmic decrease in higher fields. Fig. 4.8c shows that the implied peak in the field dependent C_M/T is indeed experimentally observed, confirming the crossover between the non-Fermi liquid behavior at low fields and high temperatures, and the Fermi liquid at high fields and low temperatures.

4.4.4 Zero Field Specific Heat

Up to now, the scaling seems to explain our experimental observations quite well. However, remember that we have separated the zero field part of the specific heat from the field dependent part of the specific heat. It is natural to ask whether our choice of free energy and the exponents α, γ and y_b/z that we determined from the scaling of the magnetization and the field-dependent part of the specific heat implies a particular form for the zero field specific heat. The answer is of course yes.

We have written the $B = 0$ specific heat $C(0,T)$ in terms of the scaling function f_C:

$$C(0,T)/T = T^{-\alpha} f_C(0) = T^0 f_C(0). \quad (4.35)$$

Based on the scaling we have described above, $\alpha \simeq 0$. Thus the logarithmic temperature divergence of $C(0,T)/T$ is more consistent with the experimental data $C_M(0,T)$ than the power law divergence. With this assumption, we are now in a position to propose a more specific function for the free energy as

follows:

$$F(B,T) = T^{2-\alpha} f_F(B/T_b^y/z) = F(0,T) + \int_0^B M(B,T)dB$$

$$= T^2 logT^2 + T^{2-\alpha} f(B/T^{y_b/z}) \tag{4.36}$$

Since magnetization is the field derivative of the free energy, only the second term of the free energy in 4.36 contributes to the magnetization. This term gives all the scaling of the susceptibility we showed before, and it also dominates the field dependence of the specific heat. However, for the zero field properties, the first term of the free energy dominates, although it does not contribute to the magnetic susceptibility at all.

Below in Table 4.1, we have summarized the temperature and field dependent behaviors of the measured properties in different limits as $T \gg B$, and $T \ll B$. We note that function 4.13 does provide an excellent description of the measured magnetic susceptibility and the field dependent specific heat, not only their limiting behaviors, but for intermediate values of the scaling parameter $T/B^{z/y_b}$ as well. We concur with the proposal in [20], which suggests the non-Fermi liquid quantum critical point can be connected to a Fermi liquid by the magnetic fields.

Table 4.1: The temperature and field dependent behaviors of the magnetization M, magnetic susceptibility χ, and the specific heat $C_M(B,T)/T$ in different limits as $T \gg B$, and $T \ll B$ (keeping only the leading terms). Here $d = z$, $z/y_b \simeq 0.59$, and $\gamma \simeq 1.4$ as defined above.

	M	χ	$C_M(B,T)/T$
$T \gg B$, nFL	$BT^{-\gamma}$	$T^{-\gamma}$	$-logT + B^2T^{-\gamma}$
$T \ll B$, FL	$B^{(d+z)/y_b-1}$	$B^{(d+z)/y_b-2}$	$-logB$

4.4.5 Magnetocaloric effect (MCE)

An important observation from the scaling analysis of YFe_2Al_{10} is that the spatial dimension d is equal to the dynamic scaling exponent z. The direct consequence of this is the logarithmic divergence of the zero field specific heat. Although this relation may not necessarily be found for other other quantum critical systems, logarithmic divergencies are reported in many heavy fermion systems when they are tuned to QCPs [10, 19, 20]. It has been argued that the universal behaviors around different QCPs can be established through

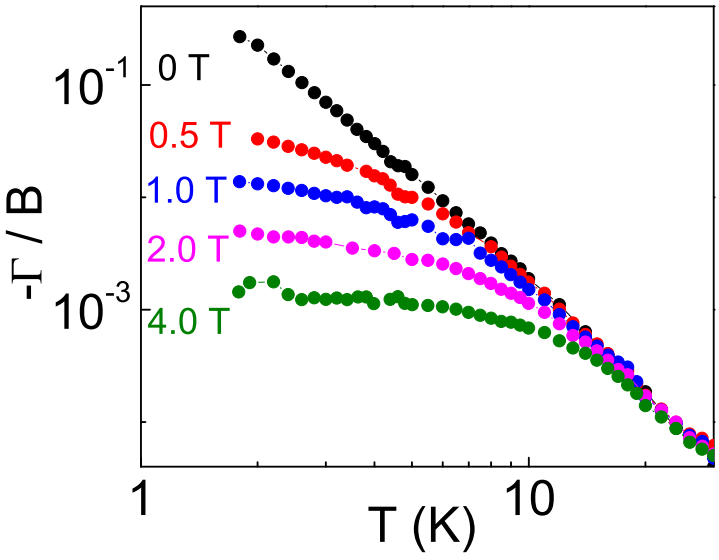

Figure 4.11: The calculated magnetocaloric effect Γ/B as a function of temperature at different fixed fields. Since the power law is much stronger than the logarithmic divergence, the overall magnetocaloric effect is divergent at low temperatures.

the Grüneisen ratio [93, 94]. For field tuned magnetic systems, the magnetic Grüneisen ratio is just the magnetocaloric effect (MCE) which diverges as [93]

$$\Gamma_{cr} = \frac{-(dM/dT)/T}{C/T} \propto \frac{1}{T^{1/\nu z}} = \frac{1}{T^{y_b/z}}. \tag{4.37}$$

Since we have a QCP at $B = 0$ in YFe_2Al_{10} , it is not practical to measure the zero field static magnetization M, and calculate Γ_{cr} using the equation above. However, it is possible to measure the magnetic susceptibility $\chi = dM/dB$ in the $B \to 0$ limit, and thus the field divided MCE diverges as

$$\Gamma/B = \frac{-(d(M/B)/dT)/T}{C(0,T)/T} \propto \frac{T^{-\gamma-2}}{logT} = \frac{T^{-2y_b/z}}{logT} \sim T^{-3.4}/logT. \tag{4.38}$$

Here, we have used the relation $\nu_b z = z/y_b = 0.6$ found in 4.9. Since the power law divergence is much stronger than logarithmic, the overall magnetocaloric effect is expected to be divergent at low temperatures. This is consistent with the experimental data, where the MCE is calculated indirectly from the measured ac magnetic susceptibility χ_{ac} with $B_{ac} = 4.17$ Oe and the measured specific heat$C(0,T)/T$ in zero fields (fig. 4.11).

On inspection of table 1.2, there does not seem to be a single model that describes the divergence of the MCE found for YFe_2Al_{10} , and the value of $\nu_b z = 0.6$ does not match any known AF-QCP ($z = 2, \nu_b = 1/2$) or FM-QCP ($z = 3, \nu_b = 1/2$) models [24, 25]. Since no long-ranged order is observed in YFe_2Al_{10} down to the lowest measured temperature 0.05 K, there is at present no way to determine the nature of the QCP. Experiments that use compositional variations to drive YFe_2Al_{10} through the QCP into the ordered phase would be most useful for resolving this issue. $LuFe_2Al_{10}$ and $YbFe_2Al_{10}$ are compounds from the same formula as YFe_2Al_{10} , and their properties are studied in the next sections.

4.4.6 Thermal Expansion

Our collaborators in the group of M. Brando in the Max Planck Institute for Chemical Physics in Dresden have also measured the thermal expansion of YFe_2Al_{10} in zero field [178]. Assuming that pressure P is another tuning parameter, we could add a similar scaling term to the free energy as

$$F(B,T) = T^2 log T^2 + B^{(d+z)/y_b} \tilde{f}_B(T/B^{z/y_b}) + P^{(d+z)/y_p} \tilde{f}_P(T/P^{z/y_p}). \quad (4.39)$$

Here y_p is the scaling dimension relate to the presssure P. The singularity of the thermal expansion is

$$\alpha = \frac{1}{V}\frac{\partial V}{\partial T} = \frac{1}{V}\frac{\partial^2 F}{\partial P \partial T} \propto T^{(d-y_p)/z}, \quad (4.40)$$

and thus

$$\alpha/T \propto T^{(d-y_p)/z-1} = T^{-y_p/z}. \quad (4.41)$$

Here, we have again used the relation $d = z$ for YFe_2Al_{10} .

Shown in fig. 4.12 is the temperature dependent thermal expansion α of YFe_2Al_{10} measured in different fields along the crystal a direction. A weak upturn was observed at low temperatures, and no significant field dependencies were observed. The log-log plot of the thermal expansivity divided by temperature α/T was plotted in fig. 4.13, and divergent behaviors were observed below about 1 K. Power law fits were made for three different fields, and the fitted exponents are 1.25 for $B = 0$ T, 1.55 for $B = 0.5$ T, and 1.65 for $B = 7$ T. The slight differences are likely to reflect experimental errors, and we have averaged these three values to 1.5 ± 0.2 as indicated in fig. 4.13b. If we assume that YFe_2Al_{10} is located just at the critical point with $P = 0$, we could then compare this experimentally observed divergent thermal

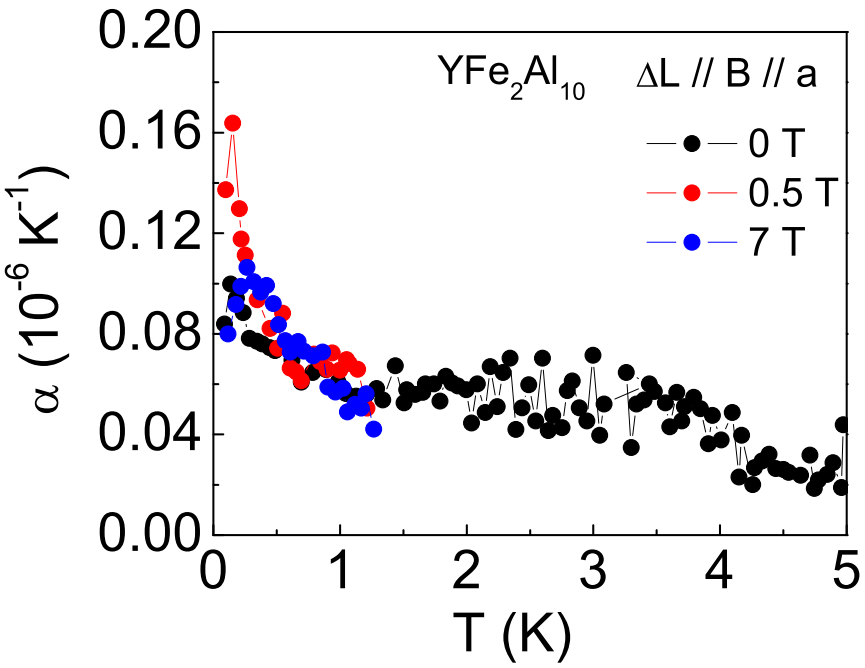

Figure 4.12: As measured thermal expansivity α of YFe_2Al_{10} as function of temperature in different magnetic fields. A small upturn was observed at low temperatures, but otherwise α is field independent. (Figure is courtesy of Manuel Brando [178].)

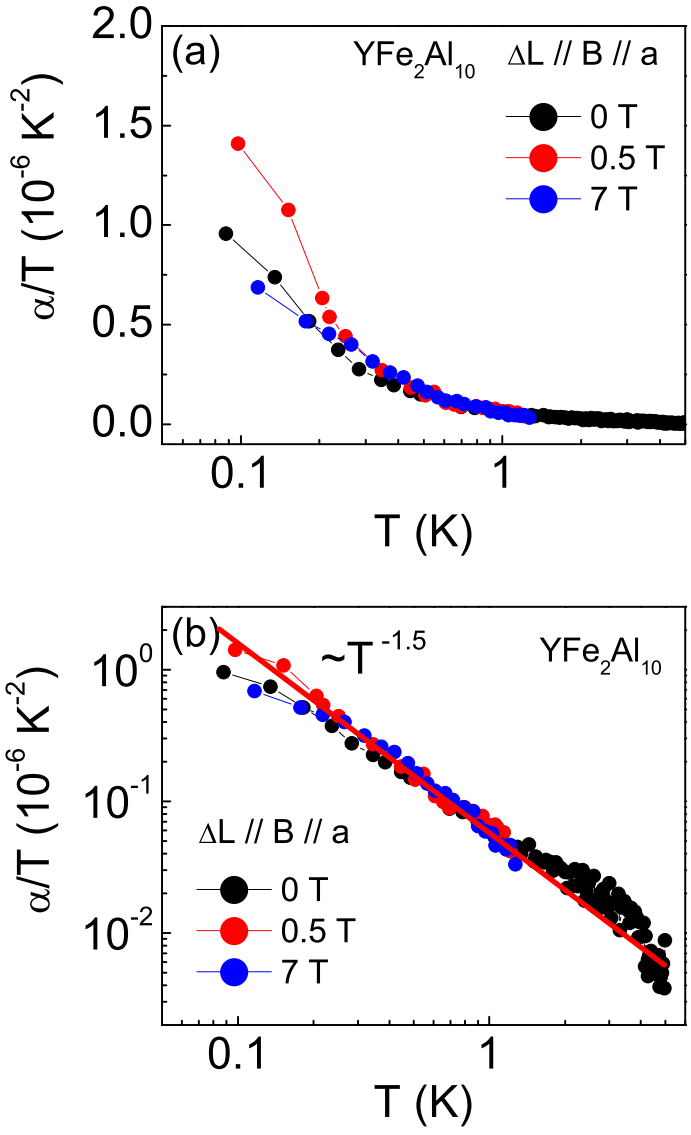

Figure 4.13: (a)Temperature dependent thermal expansivity α/T of YFe_2Al_{10} measured in magnetic fields as indicated. (b) Log-log plot of the thermal expansio α/T of YFe_2Al_{10} . A power law divergence was observed at low temperatures with $\alpha/T \sim T^{-1.5}$. (Figure is courtesy of Manuel Brando [178].)

expansion

$$\alpha/T \sim T^{-1.5} \tag{4.42}$$

to equation 4.41, and we find that

$$y_p/z = 1.5$$

for YFe_2Al_{10} . The divergence of the thermal expansion indicates that it may be interesting to pursue some pressure experiments in the future.

We mention that no significant field dependencies were observed in the thermal expansivity α. Since there are no terms that couple field and pressure in the free energy 4.39, the only property that could be affected by field B is the conjugate magnetization M. This is similar to what was observed in the organic compounds κ-(BEDT-TTF)$_2X$ [50, 179]. With field B, the magnetic properties of the ordered insulating states may change, but the MIT phase line and the critical end point are not affected at all in this system.

4.5 Magnetic Properties of $LuFe_2Al_{10}$

4.5.1 Magnetization

Temperature Dependent Magnetization

Shown in fig. 4.14a is the temperature dependent dc magnetic susceptibility of $LuFe_2Al_{10}$ measured in fields along the three principal crystal axes from 1.8 K to 300 K. Similar to YFe_2Al_{10} , anisotropy was observed among the measurements with fields in different directions. The most divergent direction is still the a axis. We also noticed that although $\chi_{B\|a} > \chi_{B\|c} > \chi_{B\|b}$ at low temperatures, it turns out that $\chi_{B\|a} < \chi_{B\|c} < \chi_{B\|b}$ at high temperatures. Another significant feature is that power law behavior with $\chi_{B\|a} \sim T^{-\gamma}(\gamma = 0.57)$ was observed at low temperatures as indicated in fig. 4.14b. This power law divergence was suppressed with increasing fields, and a Fermi liquid like state with temperature independent susceptibility at low temperatures was observed. Although the overall trend of the magnetic susceptibility in $LuFe_2Al_{10}$ is similar to what we observed in YFe_2Al_{10} , two things are different. First, the critical exponent from the magnetic susceptibility in $LuFe_2Al_{10}$ is $\gamma = 0.57$, which is much smaller than the one we observed in YFe_2Al_{10} where $\gamma = 1.4$ for $B\|a$. Second, the magnitude of the magnetic susceptibility at low temperatures in $LuFe_2Al_{10}$ is much smaller than the one we measured in YFe_2Al_{10} . These results indicate that if YFe_2Al_{10} is very close to a QCP, then $LuFe_2Al_{10}$ may be somewhat farther from the

same QCP. The similarities between the observed behaviors suggest that the magnetic properties in $LuFe_2Al_{10}$ may be dominated by the same type of critical fluctuations.

Field Dependent Magnetization

We have measured the field dependent dc magnetization of $LuFe_2Al_{10}$ at different temperatures up to 100 K (fig. 4.15a). The highest field ($B = 7$ T) magnetization at 1.8 K is about $0.004\mu_B$/Fe. If we assume the measured magnetization comes from some Fe local moments related to vacancies or other defects, then the estimated ratio for such Fe moments must less than $0.004/5 \approx 0.08\%$ (for Fe^{3+}: $\mu_{\text{eff}} = 5.9\mu_B$, for Fe^{2+}: $\mu_{\text{eff}} = 5.4\mu_B$). This gives the upper limit for any impurity or site disorder scenarios.

There is additional evidence that this measured magnetization cannot come from local moment impurities. We have already seen that even at the lowest measured temperature 1.8 K, the magnetization curve did not saturate below 7.0 T. We re-plotted the same data in fig. 4.15a as function of B/T, as shown in fig. 4.15b. The isotherms of the field dependent magnetization do not saturate or collapse on to each other at all. The red solid line is the scaled Brillouin function, assuming localized moments with spin $S = 1/2$. The measured magnetization curves can not be described by the Brillouin function. This observation rules out the possibility that contamination by localized moments is responsible for the measured magnetization. Similar to what we found in YFe_2Al_{10} , this suggests that interactions are also important in $LuFe_2Al_{10}$.

Scaling of the Magnetic Susceptibility

We try to understand the magnetic susceptibility in $LuFe_2Al_{10}$ using the critical scaling analysis. As we have shown earlier in YFe_2Al_{10} , where scalings of the magnetic susceptibility χ as functions of $T/B^{0.6}$

$$-\frac{d\chi}{dT}B^{1.4} = \phi(\frac{T}{B^{0.6}})$$

were observed in different fields and temperatures. We have tried the same scaling in $LuFe_2Al_{10}$ for the temperature derivative of the dc magnetic susceptibility $\chi_{dc} = M/B$ at temperatures from 1.8 K to 30 K in fields up to 6.0 T as functions of the scaling variable $T/B^{0.6}$. Note that the very small magnitude of $\chi_{ac} = dM/dB$ in YFe_2Al_{10} limits our analysis to the dc susceptibility $\chi_{dc} = M/B$. However, as shown in fig. 4.16, the measured magnetic susceptibility curves do not undergo a scaling collapse, and the scaling function shown above does not describes the data well at all. So

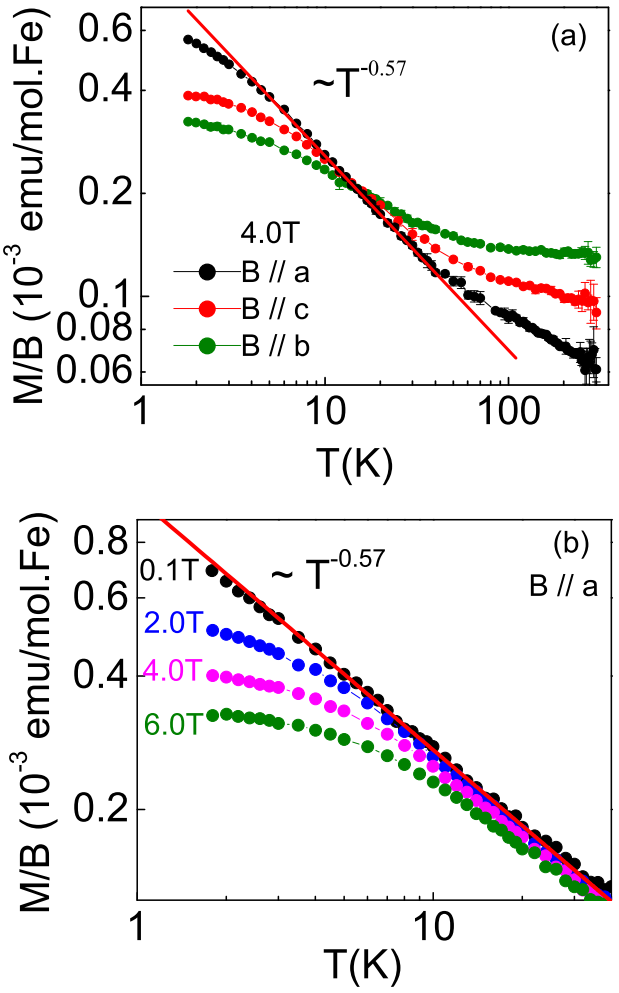

Figure 4.14: (a)Temperature dependent dc magnetic susceptibility $\chi_{dc} = M/B$ of $LuFe_2Al_{10}$ measured in 4.0 T with field along the three principal crystal axes as indicated. (b) Temperature dependence of the dc magnetic susceptibility $\chi_{dc} = M/B$ in magnetic fields along the a axis from 0.1 T to 6.0 T. The magnetic susceptibility is most divergent with fields along the a direction, where a power law behavior $\chi_{dc} \sim T^{-0.57}$ is found, as indicated by the red lines.

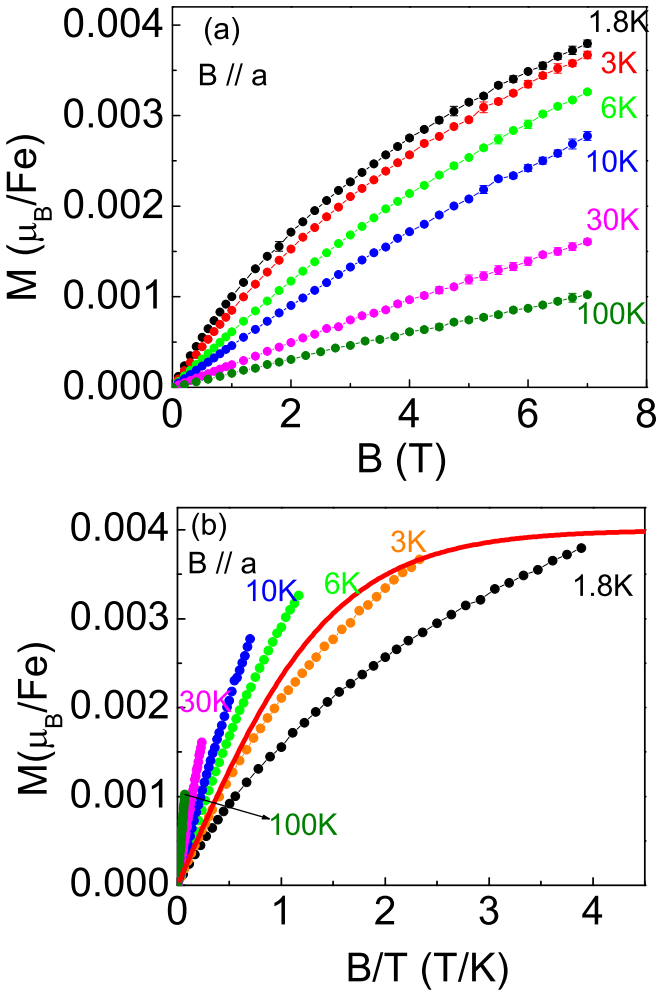

Figure 4.15: (a) Magnetic field dependent magnetization M of $LuFe_2Al_{10}$ measured at different temperatures from 1.8 K to 100 K. (b) The field dependent magnetization M at different temperatures as functions of B/T. The red line is the re-scaled Brillouin function assuming independent local moments with spin $S = 1/2$.

does this suggest that the critical fluctuations in $LuFe_2Al_{10}$ are different from those that we have seen in YFe_2Al_{10} ? Since the magnetic properties of $LuFe_2Al_{10}$ resemble those of YFe_2Al_{10} , we still have reason to believe that these two materials may be linked to the same QCP. Then why does the same scaling fail in $LuFe_2Al_{10}$?

The answer is as following. The observed scaling variable $T/B^{0.6}$ determined by $z/y_b \simeq 0.6$ in YFe_2Al_{10} is not necessarily valid for $LuFe_2Al_{10}$. To find the corresponding value of z/y_b for $LuFe_2Al_{10}$, we can start from the exponent γ of the temperature divergent magnetic susceptibility. We know from the definition of γ that in $LuFe_2Al_{10}$

$$\gamma = 2y_b/z - (d+z)/z = 0.57$$

different from $\gamma = 1.4$ in YFe_2Al_{10} . Since the spatial dimension d and the dynamical exponent z are determined by the nature of the QCP itself at $B = 0$, and they are not field dependent, it is thus reasonable to take $d = z$ in $LuFe_2Al_{10}$ as in YFe_2Al_{10} . In this way, the different value of γ in $LuFe_2Al_{10}$ is caused by a different value of z/y_b, where

$$\frac{z}{y_b} = \frac{2}{0.57 + (d+z)/z} \simeq 0.78.$$

The scaling analysis we demonstrated in YFe_2Al_{10} still applies, and the scaling function for $LuFe_2Al_{10}$ now becomes

$$\frac{d\chi}{dT} = B^{d/y_b-2}\psi(\frac{T}{B^{z/y_b}}) \Rightarrow \frac{d\chi}{dT} = B^{-1.22}\psi(\frac{T}{B^{0.78}}). \tag{4.43}$$

This new scaling of the dc magnetic susceptibility of $LuFe_2Al_{10}$ is plotted in fig. 4.17. Both the log-log and semi-log plots show well behaved scaling for temperatures from 1.8 K to 30 K in fields up to 6.0 T. The red solid line is the fit using the same function that are proposed earlier

$$\frac{d\chi_{dc}}{dT} = -c\gamma B^{d/y_b-2}x(a^2+x^2)^{-\gamma/2-1},$$

with modified fitting parameter $a = 1.5$, and $c = 9$, where $\gamma = 0.57, x = T/B^{z/y_b} = T/B^{0.78}$. Similar to the scaling curve observed in YFe_2Al_{10} , a broad maximum in $d\chi/dT$ was observed, which indicates the crossover behavior from the low field ($T \gg B$) quantum critical region to the high field ($k_BT \ll g\mu_BB$) Fermi liquid state. The position of this crossover is determined by the fitting parameter a, and its value is smaller than the one we found for YFe_2Al_{10} . We also noticed that the fitting parameter c here in $LuFe_2Al_{10}$ is much smaller

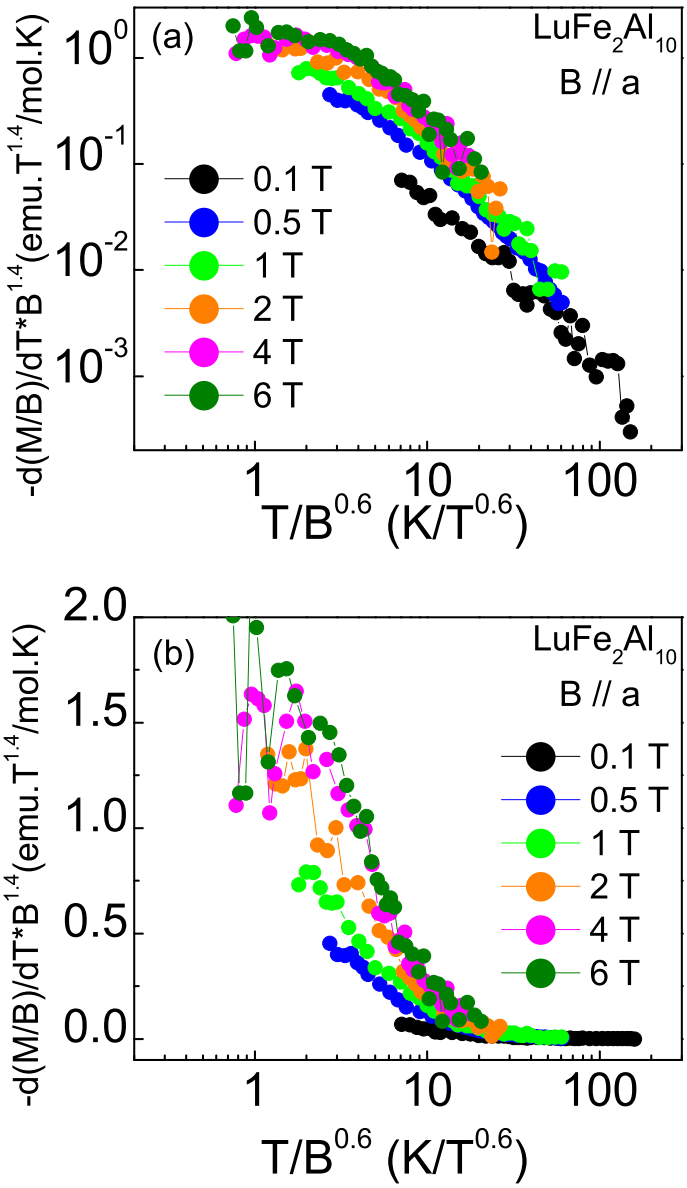

Figure 4.16: Log-log plot (a) and semi-log plot (b) of the scaling curve of the dc magnetic susceptibility $\chi_{dc} = M/B$ at temperatures from 1.8 K to 30 K in fields up to 6.0 T as function of the scaling variable $T/B^{0.6}$.

than the value in the fitting of YFe_2Al_{10} , where $c \simeq 1300$. This means that the overall magnetic susceptibility in $LuFe_2Al_{10}$ is about two orders of magnitude weaker than that of YFe_2Al_{10} , suggesting $LuFe_2Al_{10}$ may be located much farther away from the QCP than YFe_2Al_{10} .

Despite the differences in the values of the fitting parameters, the overall scaling behaviors of YFe_2Al_{10} and $LuFe_2Al_{10}$ can be explained in the same way. More importantly, the relation between the spatial dimension d and the dynamical scaling exponent z

$$d = z$$

is likely valid. Since this relation is not dependent on the tuning parameter field B, it may represent the intrinsic nature of the QCP that governs the low temperature properties of YFe_2Al_{10} and $LuFe_2Al_{10}$.

4.5.2 Specific Heat

A direct consequence of the relation $d = z$ is that the temperature dependent specific heat should follow:

$$C/T = \partial^2 F/\partial T^2 \sim T^{d/z-1} = T^0,$$

and the temperature divergence of the zero field specific heat can be at most logarithmic. As was shown in fig. 4.18, the specific heat of $LuFe_2Al_{10}$ in zero field does indicate a logarithmic divergence below about 3 K. This small upturn was suppressed in high fields, and finally the expected Fermi liquid state was reached in fields as large as 9.0 T, where approximately constant values of C/T were observed below about 2 K. Compared to the specific heat in YFe_2Al_{10} , the magnitude of the divergence in specific heat in $LuFe_2Al_{10}$ is much weaker.

4.6 Magnetic Properties of $YbFe_2Al_{10}$

In the above sections, we have discussed the magnetic properties of the materials YFe_2Al_{10} , and $LuFe_2Al_{10}$. Both of their properties can be described by critical scaling functions. Based on the scaling analyses, we conclude that $LuFe_2Al_{10}$ is further away from the critical point than YFe_2Al_{10} . It is thus worthwhile to study a third isostructural compound to trace the trend of quantum criticality in this family of compounds.

It was reported that $YbFe_2Al_{10}$ is also located close to the QCP, where non-Fermi liquid behaviors have been observed in polycrystalline samples [180, 181]. Our studies here are performed on $YbFe_2Al_{10}$ single crystal samples, and different behaviors were observed.

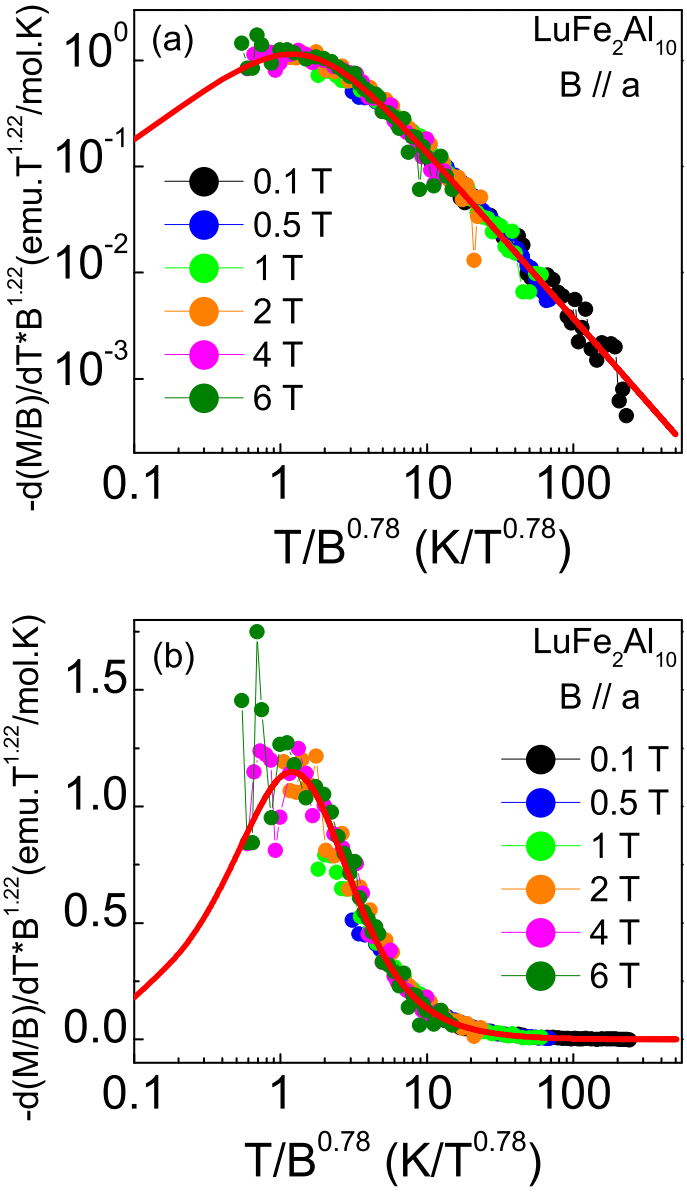

Figure 4.17: Log-log plot (a) and semi-log plot (b) of the scaling curve of the dc magnetic susceptibility $\chi_{dc} = M/B$ at temperatures from 1.8 K to 30 K in fields up to 6.0 T as function of the scaling variable $T/B^{0.78}$. The red line is the fitting as explained in the text.

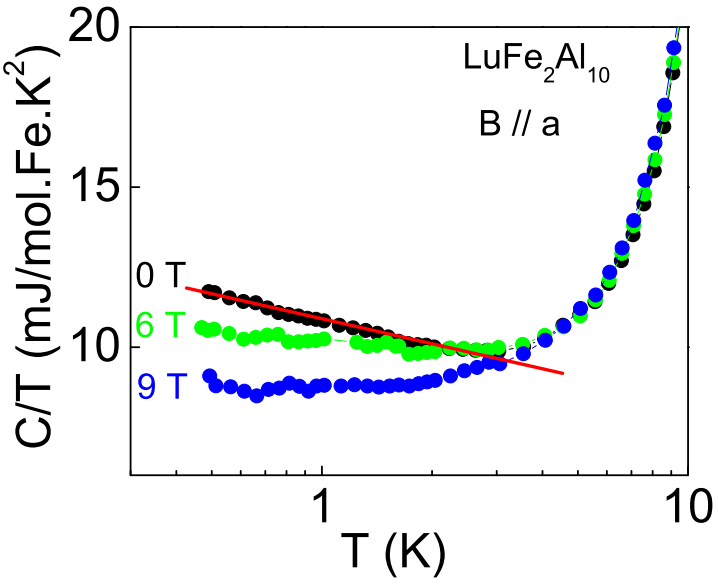

Figure 4.18: Measured specific heat of $LuFe_2Al_{10}$ in different fields from 0 T to 9 T. The red line implies the logarithmic temperature dependence.

4.6.1 Magnetization

Shown in fig. 4.19 is the temperature dependent magnetization of $YbFe_2Al_{10}$ measured in 1.0 T with the field along the crystal a axis. The dc magnetic susceptibility first decreases with increasing temperature, and a small upturn was observed at low temperatures. With increasing temperature, the dc magnetization starts to increase at about 50 K, and a broad maximum was then observed, centered around 410 K. This maximum has been identified as a characteristic feature for mixed-valence materials, and the maximum position provide an approximate temperature scale T_{sf} for the spin excitations [182, 183]. This kind of valence fluctuation behavior is usually observed in rare earth based compounds, where the $4f$ level is located very close to the Fermi energy [182, 183]. For $YbFe_2Al_{10}$, the Yb moments fluctuate between the non-magnetic Yb^{2+} ($4f^{14}$) ground state and the magnetic Yb^{3+} ($4f^{13}$) excited state where the total angular momentum $J = 7/2$, with effective moment $\mu_{eff} \simeq 4.5\mu_B$. Assuming the excitation energy between these two states is $E_{\rm exc}$, the measured susceptibility could be expressed as [182, 183]

$$\chi(T) = \frac{C * p(T)}{T + T_{sf}} + \chi_0, \tag{4.44}$$

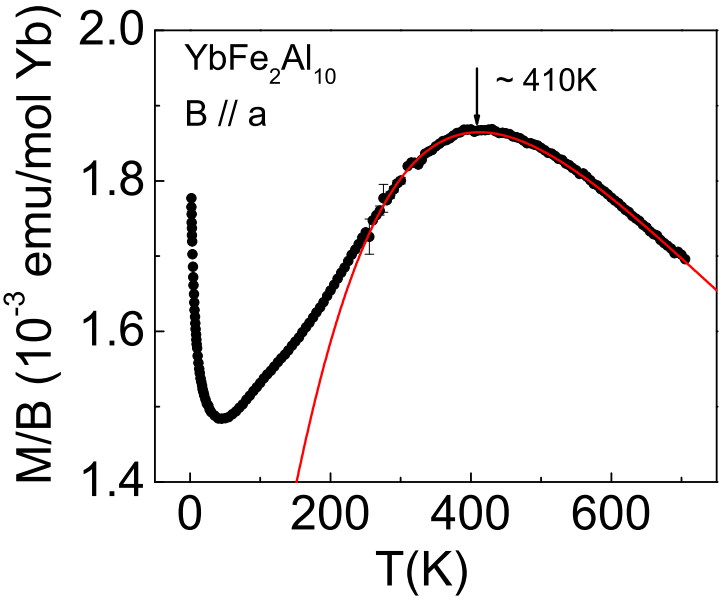

Figure 4.19: Temperature dependent magnetization of $YbFe_2Al_{10}$ with field 1.0 T along the crystal a axis. A broad maximum was observed around 410 K. The red line is the fit as explained in the text.

where $p(T)$ is the fractional occupancy of the excited magnetic Yb^{3+} ($4f^{13}$) state, with

$$p(T) = \frac{8}{8 + exp(E_{exc}/(T + T_{sf}))}. \tag{4.45}$$

Here, C is the Curie constant, which is equal to 2.59 for Yb^{3+} ($\mu_{\text{eff}} = 4.54$), χ_0 is the temperature independent susceptibility, T_{sf} is the spin fluctuation temperature, which characterizes the broadening of the $4f$ electron level induced by the hybridization between the conduction electrons. The red line shown in fig. 4.19 is a typical fit based on expression 4.44 with the fitting parameters $E_{\text{exc}} = 1448.6$ K, $T_{\text{sf}} = 298.2$ K, and $\chi_0 = 5.0 \times 10^{-6}$emu/mol.Yb. Based on this fitting, we estimate that the effective Yb moments are about $\mu_{eff} \simeq 0.3\mu_B$ at temperatures below 10 K, making only a very small contribution to the magnetic properties of $YbFe_2Al_{10}$. The weak upturn in the magnetic susceptibility at low temperatures is too weak to be fitted with the power law, and it is unclear whether it is intrinsic or if it may from some sort of magnetic contamination.

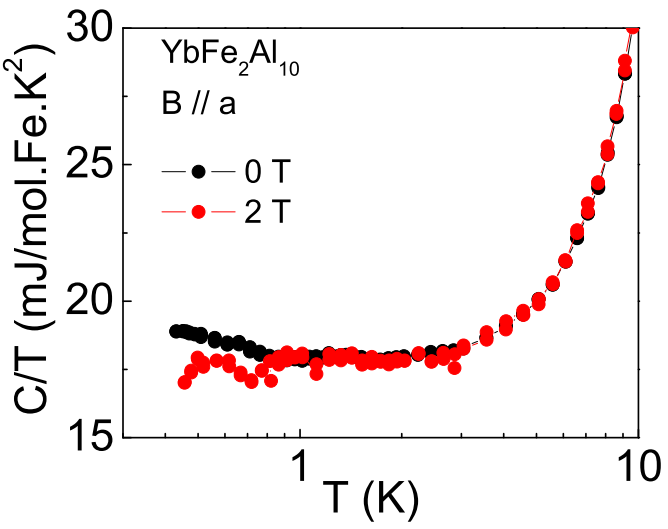

Figure 4.20: Temperature dependent specific heat of $YbFe_2Al_{10}$ measured in 0 T and 2 T with field along the crystal a axis.

4.6.2 Specific Heat

The as measured specific heat of $YbFe_2Al_{10}$ is shown in fig. 4.20. A logarithmic divergence has been observed in [180, 181] on polycrystalline samples, and it has been claimed that $YbFe_2Al_{10}$ may be close to an antiferromagnetic (AF) QCP. However, no strong divergence was observed in our $B = 0$ specific heat on YFe_2Al_{10} single crystal samples. A weak upturn was seen below about 0.8 K in the temperature dependent C/T curve, which was further suppressed in an applied field of about 2.0 T along the crystal a direction. C/T is almost constant at low temperatures in fields, indicating a Fermi liquid state with the Sommerfeld coefficient $\gamma \sim 18$ mJ/mol.Fe.K^2.

Based on the magnetization and specific heat measurements, we conclude that $YbFe_2Al_{10}$ is a Yb-based mixed-valence compound. No significant critical or non-Fermi liquid behaviors were observed, and we consider that $YbFe_2Al_{10}$ is very far away from the QCP in the phase space that is jointly inhabited by the compounds YFe_2Al_{10} and $LuFe_2Al_{10}$.

4.7 Comparing YFe_2Al_{10} , $LuFe_2Al_{10}$, and $YbFe_2Al_{10}$

In the above sections, we have discussed the magnetic properties of YFe_2Al_{10} , $LuFe_2Al_{10}$, and $YbFe_2Al_{10}$. Here, we summarize the main properties of these three materials, and discuss these observations in the larger context of quantum critical systems, to have a more complete understanding of this family of compounds.

4.7.1 Magnetization

Plotted in fig. 4.21 are the temperature dependent magnetic susceptibilities of YFe_2Al_{10} , $LuFe_2Al_{10}$ and $YbFe_2Al_{10}$ with fields along the crystal a axes. YFe_2Al_{10} has the strongest divergence ($\chi \sim T^{-1.4}$), and the magnitude of the magnetic susceptibility in YFe_2Al_{10} is almost two orders higher than that observed in $LuFe_2Al_{10}$. Despite the greatly reduced magnitude, the overall behavior of the magnetic susceptibility in $LuFe_2Al_{10}$ is very similar to that in YFe_2Al_{10} , and a power law like behavior with $\chi \sim T^{-0.57}$ was observed at low temperatures. The overall magnetic susceptibility in $YbFe_2Al_{10}$ is almost temperature independent in the log-log plot, with a broad maximum at 410 K indicating valence fluctuations. Although $YbFe_2Al_{10}$ is the only member of these three compounds that has magnetic rare earth (Yb) ions, the magnitude of the magnetic susceptibility in $YbFe_2Al_{10}$ is still more than one order of magnitude smaller than the one in YFe_2Al_{10} at low temperatures. This is consistent with our discussion above that $YbFe_2Al_{10}$ is a mixed valence compound, and the Yb ions are essentially nonmagnetic as $T \to 0$.

4.7.2 Specific Heat

Shown in fig. 4.22 are the specific heats of YFe_2Al_{10} , $LuFe_2Al_{10}$, and $YbFe_2Al_{10}$ in zero fields. From fig. 4.22, we can see that the magnitude of the low temperature specific heat goes as $C/T_{YFe_2Al_{10}} > C/T_{YbFe_2Al_{10}} > C/T_{LuFe_2Al_{10}}$. Like the magnetic susceptibility, the specific heat of $YbFe_2Al_{10}$ is nearly temperature independent at low temperatures, indicating that interactions in $YbFe_2Al_{10}$ are very weak, and that $YbFe_2Al_{10}$ should be considered as a simple metal with minimal mass enhancement. These overall behaviors are consistent with the magnetic susceptibility measurements shown in fig. 4.21, where YFe_2Al_{10} has the strongest fluctuations, and so is located closest to the QCP, while $LuFe_2Al_{10}$ is a little further away from this QCP, and $YbFe_2Al_{10}$ is so far from the QCP, that it appears to have no quantum

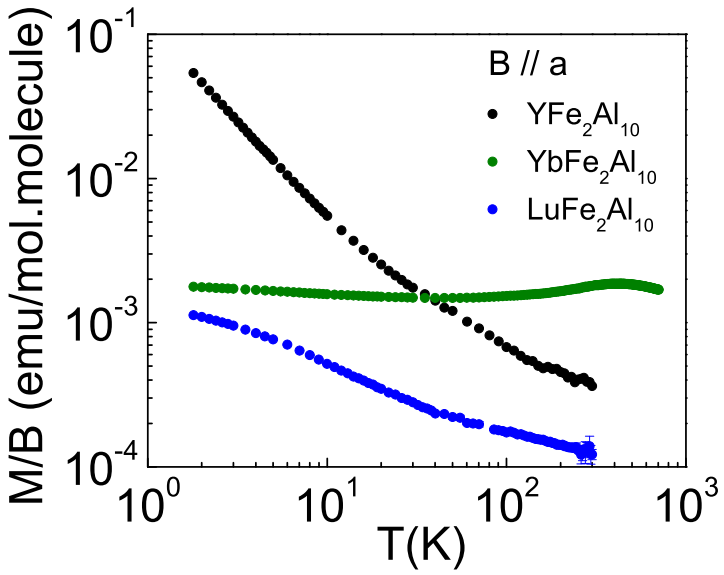

Figure 4.21: Temperature dependent magnetic susceptibility of YFe_2Al_{10} , $LuFe_2Al_{10}$ and $YbFe_2Al_{10}$ with field along the crystal a axis. YFe_2Al_{10} has the strongest divergence at the whole temperature range comparing to $LuFe_2Al_{10}$ and $YbFe_2Al_{10}$.

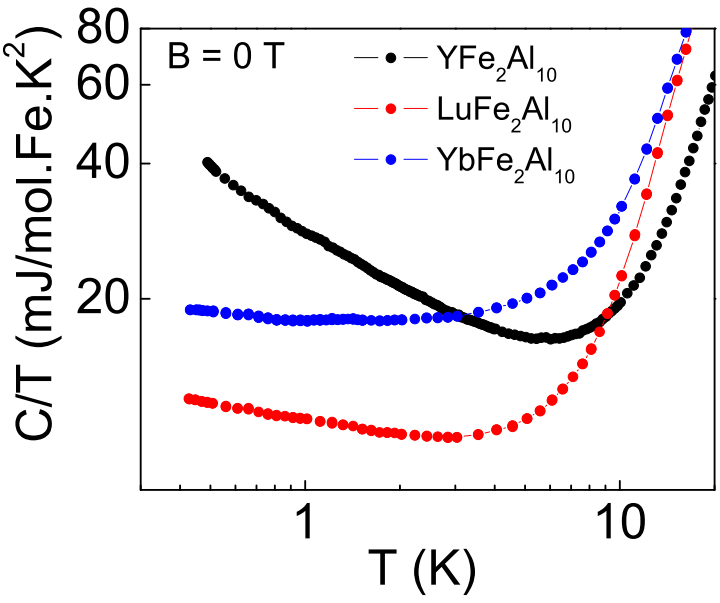

Figure 4.22: Plot of the temperature dependent zero field specific heat of YFe_2Al_{10} , $LuFe_2Al_{10}$ and $YbFe_2Al_{10}$ as indicated.

critical behaviors at all.

4.7.3 Resistivity

Shown in fig. 4.23 is the plot of the $B = 0$ resistivity of the three materials YFe_2Al_{10} , $LuFe_2Al_{10}$, and $YbFe_2Al_{10}$ from 0.4 K to 300 K. YFe_2Al_{10} has the highest value of the residual resistivity ($\rho_0 \simeq 75\mu\Omega$ cm at 0.4 K). In addition, a small upturn was observed at low temperatures. However, $YbFe_2Al_{10}$ has the lowest residual resistivity ($\rho_0 \simeq 5\mu\Omega$ cm at 0.4 K), and no upturn was observed down to 0.4 K. The resistivity of $LuFe_2Al_{10}$ is in between the observed values of YFe_2Al_{10} and $YbFe_2Al_{10}$. On the basis of these resistivity data, one may suspect that YFe_2Al_{10} may not be a good metal, and hypothetically this could reflect bad sample quality. However, we argue here that the upturn behaviors seen in YFe_2Al_{10} resistivity is likely to be intrinsic and should be considered to be the consequence of the dominant critical fluctuations.

Different samples give different ratios of $R_{300K}/R_{0.4K}$, which is a conventional measure of sample quality in metals. This differences could be compensated by rescaling the magnitude of the different measured resistivities. As shown in fig. 4.23a, the measured $\rho(T)$ for $LuFe_2Al_{10}$ and $YbFe_2Al_{10}$ can be scaled to closely resemble that of YFe_2Al_{10} from $\sim 40 - 300$ K (fig. 4.23b).

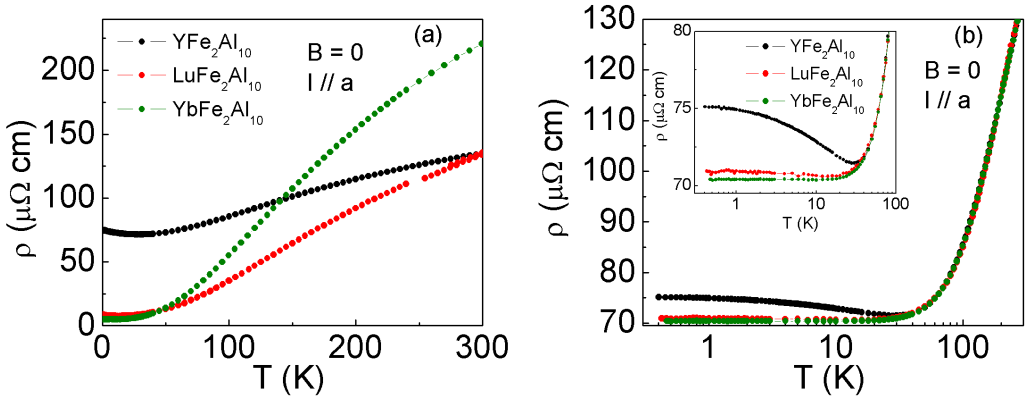

Figure 4.23: (a) Temperature dependent resistivity of YFe_2Al_{10} , $LuFe_2Al_{10}$ and $YbFe_2Al_{10}$ measured in zero field from 0.4 K up to 300 K. (b) As measured resistivity of YFe_2Al_{10} , and the scaled resistivity of $LuFe_2Al_{10}$ and $YbFe_2Al_{10}$ according to YFe_2Al_{10} . All the three curves behave in the same way from 300 K down to about 40 K, where upturns were seen in YFe_2Al_{10} . Inset: An expanded view of the resistivity upturn at low temperatures.

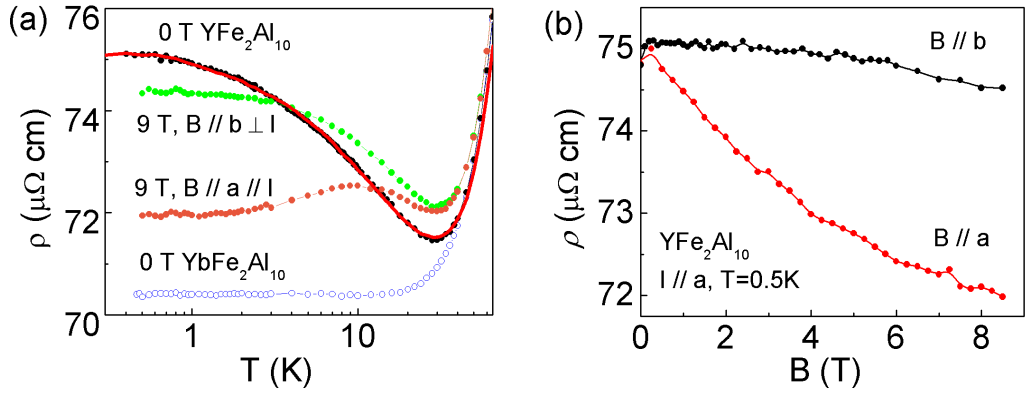

Figure 4.24: (a) As-measured electrical resistivity $\rho(T)$ for YFe_2Al_{10} (•) and scaled resistivity of $YbFe_2Al_{10}$ (○), comparing with data taken with a 9 T magnetic field oriented both parallel to the a and b axes (as indicated). Red dashed lines indicate fits to the Kondo expression described in the text. (b) Field dependent electrical resistivity $\rho(T)$ for YFe_2Al_{10} measured at 0.5 K for both $B\|a$, and $B\|b$ directions, as indicated. [78]

All three of these scaled resistivity curves behave in almost exactly same way at high temperatures. However, below 40 K, the resistivity in YFe_2Al_{10} , $LuFe_2Al_{10}$ and $YbFe_2Al_{10}$ become different from each other, as seen from the expanded view of the low temperatures in fig. 4.23b. The resistivity of $YbFe_2Al_{10}$ decreases monotonically with decreasing temperature, and it is almost temperature independent below about 10 K. This is just as expected in mixed valence systems like $YbFe_2Al_{10}$, where the Yb moments are almost fully compensated at low temperatures. The resistivity in $LuFe_2Al_{10}$ is slightly different from that of $YbFe_2Al_{10}$, showing a weak upturn below about 10 K. This weak upturn becomes stronger in YFe_2Al_{10} , and the resistivity in YFe_2Al_{10} clearly increases with decreasing temperature below 40 K. If we assume this kind of increase at low temperature resistivity is due to the Kondo effect caused by rare earth local moments, we could estimate the total change of resistivity $\Delta\rho(T) = \rho(T)_{YFe_2Al_{10}} - \rho(T)_{YbFe_2Al_{10}}$ that provides the low-temperature upturn in YFe_2Al_{10} using the measured resistivity of isoelectronic and isostructural YFe_2Al_{10} compound as background. This low temperature upturn was fitted with Kondo the expression [184], where

$$\rho = \rho_0 \left(1 - \frac{ln(T/T_K)}{[(ln(T/T_K))^2 + \pi^2 S(S+1)]^{1/2}}\right) \tag{4.46}$$

A good fitting was observed for the $B = 0$ data with the Kondo temperature $T_K = 20 \pm 1$ K in fig. 4.24a. We have also investigated the anisotropy with magnetic fields parallel to both the a and b axes on $\rho(T)$. As shown in fig. 4.24b, and the magnitude of the upturn resistivity is decreased with increasing field. Substantial anisotropy is observed when a 9 T field is applied parallel to the a and b axes. The anisotropic Kondo effect has been observed in the system (La, Ce)B_6, where there is an electric quadrupole moment related to the rare earth Ce ions [185]. However, there are a few things that are different in the field dependent magnetoresistivity of YFe_2Al_{10} . First, the transverse magnetoresistance ($B \perp I$) was observed to be stronger than the longitudinal magnetoresistance ($B \| I$) in the system (La,Ce)B_6, which is in contrast to our observation here in YFe_2Al_{10} . Second, the relative difference of the magnetoresistivity

$$\Delta\rho_{\perp\|}/(\rho(0) - \rho_0) = (\rho_\perp(T) - \rho_\|(T)/(\rho(0) - \rho_0)$$

amounts up to $\sim$ 8% for (La,Ce)B_6 [185]. However, this anisotropic magnetoresistivity is up to $\Delta\rho_{\perp\|}/(\rho(0) - \rho_0) = (74.3 - 71.94)/(75.1 - 70.4) \simeq 50\%$ for $B = 9$ T in YFe_2Al_{10} , which is much higher than the effect that one would expect from the anisotropic angular momentum of a small number of

rare earth impurities. Third, the negative magnetoresistivity is expected to be isotropic in the high field limit. Accordingly, no difference was observed in the magnetoresistance of (La,Ce)B_6 when $B \geq 4$ T [185], in contrast to what we observed here in YFe_2Al_{10} . The field dependent magnetoresistivity of YFe_2Al_{10} with field along both a and b directions is shown in fig. 4.24b. The anisotropic behavior actually becomes more significant in fields up to 9 T at 0.5 K.

Although the Kondo expression describes the zero field upturn, we want to emphasize that the anisotropic behaviors observed in the field dependent magnetoresistivity cannot be fully explained as the consequence of rare earth contamination. We also noticed that the field dependencies of the magnetoresistivity are consistent with the field dependent magnetization and specific heat, where the crystal a direction is always the most sensitive direction. From this point of view, it is likely that the low temperature resistivity is also dominated by the same critical fluctuations at $T = 0$. This low temperature upturn in resistivity may indicate that the QCP is related to the the localization of electrons as $T \to 0$.

4.8 Discussion and Conclusion

4.8.1 Universal Critical Behaviors

We have studied the magnetization and specific heat of the three related compounds YFe_2Al_{10} , $LuFe_2Al_{10}$, and $YbFe_2Al_{10}$. Critical scalings were found in YFe_2Al_{10} and $LuFe_2Al_{10}$, indicating that these two materials are located close to the QCP. However, it is still unclear what kind of QCPs are present in these compounds. From the scaling we showed earlier, we know that the critical behaviors in YFe_2Al_{10} and $LuFe_2Al_{10}$ are very similar to each other. All the magnetic properties could be described equally well using the same scaling analysis. Most importantly, the assumption with relation ($d = z$) describes the scaling functions in both YFe_2Al_{10} and $LuFe_2Al_{10}$.

To further understand the meaning behind this relation, we have compared our results on YFe_2Al_{10} and $LuFe_2Al_{10}$ to those obtained in some other well studied quantum critical systems. We choose three different compounds as examples: $CeCu_{6-x}Au_x$, which was tuned to a AF-QCP at $x = 0.1$ [17], the Yb-based mixed-valence compound $\beta - YbAlB_4$, which is believed to be close to a QCP at $B = 0$ without tuning [20], and the layered organic Mott system κ-(BEDT-TTF)$_2$Br, which is located close to the MIT critical end point [50].

$\mathbf{CeCu_{6-x}Au_x}$

Shown in fig. 4.25a is the scaling of the dc magnetic susceptibility of $CeCu_{6-x}Au_x$ [17] as

$$\chi = T^{-0.75} f(B/T).$$

To make the scaling comparable to the one we found in YFe_2Al_{10} and $LuFe_2Al_{10}$, we rewrote this scaling function in a slightly different form as

$$\frac{d\chi}{dT} = B^{-1.75}\psi(\frac{T}{B}). \tag{4.47}$$

By comparing this to equation 4.6, we can see that

$$\begin{cases} d/y_b - 2 = -1.75 \\ \\ z/y_b = 1. \end{cases}$$

Thus, we have

$$\begin{cases} d/y_b = 1/4 \\ \\ z/y_b = 1, \end{cases} \tag{4.48}$$

and

$$d/z = 1/4 \tag{4.49}$$

for the AF-QCP in $CeCu_{6-x}Au_x$. Based on this, we can also calculate the critical exponent

$$\gamma = 2y_b/z - (d+z)/z = 0.75. \tag{4.50}$$

This is consistent with the experimental results where a low temperature divergence in the magnetic susceptibility $\chi \sim T^{-0.75}$ was observed near the critical concentration $x = 0.1$ of $CeCu_{6-x}Au_x$ [17].

$\beta-\mathbf{YbAlB_4}$

Different from $CeCu_{6-x}Au_x$, $\beta - YbAlB_4$ is a mixed valence compound, and it was proposed to be a critical nodal metal [186], where the hybridization gap induced by the interaction of the $4f$ magnetic moments and the conduction electrons vanishes along a line in momentum space. B/T scalings were observed in the dc magnetization, and the magnetic susceptibility diverges as a power law as $\chi \sim T^{-\gamma}$ ($\gamma = 1/2$) at low temperatures. The scaling of the

dc magnetization of $\beta - YbAlB_4$ is shown in fig. 4.25b, where

$$-\frac{dM}{dT} = B^{-1/2}\varphi(\frac{T}{B})$$

was observed for a wide temperature and field range [20]. As we did for $CeCu_{6-x}Au_x$, we again wrote the scaling function as

$$\frac{d\chi}{dT} = B^{-1.5}\psi(\frac{T}{B}). \tag{4.51}$$

This directly gives that

$$\begin{cases} d/y_b - 2 = -1.5 \\ \\ z/y_b = 1, \end{cases}$$

and so

$$\begin{cases} d/y_b = 1/2 \\ \\ z/y_b = 1. \end{cases} \tag{4.52}$$

with

$$d/z = 1/2. \tag{4.53}$$

For the material $\beta - YbAlB_4$

$$\gamma = 2y_b/z - (d+z)/z = 1/2, \tag{4.54}$$

and this is what observed experimentally [20].

By comparing these results for $CeCu_{6-x}Au_x$ and $\beta - YbAlB_4$ to the scaling analysis we did for YFe_2Al_{10} and $LuFe_2Al_{10}$, we can clearly see that here the critical exponents and relations between the scaling dimensions are totally different from those found in either the AF-QC $CeCu_{6-x}Au_x$ or the critical nodal metal $\beta - YbAlB_4$. This indicates that YFe_2Al_{10} and $LuFe_2Al_{10}$ belong to different universality classes than $CeCu_{6-x}Au_x$ and $\beta - YbAlB_4$. However, the scaling could still be related to the same critical form of the free energy in all these compounds

$$F(B,T) = T^{\frac{d+z}{z}} f_F(\frac{B}{T^{y_b/z}}) = B^{\frac{d+z}{y_b}} \tilde{f}_F(\frac{T}{B^{z/y_b}}).$$

This is not surprising, and actually it is what we should expect from the universality of systems close to critical points. The differences between these compounds appear to come from the different values of scaling dimensions d, z, and y_b, which define the different universality classes.

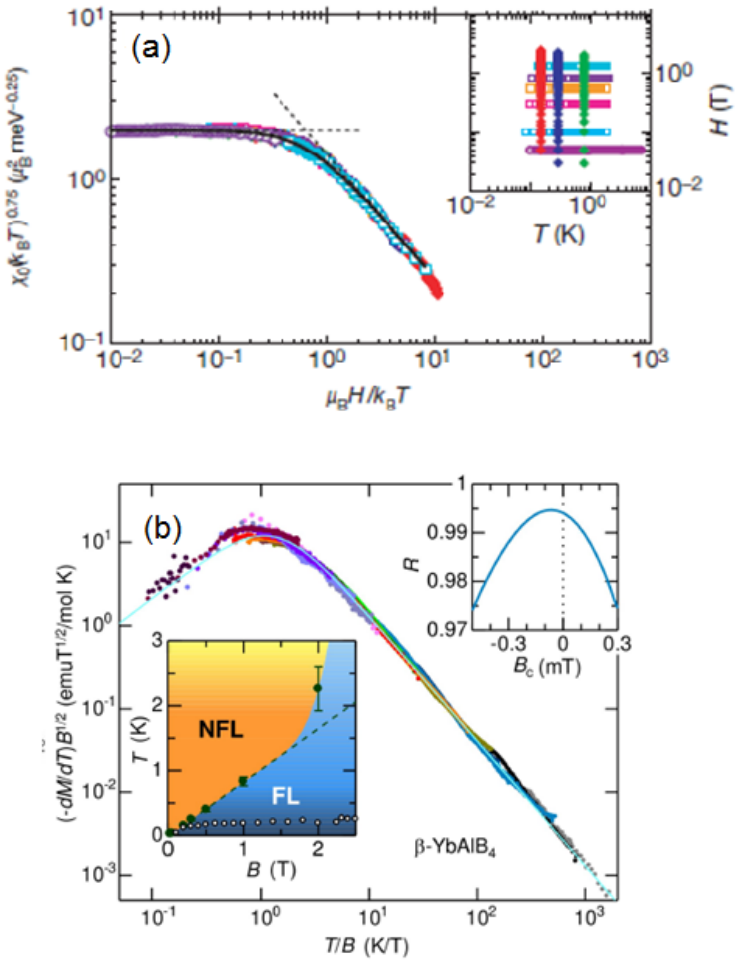

Figure 4.25: (a) B/T scaling of the dc magnetic susceptibility of $CeCu_{6-x}Au_x$ as $\chi = T^{-0.75} f(B/T)$. Solid line is the scaling function $f = (1 + x^2)^{-0.75/2}$, where $x = B/T$. Inset shows the $B-T$ range that the scaling applies. (Figure from [17].) (b) Scaling of the observed dc magnetization of $\beta - YbAlB_4$. The data were fitted to the scaling function $\varphi(x) = \Lambda x(A + x^2)^{-1.25}$, where $x = T/B$. (Figure from [20].)

κ-(BEDT-TTF)$_2X$

The layered organic charge-transfer salts κ-(BEDT-TTF)$_2X$ have been well studied as excellent examples of systems undergoing metal insulator transitions (MIT) [48, 49, 50]. The temperature pressure $(T-P)$ phase diagram has been established by studying on κ-(BEDT-TTF)$_2$X with increasing pressure or with changing different monovalent anions X (fig. 1.11) [48, 49, 50]. Scaling behaviors were observed near the MIT critical end point. The scaling function and critical exponents are found to belong to the two dimensional (2D) Ising universality class. The singular part of the free energy is written in the scaling form as [50]

$$f(t,h) = \frac{1}{8\pi} t^2 log t^2 + |h|^{d/y_h} \Phi(t/|h|^{z/y_h}). \tag{4.55}$$

Disregarding the details, this free energy is surprisingly similar to what we have proposed for YFe_2Al_{10} , where

$$F(B,T) = T^2 log T^2 + B^{(d+z)/y_b} \tilde{f}_B(T/B^{z/y_b}). \tag{4.56}$$

The differences between the above two equations are that the scaling performed in κ-(BEDT-TTF)$_2$Cu[N(CN)$_2$]Br is close to the finite temperature critical end point at $T_c \simeq 39.7$ K, and $P_c \simeq 248$ bar [49]. Since this is a nonzero temperature CEP, the scaling theory for κ-(BEDT-TTF)$_2$Cu[N(CN)$_2$]Br is the same as a classical scaling analysis. In contrast, the scaling performed in YFe_2Al_{10} and $LuFe_2Al_{10}$ relates to a QCP located at $T=0$, and $B=0$, where the scaling variables are absolute temperature T and external field B instead of the renormalized t and h in 4.55. The quantum critical scaling in YFe_2Al_{10} differs as well from the classical scaling in κ-(BEDT-TTF)$_2X$ by the effective dimension, where d is replaced by $d+z$. Except for this, the two scaling functions above are interchangeable.

4.8.2 Conclusion

In this chapter, we have studied the magnetic properties of the family of compounds YFe_2Al_{10} , $LuFe_2Al_{10}$ and $YbFe_2Al_{10}$. Scaling analyses of the magnetic susceptibility and specific heat were performed, and they suggest that these materials are located close to a QCP at $T=0$, and $B=0$. Further analysis of the critical exponents indicate that the critical behaviors may not be dominated by a normal magnetic QCP. Measurements of resistivity and thermal expansion hint that these compounds may be close to an itinerant-localization transition, like a metal-insulator transition (MIT).

A schematic MIT phase diagram with tuning parameter g is shown in

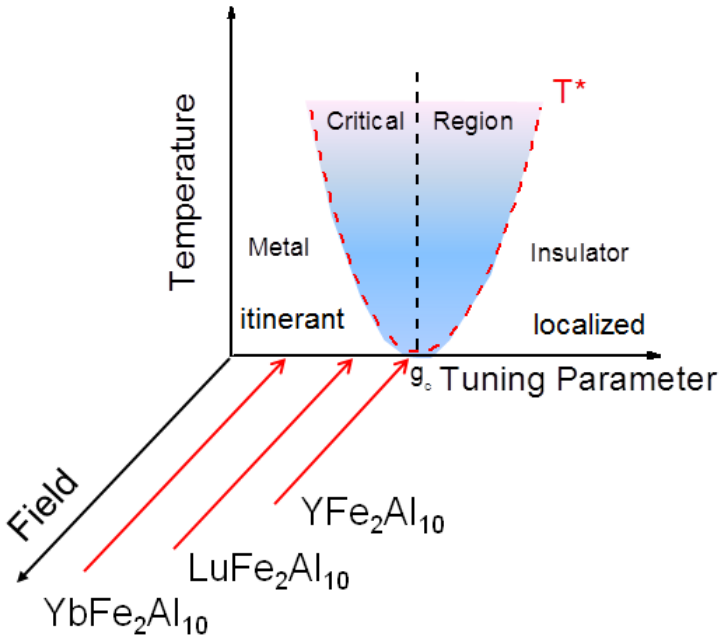

Figure 4.26: Schematic view of a general Metal-Insulator transition phase diagram with tuning parameter g. We have proposed that the family material YFe_2Al_{10} , $LuFe_2Al_{10}$ and $YbFe_2Al_{10}$ may locate close to the MIT QCP at g_c in a sequence indicated by the red arrows. [47]

fig. 4.26 [47]. The critical region is delineated by the dashed line, below which the quantum fluctuations dominate. The MIT QCP sits at the critical tuning parameter g_c. When the system is tuned above this critical value $g > g_c$, the ground state is a localized insulator, while when $g < g_c$, the ground state turns out to be an itinerant metal. From this point of view, the MIT QCP is similar to the delocalization-localization QCP seen in the heavy fermion magnetic compounds. Since the electrons change from itinerant states on the metallic side to localized and moment-bearing states in the insulating side, the MIT QCP is usually accompanied by the emergence of magnetic order. This is why a strong divergence of the magnetic susceptibility is always observed near the MIT QCP. However, this is the consequence of the formation of non-interacting localized moments at $g \geq g_c$ in zero temperature, and no universal critical exponents that relate to the magnetic susceptibility χ are expected as in magnetic QCPs [22]. These observations are all consistent with our scaling analysis in YFe_2Al_{10} and $LuFe_2Al_{10}$, and here we suggest that the zero temperature MIT QCP is approached in the sequence of $YbFe_2Al_{10}$ $\rightarrow$$LuFe_2Al_{10}$ $\rightarrow$$YFe_2Al_{10}$ as indicated by the red arrows in fig. 4.26. Although the electrons have distinct ground states that are either metal or insulator at $T = 0$, it is very hard to find a proper order parameter for MIT-QCPs that identifies their broken symmetry as in traditional magnetic QCPs. This makes the studying of the behaviors in the critical region a rather difficult problem [46, 47]. In our case of YFe_2Al_{10} and $LuFe_2Al_{10}$, it is likely that the MIT is driven by interactions like a Mott transition, rather than disorder or frustration, and the scaling of the magnetic susceptibility and specific heat has helped us to have some insight into the critical region. However, more work, especially the pressure and doping measurements, needs to be done in the future to have a better understanding of this system.

Chapter 5

Neutron Scattering of the Quantum Antiferromagnet Yb_2Pt_2Pb

This chapter presents a selection of experimental results, including neutron scattering, that establish the basic properties of the quantum antiferromagnet Yb_2Pt_2Pb, which orders at $T_N \simeq 2.07$ K in zero field. The Yb atoms in this material are paired with nearest neighbors that are orthogonally arranged to each other in the tetragonal ab plane. This structure is topologically equivalent to the frustrated two-dimensional (2D) Shastry-Sutherland Lattice (SSL). Magnetic properties indicate that the Yb atoms form two sublattices with a well separated doublet ground states of strongly Ising-like spins along the orthogonal (110) or (1-10) directions. This was confirmed by single crystal elastic neutron scattering experiments. Further study of the single crystal inelastic neutron scattering data suggests that interactions in the crystal c direction are very important, and that the Ising like Yb moments are aligned into one-dimensional (1D) antiferromagnetically coupled chains along the c axis. This is in contrast to our expectation of the 2D SSL physics from the crystal structure. A broad continuum of spinon like excitations is observed at low temperatures. Non-Fermi liquid behaviors were also observed near the field induced AF-QCP, indicating that heavy fermion physics may also be relevant in this system.

5.1 Introduction

Yb_2Pt_2Pb has attracted a lot of interest, mostly because of its particular crystal structure. This ternary compound belong to a large family of composition R_2T_2M (R=rare earth, T=transition metals, M=main group), where the rare earth atoms R form into a two dimensional Shastry-Sutherland Lattice (SSL), with orthogonal arranged dimers [60, 66, 222, 223]. Frustration induced by the competing exchange interactions of the intra-dimer J and inter-dimer J' is considered to be important in this compound [66, 67, 222]. Extensive measurements of different thermal, transport, and magnetic properties have been performed, and a complex field temperature phase diagram has been established based on the magnetization, and specific heat data [67, 97]. Interest also arises from the heavy fermion point of view [66, 67, 222]. Yb_2Pt_2Pb orders antiferromagnetically at about $T_N \simeq 2.07$ K in zero field. Applying field along the crystal (110) direction leads to a suppression of the antiferromagnetic order, forming an AF-QCP at about 1.25 T, with a new dome like phase near the critical point observed between 1.25 T and 2.3 T [67, 97, 224, 225].

What we are going to stress in this chapter is the neutron scattering measurements performed on an array of aligned single crystals. Both the elastic neutron diffraction and inelastic neutron scattering data will be discussed. Counter to our expectations, excitations with a spinon like dispersion along the $(00l)$ momentum direction were observed in zero field, indicating that the one-dimensional Luttinger liquid may be the dominant ground state physics in this material. Resistivity measurements were also reported, and non-Fermi liquid behaviors with linear temperature dependent resistivity were observed near the AF-QCP. An additional energy scale can be traced in the field dependent resistivity, which is similar to what was observed in the heavy fermion AF-QCP in $YbRh_2Si_2$ [10, 43], suggesting that heavy fermion physics may also be relevant in Yb_2Pt_2Pb as well.

5.1.1 Experimental Details

Thermal property measurements

Yb_2Pt_2Pb single crystals with a typical size about 0.5 mm in the ab direction and 4 $\sim$ 5 mm in the c direction were grown from lead flux [66, 76]. Measurements of the dc magnetization were performed using the commercial Quantum Designs Magnetic Properties Measurement System (MPMS) for $T > 1.8$ K in fields up to 7 T, and a Hall sensor magnetometer for $T < 1.8$ K in fields up to 14 T [66, 67, 97]. Electrical resistivity was measured down to 0.1

K in the Quantum Design Physical Property Measurement System (PPMS) with the dilution refrigerator (DR) option [66, 97].

Neutron scattering experiments

Single crystal neutron scattering measurements were performed at the Disk Chopper Spectrometer (DCS) at NCNR, NIST [109], and the Cold Neutron Chopper Spectrometer (CNCS) at SNS, Oak Ridge [110]. Pictures of the sample holder and the experimental scattering configuration are shown in fig. 5.1. Yb_2Pt_2Pb single crystals were assembled layer by layer on Aluminum plates, taking advantage of the fact that the crystals form with the (110) direction perpendicular to the surface, while the long edge is the (001) direction. About six layers of crystals with total mass about 6 g were stacked together in this sample holder in fig. 5.1. For each layer, the crystals are co-aligned with the (110) direction normal to the holder surface, and neutrons scattered in the (h, h, l) plane. The vertical magnetic field B is along the $(h, -h, 0)$ direction in both DCS and CNCS measurements.

For the DCS experiment, a dilution refrigerator insert that can access temperatures as low as 70 mK was used in a 10 T magnet. A beam mask with size about 1.5cm × 2.5cm was used in front of the sample to reduce background scattering. For the zero field measurements at base temperature, a small bias field of about 200 Oe was used to suppress the superconductivity of the aluminum sample holder. By setting the dark angle at 75^0 from the (110) direction and the incident neutron energy $E_i = 3.27$ meV ($\lambda_i = 5.0$Å), we could totally avoid undesired background scattering due to the magnet. Limited by the height of the magnet window, only neutrons scattering from the sample within angle the θ are counted by the detector with a height H. In this DCS set up, the distance from the sample to the detector is about $D = 4010$ mm, and only the data of the central bank detector were analyzed, where the detector tubes are about $H = 400$ mm high. Based on this, we could estimate the scattering angle θ to be about 5.7^0 in this experiment. So although the scattering plane is (h, h, l), there is some scattering from the $(h, k, 0)$ plane that also contributes to the overall integrated scattering intensity.

For the CNCS experiment, a cryostat that reaches temperatures down to 1.5 K was used in a 5 T magnet. For this experiment, the window of the magnet is big enough that we do not need to consider whether it blocks the scattered beams. The incoming neutron energy was fixed at 3.316 meV ($\lambda_i = 4.97$Å), and the high-flux mode was used to maximize the neutron intensity. The distance from the sample to the detector in the CNCS experiment is about $D = 3500$ mm, and the entire detector is about 2000 mm high. Since we only integrate 88 pixels of the total 128 pixels of the detectors to avoid some

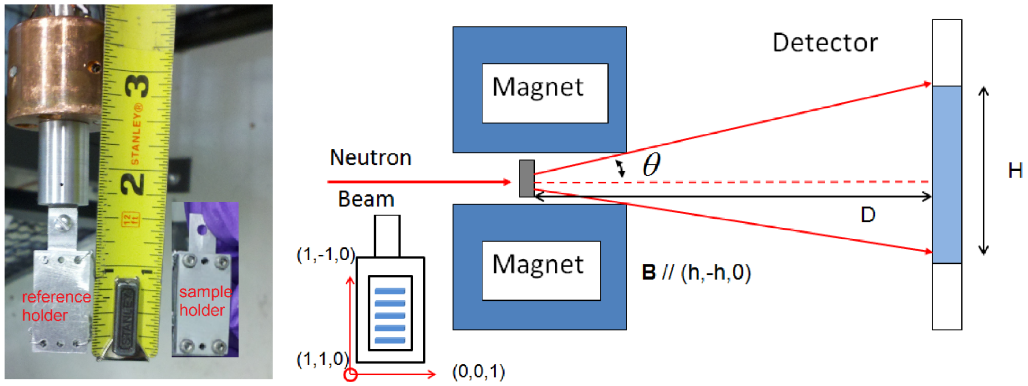

Figure 5.1: Left: Sample holders for the single crystal neutron scattering experiments at DCS in NCNR, NIST, and CNCS, SNS, Oak Ridge. Six layers of Yb_2Pt_2Pb crystals were included in the sample holder shown in the picture. For each layer, Yb_2Pt_2Pb single crystals were aligned with the (110) direction normal to the holder surface, with the neutrons scattering in the (h, h, l) plane. A reference holder with Vanadium foil inside was used for the normalization analysis. Right: Schematic view of the configuration for both the DCS and CNCS neutron scattering set ups. The sample holder was mounted with vertical magnetic field B along the $(h, -h, 0)$ direction. Limited by the height of the magnet window, only neutrons scattering from the sample within the angle θ are counted by the detector within height H. This scattering angle θ was estimated by knowing the distance D and height H as marked in the figure.

scattering from the edge of the magnet, the effective height of the detector in this experiment is about $H = 2000 * 88/128 = 1375$ mm, and we estimate $\theta \simeq 11^0$ in this measurement, which is about twice the scattering angle in DCS. This small angle would not make much difference in the scattering pattern for inelastic neutron scattering measurements, and actually a little wider angle θ usually helps to improve the overall scattering intensity. But for the elastic diffraction measurements, the peaks which are close to but not in the exact scattering plane may give misleading information if one simply summed over all the scattering intensity of the detectors. Fortunately, the CNCS detector is not just long arrays of tubes which are only sensitive to the horizontal positions as in DCS, it also has spatial resolution in the vertical direction [110]. We take advantage of this to get exact information in the (h, h, l) scattering plane and also part of the information in the $(h, k, 0)$ plane. This in turn helps to understand better the scattering data taken in DCS at lower temperatures.

5.1.2 Crystal Structure

Yb_2Pt_2Pb crystallizes in the tetragonal U_2Pt_2Sn-type structure (space group: $P4_2/mnm$, NO. 136), with the lattice parameters $a = 7.7651$Å, $c = 7.0207$Å. Details of this crystal structure were reported in [66, 222, 226]. Here, to be clear, we only plot the simplified crystal structure with the two Yb site atoms in fig. 5.2. In the tetragonal ab plane, Yb atoms form in pairs of nearest neighbor atoms, and these pairs are arranged orthogonally to each other. This structure with pairs of Yb atoms is topologically equivalent to the Shastry-Sutherland Lattice (SSL) [60]. The layer at $z = 1/2$ is different from the layer at $z = 0$ by just switching both Yb1 and Yb2 sites simultaneously, and these two layers are stacked alternately along the crystalline c axis [66, 222]. We use the same notation as in [66] for the distance of the Yb near neighbor atoms to emphasize this SSL structure, as shown in fig. 5.2b. The intra-pair distance between Yb1-Yb1, and Yb2-Yb2 sites are $d_1 = 3.9646$Å, $d_2 = 3.5451$Å, and the inter-pair distance between Yb1-Yb2 sites are $d_3 = 4.196$Å, $d_4 = 3.889$Å, respectively. In this SSL picture, the system is dominated by the interactions in the two dimensional ab plane, assuming that the interactions between the planes are not important [66]. However, when we consider the distances between the Yb1-Yb2 atom along the c axis, we found that $d_5 = 3.5169$Å, which is actually the smallest bond distance among all the Yb atoms. An alternative way to view the crystal structure is as one-dimensional (1D) chains or ladders extending along the c axis, as shown in fig. 5.2a. The Yb ions are first coupled into chains or ladders along in the c direction through the bonds d_1, d_2 and d_5, and these orthogonal arranged chains or ladders are then interact with each other through bonds d_3 and d_4. However, we can not tell whether the 1D

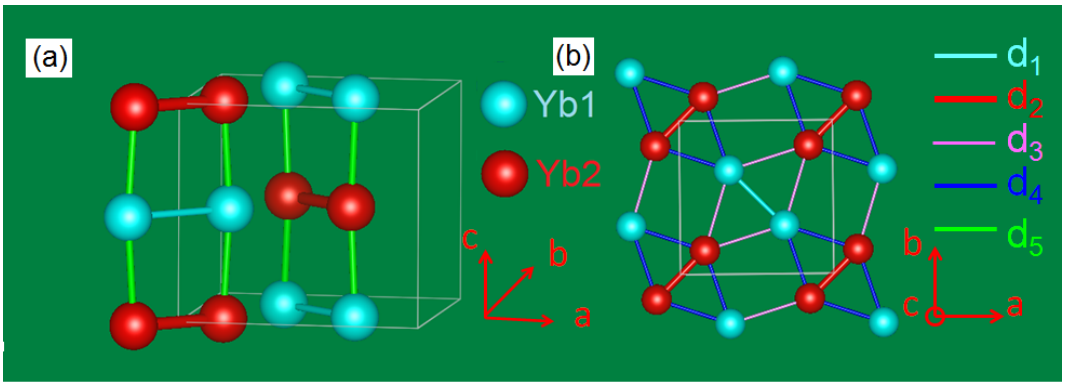

Figure 5.2: (a) A simplified crystal structure of Yb_2Pt_2Pb with Yb atoms sitting at two Wyckoff sites: Yb1 ($4f$ site) and Yb2 ($4g$ site). (b) Pairs of Yb nearest neighbor atoms are orthogonally arranged to each other in the ab plane, which is topologically equivalent to the Shastry-Sutherland Lattice (SSL). [66]

chain model or the 2D SSL is more suitable for the material just based on the crystal structure. We will use magnetic properties and neutron scattering experiments to answer this question.

5.1.3 Magnetic Properties

Curie-Weiss behaviors were found at high temperature magnetic susceptibilities for fields both along the crystal c axis and in the ab plane. The fitted effective moments $\mu_{\text{eff}} = 4.42\mu_B$ for $B\|(110)$ and $\mu_{\text{eff}} = 4.54\mu_B$ for $B\|(001)$ are very close to the expected value $4.54\mu_B$ for free Yb^{3+} ions with $J = 7/2$ [66]. The eight degenerate states ($2J + 1 = 2 * 7/2 + 1 = 8$) were split into four doublet states due to the tetragonal crystal environment in Yb_2Pt_2Pb [66]. The low temperature magnetic properties are dominated by the the ground doublet state.

The temperature dependence of the $B = 0$ specific heat is shown in fig. 5.3, where the phonon contribution estimated from the Debye model has been subtracted from the as-measured specific heat [66]. At the antiferromagnetic phase transition around 2.07 K, only about half of the entropy ($S = 0.58R\ln 2$) of the doublet ground states was recovered, and a tail extending to about 8 K was observed, indicating that strong fluctuation exist above the AF transition [66]. The full entropy $S = R\ln 2$ was only recovered for temperatures $T \geq 10$ K, which is significantly different from the situation found in the local moment antiferromagnet Yb_3Pt_4, shown earlier in Chapter 3. A broad peak

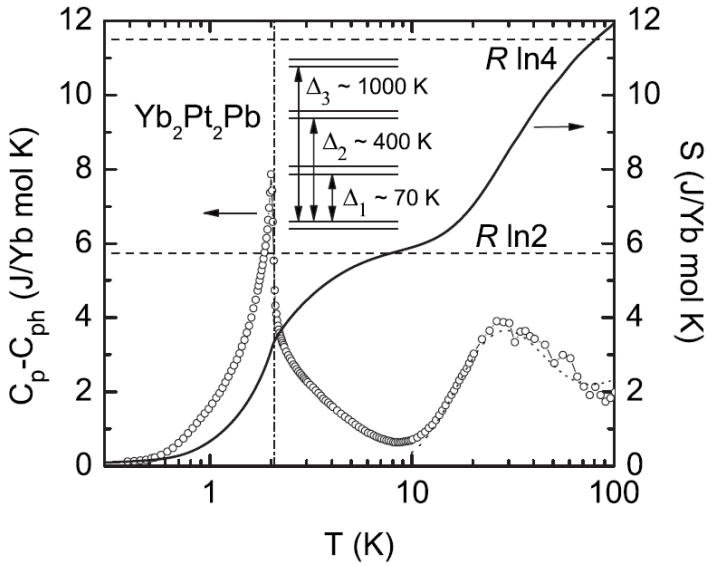

Figure 5.3: Temperature dependent specific heat of Yb_2Pt_2Pb in zero field. The phonon contribution has been estimated from the Debye model, and subtracted from the measured specific heat. The full entropy $S = R\ln 2$ of the ground doublet states is only recovered for $T \simeq 10$ K, indicating that strong fluctuations exist above the transition at 2.0 K. A sketch of the four CEF doublets is shown in the inset, where the first excited states are about $\Delta_1 \simeq 70$ K above the doublet ground states. [66]

was observed in Yb_2Pt_2Pb at temperatures for $T \sim 30$ K, which comes from the excitations to higher CEF levels. This broad maximum was fitted to the Schottky expression with three excited doublet states, and the schematic view of the full CEF configuration was shown in fig. 5.3(inset), where the first excited states are about $\Delta_1 \simeq 70$ K above the doublet ground states [66].

Ising Spin, Two Yb Sublattice Model

The full CEF configuration of Yb_2Pt_2Pb with four separated doublet states is also found in many other Yb based systems [123, 135, 227], however, the particular wave function of the ground doublet in Yb_2Pt_2Pb is more unusual. Shown in fig. 5.4 is the field dependent magnetization of Yb_2Pt_2Pb for fields along the crystal (001), (110) and (100) axes, respectively [66]. Very strong anisotropy was observed between the tetragonal ab plane and the crystal c axis. For magnetic field $B \parallel 001$, the measured dc magnetization at 1.9 K does not saturate in fields as large as 14 T, and the measured magnetization

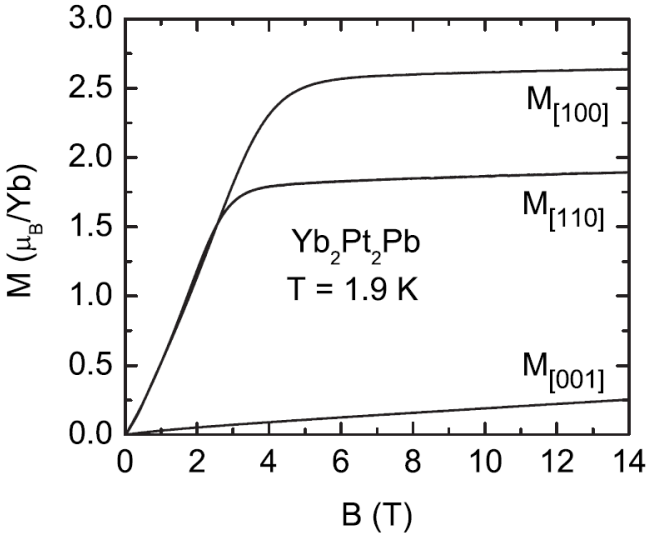

Figure 5.4: Field dependent magnetization of Yb_2Pt_2Pb measured at $T = 1.9$ K, for B along the crystal (001), (110) and (100) axes as marked. [66, 67]

$M_{001}(14T) \simeq 0.25\mu_B$ is about 10 times smaller than the saturation value in the *ab* plane. This means that the Yb moments are confined to the *ab* plane at low temperatures. Anisotropic behaviors were also observed in the *ab* plane. The measured magnetization saturates to the value $M_{100} \sim 2.6\mu_B$ for fields $B\|(100) \simeq 3.5$ T, and $M_{110} \sim 1.9\mu_B$ for fields $B\|(110) \simeq 2.3$ T [66, 224].

A two sublattice model of Ising spins along the orthogonal (110) and (1-10) axes was first proposed by [224], assuming $j_z = |\pm 7/2\rangle$ as the ground states for the Yb doublet ground state. With this assumption, the full saturation moments would be $M_s = g_J J\mu_B = 8/7 * 7/2\mu_B = 4\mu_B$ if all the Yb ions are fully polarized. However, due to the strong Ising structure, only half of the Yb moments are saturated in this field range when $B\|110$, and this gives about $M_{110} = 2\mu_B$, which is close to the observed value $M_{110} \sim 1.9\mu_B$. Accordingly, for fields $B\|100$, all the Yb moments will be eventually polarized, but since the moments are rigidly fixed in the orthogonal (110) and (1-10) directions, $M_{100} = M_s/\sqrt{2} = 4/\sqrt{2} = 2.8\mu_B$ was observed. This also explains the relative value of the two critical fields Bc_{110} and Bc_{100}, where $Bc_{100} = \sqrt{2}Bc_{110} \simeq 3.25$ T, which is also close to the observation [224]. Based on this model, two different configurations for the Yb Ising moments are possible. As shown in fig. 5.5, the Yb moments could point either along the diagonal direction (fig. 5.5a) or perpendicular to the diagonal direction (fig. 5.5b). The first scenario shown in fig. 5.5a is similar to the magnetic

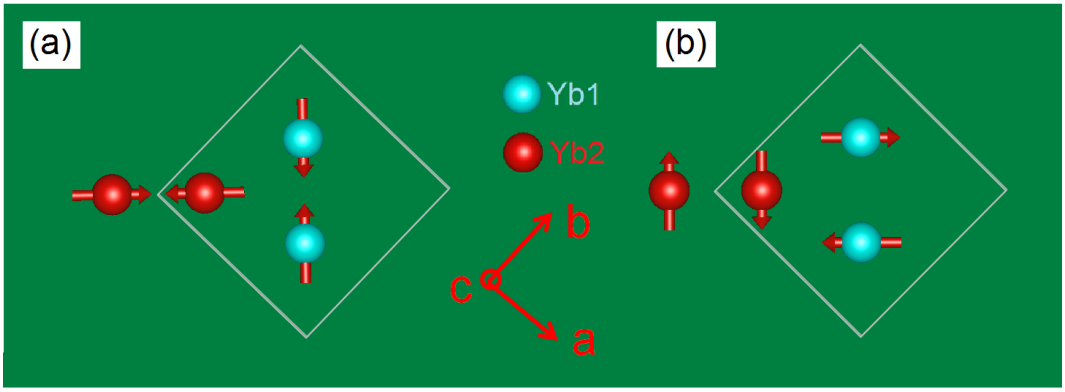

Figure 5.5: Two possible Yb spin configurations in the *ab* plane. The Yb ions are divided into two sublattice with Ising spins along the orthogonal (110) and (1-10) axes. The Ising spins are aligned along the diagonal pair direction in (a), and are perpendicular to the diagonal direction in (b).

structure of the compounds U_2Pt_2Sn and GdB_4 [228, 229], as also noted by Moosung Kim in [66]. Recently, Wojciech Miiller of our group made a heroic breakthrough with solving the magnetic structure in zero field, where the spin configuration in fig. 5.5b gives the better fitting of the diffraction pattern [230].

Magnetic Phase Diagram

Extensive studies of magnetic properties such as the magnetization, specific heat, and MCE have been performed, and a very rich phase diagram in fields $B\|110$ at low temperatures was established [97], as shown in fig. 5.6. The many vertical phase lines inside the magnetic order at low temperatures are related to plateau phases in the field dependent dc magnetization [67, 97], as shown in fig. 5.6a. The two dashed horizontal lines are determined from the temperature dependent resistivity and specific heat measurements, but they are not seen in dc magnetization measurements. X-ray diffraction has been performed in fields up to 4.0 T at temperatures down to 1.8 K, and no new diffraction peaks were observed across the horizontal phase line at 2.0 K, indicating that this is not a structural transition. One of our questions is how to understand this phase line. Is it a magnetic transition? If it is, then why is no signature observed in the temperature dependent magnetization measured in high fields? As we have explained, the slope of the phase line can be related to the thermal properties through the Clausius-Clapeyron relation:

$$\frac{dT}{dB} = -\frac{\Delta M}{\Delta S}.$$

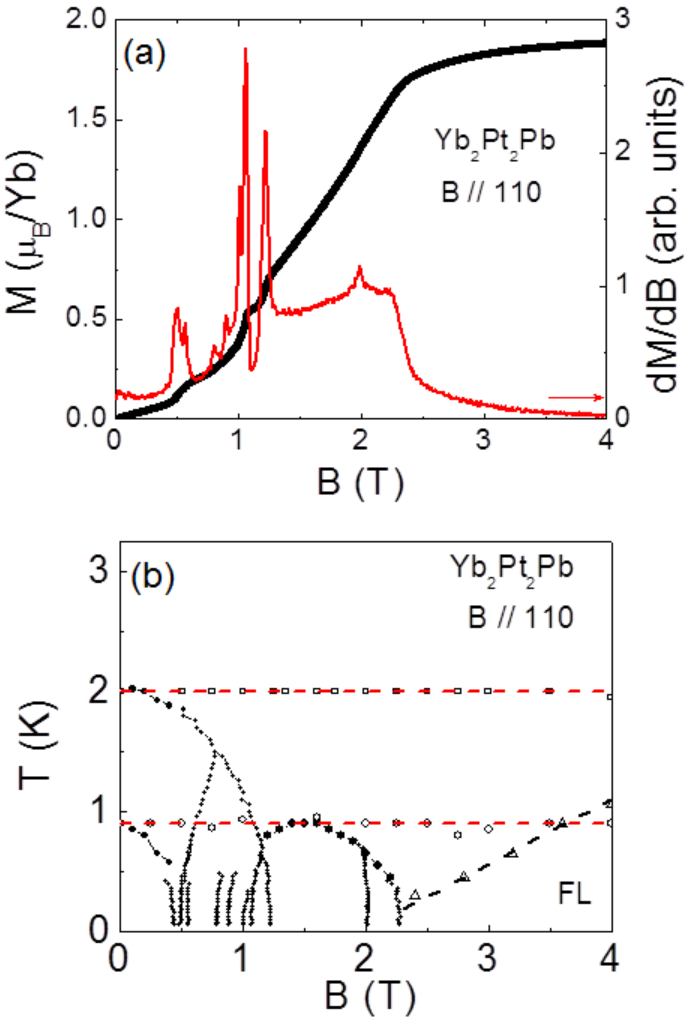

Figure 5.6: (a) Magnetic field dependent dc magnetization (black line) measured at 0.06 K with field along the (110) direction using the Hall sensor magnetormeter. The red line is the field derivative of the measured magnetization dM/dB. (b)Field-Temperature phase diagram with fields $B\|110$ from the the magnetization, specific heat, and MCE measurements. The two dashed horizontal lines at $T_{N1} \simeq 2$ K, and $T_{N2} \simeq 0.8$ K are determined from the temperature dependent resistivity and specific heat measured in fields. [97]

For first order phase transitions at finite temperatures, the entropy change is not zero ($\Delta S \neq 0$). Consequently, the only way to keep the slope of the phase line horizontal ($dT/dB = 0$) is to make the change of the magnetization zero ($\Delta M = 0$). This means that even it is a first order magnetic phase transition, there could must be no jump in the magnetization at this phase transition. For second order phase transitions, this implies that even the derivative of the magnetization will be continuous across the horizontal phase lines. We will discuss below the elastic neutron scattering experiments that will shed light on these horizontal phase lines.

5.2 Elastic Neutron Scattering Measurements

In this section, we will first focus on the CNCS data measured at 1.5 K in fields up to 4.75 T. After this, we will also discuss the elastic neutron scattering data taken at DCS at 0.1 K in fields up to 4 T. Two sets of magnetic peaks were observed, with different temperature and field dependencies, providing evidence for the two sublattice model.

5.2.1 Elastic neutron scattering in the [H, H, L] plane

Scattering at different temperatures in fields $B = 0$

Shown in fig. 5.7 is the contour plot of the elastic neutron scattering intensity in the [H, H, L] plane taken at CNCS at different temperatures from 1.5 K to 2.5 K in zero field. Here we have limited the integration along the $(H, -H, 0)$ direction to a narrow range [-0.05, 0.05] to avoid any contribution from the [H, K, 0] plane. At temperatures above the phase transition $T_N \simeq 2.07$ K, we can clearly see two nuclear peaks at positions (002), and (112) (fig. 5.7d). The (111) peak is also an allowed nuclear peak in zero field, however, its neutron scattering structure factor is very small compared to other nuclear peaks. Thus the (111) peak is almost invisible in this contour plot. Lowering the temperature from 2.5 K to 2.0 K (fig. 5.7c) leads to three broad diffuse satellites that appear around (0.2, 0.2, 1), (-0.2, -0.2, 1), and (0.8, 0.8, 1). Lowering the temperature still further to 1.8 K and 1.5 K leads to the development of well defined diffraction peaks at these three positions, as shown in fig. 5.7b and fig. 5.7a. Two new peaks appear at positions (1.2, 1.2, 1), and (1.8, 1.8, 1), but with lower peak intensities compared to the peaks at (0.2, 0.2, 1), (-0.2, -0.2, 1), and (0.8, 0.8, 1). All these new peaks have the propagation vector $q_1 = (\pm 0.2, \pm 0.2, 0)$r.l.u. We also noticed that all the new magnetic peaks appear at positions with $L = 1$, and no additional peaks have been observed

for $L = 0$ or $L = 2$. This gives us some hints about the zero field magnetic structure [230]. The propagation vector $q_1 = (\pm 0.2, \pm 0.2, 0)$ indicates that we have a 5×5 superstructure in the ab plane, and the absence of magnetic peaks in $L = 0$, and $L = 2$ plane suggests that the magnetic moments are antiferromagnetically coupled between the planes. The scattering intensity at magnetic peak positions (0.2, 0.2, 1), (-0.2, -0.2, 1), (0.8, 0.8, 1) and nuclear peak positions (002), (112) have been fitted to Gaussian expressions, and the fitted peak intensities are plotted in fig. 5.8 as functions of temperatures. With increasing temperature, the scattering intensity of the magnetic peaks decreases rapidly as the 2.07 K phase transition is approached. However, the magnetic intensity does not go to zero at 2.0 K, and a small tail was observed that extends up to $\sim 3 - 4$ K. The continuous change of the peak intensity across the phase transition indicates that this is a second order phase transition, and the tail above the transition temperature suggests that critical fluctuations are important near the phase transition. This result is consistent with the specific heat measurements shown in fig. 5.3, where a long tail in the specific heat was also observed above 2.0 K. No significant change has been observed for the two nuclear peaks (002) and (112) across the phase transition around 2.07 K.

To have a better understanding of the phase transition in zero fields around T_N, we did a more careful analysis by using the scan at 1.6 K in a field of 4.75 T as a background. The subtracted zero field data are shown in fig. 5.9 for temperatures from 1.5 K to 5.0 K. With this subtraction, the nuclear contributions at positions (001) and (112) are completely removed, and the diffuse scattering above 2.0 K is now more pronounced in the relative intensity, as seen in fig. 5.9b, and fig. 5.9c. With decreasing temperature, the broad diffuse scattering quickly develops into the narrow elastic magnetic diffraction peaks below the transition. Since the (0.8, 0.8, 1) peak has the strongest scattering intensity, we chose it for detailed analysis. Shown in fig. 5.10a and fig. 5.10b are the scattering intensities of the magnetic peak $(0.8, 0.8, 1)$ at different temperatures across the longitudinal $(0.8, 0.8, l)$ and the transverse $(h, h, 1)$ directions, respectively. With decreasing temperature, the peak intensity increases, while the peak width decreases as $T \to T_N$. For the scattering intensity integrated along one direction in the momentum space, it can be fit to the Lorentzian expression:

$$f = \frac{A}{\pi} \frac{\Gamma}{(q - q_0)^2 + \Gamma^2}, \tag{5.1}$$

as indicated by the solid lines. The fitting parameter A is proportional to the peak intensity, which serves as the order parameter of the zero field

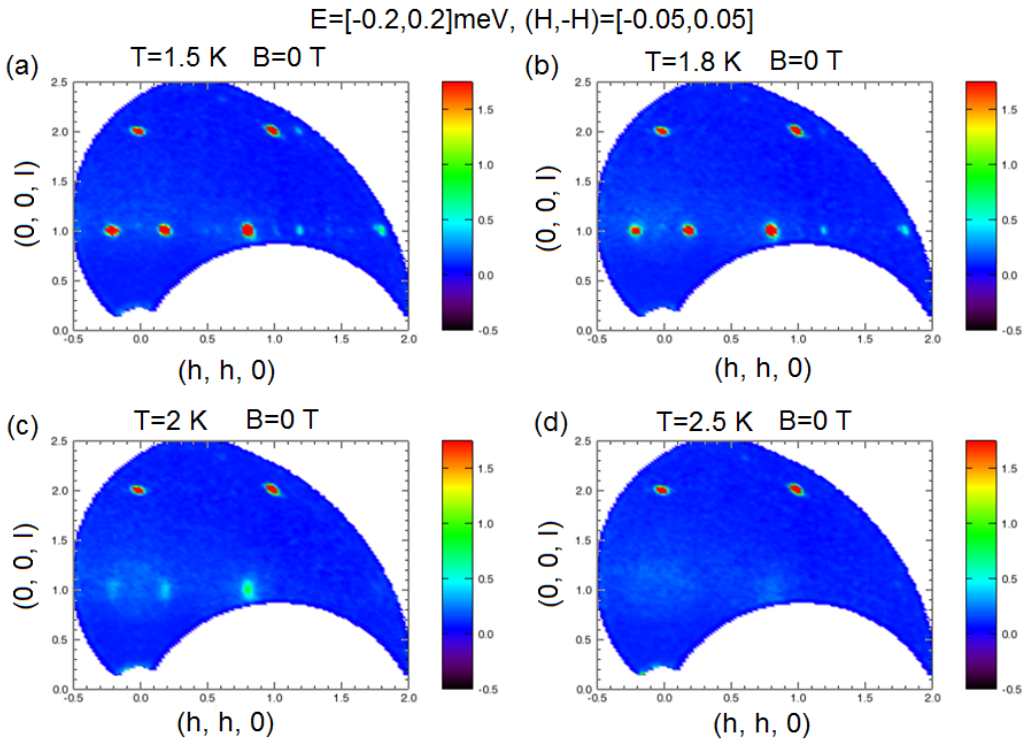

Figure 5.7: Elastic neutron scattering pattern in the [H, H, L] plane taken at CNCS at different temperatures (a) 1.5 K, (b) 1.8 K, (c) 2.0 K and (d) 2.5 K in zero fields.

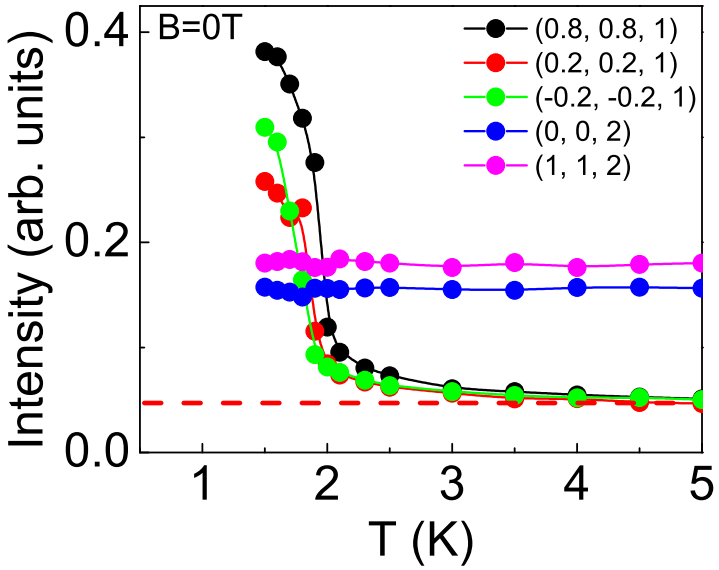

Figure 5.8: Temperature dependencies of the different elastic peak intensity in zero fields. (0.2,0.2,1), (-0.2,-0.2,1), and (0.8,0.8,1) are the three magnetic peaks, which develop rapidly below the 2 K transition temperature, and (001) and (112) are two nuclear peaks, whose intensities are almost independent of temperature.

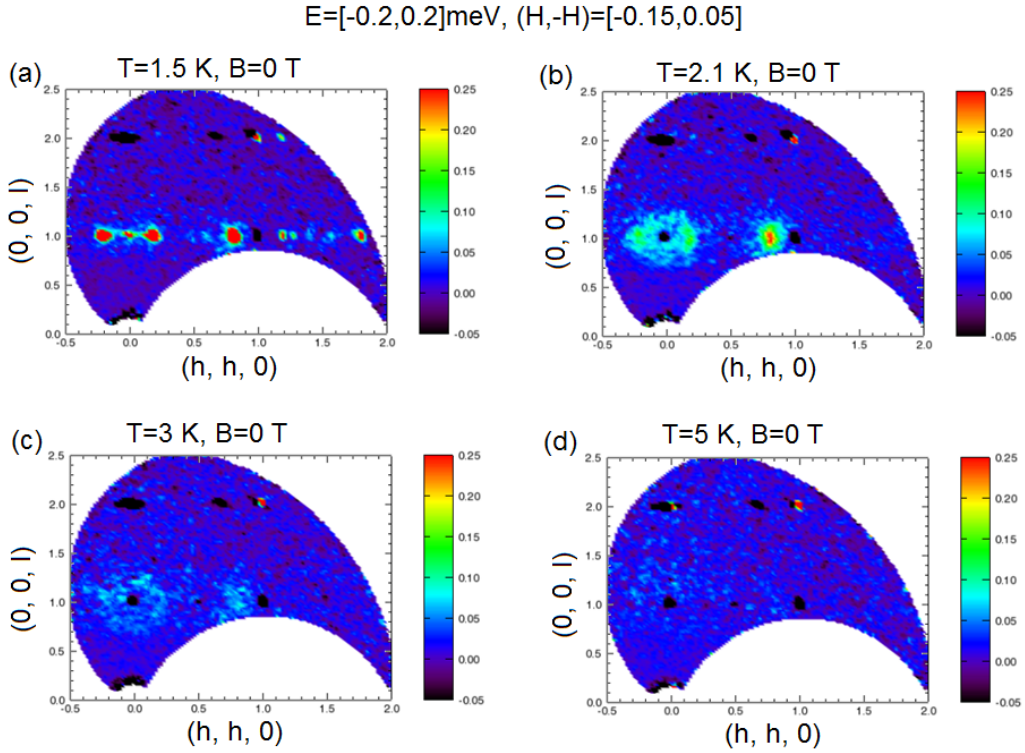

Figure 5.9: Contour plots of the zero field elastic scattering intensity in the [H, H, L] plane at temperatures (a) 1.5 K, (b) 2.1 K, (c) 3.0 K, and (d) 5.0 K with the 1.6 K, 4.75 T data subtracted as background.

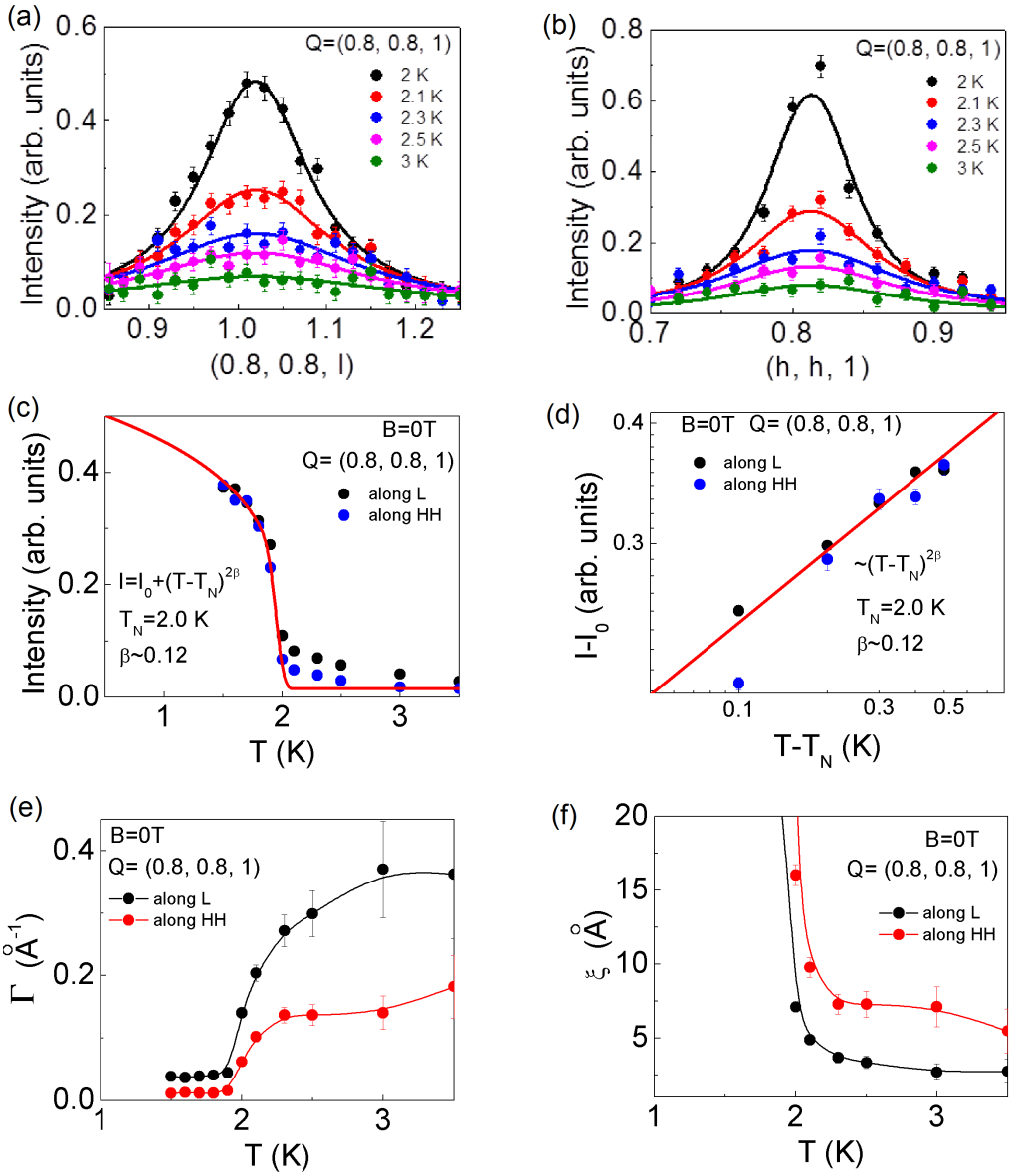

Figure 5.10: Scattering intensity of the magnetic peak $(0.8, 0.8, 1)$ at different temperatures across the longitudinal $(0.8, 0.8, l)$ (a), and the transverse $(h, h, 1)$ directions (b). The solid lines are fits to the Lorentzians. (c) Temperature dependence of the fitted peak intensity of the $(0.8, 0.8, 1)$ magnetic peak along both the $(0.8, 0.8, l)$ and $(h, h, 1)$ directions. (d) Log-log plot of the fitting of the magnetic intensity $I - I_0$ in relation to the reduced temperature $T - T_N$. The red lines in (c) and (d) are fits to power law expressions as indicated. (e) Temperature dependencies of the fitted full width at half maximum Γ along the $(0.8, 0.8, l)$ and $(h, h, 1)$ directions. (f) Plot of the correlation length $\xi = 1/\Gamma$ as a function of temperature near the phase transition at 2.0 K.

antiferromagnetic order. The temperature dependence of the fitted peak intensity is plotted in fig. 5.10c across both longitudinal and transverse directions. The red line is the fit of this peak intensity to the power law expression:

$$I = I_0 + (T - T_N)^{2\beta}. \tag{5.2}$$

By fixing the ordering temperature $T_N = 2.0$ K, a reasonable fitting is shown in fig. 5.10c and fig. 5.10d with the critical exponent $\beta \simeq 0.124 \pm 0.006$. This value is close to $\beta = 1/8$, which one would expected from the 2-dimensional Ising universality class. As we have discussed earlier, the Yb moments are constrained in the ab plane, with strong Ising like character. Thus it is not surprising that the zero field antiferromagnetic order falls into the 2-D Ising universality class. The tail of the magnetic peak intensity above the transition temperature suggests the existence of critical fluctuations,with a spatial correlation length that can be estimated from the full peak width at the half maximum Γ of the fitting. Temperature dependencies of the fitted peak width Γ along the $(0.8, 0.8, l)$ and $(h, h, 1)$ directions are shown in fig. 5.10e. With decreasing temperature, the value of Γ quickly decreases to a constant value below the transition temperature 2.0 K. The temperature dependencies of the associated correlation length $\xi = 1/\Gamma$ are plotted in fig. 5.10f. As we approach the transition temperature $T \to T_N$, the correlation length ξ increases to $\sim 5 - 10$Å, which is about the same scale as the crystal lattice parameter ~ 7Å. Anisotropic behaviors were seen in the fitted peak width Γ for cuts along the $(0.8, 0.8, l)$ and $(h, h, 1)$ directions, which may be intrinsic. However, the experiments were performed on hundreds of aligned single crystals, we have to consider the mosaic arising from the quality of the alignment. Since the crystals are long needle or bar like along the c axis, the broadening in the longitudinal $(0.8, 0.8, l)$ direction may also be due to some misalignment of crystals in the c directions.

Scattering in different fields at $T = 1.5$ K

Now we focus on the field dependencies of these magnetic peaks at $T = 1.5$K. Contour plots of the elastic neutron scattering patterns in the [H, H, L] plane in fields from 0.2 T up to 3.0 T are shown in fig. 5.11. With increasing field, the three magnetic peaks at (0.2, 0.2, 1), (-0.2, -0.2, 1) and (0.8, 0.8, 1) become very broad just above the the phase boundary in fields $B = 0.8$ T at $T = 1.5$ K (fig. 5.11c), and disappear for fields $B \geq 1.0$ T (fig. 5.11 d-f). The scattering intensity of the (0.8, 0.8, 1) peak was fitted to a Gaussian function, and the field dependence of the fitted scattering intensity is plotted in fig. 5.12. The

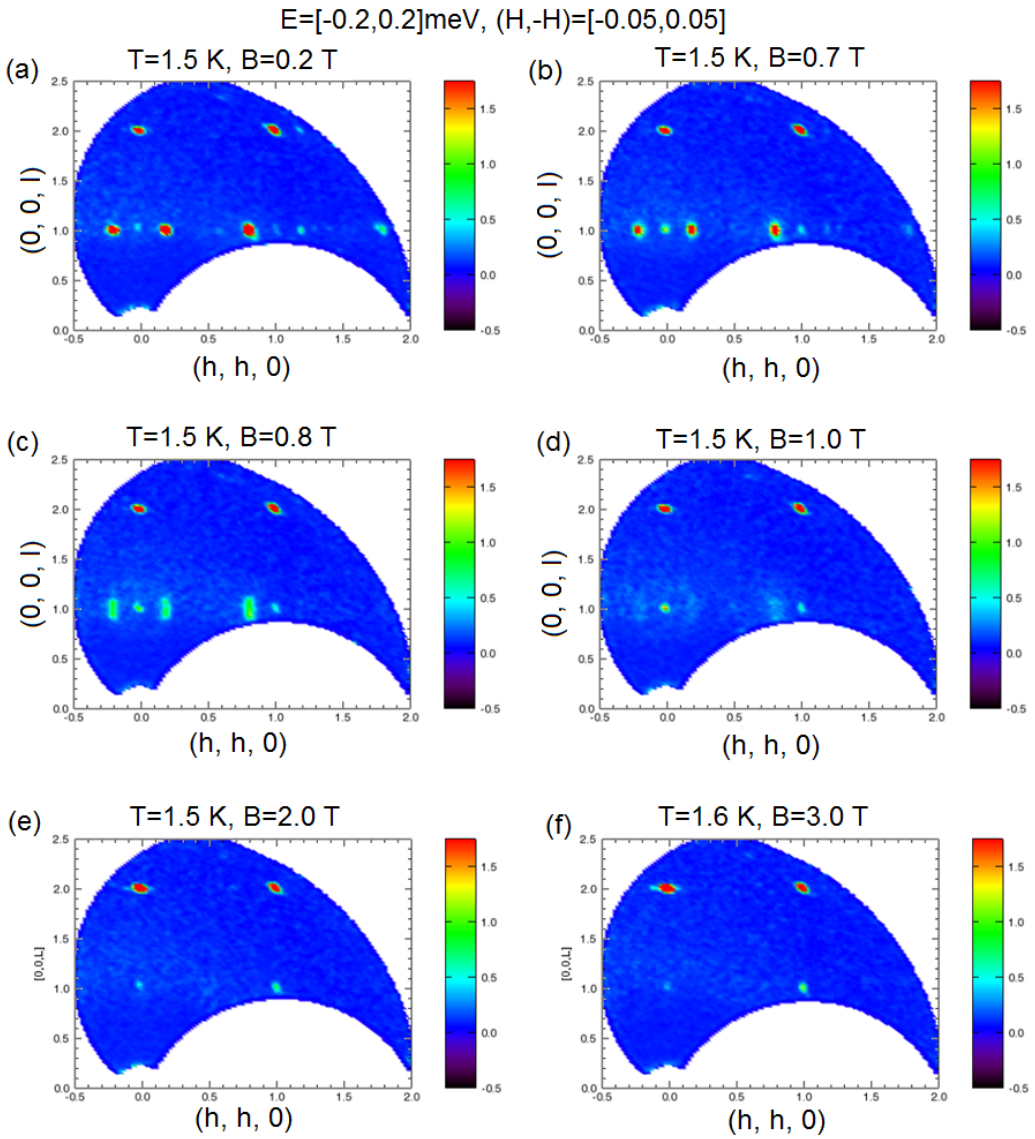

Figure 5.11: Elastic neutron scattering pattern in the [H, H, L] plane taken at CNCS in different fields (a) 0.2 T, (b) 0.7 T, (c) 0.8 T, (d) 1.0 T, (e) 2.0 T, and (f) 3.0 T at temperatures around 1.5 K.

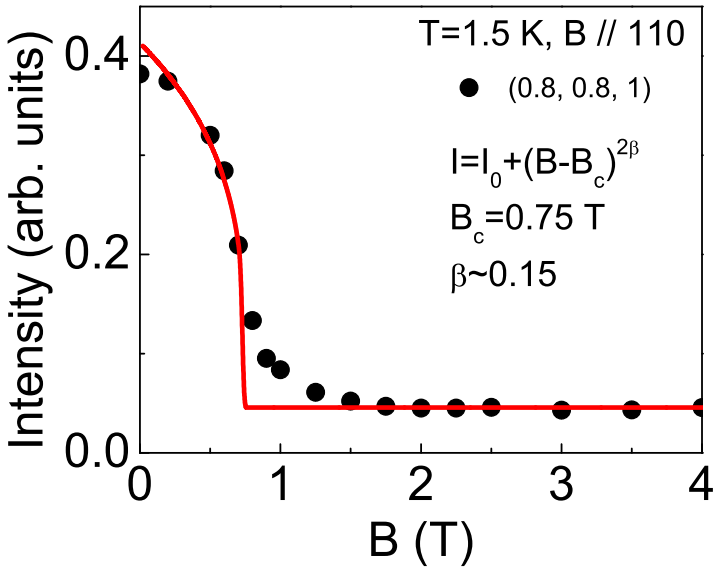

Figure 5.12: Magnetic field dependence of the scattering intensity of the peak (0.8, 0.8, 1) at temperatures around 1.5 K. The red line is the fit to the power law expression as indicated.

red line is the fit to the power law expression:

$$I = I_0 + (B - B_c)^{2\beta}, \tag{5.3}$$

with the critical field $B_c = 0.75$ T, and the critical exponent $\beta = 0.15 \pm 0.02$. This value is close to the one we obtained from the temperature dependent scattering intensity in zero fields (fig. 5.10c-d), confirming the 2D Ising universality class. Similarly, tails of diffuse scattering were observed above the critical field, indicating the importance of critical fluctuations. All three $B = 0$ magnetic peaks disappear at almost the same critical fields, and no other anomalies were observed for fields above ~ 1.0 T.

We have also checked the field dependencies of the elastic peak intensities at Q=(0, 0, 2), (1, 1, 2) and (1, 1, 1), as shown in fig. 5.13. Although all three peaks have only nuclear contributions in zero field, they behave differently in fields. With increasing fields, the (0, 0, 2) peak has an almost constant intensity up to fields of about 0.8 T. The peak intensity then increases about two times more beyond the original nuclear intensity, and finally saturates above fields ~ 2.5 T. The scattered intensity of the (1, 1, 2) peak is constant over the entire magnetic field range up to 4.75 T. The (1, 1, 1) peak is an allowed nuclear peak, but with very weak scattering intensity. With increasing

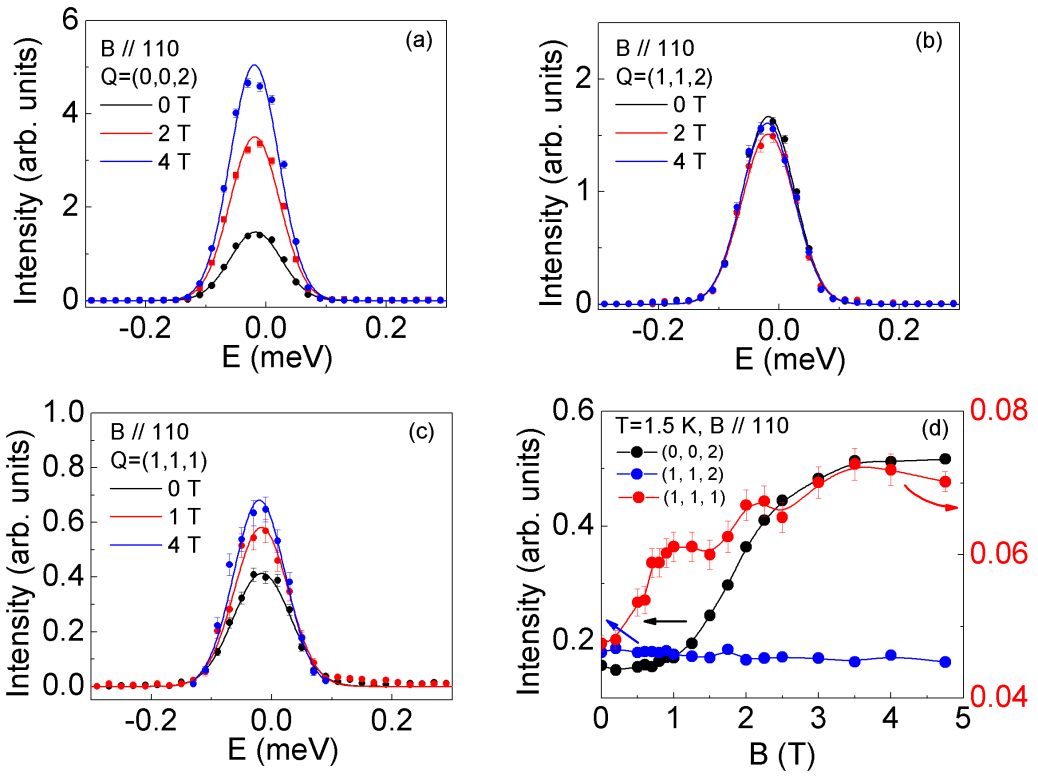

Figure 5.13: (a)Elastic neutron scattering intensity of the (0, 0, 2) peak as a function of energy, measured at 1.5 K in fields 0 T, 2 T, and 4 T as indicated. (b)Elastic neutron scattering intensity of the (1, 1, 2) peak as a function of energy measured at 1.5 K in fields 0 T, 2 T and 4 T, as indicated. (c)Elastic neutron scattering intensity of peak (1, 1, 1) as function of energy measured at 1.5 K in fields 0 T, 1 T, and 4 T as indicated. The solid lines in (a), (b) and (c) are the fits to the Gaussian expression. (d) Magnetic field dependencies of the peak intensity from the fits at Q=(0, 0, 2), (1, 1, 2) and (1, 1, 1) with $T = 1.5$ K.

fields, the peak intensity also increases, but saturates in fields larger than about $B > 2.5$ T. However, the overall change of intensity is about one order smaller compared to that of the (0, 0, 2) peak, leading to greater uncertainty in the fitted peak intensity.

5.2.2 Elastic neutron scattering in the [H, K, 0] plane

The phase diagram shown in the first section of this chapter has two horizontal phase lines that are almost independent of the magnetic field B (fig. 5.6). As we mentioned above, all three magnetic peaks with propagation vector $q_1 = (\pm 0.2, \pm 0.2, 0)$ in the [H, H, L] scattering plane disappears above the magnetic phase boundary, which is around 0.8 T at 1.5 K. No magnetic peaks in the [H, H, L] plane were observed in fields below the horizontal phase line at 2.0 K. We are able to resolve the scattering in the [H, K, 0] plane using the CNCS data, and this greatly clarifies the situation when we examine this scattering in the [H, K, 0] plane as a function of magnetic fields and temperatures.

Scattering at different temperatures for $B = 0$

Shown in fig. 5.14 are the contour plots of the $B = 0$ elastic neutron scattering intensity in the [H, K, 0] plane at different temperatures from 1.5 K to 2.5 K. The scattering is not completely symmetric around the origin, which may be caused by a misalignment of a few degrees. Although we could reach only a very small part of the [H, K, 0] plane, the accessible range within about $(h, -h) \simeq [-0.2, 0.175]$ already gives us a lot of information. It becomes very clear that there is an additional set of satellite peaks with a different propagation vector $q_2 = (\pm 0.2, \mp 0.2, 0)$ located around the positions (001), and (111), in addition to the satellite peaks with $q_1 = (\pm 0.2, \pm 0.2, 0)$ seen in the [H, H, L] scattering plane (fig. 5.14a). With increasing temperature, both sets of satellite peaks become weaker and broader around the 2.0 K transition (fig. 5.14b-c), and disappears at $T = 2.5$ K(fig. 5.14d). The scattering that remains at 2.5 K for $(h, -h) \simeq [0.15, 0.175]$ likely originates from background scattering from the edge of the magnet.

Scattering in different fields at $T = 1.5$ K

From fig. 5.14, we can see that the zero field transition at 2.0 K involves two sets of magnetic peaks with different propagation vectors $q_1 = (\pm 0.2, \pm 0.2, 0)$, and $q_2 = (\pm 0.2, \mp 0.2, 0)$. We already know from fig. 5.11 and fig. 5.12 that the satellite peaks with q_1 in the [H, H, L] plane disappear at the magnetic phase

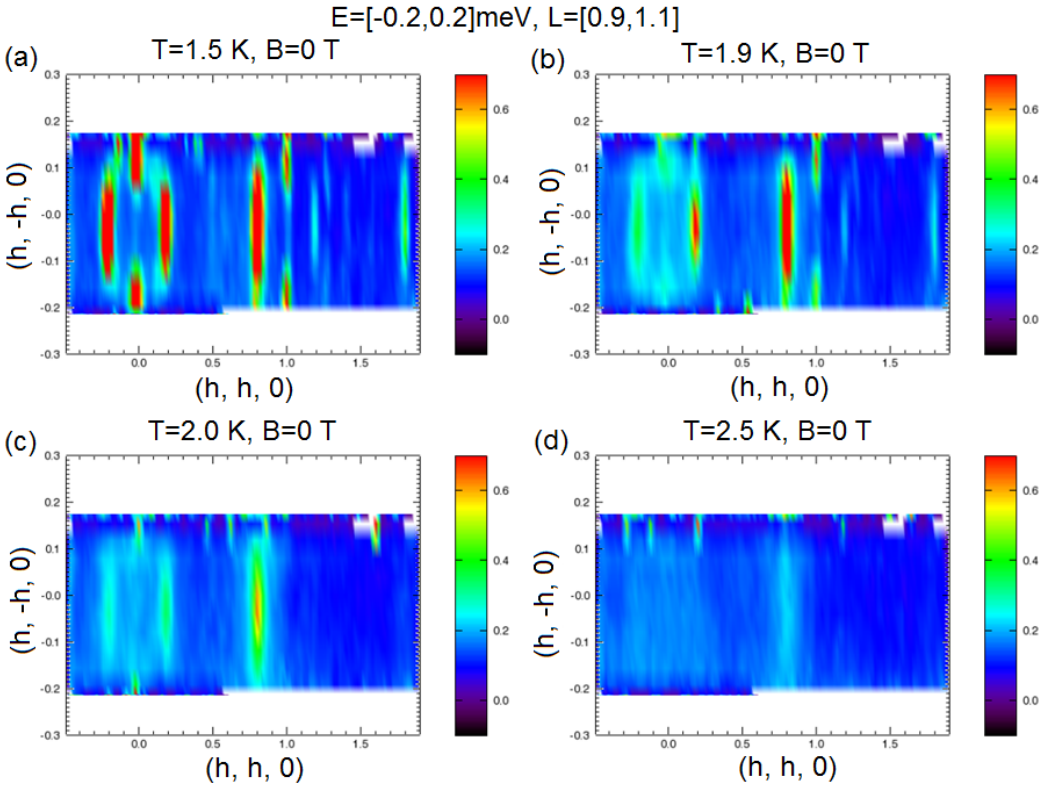

Figure 5.14: Elastic neutron scattering in the [H, K, 0] plane, taken at CNCS at different temperatures (a) 1.5 K, (b) 1.9 K, (c) 2.0 K, and (d) 2.5 K in zero fields.

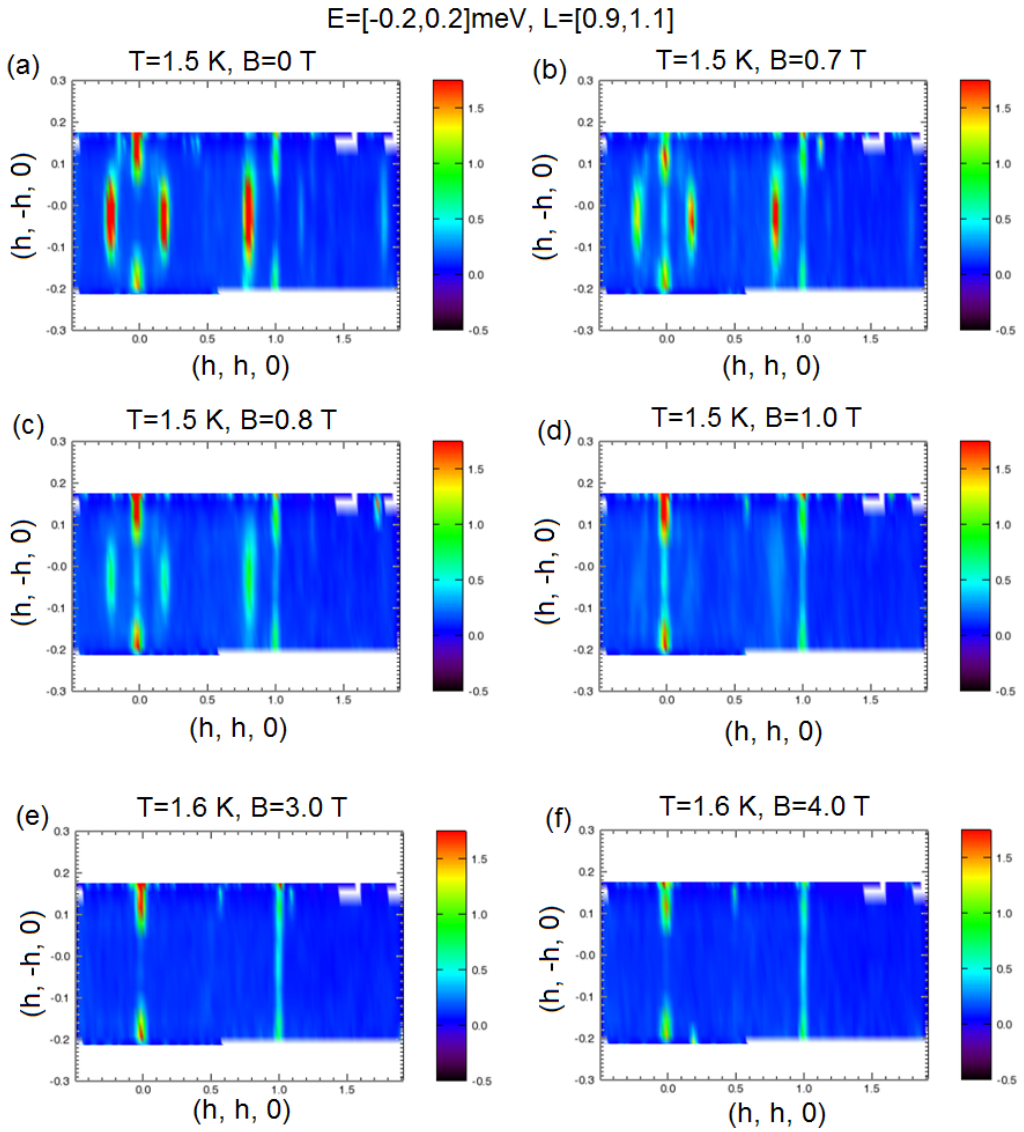

Figure 5.15: Elastic neutron scattering in the [H, K, 0] plane taken at CNCS in different fields (a) 0 T, (b) 0.7 T, (c) 0.8 T, (d) 1.0 T, (e) 3.0 T, and (f) 4.0 T at base temperature around 1.5 K.

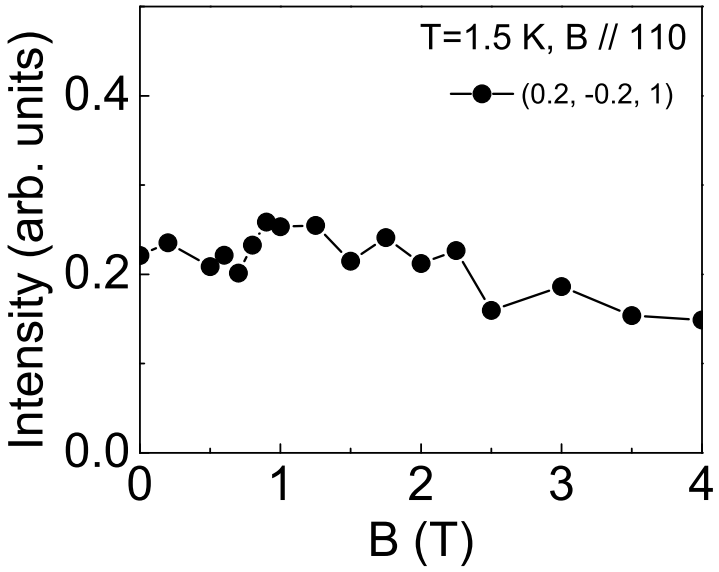

Figure 5.16: Magnetic field dependence of the measured intensity of the peak (0.2, -0.2, 1) for $T = 1.5$ K.

boundary around 0.8 T, but it is worthwhile to check the field dependencies of the other set of satellite peaks with q_2. Shown in fig. 5.15 is the elastic scattering pattern in the [H, K, 0] plane in different fields from 0 T up to 4.0 T. There is some heating, possibly due to eddy currents induced by the swept magnetic field, and the base temperature shifts from 1.5 K in zero field to about 1.6 K in 4.0 T. Despite this small difference in temperature, the satellite peaks with $q_2 = (\pm 0.2, \mp 0.2, 0)$r.l.u. survive to the highest measuring fields with almost constant intensity, as shown in fig. 5.16, while the magnetic peaks with $q_1 = (\pm 0.2, \pm 0.2, 0)$ disappear around 0.8 T, just as we expected.

Scattering at different temperatures in fields $B = 4.75$ T

Scans at different temperatures from 1.6 K to 2.5 K were also performed in fixed magnetic field $B = 4.75$ T, as shown in fig. 5.17. As the horizontal phase line at 2.0 K is approached in a fixed field of 4.75 T, the magnetic peaks with q_2 become much weaker, and finally disappear at $T = 2.5$ K. The peak intensities extracted from fig. 5.17 and fig. 5.14 are plotted together in fig. 5.18. We see that the magnetic peaks with propagation vector $q_2 = (\pm 0.2, \mp 0.2, 0)$ are not affected by the magnetic field along the (1, -1, 0) direction, but they disappear with increasing temperature at the horizontal phase line at 4.75 T. This is a direct evidence of the existence of the horizontal phase line at 2.0 K.

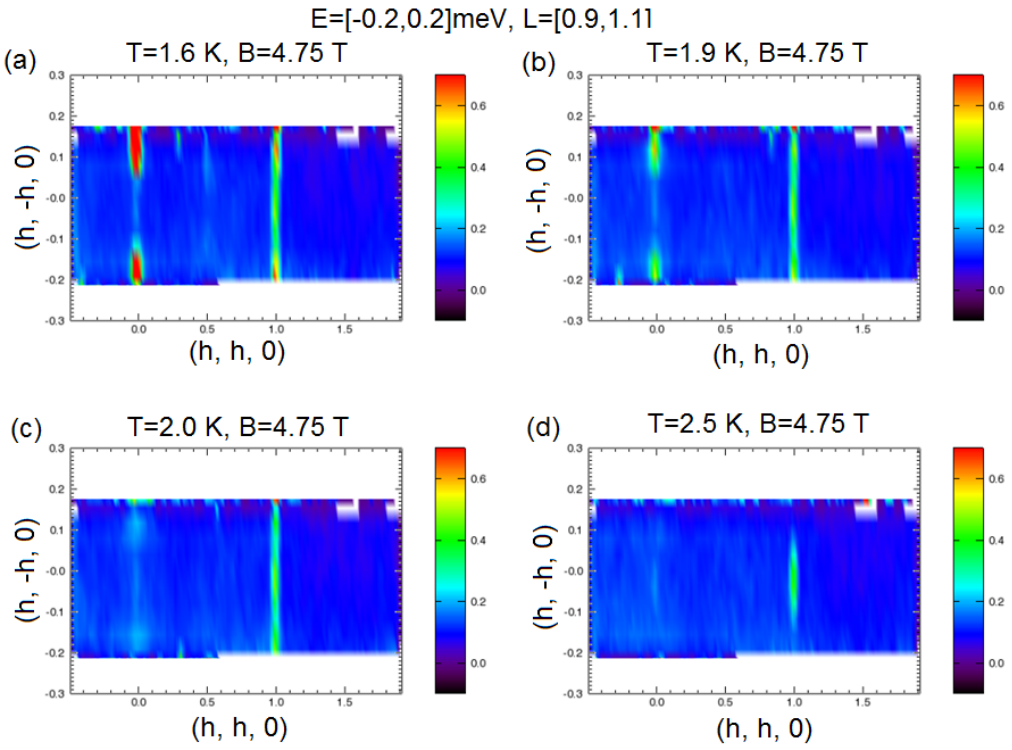

Figure 5.17: Elastic neutron scattering in the [H, K, 0] plane taken at CNCS at different temperatures (a) 1.6 K, (b) 1.9 K, (c) 2.0 K, and (d) 2.5 K in fields $B = 4.75$ T.

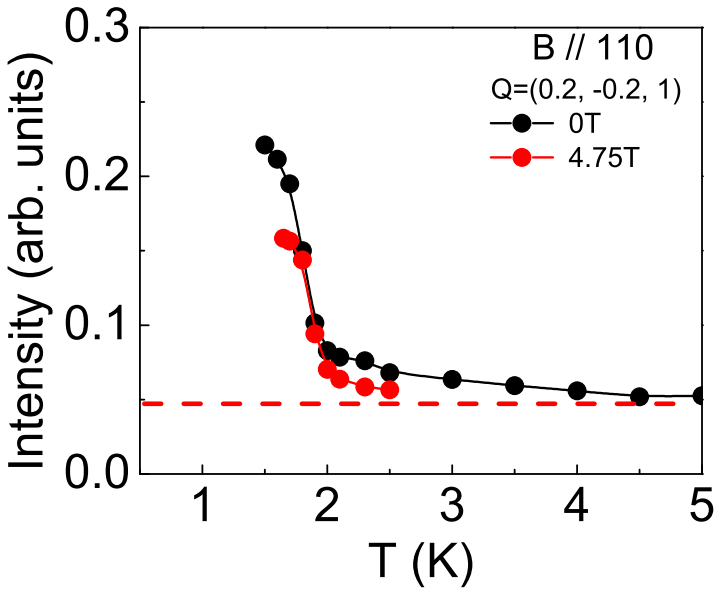

Figure 5.18: Temperature dependence of the measured intensity of the peak (0.2, -0.2, 1) in fields $B = 0$ T and $B = 4.75$ T.

Based on these observations, we divide the magnetic structure of Yb_2Pt_2Pb into two separate magnetic sublattices, and the Yb magnetic moments on each lattice are fixed along either (1, 1, 0) or (1, -1, 0) directions. When fields are applied along one of these two directions, only the sublattice with spins pointing in this direction is polarized, while the other sublattice with spins in the perpendicular direction is not affected at all, due to the strong Ising character of the moments.

5.2.3 Elastic neutron scattering at DCS

The elastic neutron scattering in the [H, H, L] scattering plane at temperature $T = 0.1$ K in different fields up to 4.0 T is extracted from the DCS data set, as shown in fig. 5.19. The scattering intensity was integrated over all the data in the the central detector bank, so some contribution from the [H, K, 0] plane within the angle θ is included. For example, the peak at $Q = (0, 0, 1)$ shown in fig. 5.19a comes from the tails of the two satellite peaks at $(0.2, -0.2, 1)$ and $(-0.2, 0.2, 1)$, outside of the [H, H, L] plane. Despite this, there are some new and interesting features at 0.1 K that are absent in the 1.5 K scans shown in fig. 5.11. The first is that the propagation vector q_1 for the satellite peaks in the [H, H, L] plane is not fixed to $q_1 = (\pm 0.2, \pm 0.2, 0)$ with increasing fields.

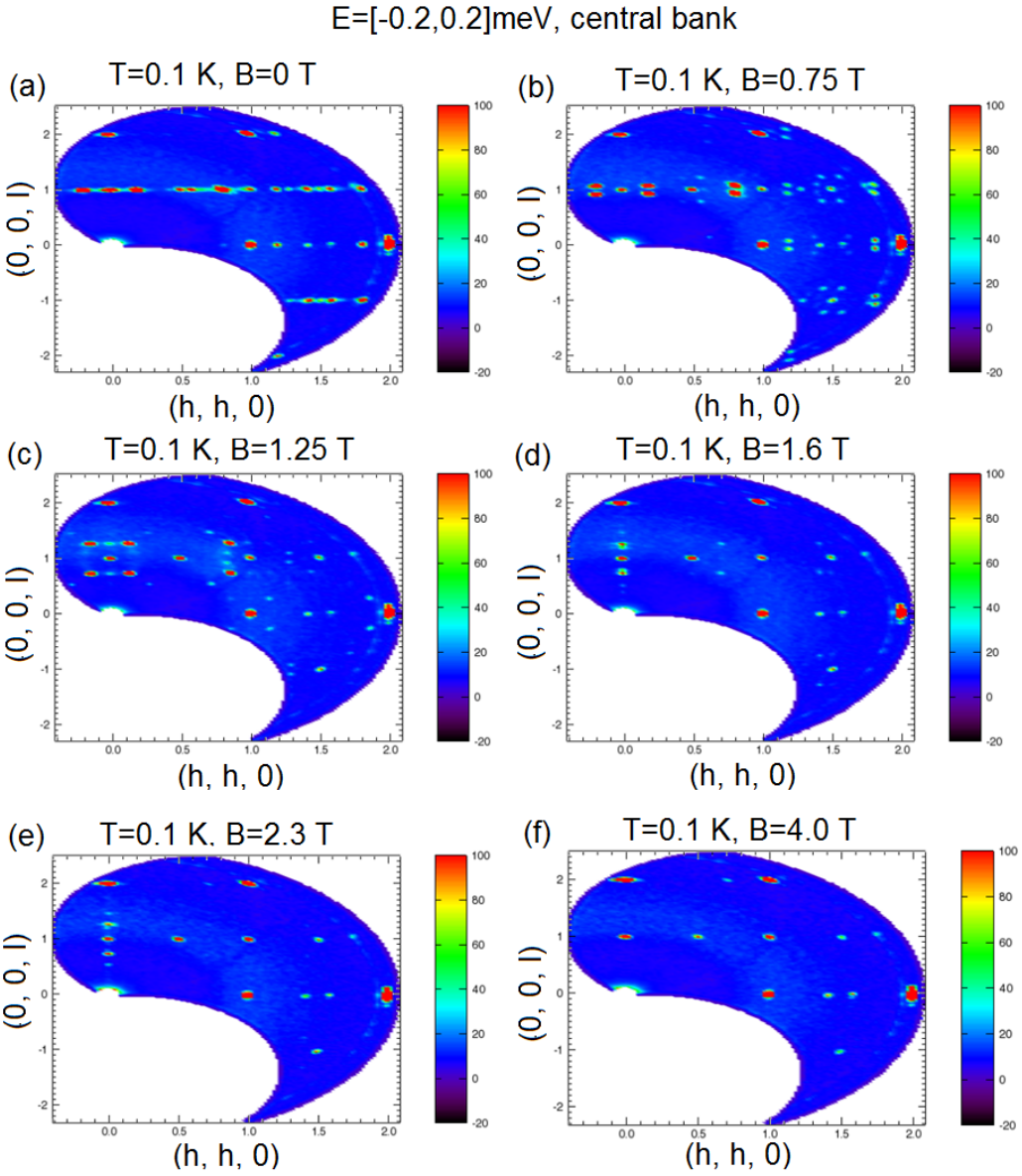

Figure 5.19: Contour plots of the elastic neutron scattering intensity in the [H, H, L] plane taken at DCS at temperature $T = 0.1$ K in different magnetic fields (a) 0 T, (b) 0.75 T, (c) 1.25 T, (d) 1.6 T, (e) 2.3 T and (f) 4.0 T. The plots were integrated with all the data in the central bank, and some contribution from the [H, K, 0] plane is included.

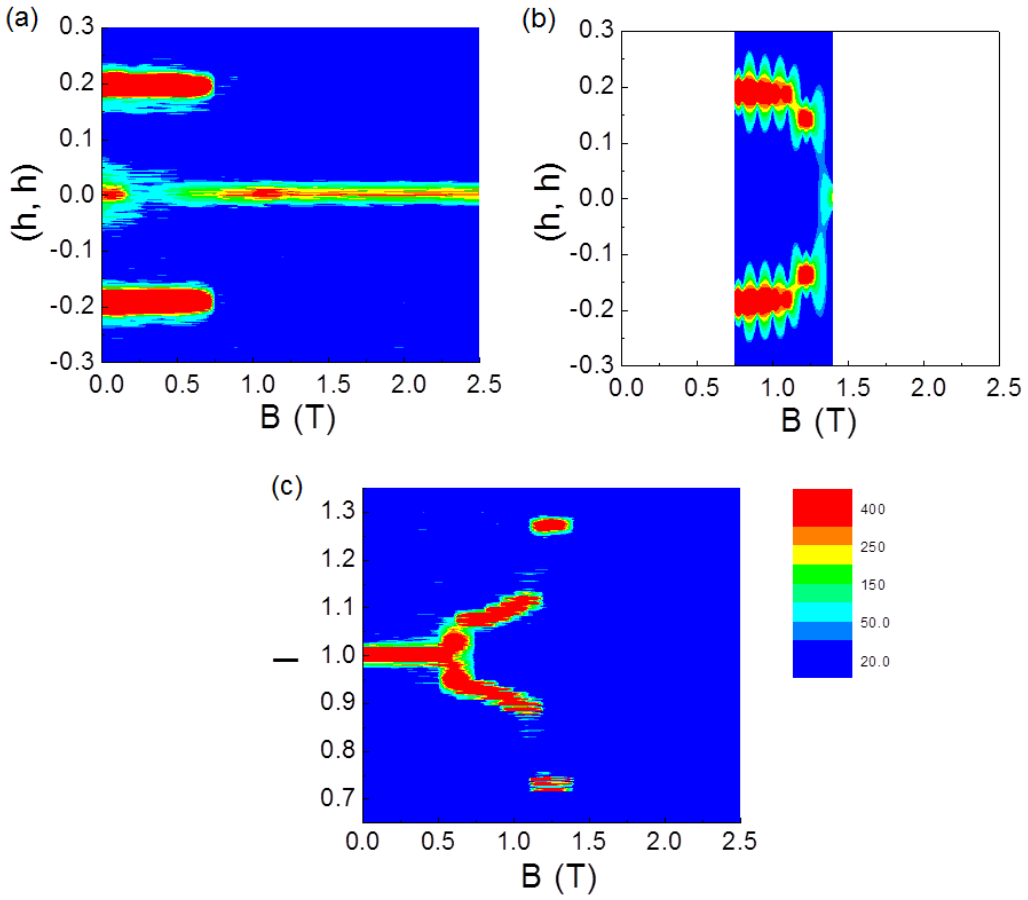

Figure 5.20: Contour plots of the propagation vector $q_1 = (\Delta q_h, \Delta q_h, \Delta q_l)$ as a function of magnetic field B at temperature $T = 0.1$ K. (a) Contour plot of the field dependent propagation vector $q = (h, h)$ with fixing $l = 1$. The two satellite peaks at $q = (0.2, 0.2, 1)$ and $q = (-0.2, -0.2, 1)$ could be traced up to the field B about 0.75 T. (b) Contour plot of the field dependent propagation vector $q = (h, h)$ with fixing l to the new peak positions for fields above 0.75 T. (c) Contour plot of the field dependent propagation vector $q = l$ with fixing (h, h) at the peak positions.

For magnetic fields $B \geq 0.75$ T, the satellite peaks start to split into two new peaks along the longitudinal l direction, and this splitting increases for fields increasing up to about 1.25 T, as shown in fig. 5.19c. These satellite peaks disappear if that field is above 1.25 T, and some new peaks remain around (0, 0, 1.25) and (0, 0, -1.25) at 1.6 T and and 2.3 T (fig. 5.19d and fig. 5.19e). This may be related to the low temperature dome phase shown in fig. 5.6. At $B = 4.0$ T, in addition to the nuclear peaks at (0, 0, 2), (1, 1, 2), (1, 1, 1), (1, 1, 0) and (2, 2, 0), there are still a few magnetic peaks left at positions (0.5, 0.5, 1), (1.5, 1.5, 1) and (1.5, 1.5, -1), and two satellite peaks at (1.4, 1.4, 0) and (1.6, 1.6, 0). These new magnetic peaks observed in $B = 4.0$ T at $T = 0.1$ K are likely to be related to the second field independent phase line around 0.8 K. The three peaks at (0.5, 0.5, 1), (1.5, 1.5, 1) and (1.5, 1.5, -1) could all be assigned to another propagation vector $q_3 = (\pm 0.5, \pm 0.5, 0)$, which suggest that the unit cell of each sublattice is doubled again below the second horizontal phase line at 0.8 K. Higher order harmonics were observed in the low field (fig. 5.19a-c), indicating that the spins may be frozen into a square wave like superstructure [230].

To have a better idea of the field dependencies of the satellite peaks at $(0.2, 0.2, 1)$ and $(-0.2, -0.2, 1)$, we have traced the peak positions in different fields, and project them onto the transverse (hh) and longitudinal l directions, as shown in fig. 5.20. First, we focus on the change of propagation vector q in the (hh) direction. Fig. 5.20a is the contour plot of the field dependent propagation vector $q = (h, h)$ with $l = 1$. The satellite peaks at $q_1 = (\Delta q_h, \Delta q_h, \Delta q_l)$ gives to $q_1 = (\pm 0.2, \pm 0.2, 0)$ for the field B up to about 0.75 T. Above this field, the satellite peaks start to shift along l, and by fixing l to the new peak positions, these satellite peaks could then be traced up to about 1.25 T (fig. 5.20b). From fig. 5.20b, we also noticed that for fields above about 0.75 T, the propagation vector Δq_h along the (h, h) direction shifts in magnitude from 0.2 reciprocal lattice units (rlu) to 0.175 rlu at about 1.1 T, and this value jumped to about 0.15 at about 1.25 T. Fig. 5.20c is the contour plot of the field dependent propagation vector projected onto the longitudinal direction l with fixed (h, h) at the peak positions. Step-like anomalies were observed in fields between about 0.5 T to 1.25 T, which correspond to those plateaus found in the field dependent magnetization. The change of Δq_h from 0.2 suggests that the unit cells in these higher field plateau phases are bigger than the 5×5 superstructure found in zero field, and the change of Δq_l from zero indicates the increase in the size of the unit cells along the chain direction in these plateau phases.

Shown in fig. 5.21 are the field dependencies of the scattering intensity at peak positions Q=(0, 0, 2) and Q=(1, 1, 2), measured at temperature $T = 0.1$

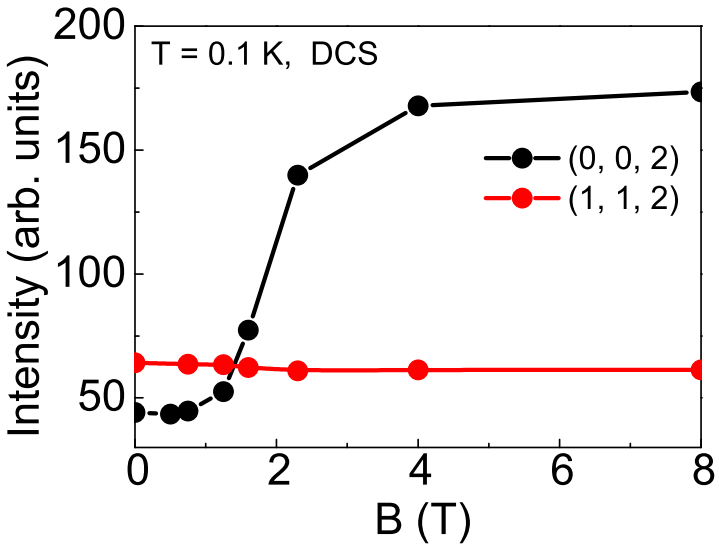

Figure 5.21: Magnetic field dependencies of the scattering intensity at peak positions Q=(0, 0, 2) and Q=(1, 1, 2) measured at temperature $T = 0.1$ K.

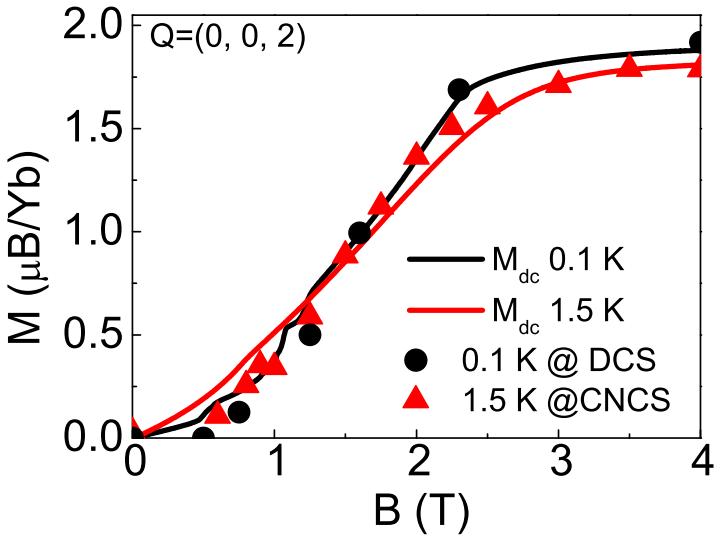

Figure 5.22: Measured magnetic field dependent dc magnetization at 0.1 K (black solid line) and 1.5 K (red solid line) plot over the re-scaled field dependent neutron scattering intensity of peak (002) at $T = 0.1$ K (DCS, black solid circle) and $T = 1.5$ K (CNCS, red solid triangle).

K. The intensity of the (1, 1, 2) peak is still almost constant over the entire field range. But for the (0, 0, 2) peak, the scattering intensity increases rapidly for fields larger than 0.5 T, and saturates for fields above 2.3 T. In order to directly compare the data measured at CNCS at 1.5 K to the data taken at DCS at 0.1 K, we have re-scaled the magnitude of the field dependent (0, 0, 2) peak intensity in both DCS and CNCS experiments to the measured dc magnetization at 1.5 K and 0.1 K, before plotting them together, as shown in fig. 5.22. The measured neutron scattering intensity matches well with the dc magnetization data. In addition, we might be able to use the scaling factor found in this figure to relate the absolute intensities of the DCS and CNCS experiments in the future. We have noticed that, even at 0.1 K, the measured dc magnetization is still finite and increases with a small slope for field $B < 0.5$ T, which is the first critical field seen in the magnetic phase diagram. However, the measured magnetic scattering intensity at the (002) peak is almost zero below 0.5 T at 0.1K. We attribute this finite dc magnetization below 0.5 T to a paramagnetic contribution, which will be corrected by subtracting a small linear background in the future analysis.

5.3 Inelastic Neutron Scattering

The elastic neutron scattering data discussed in the previous section confirms the two sublattice model with Ising spins pointing along the orthogonal (110) or (1-10) directions. However, it is still unclear how important the SSL expected from the crystal structure in the ab plane is to the physics of Yb_2Pt_2Pb . We briefly discuss the inelastic neutron scattering experiment results in this section, as a first look at this issue.

Shown in fig. 5.23 is the energy slice along the $(0, 0, l)$ direction with (hh) integrated over the range [1.4,1.6] rlu in different fields from 0 T to 1.6 T, as indicated. As was discussed earlier, the Yb ions in Yb_2Pt_2Pb can be viewed as forming in a 2D SSL with orthogonal arranged pairs of Yb nearest neighbors [66]. Our first starting point is that Yb_2Pt_2Pb consists of weakly coupled SSL planes. Since the experiments were performed at 0.1 K, where the thermal fluctuations should be very weak, we expect a narrow and almost wave vector independent excitation at this temperature for $Q \parallel (00l)$, as seen in the SSL compound $SrCu_2(BO_3)_2$ [64]. Thus it was very surprising that a broad continuum with significant dispersion in the $(00l)$ direction was observed at 0.1 K in zero field (fig. 5.23a). We have chosen $(hh) \simeq 1.5$ where two continua are symmetric around $l = 0$, which demonstrates that these particular Q dependencies are not experimental artifacts. This broad continuum of excitations shows very interesting behaviors in field. As seen in

fig. 5.23b, part of the intensity extends to lower energies, and the dispersion becomes gapless at $l = (1 \pm \Delta q_l)$, with $\Delta q_l \simeq 0.1$ for $B = 0.75$ T. Increasing the field up to 1.25 T makes it more clear that there is some dispersion connecting the points $l = (1 \pm \Delta q_l)$ with $\Delta q_l \simeq 0.3$. The dispersion inside the dome phase region at 0.1 K in 1.6 T is more complex, as shown in fig. 5.23d. The excitations are gapless around $l = (1 \pm \Delta q_l)$ with $\Delta q_l \simeq 0.4$. More careful analysis still needs to be done to understand these field dependencies, especially inside the dome phase.

Shown in fig. 5.24 is the energy slice of the DCS data with $B = 0$ at $T = 0.1$ K, along the $(h, h, 0)$ direction with l integrated over different ranges from $l = 0$ to $l = 2$. The extra intensity in the inelastic scattering in fig. 5.24a near $hh = 1$ and $hh = 2$ is not from real inelastic excitations, but comes from the tails of strong elastic diffraction peaks (110) and (220). The extra scattering in fig. 5.24b near $hh = 0.2$ and $hh = 0.8$ is also from the tails of the strong elastic diffraction peaks (0.2, 0.2, 1) and (0.8, 0.8, 1). Besides these, the excitations observed at $l = 1$(fig. 5.24b) and $l = 1.5$(fig. 5.24c) are almost flat along the $(h, h, 0)$ direction. The magnetic scattering intensities at $l = 0$ (fig. 5.24a) and $l = 2$ (fig. 5.24d) are very weak, just slightly above background, while scattering at $l = 1$ has the strongest intensity.

The significant dispersion along the l direction compared to the weak dispersion in the hh direction strongly demonstrates that the interaction along c is very important. It may even be the dominant factor for understanding the low temperature physics in Yb_2Pt_2Pb . We have plotted the field dependent dc magnetization M/M_s (solid line) measured at 0.1 K together with the l component of the propagation vector (Δq_l), as shown in fig. 5.25. The dc magnetization M shown here has already been corrected by a linear background to compensate the paramagnetic contribution below 0.5 T as discussed before, and the saturation moment $M_s = 1.9\mu_B$ is taken from the high field magnetization data 5.4 [66]. The colored contour plot is the Δq_l extracted from the elastic neutron scattering experiments, as shown in fig. 5.20c, and the empty circles are the Δq_l where the inelastic data become gapless or nearly so, as shown in fig. 5.23. It is surprising to see that the l component of the propagation vector Δq_l traces the plateaux of $M(B)/M_s$ so well. The values of Δq_l where the inelastic scattering dispersion curve become gapless roughly follow the same trend. This relation with

$$\Delta q_l = \pi(1 - M/M_s) \tag{5.4}$$

is similar to what has been observed in the quantum spin-ladder material $(C_5H_{12}N)_2CuBr_4$ [234]. In our case, Yb^{3+} ions remain in the ground doublet states ($J_z = |\pm 7/2\rangle$), which can be treated as pseudo-spin 1/2 states. The

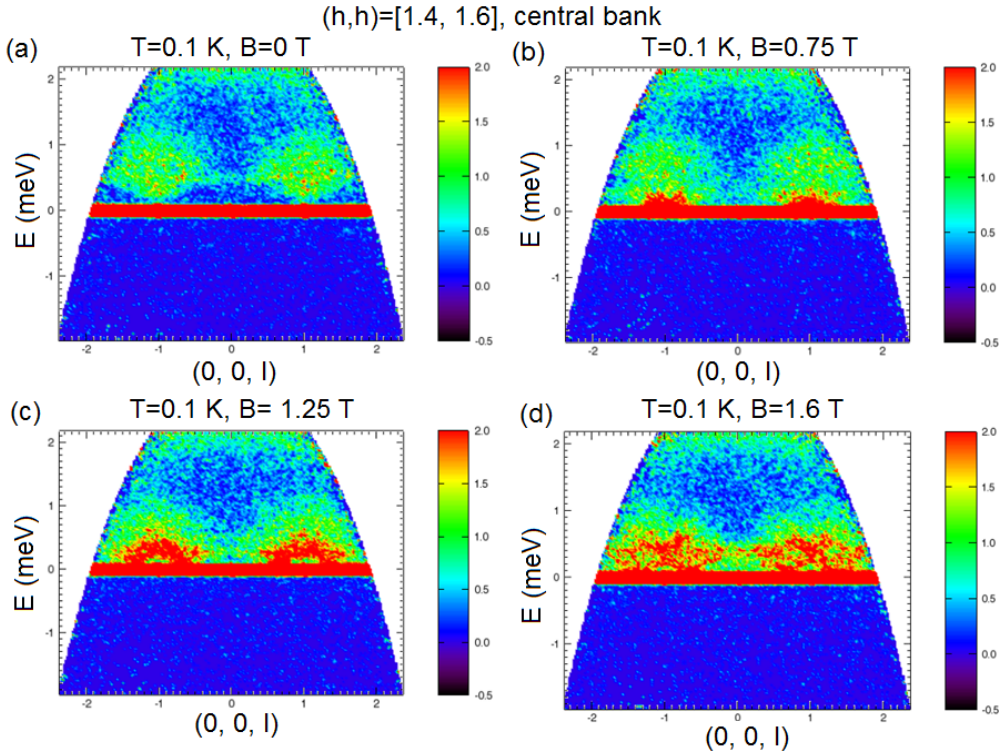

Figure 5.23: Inelastic neutron scattering measured at DCS at temperatrue $T = 0.1$ K. (a)-(d) is the energy slice along the $(0, 0, l)$ direction with (hh) integrated over the range [1.4,1.6] in different fields from 0 T to 1.6 T as indicated.

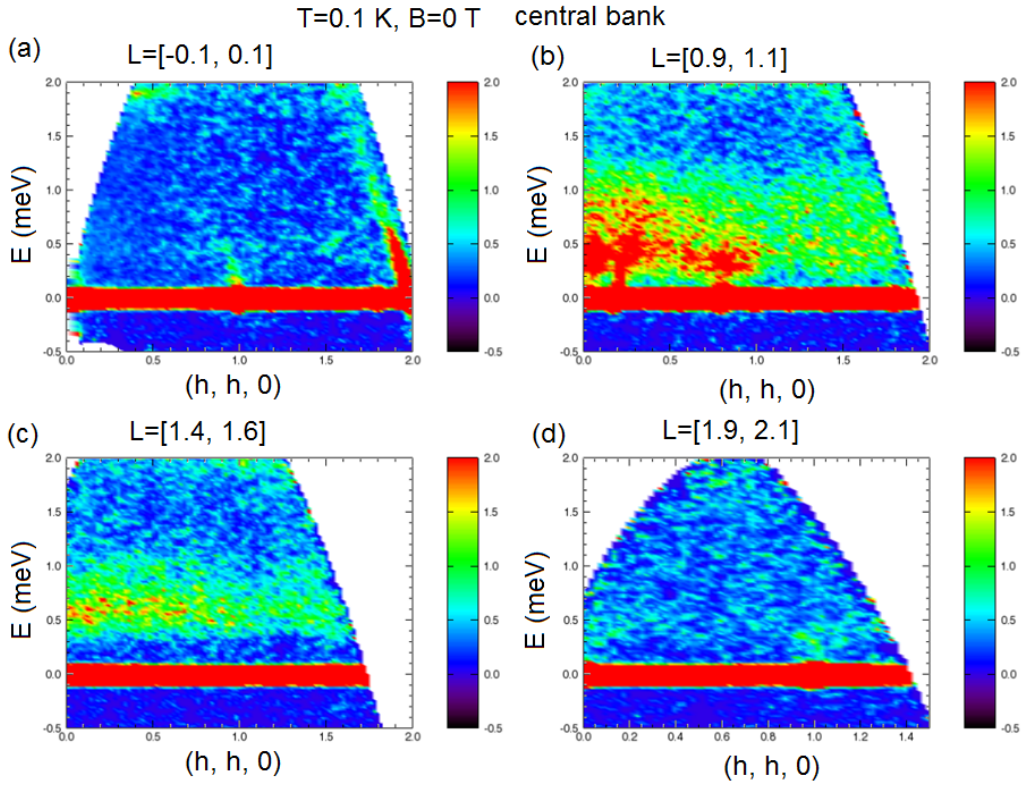

Figure 5.24: Inelastic neutron scattering pattern measured at DCS at temperatrue $T = 0.1$ K in zero fields. (a)-(d) is the energy slice along the $(h, h, 0)$ direction with l integrated over different ranges as indicated. The extra intensity in the inelastic scattering in (a) near $hh = 1$ and $hh = 2$ come from the tails of the strong elastic diffraction peaks (110) and (220). The extra scattering in (b) near $hh = 0.2$ and $hh = 0.8$ are from the tails of the strong elastic diffraction peaks (0.2, 0.2, 1) and (0.8, 0.8, 1).

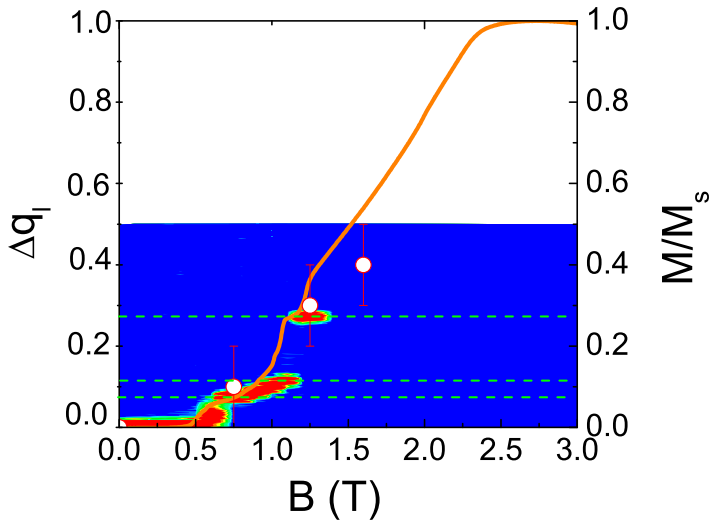

Figure 5.25: Field dependent dc magnetization M/M_s (solid line) measured at 0.1 K plotted together with the l component of the propagation vector Δq_l. The colored contour plot is the Δq_l extracted from the elastic neutron scattering experiments, as shown in fig. 5.20c, and the empty circles are the Δq_l that correspond to the wave vectors when the inelastic data become gapless, or nearly so, as shown in fig. 5.23.

observation of relation 5.4 in fig. 5.25 is strong evidence that one dimensional physics along c is crucial in Yb_2Pt_2Pb .

Shown in fig. 5.26a is the inelastic neutron scattering intensity in the [H, H, L] scattering plane, integrated over the energy range from $0.4 \sim 1$ meV, measured at CNCS at 1.8 K in zero field. The magnetic scattering is greatly suppressed for $l = 0$ and $l = 2$, and reaches a maximum intensity at $l = 1$. A cut of the inelastic neutron scattering intensity along the $(1.5, 1.5, l)$ direction is shown in fig. 5.26b. This particular Q dependence is well described by the following structure factor:

$$S(q) \sim \sin^2 (l\pi/2), \tag{5.5}$$

as indicated by the red line. This expression results from an antiferromagnetic coupling of the spins in the $z = 0$ and $z = 1/2$ planes. The modulation of the inelastic scattering intensity along the (hh) direction is not as pronounced as along the $(00l)$. Part of the reason may be that the interactions in the plane are not as significant as the interactions along the c axis. However, we can see from fig. 5.26a that the scattering is peaked around the position with $(hh) = 0$. Since this requires ferromagnetic coupling in the plane, it was initially hard to understand this within the SSL dimer picture. According to the recently solved magnetic structure in zero field, the coupled spins pairs form a 5×5 ferromagnetic superlattice in the ab plane [230]. Energy slices along the $(h, h, 1.5)$, and the $(1.5, 1.5, l)$ directions, measured at 1.8 K in zero field, are shown in fig. 5.26c and fig. 5.26d, respectively. The dispersions in both directions are not much different from the 0.1 K data shown earlier, except that the scattering is more smeared than the 0.1 K data. Similar Q dependencies of the energy slices along the $(h, h, 1.5)$, and the $(1.5, 1.5, l)$ direction were seen for temperatures as high as 50 K, as shown in fig. 5.26e, and fig. 5.26f. Since at $T = 50$ K, Curie-Weiss behaviors were always observed in the magnetic susceptibility, and Yb local moments are fully recovered, one would not expect to see any strong correlations at this high temperature range. The only energy scale that could be comparable to this temperature is the first CEF excitation energy $\Delta_1 \simeq 70$ K. One possible scenario is that for all temperatures $T < \Delta_1$, the Yb ions are constrained to the Ising $|\pm 7/2\rangle$ ground states. These Ising spins pointing in the (110) and (1-10) directions are aligned antiferromagnetically along the crystal c axis, and one has to go to temperatures that are much larger than the energy scale Δ_1 to really compromise the pure Ising character of the ground doublet states.

A simplified illustration of the magnetic coupling of the Ising spins along c are shown in fig. 5.27, corresponding to the two different possible spin configurations in the ab plane (fig. 5.5). The Yb moments are pointing

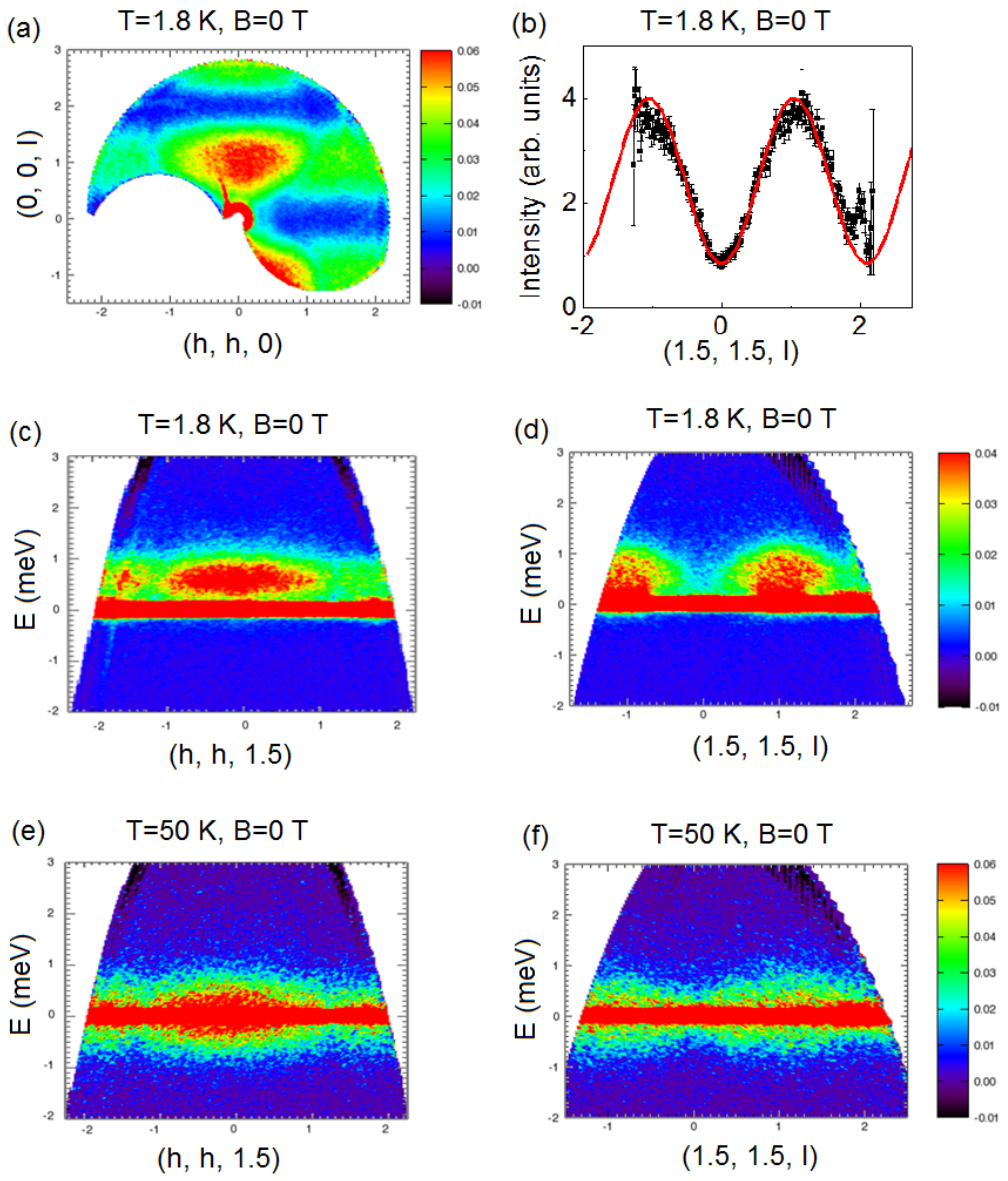

Figure 5.26: (a) Inelastic neutron scattering intensity from CNCS data in the [H, H, L] scattering plane, integrated over the energy range [0.4, 1] meV. (b) Wave vector cut of the inelastic neutron scattering intensity with E=[0.4-1]meV along the $(1.5, 1.5, l)$ direction. The red solid line is the fit to the expression $I \sim \sin^2(l\pi/2)$. (c) Energy slice along the $(h, h, 0)$ direction with l integrated over the range [1.4, 1.6] at 1.8 K in zero fields. (d) Energy slice along the $(0, 0, l)$ direction with hh integrated over the range [1.4, 1.6] at 1.8 K in zero field. (e) Energy slice along the $(h, h, 0)$ direction with l integrated over the range [1.4, 1.6] at 50 K in zero field. (f) Energy slice along the $(0, 0, l)$ direction with hh integrated over the range [1.4, 1.6] at 50 K in zero field.

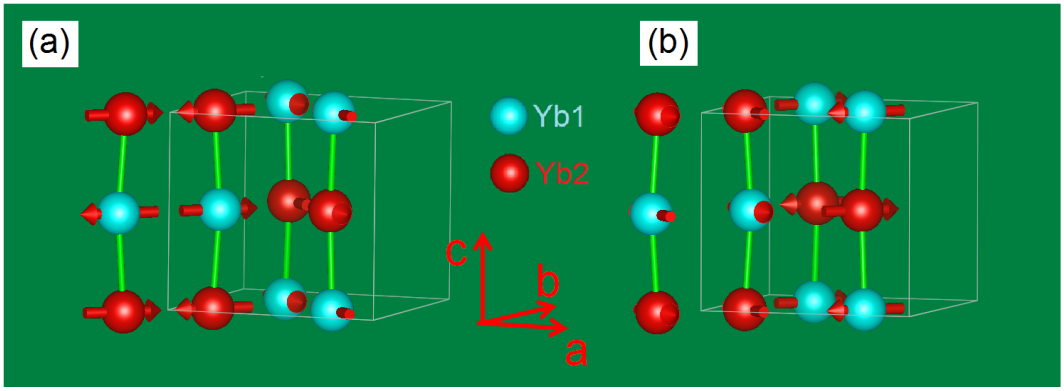

Figure 5.27: A simplified illustration of the antiferromagnetic coupled Ising spins along c axis. The moments are pointing along the diagonal direction of the nearest neighbor pairs in (a), and are pointing perpendicular to the direction of the nearest neighbor pairs in (b).

along the diagonal direction of the nearest neighbor pairs in fig. 5.27a, and are pointing perpendicular to the direction of the nearest neighbor pairs in fig. 5.27b. The real magnetic structure is much more complex in the ab plane with a 5×5 superlattice that gives the satellite peaks at $q_1 = (\pm 0.2, \pm 0.2, 0)$ and $q_2 = (\pm 0.2, \mp 0.2, 0)$ [230]. It was shown that the configuration in fig. 5.27b gives better fits to the diffraction data [230]. However, in either case, the interactions along the crystal c axis are always the same, while the Ising spins are coupled antiferromagnetically into chains along the c direction. The antiferromagnetic ordering at 2.0 K in zero field involves the locking together of these chains in the ab plane.

According to what we have discussed earlier, the elementary excitations for the one-dimensional antiferromagnetic coupled spin chains are spinons. Shown in fig. 5.28a is the energy dispersion along the $(0, 0, l)$ direction with (hh) integrated over the range [0.05, 0.95]. We have folded all the intensity to one Brillouin zone to improve the statistics of the data. The red dashed lines are the fit to the spinon dispersion in chapter 1 (relation 1.54) with the upper and lower bound as [52, 54]

$$E_{\text{upper}} = \pi J \sin\left(\frac{\pi q}{2}\right) \tag{5.6}$$

$$E_{\text{lower}} = \frac{\pi J}{2} \sin\left(\pi q\right), \tag{5.7}$$

with the antiferromagnetic coupling $J_{\|c} \simeq 0.38$ meV along the c direction inside the chain. A spinon excitation with much weaker intensity was also

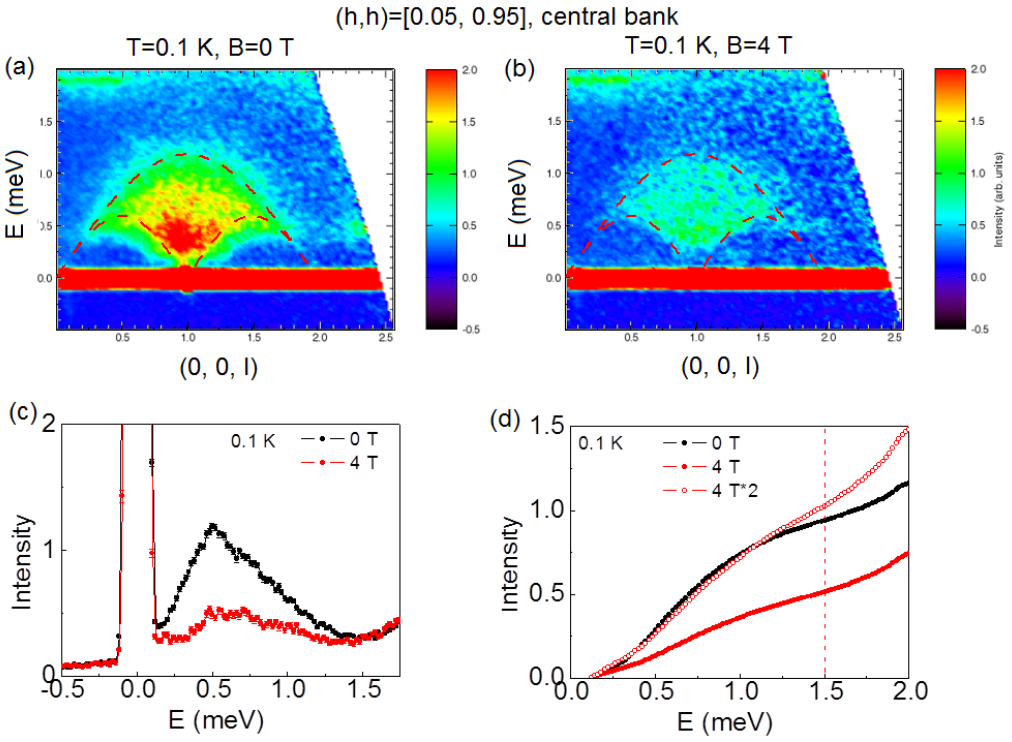

Figure 5.28: (a) Energy slice along the $(0, 0, l)$ direction with (hh) integrated over the range [0.05, 0.95] measured at 0.1 K in zero fields. (a) Energy slice along the $(0, 0, l)$ direction with (hh) integrated over the range [0.05, 0.95] measured at 0.1 K in $B = 4.0$ T. The red dashed lines in (a) and (b) are the fits to spinon expressions with $J \simeq 0.38$ meV. (c) Integrated intensity of one entire Brillouin zone with $(hh) = [0.05, 0.95]$, and $l = [0, 2]$ for fields $B = 0$ T, and $B = 4$ T at 0.1 K. (d) Integrated intensity from 0.2 meV to 2 meV. The zero field inelastic intensity in one Brillouin zone is almost twice the inelastic intensity of $B = 4$ T.

observed at 0.1 K in $B = 4.0$ T, as shown in fig. 5.28b. The red dashed line is the same fit as in fig. 5.28a. We have integrated the inelastic scattering intensity of one entire Brillouin zone with $(hh) = [0.05, 0.95]$, and $l = [0, 2]$ for fields $B = 0$ T, and $B = 4$ T at 0.1 K, as plotted in fig. 5.28c. A broad peak was observed around the energy $E_c \simeq 0.6$ meV. Most interestingly, when we integrate the intensity under this peak from energy of 0.2 meV to 2 meV, the zero field inelastic intensity in one Brillouin zone is almost twice the inelastic intensity found for $B = 4$ T, as shown in fig. 5.28d. This further confirms the two sublattice model with orthogonal aligned spin chains or ladders. When the magnetic field is applied along the diagonal (1, 1, 0) or (1, -1, 0) directions, only one of the two sublattices is polarized in high fields, while the other one is basically unaffected.

The expression we used above for the fitting of the spinon dispersion is based on the model of 1D antiferromagnetically coupled isotropic Heisenberg spins. For this model, the dispersion is always gapless at $l = 0$, and $l = 1$. However, this is a little different from what we see, as shown in fig. 5.28a and fig. 5.28b. This difference may result from the strong Ising character of the Yb moments in Yb_2Pt_2Pb [56, 57]. However, the overall shape of the excitation is still well described by this expression.

5.4 non-Fermi Liquid Behavior near the QCP

The spinon like excitations observed in the inelastic neutron scattering experiments clearly demonstrate that the 1D model is more suitable for the understanding of the peculiar properties of Yb_2Pt_2Pb , at least in zero field, where the usual Fermi liquid is replaced by a Luttinger liquid. Two main properties are related to the 1D Lutinger liquid [52, 53]. One is the presence of the fractional excitations, such as spinons as discussed above [52, 53]. The other is the power law dependence of the correlation function, which may be reflected in transport measurements, such as the linear temperature dependence of the conductivity that is observed in the one dimensional organic compounds [52, 58]. Since Yb_2Pt_2Pb is a good metal, the resistivity measurements may help provide a better understanding of the physics in Yb_2Pt_2Pb . Both the temperature and field dependent resistivity will be discussed below.

Shown in fig. 5.29(a-f) is the temperature dependent resistivity ρ_c with current along the crystal c axis measured in different fields ($B \parallel 110$) from 0 T to 5.0 T. The blue lines are the temperature derivatives of the resistivity ($d\rho/dT$). The red vertical dashed lines indicate the two field independent phase lines at 2 K and 0.8 K, shown in fig. 5.6. The most interesting thing

is that the resistivity becomes linear in temperature at fields around 1.0 T (fig. 5.29b) and 2.0 T(fig. 5.29c), but takes a stronger power-law in both lower and higher fields. This is further explored in fig. 5.30. The temperature dependent resistivity measured in different fields between 1.25 T and 2.25 T is shown in fig. 5.30a. Linear resistivity was observed below 2.0 K for fields in this range. Assuming the temperature dependent resistivity has the form

$$\rho = \rho_0 + AT^n, \tag{5.8}$$

we calculate the power law exponent n via the logarithmic derivative

$$n = d(log\ (\rho - \rho_0))/d(log\ T). \tag{5.9}$$

This exponent is shown in the contour plot in fig. 5.30b, and a large region with $n \simeq 1$ was observed in the range of fields and temperatures around and inside the dome phase region. Fermi liquid behavior with $n \sim 2$ was recovered in smaller and larger fields.

The field dependent resistivities from 0 T to 5.0 T at temperatures from 0.1 K to 2.0 K are shown in fig. 5.31. Steps are observed at 0.1 K, which resemble the plateaux phases in the dc magnetization [67, 97]. We are interested in the upper critical field boundary $B_c \simeq 2.3$ T and the dome phase region that appears in the field range between 1.25 T and 2.3 T. Although the inelastic neutron scattering experiments show that one dimensional physics is more suitable than the singlet-triplet dimer picture for explaining the zero field spinon excitations, we still do not known how important the SSL physics may be for explaining field dependent properties such as the magnetic plateaux and the domed phases.

For the picture of SSL dimers with a singlet-triplet gap Δ, a dome like phase will appear between the critical field B_{c1} and B_{c2}, where Δ is suppressed to zero by magnetic fields [61, 63, 231, 232]. Based on the broad maximum shown in the temperature dependent magnetic susceptibility, it was established in [67] that the field dependent gap Δ approximately closes at about 1.6 T. If stabilizing the dome phase requires the closure of the singlet-triplet gap, as observed in the dimer compounds $BaCuSi_2O_6$ and $TlCuCl_3$ [231, 232], the critical points at B_{c1} and B_{c2} should fall into the BEC universality class with $T \simeq (B - B_c)^{2/3}$. The phase boundary near the lower critical field $B_{c1} \simeq 1.25$ T in Yb_2Pt_2Pb is complicated by proximity to other phase transitions, and we focus on the upper critical field B_{c1} T. This upper phase boundary appears as a sharp peak in the field derivative of the magnetic resistivity, as shown in fig. 5.32c. The upper critical field B_{c2} that is extracted from this resistivity measurement is about 2.4 T at 0.1 K, which could be traced to about 2.35

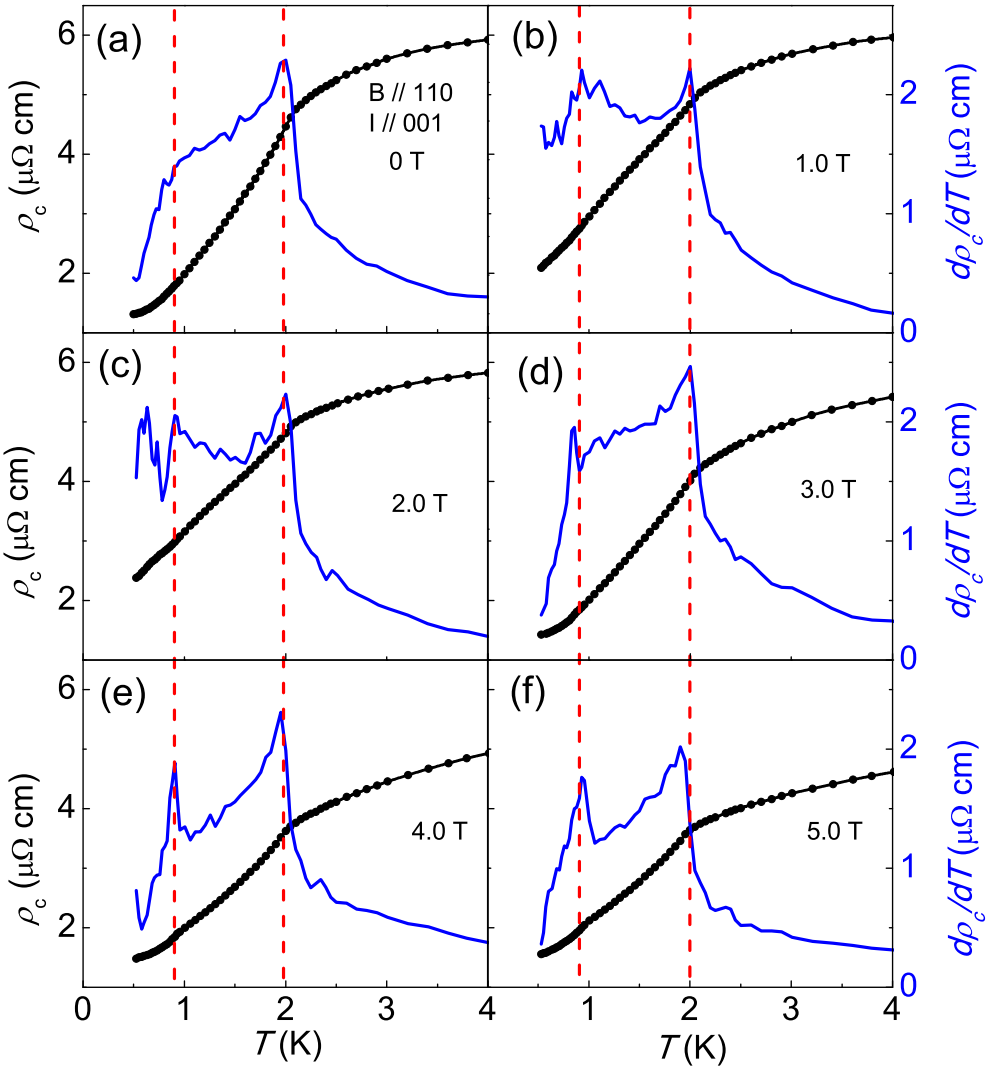

Figure 5.29: (a-f)Temperature dependent resistivity measured in different fields from 0 T to 5.0 T, as indicated. The blue lines are the temperature derivatives of the resistivity ($d\rho/dT$). The red vertical dashed lines indicate the two horizontal phase lines shown in fig. 5.6, which are shown here to be independent of field.

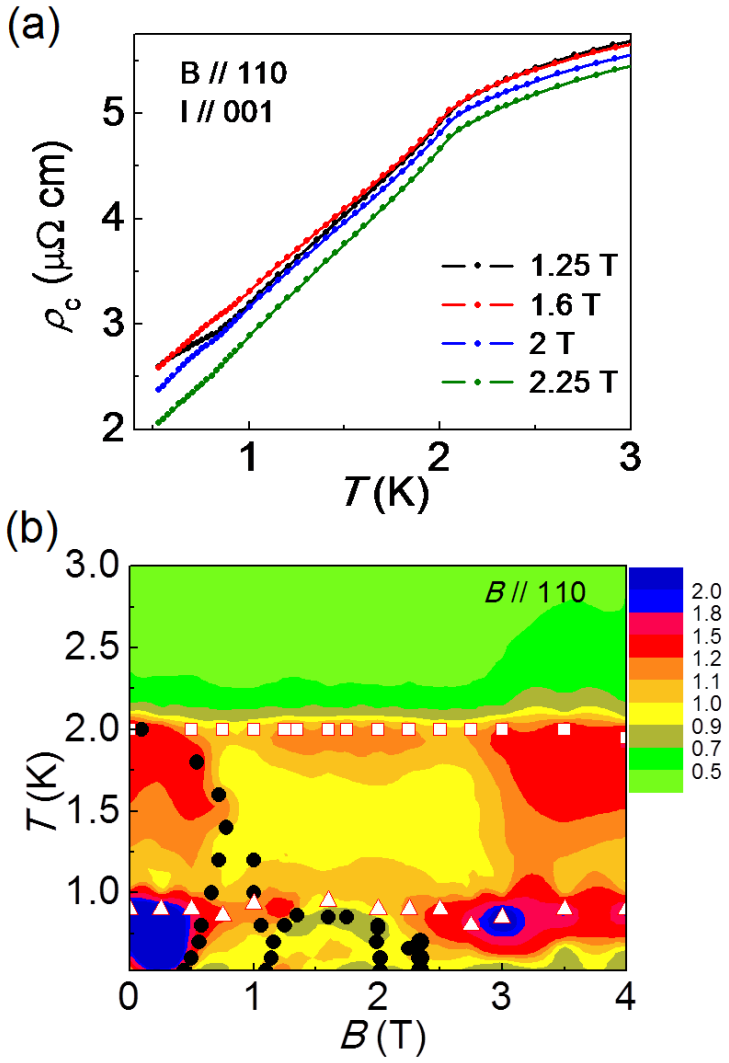

Figure 5.30: (a)Temperature dependent resistivity measured in different fields between 1.25 T and 2.25 T as indicated. (b) Contour plot of the exponent n over the field temperature phase diagram. Assuming that $\rho = \rho_0 + AT^n$, then $n = d(log\ (\rho - \rho_0))/d(log\ T)$.

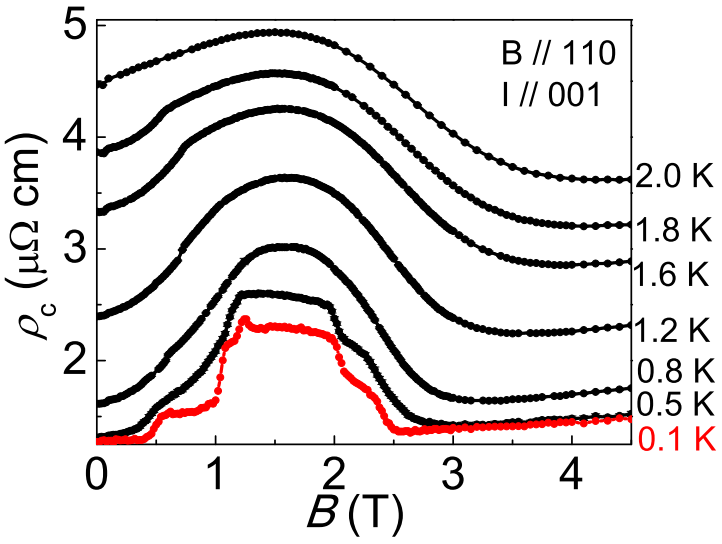

Figure 5.31: Field dependent resistivities at temperatures from 0.1 K to 2.0 K.

T at 0.6 K. From these data, the critical field B_{c2} changed less than 0.05 T when the temperature changed by 0.5 K. The overall phase boundary is more like a vertical phase line as $T \to 0, B \to B_c$ than the power law behavior expected from the BEC scenario. Based on the Clausius-Clapeyron relation, this vertical phase boundary suggests that the material is tuned to a first order phase transition at B_{c2}. This observation suggests that the dome phase may have a different origin than those seen in other dimer systems [231, 232].

Another peculiar property observed here is that the sharp peak in $d\rho/dB$ at B_{c2} can be traced to even higher temperatures, where it gradually evolves into a broad minimum for $T \geq 0.7$ K, as shown in fig. 5.32b and fig. 5.32c. Phenomenologically, this is very similar to the T^* line observed in the Yb based heavy fermion compound $YbRh_2Si_2$ near the AF-QCP [10, 31, 43]. We have added this new energy scale found in Yb_2Pt_2Pb in fig. 5.34. The solid stars below ∼0.7 K outline the real phase boundary, while only broad minima were observed at fields and temperatures marked by empty stars. However, it is still unclear what is the mechanism behind the new energy scale T^*. We have re-examined the temperature dependent magnetization in different fields up to 4.0 T. We have plotted all the temperature dependent magnetization shown in fig. 5.33a and fig. 5.33b as a function of B/T. If the new T^* line results from inflection points in the entropy, caused by the Zeeman splitting of the Yb ground doublet states, the magnetization in the paramagnetic state

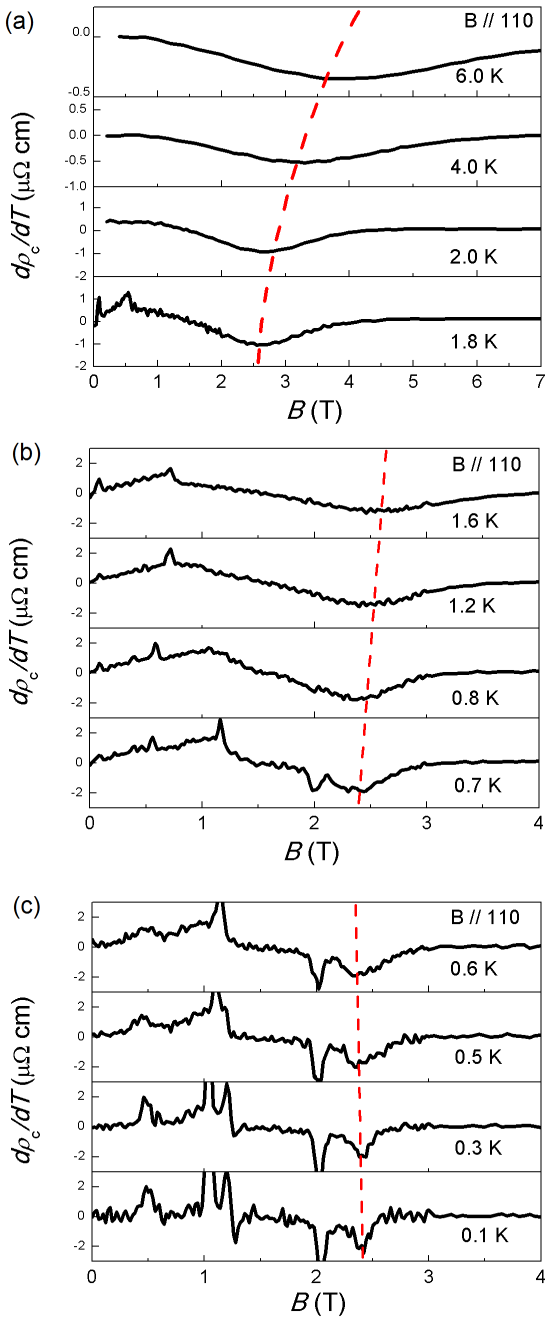

Figure 5.32: Field derivative of the measured resistivity at different temperatures (a) 1.8 K $< T <$ 6 K, (b) 0.7 K $< T <$ 1.6 K, and (c) 0.1 K $< T <$ 0.6 K. The red dashed line indicates the evolution of the sharp anomaly at 2.3 T at 0.1 K to the broad anomaly at high temperatures.

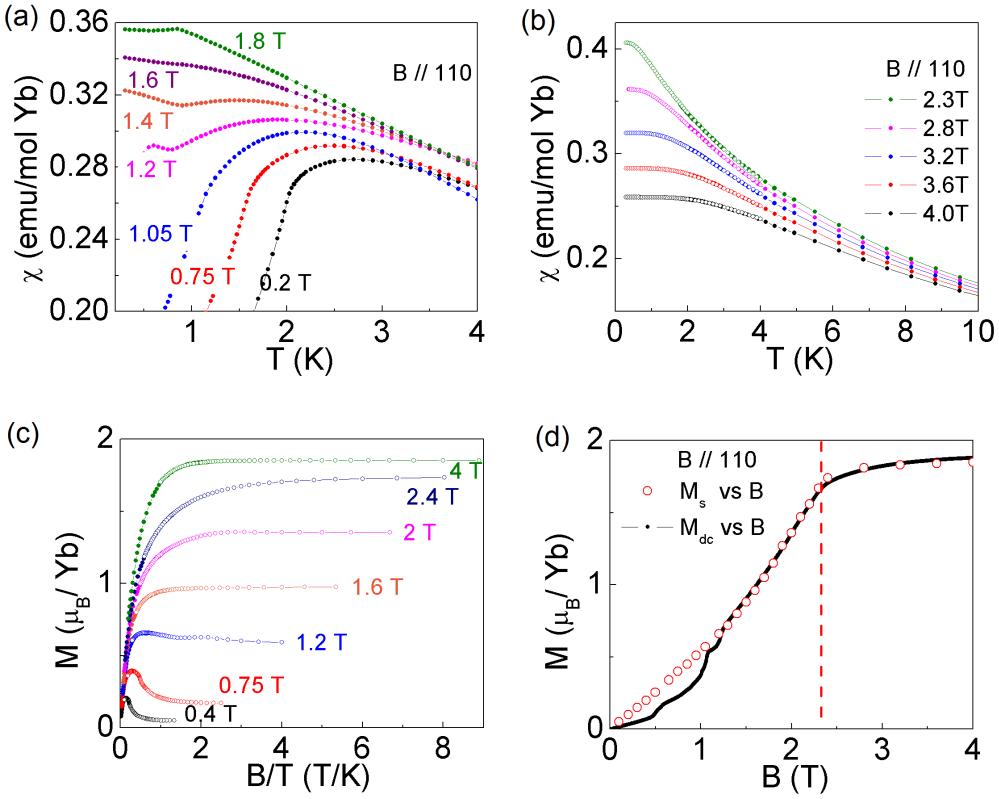

Figure 5.33: Temperature dependent magnetization measured in different fields (a) $B \leq 1.8$ T, (b) 2.3 T$\leq B \leq 4.0$ T [Moosung Kim]. (c) The temperature dependent magnetization as a function of B/T for different values of B, as indicated. (d) Plot of the saturated moment (red) extracted from (c) plotted with the measured magnetization at 0.1 K (black). [97]

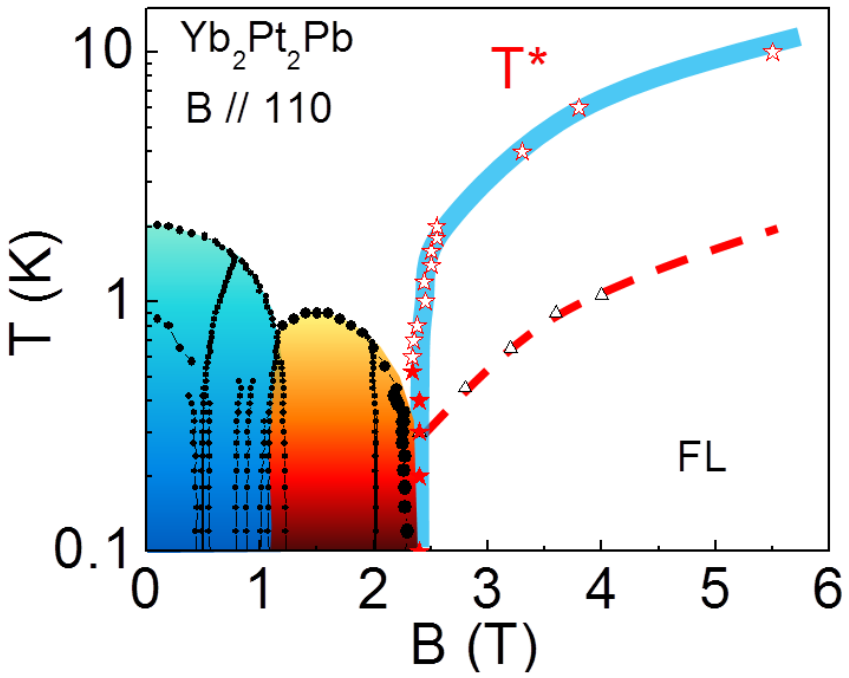

Figure 5.34: Temperature-field phase diagram of Yb_2Pt_2Pb . For simplicity, the two horizontal phase lines are not presented in this phase diagram. The red stars indicate the additional energy scale T^* extracted from the magnetic field dependent resistivity. The solid stars below 0.7 K are the real phase boundary, while the empty stars correspond to a broad minimum in the resistivity, possibly a crossover.

should collapse to a scaling curve as function of B/T, just as we observed in the local moment antiferromagnet Yb_3Pt_4 (fig. 3.16, Chapter 3). As shown in fig. 5.33c, the magnetization curve of Yb_2Pt_2Pb does not scale as B/T, and in addition, the saturation moment in the small field region is much smaller than the value expected for the localized Ising-like Yb moments. Fig. 5.33d is the plot of the saturation moments M_s extracted from fig. 5.33c with the as measured magnetization at 0.1 K. We can see that M_s only recovers the single ion moment for fields $B \geq 2.3$ T. This indicates that $B_c = 2.3$ T is not just a upper critical phase boundary of the dome phase, but it is also a true critical field, above which Yb local moments are recovered. This critical field may even extend to higher temperatures, separating the paramagnetic phase into two different regions in the field-temperature phase space.

This new energy scale T^* that is observed around 2.3 T reminds us that there is another very important aspect we have to consider, the heavy fermion physics [67, 222]. The measured specific heat is greatly enhanced in the low field antiferromagnetic state, where $\gamma = C/T \simeq 311$ mJ/mol K^2 at $B = 0$ [67]. A sharp drop was observed in the value of γ near 2.3 T, and a Fermi liquid state with $\gamma \simeq 100$mJ/mol K^2 was recovered for fields $B \geq 2.3$ T [67, 97]. Large values of γ are found in frustrated systems, including insulators and also RB_4 [233], however, it is not clear that if this is the origin of large γ in Yb_2Pt_2Pb , or if the Kondo effect is important. The non-Fermi liquid behaviors with linear temperature dependent resistivity near the domed phase region could be taken as evidence for the presence of a Luttinger liquid or quantum critical behavior as for heavy fermions. However, the key point is that strong quantum fluctuations are present in this region near the AF-QCP, where Fermi liquid theory breaks down.

5.5 Conclusion

In this Chapter, we have mainly discussed the results of neutron scattering on Yb_2Pt_2Pb single crystals. Elastic neutron scattering data confirms the two sublattice model with Yb Ising moments aligned along the orthogonal (110) and (1-10) directions. Two sets of satellite peaks with propagation vectors $q_1 = (\pm 0.2, \pm 0.2, 0)$ and $q_2 = (\pm 0.2, \mp 0.2, 0)$ were found in the zero field antiferromagnetic ordered state, indicating a 5×5 superlattice in the ab plane. The propagation vector q_1 is responsible for the field dependent order shown in the $B \parallel 110$ phase diagram, corresponding to the sublattice with moments parallel to the magnetic field, while the propagation vector q_2 is responsible for the field independent horizontal phase line at 2.0 K, corresponding to the other sublattice with moments perpendicular to the applied field. The critical

exponent $\beta \simeq 0.12$ suggests the zero field antiferromagnetic order belongs to a 2D Ising universality class.

Yb ions form pairs that are arranged orthogonally in the ab plane, resembling the frustrated SSL structure, where dimers with singlet-triplet excitations are expected. However, inelastic neutron scattering data clarifies that the interactions along the crystal c direction are the most important, and the Yb Ising moments are aligned antiferromagnetically into chains or ladders along the c direction. Spinon excitations were observed in zero field, and interesting field dependent behaviors were observed.

With increasing fields, the antiferromagnetic order is suppressed to zero temperature at a critical field of about 1.25 T. Above this field, a dome like phase was observed that extends from $\sim 1.25 - 2.3$ T. Non-Fermi liquid behaviors with linear temperature dependent resistivity were observed in this region, indicating the existence of strong quantum fluctuations. These critical fluctuations could be driven by the 1D physics, where the domed phase may be related to the Luttinger liquid phase. It is also possible that these fluctuations are related to the field induced AF-QCP, as observed in heavy fermion systems [10, 21]. A new energy scale was identified through the field dependent resistivity measurements, which resembles the T^* line in $YbRh_2Si_2$ near the field induced AF-QCP [10, 31, 43]. However, it is still unclear that whether this additional energy scale is driven by the Kondo effect or by the low dimensional fluctuations.

Chapter 6

Conclusions and Perspectives

Three systems were investigated in this thesis, through magnetic and thermodynamic property measurements and neutron scattering experiments. Our purpose is to develop a general understanding of the quantum phase transitions and the associated quantum critical behaviors from different aspects. We have explored the field induced critical end point in the local moment antiferromagnet Yb_3Pt_4 in chapter 3, the quantum critical scaling in the $3d$ electron compound YFe_2Al_{10} in chapter 4, and the quantum antiferromagnet Yb_2Pt_2Pb in chapter 5.

Compared to the numerous Ce-based heavy fermions that have been studied since the 1970s, only a few Yb-based heavy fermion systems have been well established. Most of the studies were based on the material $YbRh_2Si_2$. Yb moments are almost delocalized in $YbRh_2Si_2$ at low temperatures, and non-Fermi liquid behaviors induced by quantum critical fluctuations were observed in the vicinity of the field induced AF-QCP. It was argued that this AF-QCP in $YbRh_2Si_2$ does not fall into the Hertz-Millis theory of SDW-type QCPs. An new energy scale T^* related to the delocalization of f moments was observed at the QCP. In this 'local' Kondo-breakdown type QCP, additional quantum fluctuations are expected besides the order parameter fluctuation of the magnetic phase transition itself. Our initial interest is that how much this QCP would be modified if a localized Yb system was tuned in the same way to a critical point. Yb_3Pt_4 is such a system with well localized moments. Since the magnetic ordering temperature is low ($T_N = 2.4$ K), experimentally it could be easily suppressed by magnetic field at about 1.9 T. Based on our thermal property measurements, a field-temperature phase diagram was established, and a continuous phase line was found for temperature approaching zero. Questions we have then were: Is this also a QCP as found in $YbRh_2Si_2$? Is the delocalization of moments necessary for the observation of those anomalous critical behaviors? However, in Yb_3Pt_4, the

magnetoresistivity indicates that nFL behavior was not observed at the critical point, and no heavy fermion behavior, such as the enhancement of effective electron masses, was observed in the specific heat and magnetic susceptibility. This suggests that the fluctuations from the delocalization-localization of the f electrons may be responsible for the observed quantum critical behaviors in $YbRh_2Si_2$, which is absent in Yb_3Pt_4. In addition, our elastic neutron scattering study on the magnetic order parameter indicates that Yb_3Pt_4 was actually tuned to a first order phase transition at $T_N = 0$. Combining the magnetization and MCE, we have shown that Yb_3Pt_4 was tuned to a critical end point (CEP) at $T = 0$. We believe what we observed in Yb_3Pt_4 can be generalized to other local moment systems as they are tuned to the critical point by magnetic fields, and the critical point can be unified to a global phase diagram with a metamagnetic critical point, as we shown in fig. 3.21. The lack of quantum critical fluctuations near the field induced critical point in Yb_3Pt_4 can also be understood from the point of view of quantum critical scaling. Since the Yb moments are always localized, and no delocalization-localization like transition of the $4f$ electrons is involved at the critical point in Yb_3Pt_4, all the critical fluctuations, if they exist, are from the fluctuations of the order parameter only. However, the zero field antiferromagnetic order of Yb_3Pt_4 is three dimensional ($d = 3$) with Heisenberg like spins, thus, as it was tuned to the $T_N = 0$ QCP, the effective dimension would increase to $d_{\text{eff}} = d + z > 4$, which would be greater than the upper critical dimension. So it is actually not surprising that the critical fluctuations are cut off in this case, and only classical local moment behaviors were observed overall the phase diagram besides the antiferromagnetic order as shown in fig. 3.16 and fig. 3.17.

Most of the studies of quantum criticality are established in f-electron based heavy fermions, and the observation and description of the quantum critical behaviors in magnetic systems driven by d electrons are very limited. As we discussed in chapter 4, YFe_2Al_{10} is a rare compound that could serve as a valuable bridge between the study of the quantum criticality in f-electron and the stoichiometric d-electron systems. Non-Fermi liquid behaviors with strong divergencies in magnetic susceptibility ($\chi \sim T^{-1.4}$) and magnetic specific heat ($C_M/T \sim -log\ T$) were observed in YFe_2Al_{10} in zero field. A 'naive' scaling of magnetic susceptibility ($d\chi/dT = B^{-1.4}\phi(T/B^{0.6})$) and specific heat ($\Delta C_M/T = \varphi(T/B^{0.6})$) that assumes the existence of hyperscaling is fully established, indicating a QCP locating at $T = 0$, and $B = 0$. The $T/B^{0.6}$ scaling suggests that there is no fixed energy scale when the system is tuned to the QCP, and the free energy is only dependent on the relative distance in parameter space from the QCP. Fermi liquid behavior is restored in the high field limit as the system was tuned far from the QCP. A scaling function of the

singular part of the free energy was proposed, which explains all the measured thermal properties in a self-consistent way. Detailed scaling analysis indicates that the spatial dimension d is equal to the dynamical exponent z ($d = z$). No static order has been observed down to 0.1 K and thus it is hard to determine the nature of the QCP and the exact values of the dimension d. However, the strong anisotropy between the ac plane and the b axis indicates that the critical fluctuations may be two dimensional with $d \leq 2$. The validation of the hyperscaling suggests that the effective dimension may be in the range of $1 < d_{\text{eff}} = d + z \leq 4$. Based on the scaling analysis, the QCP in YFe_2Al_{10} does not follow the Hertz-Millis picture for itinerant FM-QCP or AF-QCP. One possible scenario is that this system is located close to an itinerant-localization like transition, such as a metal-insulator transition, and the divergence in magnetic susceptibility is thus induced by the formation of localized moments. A lot of interest has been attracted to the isostructural compounds $CeRu_2Al_{10}$, and $CeFe_2Al_{10}$ [238, 239, 240, 241]. No magnetic ordering was observed in the compound $CeFe_2Al_{10}$, and a semiconducating resistivity was observed below about 100 K [238, 239, 240, 241]. Antiferromagnetic order has been observed at $T_N \simeq 27$ K in $CeRu_2Al_{10}$. Considering that the nearest neighbor distance between Ce ions is more than 5Å, this antiferromagnetic ordering temperature is extremely high considering that it maybe mediated by the RKKY exchange interaction [238, 239, 240, 241]. Although the Ce $4f$-electrons are responsible for this magnetic ordering, the driving mechanism is still under debate. Strong anisotropy between the ac plane and the b axis has been observed in $CeRu_2Al_{10}$ and $CeFe_2Al_{10}$, which is similar to that observed in YFe_2Al_{10}, and it was proposed that a charge density wave (CDW) instability of the electronic background may drive the magnetic ordering of the f electrons [242]. It thus will be very interesting to see whether this scenario applies to the critical behavior observed in YFe_2Al_{10}, since they share a very similar electron environment. Future work is needed to verify this hypothesis.

Yb_2Pt_2Pb is a quantum antiferromagnet that orders at $T_N = 2.07$ K in zero field. The Yb ions in the ab plane crystallize into pairs that are arranged orthogonally to each other, which is equivalent to the 2D Shastry-Sutherland lattice (SSL). At low temperatures, the Yb ground doublet states of $J_z = \pm \mid 7/2\rangle$ are well separated from the excited states, producing a pseudo-spin $S = 1/2$ state with the Yb Ising moments pointing along the crystal (110) and (1-10) directions. We have focused on exploring the magnetic properties of Yb_2Pt_2Pb using elastic and inelastic neutron scattering experiments of aligned single crystals in this thesis in chapter 5. Elastic neutron diffraction confirms the two sublattice model of the magnetic structure. With magnetic field applied along the (110) direction, only one of the two sublattices with moments

along the field direction is polarized, while the other one with moments perpendicular to the field is not affected, which explains the field independent horizontal phase lines shown in fig. 5.6. The most interesting behaviors come from the inelastic neutron scattering results. In contrast to the expectation of the two dimensional physics of SSL in the ab plane, spinon like excitations with broad continuum which disperse along the $(00l)$ direction were observed, indicating that the interactions along the crystal c axis are actually very important. Based on the newly solved magnetic structure in zero field [230] and the dynamical structure factor of the neutron scattering intensity, we propose that the Yb Ising moments may be coupled antiferromagnetically into chains or ladders along the crystal c direction, and the zero field magnetic order at $T_N \simeq 2.07$ K corresponds to the ordering among the coupled chains or ladders. The spinon dispersion has been fit to the one dimensional model of antiferromagnetically coupled isotropic Heisenberg spins half ($s = 1/2$) chains, which gives an interaction along the c axis $J_{\|c} \simeq 0.38$ meV. In contrast to the first two compounds, Yb_3Pt_4 and YFe_2Al_{10}, Yb_2Pt_2Pb is dominated by the one-dimensional Luttinger liquid physics. The magnetic properties of Yb_2Pt_2Pb with magnetic fields are also very interesting. A dome phase emerges in the vicinity of the antiferromagnetic QCP in $\sim$ 1.25 T and it extends to the upper critical field of $\sim$ 2.3 T. The phase boundary of the dome phase does not correspond to the dimer model with a BEC state. Non-Fermi liquid behaviors with linear temperature dependent resistivity were observed in a wide field and temperature range around and inside the dome phase, indicating that strong quantum critical fluctuations exist in this region. A new energy scale or T^* line was observed in the field derivative of the magnetoresistivity, which originates from 2.3 T, and extends to higher temperatures up to $\sim$ 10 K in fields. Phenomenologically, this T^* line is similar to what observed in the heavy fermion system $YbRh_2Si_2$ at the field induced AF-QCP. Although a great enhancement of the Sommerfeld constant was observed in the field dependent specific heat, there is not enough evidence in Yb_2Pt_2Pb that Kondo effect is sufficient to drive these critical fluctuations. Another scenario is that the one dimensional physics fully accounts for the field induced physics and the emergent dome phase. The region bounded between 1.25 T and 2.3 T with significant non-Fermi liquid behavior in the temperature dependent resistivity established in fig. 5.6 then can be understood as a Luttinger liquid phase, as observed in the weakly coupled spin ladder system $CuBr_4(C_5H_{12}N)_2$ (BPCB) [235, 236, 237]. Thus the T^* line extends from the upper critical field 2.3 T is the crossover above which the Luttinger liquid phase is suppressed to a polarized moment state. However, a detailed analysis of the neutron scattering data and the thermodynamical properties such as

specific heat and MCE is needed to clarify this scenario. Up to now, all we have studied is with field in the *ab* plane (110) or (1-10) directions, and since the Ising moment is also confined in these orthogonal directions, the magnetic field acts as a chemical potential for the Ising spins. However, it will also be interesting to have high field measurements along the crystal *c* direction. In that case, the field is perpendicular to the Ising spin, and the magnetic field induced critical point will correspond to the model of the one dimensional Ising spin chain in transverse field, where a different universality class of the QCP may be expected.

In conclusion, we have studied three different materials in this thesis. Although they behave very differently from each other, the overall quantum critical physics can be understood in a united way. For Yb_3Pt_4, the effective dimension of the field induced critical point is above the upper dimension, and so the critical fluctuations are very weak. For YFe_2Al_{10}, the self-consistent quantum critical scaling indicates an effective dimension $1 < d_{\text{eff}} = d + z \leq 4$, and hence quantum critical fluctuations are very strong. The most interesting properties were observed in Yb_2Pt_2Pb, where the one dimensional (1D) Luttinger liquid physics are dominant. Fermi liquid physics broke down in both YFe_2Al_{10} and Yb_2Pt_2Pb where the quantum fluctuations are significant. Although the non-Fermi liquid behaviors in YFe_2Al_{10} are believed to be driven by the $B = 0, T = 0$ QCP, while the quantum fluctuations in Yb_2Pt_2Pb are driven by the low dimensionality, they are all related to the quantum critical physics in a particular way. These studies enable us to have a more comprehensive view of the quantum phase transitions and quantum criticality.

Bibliography

[1] S. J. Blundell and K. M. Blundell, Concepts in Thermal Physics. *Oxford University Press,* (2008), ISBN 978-0-19-856770-7.

[2] D. I. Uzunov, Introduction to the theory of critical phenomena: mean field, fluctuations and renormalization. *World Scientific Pub. Co. Inc.,* (1992).

[3] N. Goldenfeld, Lectures on Phase Transitions and the Renormalization Group. *Addison-Wesley, Reading* (1992).

[4] J. L. Cardy, Scaling and Renormalization in Stastical Physics. *Cambridge University Press, Cambridge, England* (1996)

[5] Online lecture notes, The Scaling Hypothesis. http://www.tcm.phy.cam.ac.uk/ bds10/phase/scaling.pdf

[6] J. Flouquet and H. Harima, Heavy fermion material: Ce versus Yb case. (2009).

[7] D. Belitz, T. R. Kirkpatrick, and J. Rollbuhler, *Phys. Rev. Lett,* **94**, 247205 (2005).

[8] M. Uhlarz, C. Pfleiderer, and S. M. Hayden, *Phys. Rev. Lett,* **93**, 256404 (2004).

[9] V. Taufour, D. Aoki, G. Knebel, and J. Flouquet, *Phys. Rev. Lett,* **105**, 217201 (2010).

[10] P. Gegenwart, Q. Si, and F. Steglich, *Nature Physics* **4**, 186 (2008).

[11] S. Sachdev, Quantum Phase Transitions. *Cambridge University Press,* (2001).

[12] G. R. Stewart, *Rev. Mod. Phys.,* **73**, 797-855 (2001).

[13] S. Sachdev and B. Keimer, *Physics Today ,* **64** (2), 29 (2011).

[14] W. A. C. Erkelens, et al., *Europhys. Lett.,* **1** (1), 37-44, (1986).

[15] J. E. Thomas, *Physics Today ,* **63** (5), 34 (2010).

[16] M. C. Aronson, et al., *Phys. Rev. Lett,* **75**, 725, (1995).

[17] A. Schröder et al., *Nature* **407**, 351-355 (2000).

[18] A. Bianchi,, R. Movshovich,, I. Vekhter,, P. G. Pagliuso, and J. L. Sarrao, *Phys. Rev. Lett.* **91**, 066404 (2003).

[19] H. Löhneysen, *J. Phys. Condens. Matter* **8**, 9689, (1996).

[20] Y. Matsumoto, et al., *Science* **331**, 316 (2011).

[21] H. v. Löhneysen, A. Rosch, M. Vojta, and P. Wölfle, *Rev. Mod. Phys.,* **79**, 10151075 (2007).

[22] M. A. Continentino, Quantum Scaling in Many-Body Systems. *World Scientific Pub. Co. Inc; 1st edition,* (2001).

[23] M. A. Continentino, *Brazilian journal of physics,* **35** (1), 197-203, (2005).

[24] J. A. Hertz, *Phys. Rev. B,* **14**, 1165-1184 (1976).

[25] A. J. Millis, *Phys. Rev. B,* **48**, 7183-7196 (1993).

[26] T. Moriya and T. Takimoto, *J. Phys. Soc. Jpn.,* **64**, 960-969 (1995).

[27] G. G. Lonzarich, The magnetic electron. Chapter 6 of book: Electron: a centenary volume. Editor: M. Springford, *Cambridge University Press,* (1997).

[28] N. D. Mathur, et al.,*Nature,* **394**, 39 (1998).

[29] S. Saxena, et al., *Nature,* **406**, 587 (2000).

[30] F. Steglich, et al., *Journal of Physics: Condensed Matter,* **24**, 294201, (2012).

[31] S. Paschen, et al. *Nature* **432**, 881 (2004).

[32] P. Coleman, Heavy fermions: Electrons at the edge of magnetism. *Handbook of Magnetism and Advanced Magnetic Materials, Wiley Online Library,* (2007).

[33] M.A. Ruderman and C. Kittel, *Phys. Rev. B,* **96**, 99 (1954).

[34] T. Kasuya, *Prog. Theor. Phys.,* **16**, 45 (1956).

[35] K. Yosida, *Phys. Rev.,* **106**, 893 (1957).

[36] S. Doniach, *Physica B+C,* **91**, 231-234 (1977).

[37] K. Andres, J. E. Graebner and H. R. Ott, *Phys. Rev. Lett,* **35**, 1779-1782 (1975).

[38] D. M. Newns and A. C. Hewson, *J. Phys. F: Metal Phys.,* **10**, 2429-2445, (1980).

[39] L. E. Delong, R. P. Guertin, S. Hasanain, and T. Fariss, *Phys. Rev. B,* **31**, 7059, (1985).

[40] P. Gegenwart, J. Custers, Y. Tokiwa, C. Geibel, and F. Steglich, *Phys. Rev. Lett,* **94**, 076402 (2005).

[41] K. Kadowaki and S. B. Woods, *Solid State Comm.,* **58**, 507 (1986).

[42] F. Steglich, et al., *Phys. Rev. Lett,* **43**, 1892-1896 (1979).

[43] Q. Si, S. Rabello, K. Ingersent and J. L. Smith. *Nature,* **413**, 804-808 (2001).

[44] P. Coleman, C. Pepin, Q. Si and R. Ramazashvili. *J. Phys.: Condens. Matter,* **13**, *R*723738 (2001).

[45] J. Flouquet, *Progress in Low Temperature Physics,* **15**, 139-281 (2005).

[46] F. Gebhard, The Mott Metal-Insulator Transition: Models and Methods. *Springer,* (1997).

[47] V. Dobrosavljevic, Introduction to Metal − Insulator Transitions. *Conductor Insulator Quantum Phase Transitions, Oxford* (2012).

[48] P. Limelette, et al. *Science* **302**, 89, (2003).

[49] F. Kagawa, K. Miyagawa, and K. Kanoda. *Nature* **436**, 534-537, (2005).

[50] L. Bartosch, M. Souza, and M. Lang, *Phys. Rev. Lett.* **104**, 245701 (2010).

[51] F. Kagawa, K. Miyagawa, and K. Kanoda. *Nature Physics* **5**, 880-884, (2009).

[52] T. Giamarchi. Quantum Physics in One Dimension. *Oxford University Press,* (2003).

[53] T. Giamarchi. *International Journal of Modern Physics B, World Scientific* **26**, 22, (2012).

[54] B. Lake, D. A. Tennant, C. D. Frost and S. E. Nagler. *Nature Materials* **4**, 329-334, (2005).

[55] I. A. Zaliznyak, *Nature Materials* **4**, 273-275, (2005).

[56] J. Caux, and J. Mossel, and I. Castillo, *Journal of Statistical Mechanics: Theory and Experiment,* **2008**, P08006, (2008).

[57] J. Caux, and H. Konno, M. Sorrell and R. Weston, *Phys. Rev. Lett,* **106**, 217203, (2011).

[58] M. Dressel, *Journal of Physics: Condensed Matter* **23**, (29), 293201, (2011).

[59] T. H. Han, et al., *Nature* **492**, (7429), 406-410, (2012).

[60] B. Sriram Shastry, and B. Sutherland, *Physica B+ C* **108**, (1), 1069-1070, (1981).

[61] S. Miyahara, and K. Ueda, *Journal of Physics: Condensed Matter* **15**, (9), R327, (2003).

[62] A. Koga, and N. Kawakami, *Phys. Rev. Lett,* **84**, (19) 4461 (2000).

[63] S. Sachdev, *Nature Physics***4**, (3), 173-185, (2008).

[64] B. D. Gaulin, et al., *Phys. Rev. Lett,* **93**, (26) 267202 (2004).

[65] D. C. Mattis, The Theory of Magnetism Made Simple. *World Scientific Publishing Co. Pte. Ltd.,* (2004)

[66] M. S. Kim, M. C. Bennett, and M. C. Aronson, *Phys. Rev. B,* **77**, (14) 144425 (2008).

[67] M. S. Kim, and M. C. Aronson, *Phys. Rev. Lett,* **110**, (1) 017201, (2013).

[68] K. Siemensmeyer, et al., *Phys. Rev. Lett,* **101**, (17) 177201, (2008).

[69] B. R. Pamplin, Crystal Growth.*Pergamon Press, Oxford,* (1980).

[70] Z. Fisk and J. P. Remeika, *Handbook on the Physics and Chemistry of Rare Earths,*Vol. **12**, (1989).

[71] P. C. Canfield and Z. Fisk, *Philosophical Magazine Part B,* **65**, 1117-1123 (1992).

[72] P. C. Canfield and I. R. Fisher, *Journal of Crystal Growth,* **225**, 155-161 (2001).

[73] M. C. Bennett, et al. *J. Magn. and Magn. Mater.* **321**, 2021 (2009).

[74] M. C. Bennett, Tuning the electronic and magnetic phases in CaB_6, $PtSb_2$, and Yb_3Pt_4, *The University of Michigan,* (2009).

[75] Y. Janssen, et al., *Phys. Rev. B,* **81**, 064401 (2010).

[76] C. Marques et al. Cyrstal Synthesis of Novel Yb-Pt-Pb Phases. *APS March Meeting Talk,* (2009).

[77] Aluminum (Al-X-Y) Ternary Alloys. *Springer Materials.*

[78] K. Park, L. S. Wu, Y. Janssen, M. S. Kim, C. Marques, and M. C. Aronson, *Phys. Rev. B* **84**, 094425 (2011).

[79] Quantum Design, Physical Property Measurement System: Heat Capacity Option User's Manual.

[80] R. A. Borzi, et al., *Science* **315**, 214, (2007).

[81] B. R. Gopal, R. Chahine, and T. K. Bose, *Rev. Sci. Instrum.* **68**, 1818 (1997).

[82] A. M. Tishin, *Handbook on Magnetic Materials* **12**, 395-524 (1999).

[83] V. K. Pecharsky, and K. A. Gschneidner, *J. Magn. Magn. Mater.* **200**, 44 (1999).

[84] V. K. Pecharsky, K. A. Gschneidner, Jr., A. O. Pecharsky, and A. M. Tishin, *Phys. Rev. B* **64**, 144406 (2001).

[85] J. Liu, T. Gottschall, K. P. Skokov, J. D. Moore and O. Gutfleisch, *Nat. Mater.* **11**, 620, (2012).

[86] A. A. Aczel, et al., *Phys. Rev. Lett.* **103**, 207203 (2009).

[87] M. Jaime, K. H. Kim, G. Jorge, S. McCall, and J. A. Mydosh, *Phys. Rev. Lett.* **89**, 287201 (2002).

[88] A. V. Silhanek, et al., *Phys. Rev. Lett.* **96**, 136403 (2006).

[89] A. Bianchi, et al. *Phys. Rev. Lett.* **89**, 137002 (2002).

[90] V. S. Zapf, et al., *Phys. Rev. Lett.***96**, 077204 (2006).

[91] Y. Tokiwa, and P. Gegenwart, *Rev. Sci. Instrum.* **82**, 013905 (2011).

[92] A. W. Rost, R. S. Perry, J. F. Mercure, A. P. Mackenzie, and S. A. Grigera, *Science,* **325**, 1360 (2009).

[93] L. Zhu, M. Garst, A. Rosch, and Q. Si, *Phys. Rev. Lett.* **91**, 066404 (2003).

[94] R. Küchler, et al., *Phys. Rev. Lett.* **91**, 066405 (2003).

[95] L. S. Wu, et al., *Phys. Rev. B* **84**, 134409 (2011).

[96] L. S. Wu, et al., *Phys. Rev. B* **86**, 054401 (2012).

[97] M. S. Kim and M. C. Aronson (unpublished).

[98] Quantum Design Application Note, 1084-701.

[99] A. Cavallini, B. Fraboni, F. Capotondi, L. Sorba, and G. Biasiol, *Microelectron. Engin.* **73 − 74**, 954 (2004).

[100] A. Candini, et al., *Nanotechnology,* **17**, 2105-2109 (2006).

[101] G. L. Squires, *Introduction to the Theory of Thermal Neutron Scattering,* Cambridge University Press, Cambridge, U. K. (1978).

[102] S. W. Lovesesy, *Theory of neutron scattering from condensed matter,* Vol. **2**, Clarendon Press, Oxford, (1984).

[103] C. Lacroix, *Introduction to frustrated magnetism: Materials, experiments, theory,* Vol. **164**, Springerverlag Berlin, Heidelberg, (2011).

[104] I. A. Zaliznyak and S-H. Lee, *Magnetic Neutron Scattering, Modern Techniques for Characterizing Magnetic Materials,* Springer, Heidelberg, (2005).

[105] A. Zheludev, *Neutron Scattering Lecture Notes.*

[106] T. Fennell, et al., *Nature Physics***3**, (8), 566-572, (2007).

[107] S-H. Lee, et al., *Nature* **418**, (6900), 856-858, (2002).

[108] G. Shirane, S. M. Shapiro and J. M. Tranquada, *Neutron Scattering with a Triple-Axis Spectrometer: Basic Techniques,* Cambridge University Press, Cambridge, U. K. (2006).

[109] More information of the instrument configuration on the DCS websit: http://www.ncnr.nist.gov/instruments/dcs/.

[110] More information of the instrument configuration on the CNCS websit: http://neutrons.ornl.gov/cncs/.

[111] G. Ehlers, A. Podlesnyak, J. L. Niedziela, E. B. Iverson, *Review of Scientific Instruments,* Vol. **82**, 085108, (2011).

[112] P. Coleman and A. J. Schofield, *Nature* **433**, 226 (2005).

[113] H. v. Lohneysen, A. Rosch, M. Vojta, and P. Wolfle, *Rev. Mod. Phys.* **79**, 1015 (2007).

[114] H. v. Lohneysen and P. Wolfle, *Lectures on the Physics of Strongly Correlated Systems XII: Twelfth Training Course,*ed. A. Avella and F. Mancini, American Institute of Physics (2008).

[115] F. Steglich, et al., *J. Phys. : Cond. Matt.* **22**, 164202 (2010).

[116] P. Monthoux and G. G. Lonzarich, *Phys. Rev. B* **63**, 054529 (2001).

[117] D. A. Sokolov, M. C. Aronson, W. Gannon, and Z. Fisk, *Phys. Rev. Lett.* **96**, 116404 (2006).

[118] H. v. Löhneysen, C. Pfleiderer, T. Pietrus, O. Stockert, and B. Will, *Phys. Rev. B* **63**, 134411 (2001).

[119] I. Fischer and A. Rosch, *Phys. Rev. B* **71**, 184429 (2005).

[120] N. Berry, E. M. Bittar, C. Capan, P. G. Pagliuso, and Z. Fisk, *Phys. Rev. B* **81**, 174413 (2010).

[121] J. Custers, et al., *Nature* **424**, 524 (2003).

[122] S. Friedemann, T. Westerkamp, M. Brando, N. Oeschler, and S. Wirth, *Nature Phys.* **5**, 465 (2009).

[123] M. C. Aronson, M. S. Kim, M. C. Bennett, Y. Janssen, D. A. Sokolov, and L. Wu, *J. Low Temp. Phys.* **161**, 98 (2010).

[124] A. Palenzona, *J. Less-Common Met.* **53**, 133 (1977).

[125] E. Morosan, S. L. Bud'ko, Y. A. Mozharivskyj, and P. C. Canfield, *Phys. Rev. B* **73**, 174432 (2006).

[126] A. V. Silhanek, et al., *Phys. Rev. Lett.* **96**, 206401 (2006).

[127] E. Stryjewski and N. Giordano, *Adv. Phys.* **26**, 487 (1977).

[128] R. J. Birgenau, W. B. Yelon, E. Cohen, and J. Makovsky, *Phys. Rev. B* **5**, 2607 (1972).

[129] J. F. Dillon, E. Y. Chen, and H. J. Guggenheim, *Phys. Rev. B* **18**, 377 (1978).

[130] M. Blume, L. M. Corliss, J. M. Hastings, and E. Schiller, *Phys. Rev. Lett.* **32**, 544 (1974).

[131] N. Giordano, *Phys. Rev. B* **14**, 2927 (1976).

[132] H. T. Shang and M. B. Salamon, *J. Magn. and Magn. Mater.* **15 − 18**, 419 (1980).

[133] C. Pfleiderer, *J. Phys.: Cond. Matt.***17**, S987 (2005).

[134] V. Tafour, A. Villaume, D. AOki, G. Knebel, and J. Flouquet, *J. Phys.:Conf. Series* **273**, 012017 (2011).

[135] M. S. Kim, et al., *Phys. Rev. B,* **74**, 224431, (2006).

[136] W. Knafo, et al., *Phys. Rev. B* **81**. 094403 (2010).

[137] M. A. Avila, M. Sera, and T. Takabatake, *Phys. Rev. B* **70**, 100409 (2004).

[138] S. L. Budko, P. C. Canfield, M. A. Avila and T. Takabatake, *Phys. Rev. B* **75**, 094433 (2007).

[139] E. D. Mun, S. L. Budko, A. Kreyssig, and P. C. Canfield, *Phys. Rev. B* **82**, 054424 (2010).

[140] F. Weickert, M. Brando, F. Steglich, P. Gegenwart, and M. Garst, *Phys. Rev. B* **81**, 134438 (2010).

[141] J. Flouquet, P. Haen, S. Raymond, D. Aoki, and G. Knebel, *Physica B* **319**, 251 (2002).

[142] S. A. Grigera, et al., *Science* **294**, 1063539 (2001).

[143] J. Rossat-Mignod, et al., *J. Magn. and Magn. Mater.* **52**, 111 (1985).

[144] F. S. Tautz, S. R. Julian, G. J. McMullen, and G. G. Lonzarich, *Physica B* **206 − 207**, 29 (1995).

[145] J. Flouquet, et al., *Physica B* **215**, 77 (1995).

[146] W. Wu, A. McCollam, S. A. Grigera, R. S. Perry, A. P. Mackenzie, and S. R. Julian, *Phys. Rev. B* **83**, 045106 (2011).

[147] J. Paglione, et al., *Phys. Rev. Lett.* **91**, 246405 (2003).

[148] O. Stockert, et al., *Nature Phys.* **7**, 119 (2011).

[149] R. Daou, C. Bergemann, and S. R. Julian, *Phys. Rev. Lett.* **96**, 026401 (2006).

[150] Q. Si and F. Steglich, *Science* **329**, 1161 (2010).

[151] T. Senthil, S. Sachdev, and M. Vojta, *Phys. Rev. Lett.* **90**, 216403 (2003).

[152] S. Friedemann, et al., *J. Low Temp. Phys.* **161**, 67 (2010).

[153] H. Shishido, R. Settai, H. Hariam, and Y. Onuki, *J. Phys. Soc. Japan* **74**, 1103 (2005).

[154] O. Trovarelli, et al., *Phys. Rev. Lett.* **85**, 626-629 (2000).

[155] P. Gegenwart, et al. *Phys. Rev. Lett.* **89**, 056402 (2002).

[156] P. Gegenwart, et al., *Science,* **315**, 969 (2007).

[157] A. Rosch, *Phys. Rev. Lett.* **82**, 4280 (1999).

[158] P. G. de Gennes and J. Friedel, *J. Phys. Chem. Solids* **4**, 71 (1958).

[159] M. E. Fisher, and J. S. Langer, *Phys. Rev. Lett.* **20**, 665 (1968).

[160] A. Hackl and M. Vojta, *Phys. Rev. Lett.* **106**, 137002 (2011).

[161] J. D. Thompson and J. L. Lawrence, *Handbook on the Physics and Chemistry of Rare Earths*, **19**,
ed. K A Gschneidner Jr, L Eyring, G H Lander and G R Choppin (Amsterdam: North-Holland, 1994) p 383

[162] A. V. Goltsev and M. M. Abd-Elmeguid, *J. Phys. Condens. Matter* **17**, S813 (2005).

[163] K. Ishida, et al., *Phys. Rev. B* **68**, 184401 (2003).

[164] J. Custers, et al., *Phys. Rev. Lett.* **104**, 186402(2010).

[165] H. Q. Yuan, M. Nicklas, Z. Hossain, C. Geibel, and F. Steglich, *Phys. Rev. B* **74**, 212403 (2006).

[166] T. Misawa, Y. Yamaji, and M. Imada, *J. Phys. Soc. Japan* **77**, 093712 (2008).

[167] T. Misawa, Y. Yamaji, and M. Imada, *J. Phys. Soc. Japan* **78**, 084707 (2009).

[168] C. Klingner, C. Krellner, and C. Geibel, *J. Phys.: Conf. Series* **200**, 012089 (2010).

[169] Y. Tokiwa, et al., *Phys. Rev. Lett.* **94**, 226402 (2005).

[170] P. Gegenwart, et al., *New. J. Phys.* **8**, 171 (2006).

[171] Y. Hirose, et al., *J. Phys.: Conf. Ser.* **273**, 012003 (2011).

[172] P. M. C. Rourke, et al., *Phys. Rev. Lett.* **101**, 237205 (2008).

[173] S. Viola Kusminskiy, K. S. D. Beach, A. H. Castro Neto, and D. K. Campbell, *Phys. Rev. B* **77**, 094419 (2008).

[174] G. Zwicknagl, *J. Phys.: Condens. Matter* **23**, 094215 (2011).

[175] J. Plessel, et al., *Phys. Rev. B* **67**, 180403(R) (2003).

[176] B. Andraka, and A. M. Tsvelik, *Phys. Rev. Lett.* **67**, 2886 (1991).

[177] A. M. Tsvelik, and M. Reizer, *Phys. Rev. B* **48**, 9887 (1993).

[178] M. Brando, unpublished.

[179] M. de Souza, A. Brühl, C. Strack, D. Schweitzer and M. Lang, *Phys. Rev. B* **86**, 085130 (2012).

[180] A. M. Strydom, and P. Peratheepan, RFe_2Al_{10} (R = Y, Yb). *Phys. Status Solidi B* **4**, 356 (2010).

[181] P. Khuntia, A. M. Strydom, F. Steglich, and M. Baenitz, *Phys. Status Solidi B* **250**, 525 (2013).

[182] B. C. Sales, and D. K. Wohlleben, *Phys. Rev. Lett.* **35**, 1240 (1975).

[183] D. T. Adroja, et al., *Phys. Rev. B* **42**, 2700 (1990).

[184] D. R. Hamann, *Phys. Rev.* **158**, 570, (1967).

[185] K. Samwer, and K. Winzer, *Zeitschrift für Physik B Condensed Matter* **25**, 269, (1976).

[186] A. Ramires, and P. Coleman, and A. H. Nevidomskyy, and A. M. Tsvelik, *Phys. Rev. Lett.* **109**, 176404 (2012).

[187] E. C. Stoner, *Proc. R. Soc. Lond. A* **165**, 372 (1938).

[188] G. G. Lonzarich, and L. Taillefer, *J. Phys. C: Solid State Phys.* **18**, 4339 (1985).

[189] T. Moriya, Spin fluctuations in itinerant electron magnetism. *Springer* (Berlin 1985).

[190] D. Belitz,, T. R. Kirkpatrick, and T. Vojta, *Rev. Mod. Phys.* **77**, 579 (2005).

[191] C. Pfleiderer,, S. R. Julian, and G. G. Lonzarich, *Nature* **414**, 427 (2001).

[192] D. Belitz,, T. R. Kirkpatrick, and T. Vojta, *Phys. Rev. Lett.* **82**, 4707 (1999).

[193] P. Coleman, and A. J. Schofield, *Nature* **433**, 226 (2005).

[194] G. R. Stewart, *Rev. Mod. Phys.* **73**, 797(2001).

[195] H. v. Lohneysen,, A. Rosch,, M. Vojta, and P. Wolfle, *Rev. Mod. Phys.* **79**, 1015 (2007).

[196] H. v. Lohneysen, and P. Wolfle, Lectures on the physics of strongly correlated systems XII: Twelfth Training Course, ed.*American Institute of Physics* Avella A. and Mancini, F. (2008).

[197] F. Steglich, et al. *J. Phys.: Cond. Matt.* **22**, 164202 (2010).

[198] P. Coleman, C. Pépin, Q. Si, and R. Ramazashvili, *J. Phys. Cond. Matt.* **13**, R723 (2001).

[199] Q. Si,, S. Rabello,, K. Ingersent, and J. L. Smith, *Nature* **413**, 804 (2001).

[200] T. Senthil, S. Sachdev, and M. Vojta, *Phys. Rev. Lett.* **90**, 216403 (2003).

[201] S. Friedemann, et al. *Nature* **5**, 465 (2009).

[202] S. Friedemann, et al. *J. Low Temp. Phys.* **161**, 67 (2010).

[203] H. Shishido,, R. Settai,, H. Hariam, and Y. Onuki, *J. Phys. Soc. Japan* **74**, 1103 (2005).

[204] T. Park,, M. J. Graf,, L. Boulaevskii,, J. L. Sarrao,, and J. D. Thompson, *Proc. Nat. Acad. Sci.* **105**, 6825 (2008).

[205] M. Nicklas, et al. *Phys. Rev. Lett.* **82**, 4268 (1999).

[206] D. Moroni-Klementowicz, et al. *Phys. Rev. B* **79**, 224410 (2009).

[207] N. P. Butch, and M. B. Maple, *Phys. Rev. Lett.* **103**, 076404 (2009).

[208] R. P. Smith, et al. *Nature* **455**, 1220(2008).

[209] C. Pfleiderer, et al., *J. Phys. Cond. Matt.* **21**, 164215 (2009).

[210] A. Kerkau, et al., *Zeitschrift für Kristallographie-New Crystal Structures* **227**, 289, (2012).

[211] R. Viennois, et al., *Eur. Phys. J. B* **46**, 257 (2005).

[212] S. Jia, S. L. Bud'ko, G. D. Samolyuk, and P. C. Canfield, *Nature Phys.* **3**, 334 (2007).

[213] M. Brando, et al., *Phys. Rev. Lett.* **101**, 026401 (2008).

[214] W. J. Duncan, et al., *Phys. Stat. Solidi B* **247**, 544 (2010).

[215] A. W. Rost, et al., *Phys. Stat. Solidi B* **247**, 513(2010).

[216] T. Waki, et al., *J. Phys. Soc. Japan* **79**, 043701 (2010).

[217] P. G. Niklowitz, et al., *Phys. Rev. B* **72**, 024424 (2005).

[218] M. J. Steiner, F. Beckers, P. G. Niklowitz, and G. G. Lonzarich, *Physica B* **329 − 333**, 1079 (2003).

[219] V. M. T. Thiede, T. Ebel, and W. Jeitschko, *J. Mater. Chem.* **8**, 125 (1998).

[220] L. J. Farrugia, WinGX Program. *J. Appl. Cryst.* **32**, 837 (1999).

[221] J. C. Waerenborgh, et al. *J. Alloys and Compd.* **323 − 324**, 78 (2001).

[222] M. S. Kim, and M. C. Aronson, *Journal of Physics: Condensed Matter* **23**, 164204, (2011).

[223] M. S. Kim, M. C. Bennett and M. C. Aronson, *Physica B: Condensed Matter* **403**, 1411, (2008).

[224] A. Ochiai, et al., *J. Phys. Soc. Jpn.* **80**, 3705, (2011).

[225] S. Yasuyuki, S. Toshiro, I. Ken, S. Kiyohiro and O. Yoshichika, *J. Phys. Soc. Jpn.* **81**, 103601, (2012).

[226] R. Pöttgen, et al., *J. Solid State Chem.* **145**, 668, (1999).

[227] A. S. Kutuzov, and A. M. Skvortsova, *Journal of Physics: Conference Series,* **324**, 012039, (2011).

[228] K. Prokeš, et al., *J. Magn. Magn. Mater.,* **202**, 451, (1999).

[229] J. A. Blanco, et al., *Phys. Rev. B,* **73**, 212411, (2006).

[230] W. Miiller, and M. C. Aronson (unpublished).

[231] C. Rüegg, et al., *Nature,* **423**, 62, (2003).

[232] S. E. Sebastian, et al., *Nature,* **441**, 617, (2006).

[233] V.V. Novikov, et al., *J. Appl. Phys.,* **111**, 063907, (2012).

[234] B. Thielemann, et al., *Phys. Rev. Lett.* **102**, 107204, (2009).

[235] B. Thielemann, et al., *Phys. Rev. B* **79**, 020408, (2009).

[236] C. Rüegg, et al., *Phys. Rev. Lett.* **101**, 247202, (2008).

[237] M. Klanjšek, et al., *Phys. Rev. Lett.* **101**, 137207, (2008).

[238] A. M. Strydom, et al., *Physica B: Condensed Matter* **404**, 19, 2981, (2009).

[239] Y. Muro, K. Motoya, Y. Saiga, and T. Takabatake, *Journal of the Physical Society of Japan* **78**, 8, (2009).

[240] T. Takesaka, et al., *Journal of Physics: Conference Series* **200**, 1, 012201, (2010).

[241] Y. Muro, et al., *Journal of Physics: Conference Series* **200**, 1, 012136, (2010).

[242] S. Kimura, et al., *Phys. Rev. B* **84**, 165125, (2011).